

Dissertation
submitted to the
Combined Faculty of Natural Sciences and Mathematics
of the Ruperto Carola University Heidelberg, Germany
for the degree of
Doctor of Natural Sciences (Dr. rer. nat.)

Presented by
B.Sc. Haifeng Lang

born in: Jilin, China

Oral examination: 08-11-2022

Quantum Dynamics of Chemical Systems
with Large Number of Degrees of
Freedom: Linearized Phase Space Methods
and Quantum Simulations

Referees: Prof. Dr. Oriol Vendrell Romagosa
Prof. Dr. Philipp Hans Juergen Hauke

This thesis is dedicated to you.

Abstract

Nonadiabatic quantum dynamics plays an important role in a wide range of chemical reactions and femtochemistry experiments. However, numerically converged simulations are typically only affordable for small size systems because the computational efforts generically increase exponentially. This thesis is devoted to the theoretical analysis of two candidates of simulation methods for large size systems, linearized phase space methods and quantum simulations.

Linearized phase space methods, for instance, fully linearized methods, partially linearized methods, and symmetrical quasi-classical windowing, approximate the quantum dynamics as the classical dynamics, and quantum effects are accounted for by Monte Carlo sampling of the initial quantum phase space. The major drawback is that the sampling of independent phase space trajectories neglects quantum coherence and interference. For condensed phase simulations, this limitation fortunately is only minor. Different linearized phase space methods are mainly characterized by the initial electronic phase space selections, and it is believed that the choice of electronic phase space determines the accuracy of the method. While there are lots of numerical results to support this argument, a rigorous theoretical analysis is still outstanding. Rewriting fully and partially linearized methods in a unified expression, we establish a rigorous measure of the short-time accuracy, the intra-electron correlation, which has a close connection to the initial electronic phase space. The methods with correct intra-electron correlation are more accurate in the short-time region for various chemical motivated models than the methods with a wrong one. For various popular linearized phase space methods, including many fully and partially linearized methods, we also give either a proof of correct intra-electron correlation sampling or an explicit violation example. Our theoretical analysis gives an explanation of the accuracy order of linearized phase space methods reported in the literature. Moreover, the intra-electron correlation can be a guideline for the development future linearized phase space methods.

Further, we introduce the generalized discrete truncated Wigner approximation (GDTWA), which is a well-established linearized phase space method in the field of quantum lattice models, into chemistry. The GDTWA uses the Wootters' discrete phase space for electrons, which can sample the intra-electron correlation correctly for diagonal states. We reformu-

late the GDTWA in the unified expression of linearized phase space methods, which shows that the GDTWA is a fully–partially hybrid method. With the help of this reformulation, we not only reduce the computational efforts, but also demonstrate a reduced zero-point energy accounting without an explicit zero-point energy parameter in the GDTWA. Numerical benchmarks on scattering models and linear vibronic coupling models show a robust performance on various chemical motivated models. Also, we develop two GDTWA, approach I and II, for a particle in gauge vector potentials. Theoretical analysis shows that the two approaches favor the simulation of synthetic gauge field and on-the-fly simulation of molecular dynamics in the adiabatic representation, respectively. Our numerical results of ultracold atoms, linear vibronic coupling models as synthetic gauge fields, as well as on-the-fly simulations of linear vibronic coupling models confirm the analysis.

To overcome the difficulty of simulating quantum mechanics arising from exponentially increasing Hilbert space, quantum simulations use controllable quantum devices which obey the rule of quantum mechanics. Nowadays, the imperfect controls of quantum devices have a huge impact on the accuracy of the simulations. Specifically, when the errors of the implementations break symmetries of the system, simulation results could even be qualitatively wrong. We rigorously develop an experimentally feasible linear penalty method to suppress the symmetry-breaking errors. Numerical benchmarks of the lattice gauge theory and the hydrogen molecule show good performances on protections of symmetries, local observables, and wave functions.

Our theoretical analysis on both linearized phase space methods and quantum simulations illustrate the possibilities of simulating large size systems with large potential for applications in quantum chemistry and related areas.

Kurzfassung

Die nichtadiabatische Quantendynamik spielt eine wichtige Rolle in einer Vielzahl von chemischen Reaktionen und femtochemischen Experimenten. Numerisch konvergierte Simulationen sind jedoch nur für kleine Systeme erschwinglich, da der Rechenaufwand exponentiell ansteigt. Diese Diplomarbeit widmet sich der theoretischen Analyse von zwei Kandidaten für Simulationsmethoden für große Systeme, linearisierte Phasenraummethoden und Quantensimulationen.

Linearisierte Phasenraumverfahren, beispielsweise vollständig linearisierte Verfahren, teilweise linearisierte Verfahren und symmetrisches quasi-klassisches Fenstern, approximieren die Quantendynamik als klassische Dynamik, und Quanteneffekte werden durch Monte-Carlo-Sampling des anfänglichen Quantenphasenraums berücksichtigt. Der Hauptnachteil besteht darin, dass unabhängige Phasenraumtrajektorien Quantenkohärenz und Interferenz vernachlässigen. Dies hat jedoch keine großen Auswirkungen auf Simulationen mit kondensierter Phase. Verschiedene linearisierte Phasenraumverfahren sind hauptsächlich durch die anfängliche Auswahl des elektronischen Phasenraums gekennzeichnet, und es wird allgemein angenommen, dass die Wahl des elektronischen Phasenraums die Genauigkeit des Verfahrens bestimmt. Obwohl es viele numerische Ergebnisse gibt, die dieses Argument stützen, fehlt bisher eine rigorose theoretische Analyse. Indem wir vollständig und teilweise linearisierte Methoden in einen einheitlichen Ausdruck umformulieren, etablieren wir ein rigoroses Maß für die Kurzzeitgenauigkeit, nämlich die Intra-Elektronen-Korrelation, die eine enge Verbindung zum anfänglichen elektronischen Phasenraum hat. Die Methoden mit korrekter Intra-Elektronen-Korrelation sind im Kurzzeitbereich für verschiedene chemisch motivierte Modelle genauer als die Methoden mit falscher. Für verschiedene gängige linearisierte Phasenraummethoden, einschließlich vieler vollständig und teilweise linearisierter Methoden, wir geben auch entweder einen Beweis der korrekten Intra-Elektronen-Korrelations-Sampling oder ein explizites Verletzungsbeispiel. Unsere theoretische Analyse gibt eine Erklärung für die Genauigkeit verschiedener linearisierter Phasenraumverfahren, die in der Literatur berichtet wurden. Darüber hinaus kann die Intra-Elektronen-Korrelation eine Richtlinie für zukünftig vorgeschlagene linearisierte Phasenraummethoden sein.

Weiterhin führen wir die verallgemeinerte diskrete trunkierte Wigner-Näherung (GDTWA)

in die Chemie ein, die eine etablierte linearisierte Phasenraummethode im Bereich der Quantengittermodelle ist. Das GDTWA verwendet den diskreten Phasenraum von Wootters für Elektronen, der die Intra-Elektronen-Korrelation für die diagonalen Zustände korrekt sampeln kann. Wir formulieren die GDTWA in dem vereinheitlichten Ausdruck linearisierter Phasenraumverfahren neu, und eine solche Neuformulierung zeigt, dass die GDTWA eine vollständig–teilweise hybride Methode ist. Mit Hilfe dieser Neuformulierung kann man nicht nur den Rechenaufwand reduzieren, sondern wir demonstrieren auch eine reduzierte Nullpunktenergiebilanzierung ohne expliziten Nullpunktenergieparameter in der GDTWA. Numerische Benchmarks für Streumodelle und lineare vibronische Kopplungsmodelle zeigen eine robuste Leistung für verschiedene chemisch motivierte Modelle. Außerdem entwickeln wir zwei GDTWA, Ansatz I und II, für Partikel in Eichvektorpotentialen. Theoretische Analysen zeigen, dass die beiden Ansätze für die Simulation des synthetischen Eichfelds respektive die On-the-Fly-Simulation der Molekulardynamik in der adiabatischen Darstellung zu bevorzugen sind. Unsere numerischen Ergebnisse für ultrakalten Atomen, linearen vibronischen Kopplungsmodellen als synthetische Eichfelder sowie on-the-fly-Simulationen von linearen vibronischen Kopplungsmodellen bestätigen die Analyse.

Um die Schwierigkeit zu überwinden die Quantenmechanik zu simulieren, die sich aus dem exponentiell zunehmenden Hilbert-Raum ergibt, verwenden Quantensimulationen steuerbare Quantenhardware, die der Regel der Quantenmechanik gehorcht. Heutzutage hat die unvollkommene Steuerung von Quantengeräten enorme Auswirkungen auf die Genauigkeit der Simulationen. Insbesondere wenn die Fehler der Implementierungen Symmetrien des Systems brechen, können Simulationsergebnisse sogar qualitativ falsch sein. Wir entwickeln rigoros eine experimentell durchführbare lineare Penalty-Methode, um die symmetriebrechenden Fehler zu unterdrücken. Numerische Benchmarks für Gittereichtheorien und das Wassermolekül zeigen gute Leistungen beim Schutz von Symmetrien, lokalen Observablen und Wellenfunktionen.

Unsere theoretische Analyse sowohl linearisierter Phasenraummethoden als auch Quantensimulationen illustriert Möglichkeiten zur Simulation großer Systeme, mit Auswirkungen auf eine Vielzahl von Anwendung in der Quantenchemie und verwandten Forschungsgebieten.

Contents

Abstract	vii
Kurzfassung	ix
Contents	xi
List of Figures	xv
List of Tables	xxi

I Quantum dynamics in Chemical Systems - Introduction and Background	1
1 Introduction	3
2 Hamiltonian of chemical systems	7
2.1 Molecular Hamiltonian	7
2.1.1 Born–Oppenheimer expansion	8
2.1.2 Group Born–Oppenheimer Approximation	11
2.1.3 Diabatization methods	12
2.2 Electronic Hamiltonian	14
2.2.1 Second quantization representation of electronic Hamiltonian	14
2.2.2 Hartree–Fock method and beyond	18
2.3 Multiconfiguration Time Dependent Hartree Method	24
2.3.1 Time Dependent Variational Principle	24
2.3.2 Standard Methods and Time Dependent Hartree Methods	26
2.3.3 Wave Function Ansatz and Equation of Motion	28
2.3.4 Numerical Implementations	33
2.4 Models	36
2.4.1 Tully’s models	36

2.4.2	Spin-boson models	37
2.4.3	Site-exciton Models	39
2.4.4	Linear vibronic models	40
2.4.5	Atom-in-cavity models	43
 II Linearized Phase Space Methods for Nonadiabatic Quantum Dynamics		 45
3	Linearized phase space methods - review, intra-electron correlation and short time accuracy analysis	49
3.1	Linearized Semiclassical Method for Nuclear Dynamics in one PES	51
3.2	Linearized Semiclassical Method for Nuclear Dynamics in Multi-PES	53
3.2.1	Fully linearized methods	54
3.2.2	Partially linearized methods	59
3.2.3	Symmetrical quasi-classical windowing	61
3.3	Intra-electron Correlation and Short-time Accuracy	63
3.3.1	Unified expression of linearized phase space methods	63
3.3.2	Definition of the intra-electron correlation	63
3.3.3	Classification of linearized phase space methods	65
3.3.4	Short-time analysis for general Hamiltonians	65
3.3.5	Short-time analysis for scattering models	66
3.3.6	Short-time analysis for cavity-modified molecular dynamics	67
3.3.7	Short-time analysis for spin-boson models	67
3.4	Proof of classifications of linearized phase space methods	68
3.4.1	Ehrenfest method, PBME and LSC-IVR	68
3.4.2	mLSC	69
3.4.3	Spin-LSC	71
3.4.4	Spin-PLDM and PLDM	71
3.5	Conclusions	71
4	Generalized discrete truncated Wigner approximation for nonadiabatic dynamics	73
4.1	Generalized Discrete Truncated Wigner Approximation	75
4.1.1	Theory	75
4.1.2	Numerical Results	84
4.2	GDTWA for particles in the gauge vector potentials	92
4.2.1	Theory	92

4.2.2	Numerical results	100
4.3	Conclusions	110
III Quantum Simulations for Quantum Dynamics of Chemical Systems		113
5	Background on Quantum Simulators	117
5.1	Digital quantum simulator	118
5.1.1	Basics of circuit models of quantum computations	118
5.1.2	Digital quantum simulation	122
5.1.3	Fault-tolerant quantum computation	123
5.1.4	Noisy intermediate-scale quantum era	126
5.2	Analog quantum simulator	128
6	Symmetry protected quantum simulators for quantum dynamics	131
6.1	Protection scheme based on quantum Zeno effect	132
6.1.1	Continuous quantum Zeno effect	132
6.1.2	Linear penalty method for AQSs	133
6.1.3	Unitary kicks version of the quantum Zeno effect	135
6.2	Application: lattice gauge theory	136
6.2.1	Basics of $U(1)$ lattice gauge theory	136
6.2.2	Numerical results of AQSs	138
6.2.3	Numerical results of DQSs	140
6.3	Application: Hydrogen molecule	143
6.4	Conclusion	145
7	Conclusions and Outlook	147
	Bibliography	151
	Appendices	181
A	Explicit time derivatives	183
	Acknowledgements	189
	List of Papers	191
	Eidesstattliche Versicherung	193

List of Figures

4.1	Transmission probabilities to the upper surface T_{11} (dashed line) and the lower surface T_{12} (solid line) for the Tully’s single avoided crossing model 1. GDTWA (blue) fits the quantum results (black) nearly perfect in the high momentum region ($P_0 > 10$), and is qualitatively correct in the low momentum region.	85
4.2	Transmission probabilities to the lower surface T_{11} (dashed line) and the upper surface T_{12} (solid line) for the Tully’s dual avoided crossing model 1. GDTWA (blue) fits the quantum results (black) nearly perfect in the high energy region, and is qualitatively correct in the low energy region.	86
4.3	Second diabatic state population of a three-modes two-states model based on Pyrazine (see table 4.1), computed using different methods. The GDTWA result (blue solid line) compares fairly well to the exact quantum dynamics (black solid). While GDTWA and, even more so, the Spin-PLDM method (red dashed) underestimate the mean value reached at long times, the Ehrenfest method (green dashed) overestimates it. The PLDM methods (yellow dashed) considerably overestimates the damping of the oscillations.	88
4.4	Populations of the tuning coordinates $\langle x_1 \rangle$ and $\langle x_{6a} \rangle$ of the Pyrazine-based Model I. The GDTWA (blue solid line) and Spin-PLDM (red dashed) results fail to capture the oscillation amplitudes, but still give a qualitatively fair description on the frequency. In contrast, the Ehrenfest (green dashed) and PLDM methods (yellow dashed) mismatch the oscillation pattern of the exact quantum results (black dashed) after a few periods.	89
4.5	Expectation values of second-order correlations of the tuning coordinates $\langle x_1^2 \rangle$ and $\langle x_{6a}^2 \rangle$, and the coupling coordinate $\langle x_{10a}^2 \rangle$ of the Pyrazine-based Model I. The color notations are identical to Fig. 4.3. The GDTWA (blue solid line) and Spin-PLDM (red dashed) results qualitatively predict the ideal higher-order correlation, while the Ehrenfest (green dashed) and PLDM methods (yellow dashed) deviate significantly from the exact quantum results (black dashed).	90

- 4.6 Populations of all three diabatic states of a five-modes three-states model based on Benzene radical cation (see table 4.2), computed using different semiclassical techniques. The GDTWA result (blue solid line) compares fairly well to the exact quantum dynamics (black solid) for all the three diabatic states populations, while all the other methods considered fail to describe the long time populations. 91
- 4.7 Populations of tuning coordinates $\langle x_2 \rangle$, $\langle x_{16} \rangle$, and $\langle x_{18} \rangle$ of the Model II that is based on Benzene radical cation. The GDTWA result (blue solid line) matches the exact quantum dynamics (black solid) best and slightly outperforms the Spin-PLDM result (red dashed). 91
- 4.8 The second-order correlations of the tuning coordinates $\langle x_2^2 \rangle$, $\langle x_{16}^2 \rangle$, and $\langle x_{18}^2 \rangle$ of Model II. Both GDTWA (blue solid line) and Spin-PLDM (red dashed) match the exact quantum results (black solid) for the dynamics of $\langle x_2^2 \rangle$. GDTWA slightly outperforms the Spin-PLDM result (red dashed) for the dynamics of $\langle x_{16}^2 \rangle$, while GDTWA is noticeably more accurate than all the other methods for the dynamics of $\langle x_{18}^2 \rangle$ 92
- 4.9 Second-order correlations of the coupling coordinates $\langle x_8^2 \rangle$ and $\langle x_{19}^2 \rangle$ of Model II. For the dynamics of $\langle x_8^2 \rangle$, both GDTWA (blue solid line) and Spin-PLDM (red dashed) match the exact quantum results (black solid), with GDTWA slightly outperforming the Spin-PLDM result. For $\langle x_{19}^2 \rangle$, both methods reproduce qualitative features of the exact evolution better than the other considered semiclassical techniques. 93
- 4.10 The conceptual diagram of constructing the semiclassical theory in the adiabatic representation (vanishing gauge curvature). Inequivalent results can be obtained because de-quantization and canonical transformation are not commuting operations. The blue arrows represent de-quantization then canonical transformation, which leads to the correct semiclassical theory for on-the-fly simulations. Gauge transformation then de-quantization with p_{kin} (Approach II, red arrows) also gives the correct semiclassical theory, while gauge transformation then de-quantization with p_{can} (Approach I, black arrow) cannot. We stress that “improper” and “correct” refers only to the adiabatic representation such as required for on-the-fly simulations. In other scenarios, Approach I may provide better simulation results than Approach II. 99
- 4.11 Population of $\langle x(t) \rangle$. Approach I (red solid) fits the exact result (black solid), however, Approach II (blue solid) has a huge mismatch with exact result. 101

- 4.12 Trajectories of the expectation value of $\langle y_{1,2}(t) \rangle - \langle x(t) \rangle$. Both Approach I (red solid) and Approach II (blue solid) show the separation of the projected expectation value by spin state. However, Approach II fails to reproduce the exact solution while Approach I is also quantitatively correct. 101
- 4.13 Population of the diabatic excited state of a three-modes two-states model based on pyrazine. Results are obtained by Approach I (red solid), Approach II (blue solid line), and MCTDH (black solid). While both semiclassical approximations qualitatively describe the long-time relaxation, Approach II completely fails to capture the oscillations in the short to medium time dynamics. 103
- 4.14 Population of the excited adiabatic state of a two-modes two-states model based on pyrazine. Results are obtained by aGDTWA (blue solid line), Ehrenfest method (yellow dashed line), SQC (red dashed), GDTWA in the diabatic representation (blue rectangles), PLDM (brown dashed), Spin-PLDM (green dashed) and MCTDH (black solid). All the semiclassical methods considered capture the dynamics qualitatively, but to different levels of quantitative agreement, with GDTWA being among the top-performing methods. Model parameters: $\omega_1 = 3.650 \times 10^{-3}$, $\omega_2 = 4.186 \times 10^{-3}$, $a = 48.45$, $c = 4.946 \times 10^{-4}$ and $\Delta = 0.02757$ 104
- 4.15 Similar to Fig. (4.14), but for BMA-based model. All the methods capture the dynamics qualitatively. Model parameters: $\omega_1 = 7.743 \times 10^{-3}$, $\omega_2 = 6.680 \times 10^{-3}$, $a = 31.05$, $c = 8.092 \times 10^{-5}$, and $\Delta = 0.00000$ 106
- 4.16 Similar to Fig. (4.14), but for Butatriene-based model. All the methods capture the dynamics qualitatively. Model parameters: $\omega_1 = 9.557 \times 10^{-3}$, $\omega_2 = 3.3515 \times 10^{-3}$, $a = 20.07$, $c = 6.127 \times 10^{-4}$, and $\Delta = 0.01984$ 106
- 4.17 Population of position $\langle X \rangle$ and kinematic momentum $\langle P_X \rangle$ of a two-modes two-states model based on pyrazine. Results are obtained by aGDTWA (blue solid line), Ehrenfest method (yellow dashed line), SQC (red dashed), GDTWA in the diabatic representation (blue rectangles), PLDM (brown dashed), Spin-PLDM (green dashed), and MCTDH (black solid). All the methods capture the dynamics qualitatively and even quantitatively, especially in the case of aGDTWA and SQC. 107
- 4.18 Similar to Fig. (4.17), but for BMA-based model. All the methods capture the dynamics qualitatively. 107
- 4.19 Similar to Fig. (4.17), but for Butatriene-based model. All the methods capture the dynamics qualitatively, Spin-PLDM, SQC and aGDTWA even quantitatively. 108

- 4.20 Population of the adiabatic ground state-specific position $\langle X \rangle_g$ and the adiabatic excited state-specific position $\langle X \rangle_e$ of a two-modes two-states model based on pyrazine. Results are obtained by aGDTWA (blue solid line), Ehrenfest method (yellow dashed line), SQC (red dashed), GDTWA in the diabatic representation (blue rectangle), PLDM (brown dashed), Spin-PLDM (green dashed), and MCTDH (black solid). All the methods capture the dynamics qualitatively. 108
- 4.21 Similar to Fig. (4.20), but for BMA-based model. All the methods capture the dynamics qualitatively. 109
- 4.22 Similar to Fig. (4.20), but for Butatriene-based model. All the methods capture the $\langle X \rangle_g$ dynamics qualitatively, while $\langle X \rangle_e$ dynamics is challenging for them except SQC. 109
- 5.1 Circuit diagram of [[3,1,2]] QEC code for detection and correction of single qubit error. The three-line bundle represents the other qubits in the quantum register, three physical qubits encode the logical qubit, and two additional ancilla qubits are introduced. 125
- 6.1 Time averaged gauge violation of H_0 at $\mu = 0.5J$, with the error $H_1 = \sum_j (\tau_{j,j+1}^x + \sigma_j^+ \sigma_{j+1}^+ + \sigma_j^- \sigma_{j+1}^-)$ at $\lambda = 0.05J$, under the linear penalty Eq. (6.29). The initial state is drawn on top, where the circle represents the sites are empty. As expected, sequences in (a), (b), and (c) can provide promising protection, keeping gauge-symmetry violations on a level $\sim (\lambda/V)^2$. Surprisingly, they work up to all the numerically accessible time. (d) A simple sequence completely fails to protect symmetries. 139
- 6.2 The dynamics of time averaged (a) electric field and (b) matter occupation of faulty gauge theory $H = H_0 + \lambda H_1 + V \sum_j (-1)^j G_j$ as well as the ideal gauge theory H_0 . As predicted by the QZE, linear penalty terms make the faulty dynamics coincide with the ideal dynamics up to a timescale $\propto 1/V$. Meanwhile, the differences between the ideal-theory and the faulty-theory dynamics are suppressed by V and grows linearly in time, which are shown in the insets. 140

- 6.3 Elementary unit for one Trotter step of the quantum circuit. σ_j ($\tau_{j,j+1}$) denotes a qubit representing a matter (gauge) field at matter site j [gauge link ($j, j+1$)]. The implementation of H_J can be obtained by Cirq [332]. R_x and R_z denote the x -rotation and z -rotation gates, respectively. The angles of them are determined by the Trotter step and Hamiltonian parameters. “+” denotes the unitary gate $\exp[-i(\sigma_j^+ \sigma_{j+1}^+ + \text{H.c.})\lambda\delta t]$ with Trotter time step δt 141
- 6.4 Numerical benchmarks of gauge violation dynamics in a DQS, at various values of gauge-protection strength V , with $\mu/J = 0.5$, $\lambda/J = 0.05$, and $L = 6$ matter sites. (a) Violation ε dynamics for a Trotter time step $\delta t = 0.2/J$ (solid lines), and the corresponding numerical data for the AQS are shown in dotted lines of the same color. (b) The gauge violation at final time $t_f = 20/J$ in the AQS and in the DQS for various Trotter time steps (see legend). The gauge violation reaches a broad minimum around the ideal protection strength of $V_{\text{ideal}} \approx \pi/(2\bar{c}\delta t) - \xi$, see Eq. (6.37). (c) Ideal protection strength V_{ideal} that provides the minimal time averaged gauge violation $\bar{\varepsilon}$. Blue diamonds are numerically extracted data points, and the red line is given by Eq. (6.37) with $\xi = 0.58J$. (d) Rescaled mean gauge violation depending on protection strength for various Trotter time steps δt . The results collapse around their minimum, which suggests a universal behavior. 142
- 6.5 Quench dynamics of population and overlap of a hydrogen molecule in the minimal basis for various protection strength (See legends of (a)). (a) Population of state $|0011\rangle_f$ for various protection strength. While the dynamics of zero protection (black solid) is qualitatively wrong, a moderate protection strength $V = 1$ can already yield qualitatively correct dynamics, and it is almost indistinguishable for the results of $V = 10$ (blue solid) and the exact results (purple square). (b) Similar to (a), but for the state $|1100\rangle_f$. (c,d) Dynamics of the real and imaginary part of the overlap, respectively. $1 - R \sim 10^{-4}$, and $|I| \sim 10^{-3}$ for protection strength $V = 10$ suggests a promising protection on the wave function. 145

List of Tables

4.1	Parameters of Model I that is based on Pyrazine. All quantities are given in eV.	86
4.2	Parameters of Model II based on Benzene radical cation. All quantities are given in eV.	87
5.1	Error gate, final state before measurements and correct gate circuit diagram of $[[3,1,2]]$ QEC code. Although the phase-flip errors cannot be corrected by the $[[3,1,2]]$ QEC code, it can still be efficient when bit-flip errors dominate.	126

Part I

Quantum dynamics in Chemical Systems - Introduction and Background

Chapter 1

Introduction

Understanding chemistry quantitatively at the molecular level is the theoretical foundation of many ultimate goals of chemists', for instance, designing new molecules from the bottom up, manipulating chemical reactions, etc. The particular challenge of the understanding is the complexity of numerically solving Schrödinger equation with large numbers of degrees of freedom (DOF), which are proportional to the sum of electron numbers and nuclei numbers. The fundamental limitation comes from the exponentially increasing Hilbert space in quantum mechanics. A typical strategy of reducing the computational efforts is employing the Born–Oppenheimer approximation for stationary problems. Thanks to the large mass difference between electrons and nuclei, one can treat these two types of DOFs separately. First, one can neglect the nuclear kinetic energy operator and treat nuclear configurations as parameters, then perform the electronic structures computations (solving eigenequations of the electronic Hamiltonian) for different nuclear configurations to determine the potential energy surfaces (PESs), and giving the so-called electronic states as eigenstates. The Born–Oppenheimer approximation (also called adiabatic approximation) states that the total wave function can be approximated as the product of one electronic state and the nuclear wave function [1, 2]. The number of DOF of the electronic Hamiltonian is proportional to the electron numbers under the framework of the Born–Oppenheimer approximation for stationary problems. Meanwhile, electronic structure computation algorithms with polynomial complexity are often good enough approximations [3–16], which can further reduce the computational efforts. However, high precision electronic structure computations for large size systems are still extremely expensive, or even impractical.

For many interesting phenomena, for instance, site-to-site energy transfer dynamics in light-harvesting/photosynthetic pigment complexes [17, 18], spectroscopy of molecules [2, 19], molecules in cavities [20–28], chemical reactions [29], and femtochemistry [30], stories are much more complicated. In these scenarios, transitions between electronic states are no longer negligible, and the Born–Oppenheimer approximation breaks down, which

are referred to as nonadiabatic quantum dynamics [31, 32]. One must use the group Born–Oppenheimer approximation, in which the total wave function is expressed as multi-electronic states weighted by their own time dependent nuclear wave functions [2]. Because the electronic states are time independent and pre-determined by electronic structure computations, one can regard them as an additional discrete DOF coupled with nuclear DOFs. The molecular Hamiltonian under the framework of group Born–Oppenheimer approximation can be generated accordingly, for details, see chapter 2. To summarize, solving the time dependent Schrödinger equation for a molecule is transferred as a two-step problem. The first step is performing electronic structures computations (a time independent eigenequation problem), and the second step is solving the time dependent Schrödinger equation for nuclei coupled with a discrete electronic DOF. Nonadiabatic quantum dynamics is often referred to as the second step of the problem.

The state-of-the-art numerically converged algorithm for nonadiabatic quantum dynamics, multiconfiguration time dependent Hartree (MCTDH) method [33–35], still suffers from the exponentially increase of Hilbert space. Hence, for systems with a large number of DOFs, convergence—i.e., a systematic approach towards the exact results—cannot be reached. There are similar substantial limitations in other competitors in terms of numerically converged algorithms despite a great deal of efforts that have been made in recent years. For instance, multilayer MCTDH (ML-MCTDH) [36–38] and matrix product state (MPS) [39, 40] require low entanglement between different DOFs, quantum Monte Carlo (QMC) [41, 42] suffers from the sign problem, etc. These limitations make their applications for systems with large numbers of DOFs restricted. Additionally, the computational efforts of these algorithms are not cheap either.

In a word, the requirement of huge computational efforts for systems with large DOFs, which arises from the incompatibility of quantum mechanics and classical computers, is troublesome for the simulations. In order to perform simulations for systems with large numbers of DOFs, one has to either do more approximations, or use the hardware beyond classical computers. In this thesis, we will discuss two possible solutions from these two aspects, approximating the quantum dynamics as classical dynamics, and using quantum devices simulating quantum systems, which are referred to as linearized phase space methods [43–80] and quantum simulations [81–85], respectively. Linearized phase space methods can give reasonable predictions in various models, but they cannot reach the exact results systematically. Quantum simulations can achieve accurate results but suffer from imperfect control of quantum simulators. The aim of this thesis is to understand the key factors of the accuracy of linearized phase space methods as well as quantum simulations, and improve the accuracy of them. We will mainly focus on their applications on orthodox nonadiabatic quantum dynamics, and give short discussions on the application of electronic structure

computations as well as nonadiabatic quantum dynamics under a novel framework [86, 87] in chapter 6. Also, we point out that the application ranges of the two methods are not limited to the nonadiabatic quantum dynamics. In fact, they have lots of applications in the field of gauge theories [88–94], quantum lattice models [47, 48, 52], and so on.

The linearized phase space methods, which only account for the quantum effects in the initial phase space, are not numerically converged methods. Such approximations neglect quantum coherence and interference, but still give reasonable accuracy for condensed phase problems. Independent phase space trajectories make the algorithms trivially parallelizable, and the Monte Carlo sampling of initial phase space makes the computational efforts insensitive to the numbers of DOFs. Roughly speaking, all linearized phase space methods sample the nuclear DOF in the Wigner phase space, and different methods are mainly characterized by the electronic phase space choices [32, 95, 96]. There are lots of numerical benchmarks showing the electronic phase space choices have a huge impact on the accuracy of methods, while rigorous connections are still not well-established in the existing literature. Such a connection will be established in chapter 3 of this thesis. Additionally, we will also present an advanced linearized phase space method, generalized discrete truncated Wigner approximation (GDTWA) [47, 48, 52, 95], and its two variants, GDTWA for particles in gauge vector potentials (gGDTWA) approach I and approach II, in chapter 4.

An alternative computing paradigm to calculations on classical computers is currently emerging in the form of quantum simulation. Quantum simulations require a specific type of hardware, quantum simulators [81–85], which obey the rule of quantum mechanics. The spirit of quantum simulations for nonadiabatic quantum dynamics is similar to the wind tunnel experiments for aerohydrodynamics, i.e., let nature compute itself [83]. If one can control the quantum simulators perfectly, quantum simulations can give quantitative predictions for quantum dynamics. However, realistic realizations of quantum simulations always have errors. Specifically, while errors in present quantum simulators are moderate, they are nonetheless far away from negligible, in particular also because they can violate the symmetries of the target model. In chapter 6, we will present an experimentally feasible linear penalty method to suppress errors in quantum simulations.

The thesis includes three parts. The first part has two chapters, this introduction and chapter 2, where we review the common procedures of investigating nonadiabatic quantum dynamics, including group Born–Oppenheimer approximation, constructing diabatic Hamiltonians, electronic structure simulations, numerically converged methods for nuclear dynamics, and typical models of nonadiabatic processes. Linearized phase space methods will be presented in the second part (chapter 3 and 4). In chapter 3, we will show that intra-electron correlation is a rigorous measure of the short-time accuracy for linearized phase space methods. We also use the intra-electron correlation to explain the order of the short-

time accuracy observed in previous references. In chapter 4, we will present the theoretical analysis and numerical benchmarks of GDTWA, which is a well-known linearized phase space methods for quantum lattice models, here applied to chemical systems. These results show that GDTWA is also a good method for various chemical models. We also further develop two GDTWA methods for particles in gauge vector potentials, which has a close connection with linear vibronic coupling models and on-the-fly simulations. The third part (chapter 5 and 6) will discuss quantum simulations. In chapter 5, we will review the basic knowledge of quantum simulations, including digital quantum simulations, analog quantum simulations, quantum algorithms, fault-tolerant quantum computation, noisy intermediate scale quantum era, quantum error correction, and quantum error mitigation. In chapter 6, an experimentally feasible quantum error mitigation technique, the linear penalty method, will be discussed. The method is rigorously derived from the quantum Zeno effect [97–99]. Numerical results of lattice gauge theory and hydrogen molecule show excellent performances on protecting symmetries, local observables, and wave functions. Chapter 7 concludes the thesis.

Chapter 2

Hamiltonian of chemical systems

In the last chapter, we briefly reviewed the standard routine for nonadiabatic quantum dynamics. In this chapter, we will further discuss it with detailed deviations, including the group Born–Oppenheimer approximation, diabaticization for constructing the molecular Hamiltonian, electronic structure computations, and MCTDH. Furthermore, we will also present the commonly used models in nonadiabatic quantum dynamics. Numerical results of MCTDH, and other numerically “exact” (converged) methods on typical models, provide standards for benchmarking new methods for nonadiabatic quantum dynamics.

This chapter is organized as following. In the first section, we introduce the group Born–Oppenheimer approximation and diabaticization methods. In the second section, we show how to compute the electronic structure. In the third section, we review one of the most successful numerical converged methods for quantum non-adiabatic dynamics, the Multiconfiguration Time Dependent Hartree (MCTDH) method. Tully models, spin-boson model, site-exciton model, linear vibronic coupling (LVC) model, and atom-in-cavity model are described in the fourth section.

2.1 Molecular Hamiltonian

A molecular (non-realistic) Hamiltonian is the summation of five terms [2, 100], the nuclear kinetic energy operator \hat{T}_n , the electronic kinetic energy operator \hat{T}_{el} , the Coulomb potential energy between nuclei and electrons \hat{V}_{el-n} , the Coulomb potential energy arising from nuclei nuclei repulsion \hat{V}_{n-n} , and the Coulomb potential energy arising from electrons electrons repulsion \hat{V}_{el-el} ,

$$\hat{H} = \hat{T}_n + \hat{T}_{el} + \hat{V}_{el-el} + \hat{V}_{n-n} + \hat{V}_{el-n} . \quad (2.1)$$

In the position coordinate space, the explicit form of each term can be expressed as

$$\hat{T}_n = - \sum_{j=1}^{N_n} \frac{\nabla_j^2}{2m_j}, \quad (2.2)$$

$$\hat{T}_{el} = - \sum_{\alpha=1}^{N_{el}} \frac{\nabla_{\alpha}^2}{2}, \quad (2.3)$$

$$\hat{V}_{el-n} = - \sum_{j=1}^{N_n} \sum_{\alpha=1}^{N_{el}} \frac{Z_j}{r_{j\alpha}}, \quad (2.4)$$

$$\hat{V}_{n-n} = \sum_{j=1}^{N_n} \sum_{k=1}^{N_n} \frac{Z_j Z_k}{R_{jk}}, \quad (2.5)$$

$$\hat{V}_{el-el} = \sum_{\alpha=1}^{N_{el}} \sum_{\beta=1}^{N_{el}} \frac{1}{r_{\alpha\beta}}, \quad (2.6)$$

where atomic units are used. N_{el} and N_n are the numbers of electrons and nuclei, respectively. Z_j are charges of the nuclei, and m_j represent the masses of nuclei. $R_{jk} = |\mathbf{R}_j - \mathbf{R}_k|$ is the distance between electrons, $r_{\alpha\beta} = |\mathbf{r}_{\alpha} - \mathbf{r}_{\beta}|$ is the distance between nuclei, and $r_{j\alpha} = |\mathbf{R}_j - \mathbf{r}_{\alpha}|$ is the distance between nuclei and electrons. ∇_j^2 and ∇_{α}^2 are the Laplace operators for nuclei and electrons, respectively. Notice that \mathbf{R}_j is a vector, therefore, we also use $R_{j,1}$, $R_{j,2}$ and $R_{j,3}$ to represent its three components, which will be used later.

2.1.1 Born–Oppenheimer expansion

Solving the time dependent Schrödinger equation for the Hamiltonian Eq. (2.1) directly is impracticable. However, the huge mass difference between nuclei and electrons provides the possibility to treat nuclei and electrons separately. Eq. (2.1) can be divided into two parts, the nuclear kinetic energy operator term \hat{T}_n , and the electronic Hamiltonian term $\hat{H}_{el} = \hat{T}_{el} + \hat{V}_{el-el} + \hat{V}_{n-n} + \hat{V}_{el-n}$. For given nuclear position coordinates \mathbf{R} , one can diagonalize the electronic Hamiltonian \hat{H}_{el}

$$\hat{H}_{el} |a(\mathbf{R})\rangle = V_a(\mathbf{R}) |a(\mathbf{R})\rangle, \quad a = 1, 2, \dots, N', \quad (2.7)$$

where the basis is complete when $N' \rightarrow \infty$. $|a(\mathbf{R})\rangle$ is called adiabatic basis and $E_a(\mathbf{R})$ is called potential energy surface (PES). The total wave function can be expanded as

$$\Psi(\mathbf{R}, t) = \sum_{a=1}^{N'} \chi_a(\mathbf{R}, t) |a(\mathbf{R})\rangle. \quad (2.8)$$

This type of the expansion is Born–Oppenheimer expansion. The time dependent Schrödinger equation and the molecular Hamiltonian for the column vector

$$\vec{\chi}(\mathbf{R}, t) = [\chi_1(\mathbf{R}, t), \chi_2(\mathbf{R}, t), \dots, \chi_{N'}(\mathbf{R}, t)]^T \quad (2.9)$$

can be expressed as

$$i\partial_t\vec{\chi}(\mathbf{x}, t) = \hat{H}\vec{\chi}(\mathbf{x}, t) \quad (2.10)$$

$$\hat{H} = \sum_{j=1}^{N'} \frac{(-i\nabla_j - i\hat{\mathbf{d}}_j)^2}{2m_j} + \hat{V}, \quad (2.11)$$

where $V_{ab} = V_a\delta_{ab}$, and $\hat{\mathbf{d}}_{j,ab} = \langle a(\mathbf{R}) | \nabla_j | b(\mathbf{R}) \rangle$ is called first derivative coupling. Usually, the adiabatic states are chosen as real functions. Therefore, the diagonal terms of first derivative coupling are zero $\hat{\mathbf{d}}_{j,aa} = 0$. The drawback of a real adiabatic basis is that the electronic basis could be no longer single-valued. We will discuss it more on the fourth section of this chapter. The explicit expression of off-diagonal terms of first derivative coupling can be obtained by the definition of adiabatic basis

$$\begin{aligned} 0 &= \nabla_j V_a(\mathbf{R})\delta_{ab} = \nabla_j \langle a(\mathbf{R}) | \hat{H}_{\text{el}} | b(\mathbf{R}) \rangle \\ &= (V_b(\mathbf{R}) - V_a(\mathbf{R})) \langle a(\mathbf{R}) | \nabla_j | b(\mathbf{R}) \rangle + \langle a(\mathbf{R}) | \nabla_j \hat{H}_{\text{el}} | b(\mathbf{R}) \rangle \\ &= (V_b(\mathbf{R}) - V_a(\mathbf{R}))\hat{\mathbf{d}}_{j,ab} + \langle a(\mathbf{R}) | \nabla_j \hat{H}_{\text{el}} | b(\mathbf{R}) \rangle, \quad (2.12) \\ &\Rightarrow \hat{\mathbf{d}}_{j,ab} = \langle a(\mathbf{R}) | \nabla_j | b(\mathbf{R}) \rangle = \frac{\langle a(\mathbf{R}) | \nabla_j \hat{H}_{\text{el}} | b(\mathbf{R}) \rangle}{V_a(\mathbf{R}) - V_b(\mathbf{R})} \end{aligned}$$

The first derivative coupling can be extremely huge when PESs are nearly degenerate (avoided crossing), or even singular when PESs are degenerate (conical intersection, CoI, and other types of intersections [101]). We stress that there are no approximations in Eq. (2.8) and Eq. (2.11). They are exact when $N' \rightarrow \infty$ for arbitrary values of parameters.

In fact, the wave function Eq. (2.8) and the Hamiltonian Eq. (2.11) describe a particle in a static non-Abelian gauge field (also called a non-Abelian gauge potential). For convenience, we use the gauge Hamiltonian [2, 100]

$$\begin{aligned} \hat{H} &= \sum_{j=1}^d \frac{(\hat{p}_{\text{can},j} - \hat{A}_j(\mathbf{x}))^2}{2m_j} + \hat{V}(\mathbf{x}) \\ &= \sum_{j=1}^d \left[\frac{\hat{p}_{\text{can},j}^2 - \hat{p}_{\text{can},j}\hat{A}_j(\mathbf{x}) - \hat{A}_j(\mathbf{x})\hat{p}_{\text{can},j}}{2m_j} \right] + \hat{V}(\mathbf{x}) + \hat{B}(\mathbf{x}), \quad (2.13) \end{aligned}$$

instead of Eq. (2.11) to describe the system. In Eq. (2.13), the canonical momentum $\hat{p}_{\text{can},j}$ satisfies the canonical commutation relation $[x_j, \hat{p}_k] = i\delta_{jk}$, and

$$\hat{B} = \sum_{j=1}^d \frac{\hat{A}_j^2}{2m_j}, \quad (2.14)$$

where we drop the argument for simplicity. \hat{A}_j is gauge vector potential in the language of gauge theory. The Hamiltonian Eq. (2.13) for a particle in gauge vector potentials will also be used in the last section of this chapter, and chapter 4.

One can set $d = 3N'$, $x_j = R_{j,1}$, $x_{j+N'} = R_{j,2}$, $x_{j+2N'} = R_{j,3}$, $m_j = m_{j+N'} = m_{j+2N'}$, $\hat{A}_j = id_{j,1}$, $\hat{A}_{j+N'} = id_{j,2}$ and $\hat{A}_{j+2N'} = id_{j,3}$ for $1 \leq j \leq N'$ in Eq. (2.13) to obtain Eq. (2.11). The advantage of Eq. (2.13) over Eq. (2.11) is that different degree of freedoms (DOFs) can have different mass. To be more explicit, three DOFs of \mathbf{R}_j have the same mass in Eq. (2.11), while all DOFs of Eq. (2.13) can have different masses. Such a difference could happen when non-Cartesian coordinates are used. Meanwhile, the knowledge of gauge theory also makes general conclusions easier for Eq. (2.13).

The gauge curvature of the system (Eq. (2.13))

$$\hat{F}_{jk} = \partial_j \hat{A}_k - \partial_k \hat{A}_j - i[\hat{A}_j, \hat{A}_k], \quad (2.15)$$

and kinematic momentum $\hat{p}_{\text{kin},j} = \hat{p}_{\text{can},j} - \hat{A}_j$ are gauge co-variant

$$\begin{aligned} x'_j &= x_j, \\ \hat{p}'_{\text{kin},j} &= \hat{U} \hat{p}_{\text{kin},j} \hat{U}^\dagger, \\ \hat{V}' &= \hat{U} \hat{V} \hat{U}^\dagger, \\ \hat{A}'_j &= \hat{U} \hat{A}_j \hat{U}^\dagger - i(\partial_j \hat{U}) \hat{U}^\dagger, \\ \hat{F}'_{jk} &= \partial_j \hat{A}'_k - \partial_k \hat{A}'_j - i[\hat{A}'_j, \hat{A}'_k] = \hat{U} \hat{F}_{jk} \hat{U}^\dagger, \\ |a'(\mathbf{x})\rangle &= \hat{U} |a(\mathbf{x})\rangle, \end{aligned} \quad (2.16)$$

where $\hat{U} = \hat{U}(\mathbf{x})$ is an arbitrary unitary (gauge) transformation.

The gauge curvature $\hat{F}_{jk} \equiv 0$ when the basis $|a(\mathbf{x})\rangle$ is complete

$$\begin{aligned} & \partial_j \hat{A}_k - \partial_k \hat{A}_j \\ &= \sum_{a,b} i |a\rangle \langle b| (\partial_j \langle a| \partial_k |b\rangle - \partial_k \langle a| \partial_j |b\rangle) \\ &= \sum_{a,b} i |a\rangle \langle b| (\langle \partial_j a | \partial_k b \rangle - \langle \partial_j b | \partial_k a \rangle) \\ &= \sum_{a,b,c} i |a\rangle \langle b| (\langle \partial_j a | c \rangle \langle c | \partial_k b \rangle - \langle \partial_j b | c \rangle \langle c | \partial_k a \rangle) \\ &= - \sum_{a,b,c} i |a\rangle \langle b| (\langle a | \partial_j c \rangle \langle c | \partial_k b \rangle - \langle a | \partial_k c \rangle \langle c | \partial_j b \rangle) \\ &= - i[\hat{A}_j, \hat{A}_k]. \end{aligned} \quad (2.17)$$

A more insightful proof is to construct the unitary transformation to make all gauge vector potential vanish. Consider a complete nuclear position independent basis set $|a'\rangle \langle a'|$, $a' = 1, 2, \dots, N'$, then such unitary transformation can be constructed as $U_{ab}(x) = \langle a' | b \rangle$. The basis which can make gauge vector potential vanish is so-called diabatic basis. This property simplifies simulations of nuclear dynamics a lot. Apparently, the basis $|a'\rangle \langle a'|$, $a' = 1, 2, \dots, N'$ is a diabatic basis. When $|a'\rangle$ is chosen as the eigenstate of the electronic

Hamiltonian at certain nuclear geometries \mathbf{x}_0 , $\hat{H}_{\text{el}}(\mathbf{x}_0)$, the basis is so-called crude diabatic basis. The price of using diabatic basis is that the electronic Hamiltonian is no longer diagonal $\langle a' | \hat{H}_{\text{el}} | b' \rangle \neq 0$.

2.1.2 Group Born–Oppenheimer Approximation

Modern computers can only do the finite operations. We need to find a reasonable truncation of Eq. (2.8). The huge mass difference between nuclei and electrons suggests that the time scales of nuclear motion and electronic motion are separate. Born–Oppenheimer approximation supposes that fast electrons can adjust to the slow nuclei instantly. Thus, the total wave function is always a product state of the nuclear wave function [2, 100] and adiabatic electronic state

$$\Psi(\mathbf{x}, t) = \chi_a(\mathbf{x}, t) |a(\mathbf{x})\rangle, \quad (2.18)$$

which yields the time dependent Schrödinger equation [1]

$$i\partial_t \chi_a(\mathbf{x}, t) = \left[\sum_j^d \frac{\hat{p}_{\text{can},j}^2}{2m_j} + V_a(\mathbf{x}) \right] \chi_a(\mathbf{x}, t). \quad (2.19)$$

The time-independent (stationary) form of Born–Oppenheimer approximation is more often used,

$$E_a \chi_a(\mathbf{x}, t) = \left[\sum_j^d \frac{\hat{p}_{\text{can},j}^2}{2m_j} + V_a(\mathbf{x}) \right] \chi_a(\mathbf{x}, t). \quad (2.20)$$

The application range of Born–Oppenheimer approximation is not limited in the molecular Hamiltonian. It can also be used in the other systems with time scale separation of motions. Born–Oppenheimer approximation is equivalent to ignoring the transition between $\chi_a(\mathbf{x}, t)$ and $\chi_b(\mathbf{x}, t)$ for $b \neq a$. Apparently, Born–Oppenheimer approximation breaks down when \hat{A}_j is no longer small. This happens when two or more PESs are nearly degenerate for some \mathbf{x} . Instead, group Born–Oppenheimer approximation should be used in this scenario. The idea of group Born–Oppenheimer approximation is similar to Born–Oppenheimer approximation. We suppose there is a group of adiabatic states $a = 1, 2, \dots, N$ which are energetically separated from other states [2, 100]. We denote electronic states within the group as g . Group Born–Oppenheimer approximation states that the time dependent wave function is always spanned by g , and the transition between g and other states are negligible. This ansatz yields the effective Hamiltonian

$$H^{(g)} = \sum_{j=1}^d \frac{(\hat{p}_{\text{can},j} - \hat{A}_j^{(g)})^2}{2m_j} + \hat{V}^{(g)} + \hat{K}^{(g)}, \quad (2.21)$$

where $\hat{A}_j^{(g)}$ and $\hat{V}^{(g)}$ are the operators spanned by g and $\hat{K}^{(g)}$ represents the dressed potential

$$\hat{K}_{ab}^{(g)} = \sum_{j=1}^d \sum_{c \notin g} \frac{\langle \partial_j a | c \rangle \langle c | \partial_j b \rangle}{2m_j}. \quad (2.22)$$

Due to the fact that group states are energetically separate from other states, $\hat{K}^{(g)}$ is negligible. The major difference between Eq. (2.13) and Eq. (2.21) is that the gauge curvature of Eq. (2.21) is not always zero. In fact, the group Born–Oppenheimer approximation is the common strategy to implement artificial gauge fields in neutral-atom systems [102]. The product terms of gauge vector potential and canonical momentum are unfavorable for numerical simulations. Unfortunately, we cannot always find a diabatic representation to make all gauge vector potential vanish. However, it is possible to find a quasi-diabatic representation to make gauge vector potential non-vanish, but small enough to be negligible in practice.

2.1.3 Diabatization methods

As we mentioned in the above subsection, the non zero gauge vector potential is unfavorable for simulations, and one has to find a diabatic or quasi-diabatic representation to make gauge vector potential negligible. According to the gauge transformation Eq. (2.16), the existence of a diabatic representation requires that $\hat{F}_{jk}^{(g)}$ must be zero for all j, k . Generally, this condition does not always hold. However, when the group electronic states span the whole Hilbert space [103], or the system is one dimensional [104], a diabatic representation can exist. The first scenario can be referred to as crude diabatic basis, and has already been discussed in subsection Sec. 2.1.2. The proof for the second scenario is straightforward. When the system is one dimensional,

$$\hat{F}_{jj}^{(g)} = \partial_j \hat{A}_j^{(g)} - \partial_j \hat{A}_j^{(g)} - i[\hat{A}_j^{(g)}, \hat{A}_j^{(g)}] \equiv 0. \quad (2.23)$$

Therefore, we can construct the adiabatic-to-diabatic (ATD) gauge transformation by solving the equation [103, 105, 106]

$$0 = \hat{U}^{(g)} \hat{A}_j^{(g)} - i \partial_j \hat{U}^{(g)}, \quad (2.24)$$

which gives

$$\hat{U}^{(g)}(\mathbf{x}) = \hat{U}^{(g)}(\mathbf{x}_0) - i \int_{\Gamma} \hat{U}^{(g)}(\mathbf{x}) \hat{\mathbf{A}}^{(g)}(\mathbf{x}) \cdot d\mathbf{s}, \quad (2.25)$$

where Γ is the integration path from \mathbf{x}_0 to \mathbf{x} , and $\hat{\mathbf{A}}^{(g)}(\mathbf{x})$ is the vector of which j -th component is $\hat{A}_j^{(g)}(\mathbf{x})$.

For a general non-1d system not in the crude diabatic basis, we cannot expect that there exists a gauge transformation to make all gauge vector potential vanish. The gauge vector

potential that can be eliminated by gauge transformation is called removable part, while the other part is called nonremovable. In practical applications, it is sufficient to remove most of removable part, especially the singular part. One can use the integration of the Euclidean norm of gauge vector potential to describe the quasi-diabaticity [2, 100, 107] of quasi-diabatic basis

$$\int \prod_k dx_k \sum_j \text{Tr} \left\{ \hat{A}_j^{(g)\dagger} \hat{A}_j^{(g)} \right\}. \quad (2.26)$$

Minimizing Eq. (2.26) gives

$$\sum_j \partial_j \hat{A}_{j,\text{qd}}^{(g)} = 0, \quad (2.27)$$

$$\sum_j \partial_j (\hat{U}^{(g)} \hat{A}_j^{(g)} \hat{U}^{(g)\dagger} - i(\partial_j \hat{U}^{(g)}) \hat{U}^{(g)\dagger}) = 0, \quad (2.28)$$

where the subscript qd represents the gauge vector potential in the quasi-diabatic basis. In the language of gauge theory, Eq. (2.27) is the Lorentz gauge. It has been proved [2] that Eq. (2.27) is optimal for two-state systems, i.e., it removes all the removable part.

Now we are at the position to discuss diabatization methods. Popular diabatization methods can be classified into four categories [2], derivative-based, enforcing the smoothness of wave functions, enforcing the smoothness of observables, and fitting PESs.

Derivative-based methods try to construct quasi-diabatic basis from the gauge vector potential (first derivatives). In principle, Eq. (2.28) should be the equation to be solved. However, it is too complicated for numerical solutions. Instead, the gauge vector potential in the quasi-diabatic basis and the gauge ADT gauge transformation are obtained by Eq. (2.25). When the diabatic basis does not exist, the solution Eq. (2.25) is path-dependent. Another problem is that singularity in the gauge vector potential of adiabatic basis causes an instability. Choosing a safe integration path [108] and decomposing the gauge vector potentials [103] can mitigate these problems.

Derivative-based methods are the most accurate diabatization methods. When the diabatic basis exists, they will give the exact results. The major drawback is that to compute first derivatives in lots of grids is very expensive. Instead, more approximate but numerically cheap diabatization methods are sufficient to remove most of removable part for practical applications. Usually, the huge gauge vector potential suggests the rapid change of wave functions. Hence, quasi-diabatic basis can be obtained by enforcing the smoothness of wave functions. The methods belonging to this category include block-diagonalization [107, 109], the principle of configurational uniformity, effective Hamiltonian formalism [110, 111] based on quasidegenerate perturbation theory, and so on [112–114]. One can also enforce the smoothness of observables to obtain the quasi-diabatic basis. Possible choices include dipole moments [115–118], quadrupole moment [119], the transition dipole mo-

ment [120]. Specifically, it has been shown that singular part of gauge vector potentials can be removed by diagonalizing almost any Hermitian operators [121].

When the symmetry of the system is known, using quasi-diabatic basis to fit PESs without the information of wave function is possible. The simplest fitting is Landau–Zener approach for collision problems [122–125]. Consider a two-level $1d$ system with an avoided crossing, the electronic Hamiltonian near the crossing in the diabatic representation can be expressed as

$$\hat{H}_{\text{el;d}} = \begin{pmatrix} aq & b \\ b & -aq \end{pmatrix}, \quad (2.29)$$

where a, b are fitting parameters, and q is the nuclear DOF. Diagonalizing this Hamiltonian gives the following PESs

$$V_{\pm} = \pm \sqrt{a^2 q^2 + b^2}. \quad (2.30)$$

Fitting PESs methods can also remove the singularity of gauge vector potentials [126–128]. The details will be discussed in the Sec. 2.4.4 with an explicit example of two-state-two-mode LVC model.

To summarize, we briefly reviewed the construction of the molecular Hamiltonian under the framework of the group Born–Oppenheimer approximation for MCTDH computations in this section.

2.2 Electronic Hamiltonian

In this section, we briefly review the electronic structure theory of the molecular Hamiltonian. As we stated in the last section, the PES calculation is necessary for quantum non-adiabatic dynamics. We will start from the second quantization representation of the electronic Hamiltonian, then introduce the Hartree–Fock method and post-Hartree–Fock methods. We will focus on the state ansatz of each method, rather than numerical implementations.

2.2.1 Second quantization representation of electronic Hamiltonian

For a general many-body system, the most convenient representation is second quantization. First, we will construct the second quantization representation of fermions. Consider a complete basis set (spin orbitals) of a single particle $\{|\phi_1\rangle, |\phi_2\rangle, \dots, |\phi_L\rangle\}$. For a particle in the continuum space, the completeness is achieved when $L \rightarrow \infty$. The Fock states [129, 130] are defined as

$$|n_1, n_2, \dots, n_L\rangle, \quad (2.31)$$

meaning that n_α particles reside in the state $|\phi_\alpha\rangle$, $\alpha = 1, 2, \dots, L$. The occupation numbers satisfy $n_\alpha \in \{0, 1\}$ because of Pauli principle. The state with all zero occupation numbers is called vacuum state $|\text{vac}\rangle$. As a comparison, the first quantization representation (wave function) of state Eq. (2.31) cannot be written as a naive product-form because it contains the unphysical information, “which particle is in which state”. Additionally, the naive product-form wave function cannot account for the correct particle exchange symmetry, either. To be more explicit, suppose that the total occupation number of the Fock state is $N_L = \sum_\alpha n_\alpha$, and the state the particles occupy is q_1, q_2, \dots, q_{N_L} , then the naive product-form wave function is

$$\Psi(\mathbf{r}_1\sigma_1, \mathbf{r}_2\sigma_2, \dots, \mathbf{r}_{N_L}\sigma_{N_L}) = \phi_{q_1}(\mathbf{r}_1, \sigma_1)\phi_{q_2}(\mathbf{r}_2, \sigma_2)\cdots\phi_{q_{N_L}}(\mathbf{r}_{N_L}, \sigma_{N_L}), \quad (2.32)$$

where \mathbf{r} labels the spatial coordinate and σ labels the spin coordinate. Eq. (2.32) tells us that particle q_j is in the state ϕ_{q_j} . To eliminate the redundant information and account for the anti-symmetric property, the correct wave function must be a Slater determinant which is generated by the symmetrization procedure,

$$\Psi(\mathbf{r}_1\sigma_1, \mathbf{r}_2\sigma_2, \dots, \mathbf{r}_{N_L}\sigma_{N_L}) = \frac{1}{\sqrt{N_L!}} \begin{vmatrix} \phi_{q_1}(r_1, \sigma_1) & \cdots & \phi_{q_{N_L}}(r_{N_L}, \sigma_{N_L}) \\ \vdots & \ddots & \vdots \\ \phi_{q_1}(r_{N_L}, \sigma_{N_L}) & \cdots & \phi_{q_{N_L}}(r_{N_L}, \sigma_{N_L}) \end{vmatrix}. \quad (2.33)$$

The Fock state avoids the complicated symmetrization procedure. First, it only tells us the physical information “how many particles are in each state”. Second, the algebraic properties of creation and annihilation operators encode anti-symmetric property of fermions. The creation and annihilation operators of fermions are defined as

$$a_\alpha^\dagger |n_1, n_2, \dots, 0_\alpha, \dots, n_L\rangle = (-1)^{\sum_{\beta < \alpha} n_\beta} |n_1, n_2, \dots, 1_\alpha, \dots, n_L\rangle, \quad (2.34)$$

$$a_\alpha^\dagger |n_1, n_2, \dots, 1_\alpha, \dots, n_L\rangle = (-1)^{\sum_{\beta < \alpha} n_\beta} |n_1, n_2, \dots, 0_\alpha, \dots, n_L\rangle, \quad (2.35)$$

$$[a_\alpha, a_\beta]_+ = [a_\alpha^\dagger, a_\beta^\dagger]_+ = 0, \quad [a_\alpha, a_\beta^\dagger]_+ = \delta_{\alpha\beta} \quad a_\alpha^2 = (a_\alpha^\dagger)^2 = 0, \quad (2.36)$$

where 1_α means the occupation number of state $|\phi\rangle_\alpha$ is one, 0_α means the occupation number of state $|\phi\rangle_\alpha$ is zero, and $[\ , \]_+$ is the anti-commutator.

The particle number operator on the state $|\phi_\alpha\rangle$ is $\hat{n}_\alpha = a_\alpha^\dagger a_\alpha$. The other operators can also be constructed in the second quantization representation. In the molecular Hamiltonian, the electronic operator can be divided into two parts, the one-body operator H_1 and two-body operator H_2 . The one-body operator $H_1 = \hat{T}_{\text{el}} + \hat{V}_{\text{el-n}} = \sum_j^{N_e} \hat{h}(\mathbf{r}_j)$ acts on a single electron, and the two-body operator $H_2 = \hat{V}_{\text{el-el}} = \frac{1}{2} \sum_{j \neq k}^{N_e} \hat{g}(\mathbf{r}_j, \mathbf{r}_k)$ acts on two electrons. H_1 , H_2 and H_{el} in the second quantization representation can be expressed as

$$H_1 = \sum_{\alpha,\beta} h_{\alpha\beta} a_{\alpha}^{\dagger} a_{\beta}, \quad (2.37)$$

$$H_2 = \frac{1}{2} \sum_{\alpha,\beta,\gamma,\delta} g_{\alpha\beta\gamma\delta} a_{\alpha}^{\dagger} a_{\beta}^{\dagger} a_{\delta} a_{\gamma}, \quad (2.38)$$

$$H_{\text{el}} = \sum_{\alpha,\beta} h_{\alpha\beta} a_{\alpha}^{\dagger} a_{\beta} + \frac{1}{2} \sum_{\alpha,\beta,\gamma,\delta} g_{\alpha\beta\gamma\delta} a_{\alpha}^{\dagger} a_{\beta}^{\dagger} a_{\delta} a_{\gamma}, \quad (2.39)$$

where

$$h_{\alpha\beta} = \sum_{\sigma} \int d\mathbf{r} \phi_{\alpha}^{*}(\mathbf{r}, \sigma) \hat{h}(\mathbf{r}) \phi_{\beta}(\mathbf{r}, \sigma), \quad (2.40)$$

$$g_{\alpha\beta\gamma\delta} = \sum_{\sigma,\sigma'} \int d\mathbf{r} d\mathbf{r}' \phi_{\alpha}^{*}(\mathbf{r}, \sigma) \phi_{\beta}^{*}(\mathbf{r}', \sigma') \hat{g}(\mathbf{r}, \mathbf{r}') \phi_{\gamma}(\mathbf{r}, \sigma) \phi_{\delta}(\mathbf{r}', \sigma'). \quad (2.41)$$

For convenience, we dropped out hats in annihilation and creation operators. One can check that matrix elements of operators in the first quantization and second quantization representation coincide with each other. Eq. (2.39) is the most general formalism of an electronic Hamiltonian in the second quantization representation. One of the major advantage of second quantization representation is that the operator takes a unified formalism regardless of the particle numbers. One can also use the second quantization representation to describe the system with particle creation and annihilation, in which first quantization representation completely fails.

For closed-shell molecules, the single particle basis set is usually chosen as the product of the same spatial orbital and spin-z polarized spin functions,

$$\langle \mathbf{r} | \phi_{\alpha} \rangle = \varphi_p(\mathbf{r}) |\uparrow\rangle, \quad \langle \mathbf{r} | \phi_{\alpha+1} \rangle = \varphi_p(\mathbf{r}) |\downarrow\rangle, \quad (2.42)$$

where $\alpha = 2p - 1$. Therefore, we will use the symbol $p\sigma$, where $p = 1, 2, \dots, L/2$ and $\sigma = \uparrow, \downarrow$, instead of α to label the closed-shell single particle basis. We also define the complete basis for the spatial orbitals $|\varphi_1\rangle, |\varphi_2\rangle, \dots, |\varphi_{L/2}\rangle$. Because of the absence of the spin variables in H and \hat{g} , we can shift the summation of the spin variables in Eq. (2.40) and (2.41) to Eq. (2.39), then the electronic Hamiltonian can be expressed as

$$H_{\text{el}} = \sum_{\sigma} \sum_{p,q} h_{pq} a_{p\sigma}^{\dagger} a_{q\sigma} + \frac{1}{2} \sum_{\sigma,\sigma'} \sum_{p,q,r,s} g_{pqrs} a_{p\sigma}^{\dagger} a_{q\sigma'}^{\dagger} a_{s\sigma'} a_{r\sigma}, \quad (2.43)$$

where

$$h_{pq} = \int d\mathbf{r} \varphi_p^{*}(\mathbf{r}) \hat{h}(\mathbf{r}) \varphi_q(\mathbf{r}), \quad (2.44)$$

$$g_{pqrs} = \int d\mathbf{r} d\mathbf{r}' \varphi_p^{*}(\mathbf{r}) \varphi_q^{*}(\mathbf{r}') \hat{g}(\mathbf{r}, \mathbf{r}') \varphi_r(\mathbf{r}) \varphi_s(\mathbf{r}'). \quad (2.45)$$

The total electronic spin and electronic number are conserved quantities. The expression of them [129–131] for the closed-shell molecules are

$$\hat{N} = \sum_{\sigma} \sum_p a_{p\sigma}^{\dagger} a_{p\sigma}, \quad (2.46)$$

$$\hat{S}_z = \frac{1}{2} \sum_p (a_{p\uparrow}^{\dagger} a_{p\uparrow} - a_{p\downarrow}^{\dagger} a_{p\downarrow}), \quad (2.47)$$

$$\hat{S}_+ = \sum_p a_{p\uparrow}^{\dagger} a_{p\downarrow}, \quad (2.48)$$

$$\hat{S}_- = \sum_p a_{p\downarrow}^{\dagger} a_{p\uparrow}, \quad (2.49)$$

$$\hat{S}^2 = \hat{S}_- \hat{S}_+ + \hat{S}_z + \hat{S}_z^2. \quad (2.50)$$

A complete set of commuting observables of the electronic Hamiltonian without other symmetries consist of H_{el} , \hat{S}_z , \hat{N} and \hat{S}^2 . Therefore, we should choose the approximate energy eigenstates as eigenstates of \hat{S}_z and \hat{S}^2 . The multiplicity (degeneracy) of an energy level is $2S + 1$, where S is the total spin angular momentum. Singlets, doublets, triplets, quartets and quintets are referred to as $S = 0, 1/2, 1, 2, 3/2$. It is instructive to consider common examples of singlet, doublet and triplet states. A Fock state with zero unpaired electrons is a singlet state ($S = 0$), and a Fock state with one unpaired electron is a doublet state ($S = 1/2$). The triplet state is little bit complicated. For simplicity, we consider a Fock state with two unpaired electrons and two spatial orbitals. There are four different possible Fock states. Triplet ($S = 1$) and singlet ($S = 0$) states are the superpositions of them

$$\begin{aligned} S = 1 : & \quad \left\{ \begin{array}{l} |0_{1\uparrow}, 1_{1\downarrow}, 0_{2\uparrow}, 1_{1\downarrow}\rangle, \\ |1_{1\uparrow}, 0_{1\downarrow}, 1_{2\uparrow}, 0_{1\downarrow}\rangle, \\ \frac{1}{\sqrt{2}}(|1_{1\uparrow}, 0_{1\downarrow}, 0_{2\uparrow}, 1_{1\downarrow}\rangle + |0_{1\uparrow}, 1_{1\downarrow}, 1_{2\uparrow}, 0_{1\downarrow}\rangle), \end{array} \right. \\ S = 0 : & \quad \frac{1}{\sqrt{2}}(|1_{1\uparrow}, 0_{1\downarrow}, 0_{2\uparrow}, 1_{1\downarrow}\rangle - |0_{1\uparrow}, 1_{1\downarrow}, 1_{2\uparrow}, 0_{1\downarrow}\rangle). \end{aligned} \quad (2.51)$$

One can construct other singlet and triplet states by adding arbitrary paired electrons to Eq. (2.51).

We also introduce the Fock state, as well as creation and annihilation operators of bosons [130]. The second quantization formalism of bosons is similar to the fermions. The spin-statistical theorem for bosons states that the wave function of bosons (spin-integer-particles) system is invariant if two particles are swapped. Therefore, the occupation number for each single particle state $n_{\alpha} \in \mathbb{N}_0$, and the wave function in the first quantization representation should be a permanent rather than the determinant. In order to encode the symmetric

property, the creation and annihilation operators of bosons are defined as

$$a_{\alpha}^{\dagger} |n_1, n_2, \dots, n_{\alpha}, \dots, n_L\rangle = \sqrt{n_{\alpha} + 1} |n_1, n_2, \dots, n_{\alpha} + 1, \dots, n_L\rangle, \quad (2.52)$$

$$a_{\alpha} |n_1, n_2, \dots, n_{\alpha}, \dots, n_L\rangle = \sqrt{n_{\alpha}} |n_1, n_2, \dots, n_{\alpha} - 1, \dots, n_L\rangle, \quad n_{\alpha} \neq 0, \quad (2.53)$$

$$a_{\alpha}^{\dagger} |n_1, n_2, \dots, 0_{\alpha}, \dots, n_L\rangle = 0, \quad (2.54)$$

$$[a_{\alpha}, a_{\beta}] = [a_{\alpha}^{\dagger}, a_{\beta}^{\dagger}] = 0, \quad [a_{\alpha}, a_{\beta}^{\dagger}] = \delta_{\alpha\beta}. \quad (2.55)$$

The boson creation and annihilation operators directly connects to the position and momentum operators of quantum harmonic oscillators because the energy quanta of quantum harmonic oscillator is the phonon,

$$\hat{x}_{\alpha} = \frac{a_{\alpha} + a_{\alpha}^{\dagger}}{\sqrt{2}}, \quad \hat{p}_{\alpha} = \frac{a_{\alpha} - a_{\alpha}^{\dagger}}{\sqrt{2}i}. \quad (2.56)$$

We will use the harmonic oscillator representation of bosons in Sec. 2.4.5.

2.2.2 Hartree–Fock method and beyond

The Hartree–Fock method is the simplest method for the electronic structure calculations, and it is also the foundation of most of the more advanced methods. The Hartree–Fock method approximates the wave function as a single Slater determinant, i.e., electronic configurations where we can clearly know which orbitals are occupied and which are not. Historically speaking, Douglas Hartree approximated the many-body electron wave function as a product of single particle wave functions in 1927 [132–135]. In 1930, Vladimir Fock [136, 137] and John C. Slater [138] independently pointed out that Hartree’s approximation does not preserve the particle exchange symmetry. Futhermore, Fock [136, 137] used the Slater determinant wave function to resolve the problem.

The wave function ansatz of the Hartree–Fock method [129, 130, 139] for the ground state of a close-shell system is

$$|\Psi_0\rangle_{\text{HF}} = \prod_{j=1}^{N_e/2} (a_{j\uparrow}^{\dagger} a_{j\downarrow}^{\dagger}) |\text{vac}\rangle. \quad (2.57)$$

In this subsection, we use j, k, \dots to represent occupied orbitals, and a, b, \dots to represent virtual orbitals. p, q, \dots represent an orbital regardless of occupied or virtual. Let us check the application range of the Hartree–Fock method first. The exact wave function is a superposition state of all possible configurations (up to a normalization factor),

$$|\Psi\rangle = |\Psi_0\rangle_{\text{HF}} + \sum_{\sigma, \tau} \sum_{a, j} c_{j\sigma}^{a\tau} a_{a\sigma}^{\dagger} a_{j\sigma'} |\Psi_0\rangle_{\text{HF}} + \dots. \quad (2.58)$$

We call $|\Psi_0\rangle_{\text{HF}}$ ground state configuration or physical vacuum, $a_{a\sigma}^{\dagger} a_{j\sigma'} |\Psi_0\rangle_{\text{HF}}$ single excitation configuration or 1p-1h (one particle one hole) configuration, and so on. Hartree–Fock

wave function is a good approximation when the weight of ground state configuration dominates. However, when the weights of two or more configurations of the ground/excited state are competitive, the single configuration Hartree–Fock completely breaks down. This happens when the state is approximately degenerate. Multiconfigurational self-consistent field (MCSCF) methods [140–143], for instance complete active space self-consistent field (CASSCF) are often used in this scenario, rather than the Hartree–Fock method.

The energy of the Hartree–Fock wave function (Hartree–Fock energy) is

$$E_{\text{HF}} = {}_{\text{HF}}\langle \Psi_0 | H_{\text{el}} | \Psi_0 \rangle_{\text{HF}} = 2 \sum_j h_{jj} + \sum_{j,k} (2g_{jkjk} - g_{jkkj}). \quad (2.59)$$

Hartree–Fock orbitals are determined by minimizing E_{HF} with the restriction $\langle \varphi_p | \varphi_q \rangle = \delta_{pq}$,

$$\min_{\varphi} [E_{\text{HF}} - 2 \sum_{j,k} \mu_{kj} (\langle \varphi_j | \varphi_k \rangle - \delta_{jk})], \quad (2.60)$$

where μ_{jk} are Lagrange multiplies. This yields the equation

$$\hat{F} |\varphi_l\rangle |\tau\rangle = \sum_k \mu_{kl} |\varphi_k\rangle |\tau\rangle, \quad |\tau\rangle = |\uparrow\rangle, |\downarrow\rangle \quad (2.61)$$

$$\hat{F} = \sum_{\sigma} \sum_{p,q} f_{pq} a_{p\sigma}^{\dagger} a_{q\sigma}, \quad (2.62)$$

$$f_{kl} = \mu_{kl} = h_{kl} + \sum_j (2g_{jkjl} - g_{jklj}), \quad (2.63)$$

$$f_{al} = f_{la}^* = h_{al} + \sum_j (2g_{jajl} - g_{jalj}) = 0, \quad (2.64)$$

where \hat{F} is the Fock operator, and the matrix elements between two virtual orbitals of Fock operator f_{ab} is undetermined by variational principle. Eq. (2.61) is a remarkable property of the Hartree–Fock ansatz. It states that acting with the Fock operator on an occupied spin orbital can only get a superposition of occupied spin orbitals. The corollary of Eq. (2.61) is Brillouin’s theorem: the Hamiltonian matrix elements between the ground state configuration and single excitation configurations are always zero.

It is not hard to verify that the Hartree–Fock wave function is invariant under unitary transformations.

$$|\varphi'_j\rangle = \sum_k U_{jk} |\varphi_k\rangle. \quad (2.65)$$

Therefore, we can choose a specific basis to make Fock operator diagonal,

$$\hat{F} |\varphi_l\rangle |\sigma\rangle = \epsilon_l |\varphi_l\rangle |\sigma\rangle, \quad (2.66)$$

$$\hat{F} = \sum_{\sigma} \sum_{k,l} f_{kl} a_{k\sigma}^{\dagger} a_{l\sigma}, \quad (2.67)$$

where ϵ_l is the orbital energy, and the spatial orbitals $|\varphi_l\rangle$ which satisfy Eq. (2.66) are canonical Hartree–Fock orbitals. Eq. (2.66) is a self-consistent equation since the electron is in the mean field generated by all the other electrons. For this reason, Hartree–Fock method is also called the self-consistent field method (SCF). In practical numerical simulations, canonical Hartree–Fock orbitals are expanded as linear combination of atomic orbitals (LCAO)

$$|\varphi_j\rangle = \sum_v c_{jv} |\chi_v\rangle . \quad (2.68)$$

Subjecting Eq. (2.68) to Eq. (2.61) and projecting on $\langle\chi_u|$,

$$\sum_v F_{uv} c_{lv} = \sum_v S_{uv} \epsilon_l c_{lv} , \quad (2.69)$$

where F_{uv} are matrix elements of the Fock operator between the atomic spin orbitals,

$$F_{uv} = \langle\tau| \langle\chi_u| \hat{F} |\chi_v\rangle |\tau\rangle , \quad (2.70)$$

and $S_{uv} = \langle\chi_u|\chi_v\rangle$ are matrix elements of the overlap matrix. Eq. (2.69) is called Roothaan equations, and it is a set of generalized eigen-equations because of the non-orthogonality of atomic orbitals.

The variational principle here only determines the occupied orbitals. However, one can assume that virtual orbitals also satisfy the similar eigen-equations of the Fock operators. Regardless whether the orbitals are occupied or virtual, the eigen-equations, Fock operators, and orbital energies are

$$\hat{F} |\varphi_q\rangle |\tau\rangle = \epsilon_q |\varphi_q\rangle |\tau\rangle , \quad (2.71)$$

$$\hat{F} = \sum_{\sigma} \sum_{p,q} f_{pq} a_{p\sigma}^{\dagger} a_{q\sigma} , \quad (2.72)$$

$$f_{pq} = h_{pq} + \sum_j (2g_{jppq} - g_{jppq}) = \epsilon_p \delta_{pq} , \quad (2.73)$$

where τ can be either spin up or spin down. The Hartree–Fock wave function is the eigenstate of Fock operator. The eigenenergy of the Fock operator is the summation of the occupied orbital energies, rather than Hartree–Fock energy,

$$\hat{F} |\Psi_0\rangle_{\text{HF}} = 2 \sum_{j=1}^{N_e/2} \epsilon_j |\Psi_0\rangle_{\text{HF}} . \quad (2.74)$$

The physical meaning of orbital energies is given by Koopmans' theorem,

$$\epsilon_j = E_{\text{HF}} - {}_{\text{HF}}\langle\Psi_0| a_{j\sigma}^{\dagger} H_{\text{el}} a_{j\sigma} |\Psi_0\rangle_{\text{HF}} , \quad (2.75)$$

$$\epsilon_a = {}_{\text{HF}}\langle\Psi_0| a_{a\sigma} H_{\text{el}} a_{a\sigma}^{\dagger} |\Psi_0\rangle_{\text{HF}} - E_{\text{HF}} , \quad (2.76)$$

where σ can be either spin up or spin down. Clearly, the orbital energy of occupied orbital is the ionization potential under the conditions that all orbitals are frozen, and the orbital energy of virtual orbital is the electron affinity under the conditions that all orbitals are frozen. The ionization potential predicted by Koopmans' theorem for the outer shell orbitals are usually reasonable. However, Koopmans' estimations for ionization potential of inner shell orbitals and electron affinity are less accurate, because the relaxation of orbitals and electron correlations are not negligible.

Although the variation procedure of Hartree–Fock method is for the ground state, we can approximate excited states as the excitation configurations. One can also perform the SCF for the excited states to construct more precise virtual orbitals [144].

Before moving to post-Hartree–Fock methods, we point out that the Hartree–Fock method is not limited to the closed-shell system. The Hartree–Fock method for the open-shell system is similar to the closed-shell scenario. Due to the fact that spin up states and spin down functions share the same spatial orbitals, the closed-shell Hartree–Fock is also called Restricted Hartree–Fock (RHF). The RHF wave function is a singlet state. For the open-shell system, one can choose either spin up and spin down functions that share the same spatial orbitals (restricted open-shell Hartree–Fock method, ROHF), or spin up and spin down functions that have different spatial orbitals (unrestricted Hartree–Fock method, UHF). ROHF and RHF wave functions are the eigenstates of \hat{S}^2 . However, UHF wave function ansatz suffers from the spin contamination, i.e., the solutions of UHF methods are not the eigenstates of \hat{S}^2 .

The accuracy of Hartree–Fock is not enough for the usual chemical systems. The electron correlation energy can measure the accuracy of Hartree–Fock method

$$E_{\text{corr}} = E_{\text{HF,lim}} - E_{\text{exact}}, \quad (2.77)$$

where $E_{\text{HF,lim}}$ is the Hartree–Fock limit energy. It is the Hartree–Fock energy in the complete basis, which represents the lowest energy of a single Slater determinant. The Hartree–Fock limit energy can be obtained by extrapolating with increasing the atomic orbitals. Despite its limitations, the Hartree–Fock method is the starting point of post-Hartree–Fock methods. The computational cost of Hartree–Fock is low, and it is qualitatively correct in lots of cases. Many advanced methods based on Hartree–Fock method, so-called post-Hartree–Fock methods, have been developed to account for the electron correlation energy. The single Slater determinant in the Hartree–Fock method is called reference state of post-Hartree–Fock methods. When single Slater determinant ansatz of Hartree–Fock method breaks down, the MCSCF wave function should be considered as reference states. Post-Hartree–Fock methods which use MCSCF wave function as reference states are called Multireference (MR) methods. The methods in this subsection are single reference methods if

not specified otherwise. We will briefly review Møller–Plesset (MP) perturbation theory, Configuration Interaction (CI) method [3], and Coupled Cluster (CC) theory [4]. There are also various methods to account for the electron correlations which we will not cover in this thesis due to the length limit, for instance, Density matrix renormalization group (DMRG) [5–7], Matrix Product States (MPS) [8, 9], Quantum Monte Carlo (QMC) [10, 11], Density functional theory (DFT) [12, 13], and time dependent density functional theory (TD-DFT) [14–16].

Møller–Plesset (MP) perturbation theory is a many-body version of Rayleigh–Schödinger (RS) perturbation method to calculate the ground state corrections. The unperturbed Hamiltonian is defined as the Fock operator, and the perturbed Hamiltonian is $H_{\text{el}} - \hat{F}$. The summation of the zeroth and first order MP energy gives the Hartree–Fock energy

$$E_{\text{MP0}} = {}_{\text{HF}}\langle \Psi_0 | \hat{F} | \Psi_0 \rangle_{\text{HF}} = 2 \sum_{j=1}^{N_e/2} \epsilon_j, \quad (2.78)$$

$$E_{\text{MP1}} = {}_{\text{HF}}\langle \Psi_0 | (H_{\text{el}} - \hat{F}) | \Psi_0 \rangle_{\text{HF}} = E_{\text{HF}} - E_{\text{MP0}},$$

and the higher order perturbations give corrections. The n -th order MP method is so-called MP_n , the simplest non-trivial MP method being MP_2 . For the excited states, a well-known method based on the MP theory is the algebraic diagrammatic construction (ADC) scheme for the polarization propagator [145, 146]. Similar to MP method, n -th order ADC method is called $\text{ADC}(n)$. There are also generalizations to multireference cases such as multireference Møller–Plesset perturbation theory and complete active space second-order perturbation theory (CASSPT2) [147–154].

The Configuration Interaction (CI) method is a wave function-based post-Hartree–Fock method. CI wave function is the linear superposition of all possible electronic configurations. The ansatz of the CI ground state wave function (up to a normalization factor) is

$$|\Psi_0\rangle_{\text{CI}} = (1 + \hat{C}) |\Psi_0\rangle_{\text{HF}}, \quad (2.79)$$

where

$$\hat{C} = \frac{1}{(1!)^1} \sum_{\sigma\tau} \sum_{a,j} c_{j\sigma}^{a\tau} a_{a\tau}^\dagger a_{j\sigma} + \frac{1}{(2!)^2} \sum_{\sigma,\sigma',\tau,\tau'} \sum_{a,b,j,k} c_{j\sigma k\sigma'}^{a\tau b\tau'} a_{a\tau}^\dagger a_{j\sigma} a_{b\tau'}^\dagger a_{k\sigma'} + \dots \quad (2.80)$$

Notice that this parameterization is identical to the exact wave function Eq. (2.58) if we account for all the possible configurations, which means that CI method is exact for the given basis set in this case. CI with all possible configurations is so-called Full CI (FCI) or exact diagonalization (ED). The cost of FCI scales exponentially with the system size, and thus can only be applied to small size systems. In practical simulations for large size systems, the truncation of the excitation configurations is required. CIS, which only accounts for the single excitation configurations, for ground state calculations is identical to

Hartree–Fock because of the Brillouin’s theorem. Therefore, the commonly used truncated CI for ground state calculations is CISD (only accounts for the single and double excitation configurations). The parameter equations of truncated CI are determined by the variational principle

$$\min_{\hat{C}} \frac{{}_{\text{CI}}\langle \Psi_0 | H_{\text{el}} | \Psi_0 \rangle_{\text{CI}}}{{}_{\text{CI}}\langle \Psi_0 | \Psi_0 \rangle_{\text{CI}}} . \quad (2.81)$$

One of the major problem of truncated CI is that it is not size-consistent, which is an important property of electronic structure calculations. If the energy summation of two non-interaction subsystems $E_A + E_B$ (calculation results) is identical to the energy of the total system E_{AB} (calculation result), the method is size-consistent. For the CISD method,

$$(1 + \hat{C}_{\text{SD}}^A) |\Psi_0\rangle_{A,\text{HF}} \otimes (1 + \hat{C}_{\text{SD}}^B) |\Psi_0\rangle_{B,\text{HF}} \neq (1 + \hat{C}_{\text{SD}}^{AB}) |\Psi_0\rangle_{AB,\text{HF}} , \quad (2.82)$$

where \hat{C}_{SD}^A is the operator \hat{C} with the truncation to single and double excitations for system A . For this reason, CISD is not size-consistent.

The excited state CI is similar to the ground state CI. We only need to replace the reference Hartree–Fock configuration with the excitation configurations [155]. For scenarios in which single reference CI fails, one can instead use multireference CI (MRCI) [154–163].

Another well-known wave function-based post-Hartree–Fock method is Coupled Cluster (CC). Unlike the CI employing a linear parameterization strategy, CC uses the exponential parameterization,

$$|\Psi_0\rangle_{\text{CC}} = \exp(\hat{T}) |\Psi_0\rangle_{\text{HF}} , \quad (2.83)$$

where

$$\hat{T} = \frac{1}{(1!)^1} \sum_{\sigma\tau} \sum_{a,j} t_{j\sigma}^{a\tau} a_{a\tau}^\dagger a_{j\sigma} + \frac{1}{(2!)^2} \sum_{\sigma,\sigma'} \sum_{a,b,j,k} t_{j\sigma k\sigma'}^{a\tau b\tau'} a_{a\tau}^\dagger a_{j\sigma} a_{b\tau'}^\dagger a_{k\sigma'} + \dots . \quad (2.84)$$

Full CC with all possible excitation configurations (up to N_{el}) is equivalent to FCI. However, truncated CC has a tremendous difference from truncated CI due to the exponential parameterization. First, truncated CCs are size-consistent. Second, the right (ket, $|\Psi_0\rangle_{\text{CC}} = \exp(\hat{T}) |\Psi_0\rangle_{\text{HF}}$) and left (bra, ${}_{\text{CC}}\langle \Psi_0 | = {}_{\text{HF}}\langle \Psi_0 | \exp(-\hat{T})$) CC wave functions are not Hermitian conjugate because the exponential coupled cluster operator $\exp(\hat{T})$ is non-unitary. Third, the parameters in CC are obtained by projecting the eigenvalue equation ansatz

$$\exp(-\hat{T}) H_{\text{el}} \exp(\hat{T}) |\Psi_0\rangle_{\text{HF}} = E_{\text{CC}} |\Psi_0\rangle_{\text{HF}} , \quad (2.85)$$

on ${}_{\text{HF}}\langle \Psi_0 |$ as well as other excited electron configurations

$$\begin{aligned} {}_{\text{HF}}\langle \Psi_0 | \exp(-\hat{T}) H_{\text{el}} \exp(\hat{T}) |\Psi_0\rangle_{\text{HF}} &= E_{\text{CC}} \\ {}_{\text{HF}}\langle \Psi_{\text{ex}} | \exp(-\hat{T}) H_{\text{el}} \exp(\hat{T}) |\Psi_0\rangle_{\text{HF}} &= 0 , \end{aligned} \quad (2.86)$$

where ${}_{\text{HF}}\langle\Psi_{\text{ex}}|$ is an arbitrary excitation configuration.

Truncated CCs can also be combined with the perturbation theory. The most successful combination CCSD(T) [164], in which triple excitation configurations are accounted for perturbatively, is known as the gold standard in quantum chemistry. The generalization to the multireference scenario is also possible [165]. CC for excited states computations are not as straightforward as for CI, and specific techniques for instance, Linear response coupled cluster (LR-CC) [166] and Equation-of-Motion Coupled-Cluster Theory (EOM-CC) [167], should be employed.

CC has a close connection to the quantum computations. In fact, unitary coupled cluster (UCC) [168, 169], of which the exponential coupled cluster operator $\exp(\hat{T} - \hat{T}^\dagger)$ is selected as a unitary operator, is widely used in variational quantum eigensolver (VQE) algorithms. For the detailed discussion, see Sec. 5.1.4.

To summarize, we briefly reviewed the Hartree–Fock method and several successful post-Hartree–Fock methods for electronic structure computations, which provide the necessary data for the construction of molecular Hamiltonian.

2.3 Multiconfiguration Time Dependent Hartree Method

In this section, we briefly review the most successful numerically “exact” (converged) quantum nuclear dynamics algorithm, Multiconfiguration Time Dependent Hartree (MCTDH) Method [33–35]. MCTDH is based on time dependent variational principle (TDVP). When the variational space is the full space, MCTDH is exact. MCTDH is very efficient for 4~18D systems. Its multilayer extension, Multilayer Multiconfiguration Time Dependent Hartree (ML-MCTDH), can be applied to systems with hundreds even thousands DOFs [36]. We will use the numerical results of MCTDH as the standard for benchmarking GDTWA in chapter 4.

MCTDH can also be used in open quantum systems. One can discretize the bath DOFs and perform computations on the wave function for the total systems. Temperature effects can be considered with the help of Monte Carlo sampling [36]. Other methods to treat open quantum systems include quasi-adiabatic path-integral (QUAPI) [170] and reduced hierarchical equations of motion (HEOM) theory [171].

2.3.1 Time Dependent Variational Principle

There are three widely used different time dependent variational principles [172]: Dirac-Frenkel variational principle, McLachlan variational principle, and Lagrange variational principle. Suppose the time dependent wave function $|\Psi(t)\rangle$ is approximated as a parametrized

trial state $|\Phi(\theta(t))\rangle$, and $|\Psi(0)\rangle = |\Phi(\theta(0))\rangle$. Generally $|\Phi(\theta(t))\rangle$ does not fulfil the Schrödinger equation

$$i \frac{d}{dt} |\Phi(\theta(t))\rangle = i \frac{\partial}{\partial \theta} |\Phi(\theta(t))\rangle \dot{\theta} = H |\Phi(\theta(t))\rangle, \quad (2.87)$$

because the restrictions of $|\Phi(\theta(t))\rangle$ make the equation overdetermined. $i \frac{\partial}{\partial \theta} |\Phi(\theta(t))\rangle \dot{\theta}$ is in the variational manifold, while $H |\Phi(\theta(t))\rangle$ is not. The Dirac-Frenkel variational principle directly projects Eq. (2.87) onto the variational manifold

$$\langle \delta \Phi(\theta(t)) | (H - i \frac{d}{dt}) |\Phi(\theta(t))\rangle = 0. \quad (2.88)$$

McLachlan variational principle solves Eq. (2.87) by least squares methods

$$\min_{\frac{d}{dt} |\Phi(\theta(t))\rangle} \| (H - i \frac{d}{dt}) |\Phi(\theta(t))\rangle \|^2, \quad (2.89)$$

which gives

$$\text{Im} \langle \delta \Phi(\theta(t)) | (H - i \frac{d}{dt}) |\Phi(\theta(t))\rangle = 0. \quad (2.90)$$

Schrödinger equation can also be obtained by minimizing the action

$$\delta \int_{t_1}^{t_2} dt L = 0, \quad \delta L(t_1) = \delta L(t_2) = 0, \quad (2.91)$$

$$L = \langle \Psi(t) | (i \frac{\partial}{\partial t} - H) |\Psi(t)\rangle.$$

Lagrange variational principle is obtained by replacing $|\Psi(t)\rangle$ with $|\Phi(\theta(t))\rangle$ in the Lagrange Eq. (2.91), which gives

$$\text{Re} \langle \delta \Phi(\theta(t)) | (H - i \frac{d}{dt}) |\Phi(\theta(t))\rangle = 0. \quad (2.92)$$

When the parameters are complex, $i |\Phi\rangle$ is in the variational manifold if $|\Phi\rangle$ is in the variational manifold, which makes three TDVPs equivalent. This is the usual case of classical computers. Many efficient algorithms have been developed based on TDVP, for instance, MCTDH and TDVP-MPS [173, 174]. Apparently, TDVP is equivalent to Schrödinger equation when the variational manifold is the full Hilbert space. TDVP preserves the norm and average energy

$$\frac{d}{dt} \langle \Phi | \Phi \rangle = 0, \quad (2.93)$$

$$\frac{d}{dt} \langle \Phi | H | \Phi \rangle = 0.$$

TDVP is also extremely useful in quantum simulations. The quantum state ansatz is generated by the unitary quantum gate, thus the variational parameters are real. In this case, McLachlan variational principle is the most convenient TDVP [172]. TDVP can also be generalized to mixed states, dissipative dynamics, and imaginary time evolution [172].

2.3.2 Standard Methods and Time Dependent Hartree Methods

Before moving to MCTDH, we will introduce standard method, and time dependent Hartree (TDH) approach first. MCTDH can be identical to both of them in certain cases.

Consider a f DOFs distinguishable particles (nuclei) quantum system with Hamiltonian H . We will show how to find the numerical solution of the time dependent Schrödinger equation of this system. Modern computers can only deal with finite number of operations. Therefore, the first step is always to truncate the basis, in one way or another. We will use spectral methods, i.e., projecting wave function and observable onto certain finite basis sets, to derive the EOMs, and discuss the discrete variable representation (DVR) in the numerical implementation subsections.

The standard method is to truncate the basis set of each DOF and use the wave function ansatz

$$\Phi(q_1, q_2, \dots, q_f, t) = \sum_{j_1=1}^{N_1} \sum_{j_2=1}^{N_2} \cdots \sum_{j_f=1}^{N_f} C_{j_1 j_2 \dots j_f}(t) \chi_{j_1}^{(1)}(q_1) \chi_{j_2}^{(2)}(q_2) \cdots \chi_{j_f}^{(f)}(q_f), \quad (2.94)$$

where $\chi_{j_f}^{(f)}(q_f)$ is time independent basis set for DOF f , and N_f is the number of basis. For convenience, we introduce the symbol $J = (j_1, \dots, j_f)$, $\chi_J = \prod_{\kappa=1}^f \chi_{j_\kappa}$. Applying TDVP to the ansatz Eq. (2.94), the EOMs are obtained

$$i\dot{C}_L = \sum_J \langle \chi_L | H | \chi_J \rangle C_J. \quad (2.95)$$

The convergence is checked by increasing N_κ . Eq. (2.95) is formally identical to the Schrödinger equation, and thus is exact for the given basis sets. The standard method is an analog of FCI. N^f time dependent coefficients need to be solved in the standard method. When we estimate the numerical efforts and memory, we always suppose the number of basis sets of all DOFs are identical to N for simplicity. The computational effort and memory of the standard method blow up exponentially. Usually, the convergence requires at least $N = 10$. Therefore, the standard method can only be used in 4 atoms (6D) systems (10^6 coefficients). For the detailed estimation on the computational efforts, see the numerical implementation subsection.

TDH is the simplest time dependent method for a f DOFs distinguishable particles quantum system. The relation of TDH and MCTDH is similar to Hartree–Fock method and MCSCF. The wave function ansatz of TDH is

$$\Phi(q_1, q_2, \dots, q_f, t) = a(t) \prod_{\kappa=1}^f \phi_\kappa(q_\kappa, t), \quad (2.96)$$

where ϕ_κ is single particle function (SPF). SPFs are further expanded as linear superpositions

of primitive time independent basis sets

$$\phi_{\kappa}(q_{\kappa}, t) = \sum_{j_{\kappa}=1}^{N_{\kappa}} c_{j_{\kappa}}(t) \chi_{j_{\kappa}}^{(\kappa)}(q_{\kappa}). \quad (2.97)$$

The total time coefficients of TDH is $1 + Nf$, which is much less than the standard method.

The choices of SPFs and $a(t)$ are not unique even with the normalization restriction on SPFs. The wave function can be rewritten as the product of a single hole function (SHF) $\Phi^{(\kappa)}$ and a SPF ϕ_{κ}

$$\Phi(q_1, q_2, \dots, q_f, t) = \phi_{\kappa}(q_{\kappa}, t) \Phi^{(\kappa)}, \quad (2.98)$$

where κ can be arbitrary, and arguments of $\Phi^{(\kappa)}$ are t and all q except q_{κ} . The wave function is invariant under the following gauge transformation

$$\begin{aligned} \tilde{\phi}_{\kappa}(q_{\kappa}, t) &= b(t) \phi_{\kappa}(q_{\kappa}, t), \\ \tilde{\Phi}^{(\kappa)} &= \Phi^{(\kappa)} / b(t), \end{aligned} \quad (2.99)$$

where $b(t)$ is an arbitrary modulus 1 time dependent complex function.

In order to eliminate this gauge freedom [16] and make the EOMs of $a(t)$ and $\phi_{\kappa}(q_{\kappa}, t)$ unique, we introduce the constraint

$$i \langle \phi_{\kappa} | \dot{\phi}_{\kappa} \rangle = i \int dq_{\kappa} \phi_{\kappa}^*(q_{\kappa}, t) \frac{d}{dt} \phi_{\kappa}(q_{\kappa}, t) = g_{\kappa}(t). \quad (2.100)$$

The norm conservation of SPFs implies that $g_{\kappa}(t)$ are real. The EOMs of SPFs and $a(t)$ are given by

$$i \frac{d}{dt} a = (E - \sum_{\kappa=1}^f g_{\kappa}) a, \quad (2.101)$$

$$i \frac{d}{dt} \phi_{\kappa} = (\mathcal{H}^{(\kappa)} - E + g_{\kappa}) \phi_{\kappa}, \quad (2.102)$$

where E is the average energy and $\mathcal{H}^{(\kappa)}$ is called a mean-field

$$E = \langle \Phi | H | \Phi \rangle, \quad (2.103)$$

$$\mathcal{H}^{(\kappa)} = \langle \Phi^{(\kappa)} | H | \Phi^{(\kappa)} \rangle. \quad (2.104)$$

We decompose the Hamiltonian into two parts, the single DOF operator $h^{(\kappa)}$, which only acts on κ -th DOF, and the residual or non-separable part H_R

$$H = \sum_{\kappa} h^{(\kappa)} + H_R. \quad (2.105)$$

TDH is exact when different DOFs of the Hamiltonian are decoupled ($H_R = 0$)

$$H = \sum_{\kappa} H_{\kappa}, \quad (2.106)$$

$$\mathcal{H}^{(\kappa)} = \langle \Phi^{(\kappa)} | H | \Phi^{(\kappa)} \rangle = H_{\kappa}. \quad (2.107)$$

When the non-separable part of the Hamiltonian is small, we can expect that TDH will give a qualitatively reasonable results. However, it is not the case for most chemical systems. We need to find a method which can achieve exact (converged) results while remaining numerically tractable for not too small systems. Here, MCTDH, which can interpolate between standard method and TDH, is a method by choice.

2.3.3 Wave Function Ansatz and Equation of Motion

The MCTDH wave function ansatz is

$$\Phi(q_1, q_2, \dots, q_f, t) = \sum_{j_1}^{n_1} \cdots \sum_{j_f}^{n_f} A_{j_1 \dots j_f}(t) \prod_{\kappa=1}^f \phi_{j_\kappa}^{(\kappa)}(q_\kappa, t), \quad (2.108)$$

where $A_{j_1 \dots j_f}(t)$ is the A -vector, and $\phi_{j_\kappa}^{(\kappa)}(q_\kappa, t)$ are time dependent orthonormalized SPFs. Similar to TDH, $\phi_{j_\kappa}^{(\kappa)}(q_\kappa, t)$ are also expanded by the primitive time independent basis

$$\phi_{j_\kappa}^{(\kappa)}(q_\kappa, t) = \sum_{i_\kappa=1}^{N_\kappa} c_{i_\kappa}^{(\kappa, j_\kappa)}(t) \chi_{i_\kappa}^{(\kappa)}(q_\kappa). \quad (2.109)$$

Both SPFs and A -vectors are optimized by TDVP. The key idea of MCTDH is to use a relatively small optimal time dependent basis set to describe the system quantitatively. This type of wave function is also known as a Tucker tensor, one of the tree tensor networks. The convergence should be checked by increasing N_κ and n_κ for all κ . Apparently, MCTDH is equivalent to the standard method when $n_\kappa = N_\kappa$ for all κ . When $n_\kappa = 1$ for all κ , MCTDH is equivalent to TDH.

For convenience, we introduce the following notations,

$$J = (j_1, \dots, j_f), \quad (2.110)$$

$$A_J = A_{j_1, \dots, j_f}, \quad (2.111)$$

$$\Phi_J = \prod_{\kappa=1}^f \phi_{j_\kappa}^{(\kappa)}. \quad (2.112)$$

Similar to TDH, MCTDH wave function can be expressed as a summation of the product of SPFs $\phi_l^{(\kappa)}(q_\kappa, t)$ and SHFs $\Phi_l^{(\kappa)}$

$$\Phi(q_1, q_2, \dots, q_f, t) = \sum_{l=1}^{\kappa} \phi_l^{(\kappa)}(q_\kappa, t) \Phi_l^{(\kappa)}, \quad (2.113)$$

where κ can be arbitrary, and arguments of $\Phi_l^{(\kappa)}$ are t and all q except q_κ . The explicit expression of SHF is

$$\Phi_l^{(\kappa)} = \sum_{j_1=1}^{n_1} \cdots \sum_{j_{\kappa-1}=1}^{n_{\kappa-1}} \sum_{j_{\kappa+1}=1}^{n_{\kappa+1}} \cdots \sum_{j_f=1}^{n_f} A_{j_1 \dots j_{\kappa-1} j_{\kappa+1} \dots j_f} \phi_{j_1}^{(1)} \cdots \phi_{j_{\kappa-1}}^{(j_{\kappa-1})} \phi_{j_{\kappa+1}}^{(j_{\kappa+1})} \cdots \phi_{j_f}^{(1)}, \quad (2.114)$$

The wave function is invariant under the following gauge transformation

$$\begin{aligned}\tilde{\phi}_{j\kappa}^{(\kappa)}(q_\kappa, t) &= \sum_{l_\kappa=1}^{n_\kappa} U_{j\kappa l_\kappa}^{(\kappa)} \phi_{l_\kappa}^{(\kappa)}(q_\kappa, t), \\ \tilde{\Phi}_{j\kappa}^{(\kappa)} &= \sum_{l_\kappa=1}^{n_\kappa} (U^{(\kappa)})_{j\kappa l_\kappa}^{-1} \Phi_{l_\kappa}^{(\kappa)},\end{aligned}\tag{2.115}$$

where $(\)_{jk}^{-1}$ represents the matrix elements of the inverse of matrix. The constraint which fixes gauge freedom is a matrix in MCTDH

$$g_{jl}^{(\kappa)} = i \langle \phi_j^{(\kappa)} | \hat{g}^{(\kappa)} | \phi_l^{(\kappa)} \rangle = i \langle \phi_j^{(\kappa)} | \dot{\phi}_l^{(\kappa)} \rangle.\tag{2.116}$$

The common choices of $\hat{g}^{(\kappa)}$ are either $\hat{g}^{(\kappa)} = 0$ or $\hat{g}^{(\kappa)} = h^{(\kappa)}$, For convenience, we introduce the gauge modified Hamiltonian

$$H_g = H - \sum_{\kappa} \hat{g}^{(\kappa)}.\tag{2.117}$$

Apparently, $H_g = H$ when $\hat{g}^{(\kappa)} = 0$, and $H_g = H_R$ when $\hat{g}^{(\kappa)} = h^{(\kappa)}$.

In order to derive EOMs, Hamiltonian matrix elements between each configuration, the mean fields of MCTDH and density matrix of each DOF given by SHFs are required,

$$\mathcal{H}_{g;JL} = \langle \Phi_J | H_g | \Phi_L \rangle\tag{2.118}$$

$$\mathcal{H}_{g;jl}^{(\kappa)} = \langle \Phi_j^{(\kappa)} | H_g | \Phi_l^{(\kappa)} \rangle,\tag{2.119}$$

$$\rho_{jl}^{(\kappa)} = \langle \Phi_j^{(\kappa)} | \Phi_l^{(\kappa)} \rangle.\tag{2.120}$$

Notice that the mean field is a matrix for each DOF in MCTDH, rather than a number for each DOF in THD. $\mathcal{H}_{R;JL}$, $\mathcal{H}_{R;jl}^{(\kappa)}$ and $\mathcal{H}_{jl}^{(\kappa)}$ can be defined in the same way.

Applying TDVP to MCTDH wave function ansatz Eq. (2.108), we obtain EOMs of SPFs and A_J

$$i\dot{A}_J = \sum_L \mathcal{H}_{g;JL} A_L,\tag{2.121}$$

$$i\dot{\phi}_j^{(\kappa)} = \sum_l g_{jl}^{(\kappa)} \phi_l^{(\kappa)} + (1 - P^{(\kappa)}) \sum_l \sum_k (\rho^{(\kappa)})_{jk}^{-1} \mathcal{H}_{g;kl}^{(\kappa)} \phi_l^{(\kappa)},\tag{2.122}$$

where $P^{(\kappa)}$ is the projector of κ -th DOF

$$P^{(\kappa)} = \sum_{j=1}^{n_\kappa} |\phi_j^{(\kappa)}\rangle \langle \phi_j^{(\kappa)}|.\tag{2.123}$$

More explicitly, when we choose $\hat{g}^{(\kappa)} = h^{(\kappa)}$

$$i\dot{A}_J = \sum_L \mathcal{H}_{R;JL} A_L,\tag{2.124}$$

$$i\dot{\phi}_j^{(\kappa)} = \sum_l h_{jl}^{(\kappa)} \phi_l^{(\kappa)} + (1 - P^{(\kappa)}) \sum_l \sum_k (\rho^{(\kappa)})_{jk}^{-1} \mathcal{H}_{R;kl}^{(\kappa)} \phi_l^{(\kappa)},\tag{2.125}$$

and when we choose $\hat{g}^{(\kappa)} = 0$

$$i\dot{A}_J = \sum_L \mathcal{H}_{JL} A_L, \quad (2.126)$$

$$i\dot{\phi}_j^{(\kappa)} = (1 - P^{(\kappa)}) \sum_l h_{jl}^{(\kappa)} \phi_l^{(\kappa)} + (1 - P^{(\kappa)}) \sum_l \sum_k (\rho^{(\kappa)})_{jk}^{-1} \mathcal{H}_{R;kl}^{(\kappa)} \phi_l^{(\kappa)}. \quad (2.127)$$

We will examine the EOMs in some limiting cases. When H_R is zero, different DOFs of the system are decoupled. Both MCTDH and TDH are exact in this case. When $n_\kappa = 1$ for all κ , EOMs of MCTDH, Eq. (2.121) and (2.122), reduce to EOMs of TDH, Eq. (2.101) and (2.102), respectively. Eq. (2.121) is formally identical to the EOM of standard method Eq. (2.95) except two differences: 1. $\mathcal{H}_{g;JL}$ is time dependent due to the time dependent SPFs; 2. There is a gauge contribution in $\mathcal{H}_{g;JL}$. Eq. (2.122) tells us that SPFs rotate to the tangent subspace of SPFs except for the gauge contribution.

$$iP^{(\kappa)} \dot{\phi}_j^{(\kappa)} = \sum_l P^{(\kappa)} g_{jl}^{(\kappa)} \phi_l^{(\kappa)}. \quad (2.128)$$

Therefore, SPFs are time independent if they are complete and $\hat{g}^{(\kappa)} = 0$. Eq. (2.121) is also identical to the EOM of the standard method Eq. (2.95) in this scenario.

The inverse of density matrix in Eq. (2.122) suggests that EOMs of MCTDH can be singular. In fact it almost always happens since the initial state is usually prepared as a Hartree product. In numerical simulations, the singularity is solved by adding a small regularization parameter ϵ to the small eigenvalue of the density matrix. The small eigenvalue of the density matrix suggests that unoccupied SPFs rotate to the correct direction rapidly. This is known as the self-healing of MCTDH. In this sense, the initial unoccupied SPFs can be chosen arbitrarily. There are other techniques to solve the singularity of MCTDH, for instance, other advanced regularization schemes [175, 176], EOMs without singularity [177–179], and spawning optimal unoccupied SPFs on-the-fly [180].

We suppose $n_\kappa = n$ and $N_\kappa = N$ for all κ for the memory estimation. The detailed discussion of computational effort estimation will be presented in the next subsection. The total number of time dependent coefficients of MCTDH is $fnN + n^f$, which is still an exponential function of f . However, the base of the exponential function reduces from N to n . When $n \ll N$, the reduction is huge. To reduce computational efforts and memory further, we can group several DOFs into one logical DOF. This is so-called mode-combination of MCTDH. The mode-combination MCTDH wave function ansatz is

$$\Phi(q_1, q_2, \dots, q_f, t) = \Phi(Q_1, Q_2, \dots, Q_p, t) = \sum_{j_1}^{\tilde{n}_1} \dots \sum_{j_p}^{\tilde{n}_p} A_{j_1 \dots j_p}(t) \prod_{\kappa=1}^p \phi_{j_\kappa}^{(\kappa)}(Q_\kappa, t), \quad (2.129)$$

where

$$Q_\kappa = (q_{\kappa,1}, q_{\kappa,2}, \dots, q_{\kappa,d}) \quad (2.130)$$

$$\phi_j^{(\kappa)}(Q_\kappa, t) = \sum_{i_1 \dots i_d} C_{i_1 \dots i_d}^{(\kappa,j)}(t) \chi^{(\kappa,1)}(q_{\kappa,1}) \dots \chi^{(\kappa,d)}(q_{\kappa,d}), \quad (2.131)$$

and \tilde{n} represents the new numbers of SPFs to reach the convergence. Again, we suppose all \tilde{n}_κ are identical for the estimation of computation efforts. If $\tilde{n} = n^d$, the mode-combination MCTDH wave function ansatz is identical to the ordinary MCTDH wave function ansatz, thus, we gain nothing. However, \tilde{n} reaching convergence in mode-combination is usually much smaller than n^d . As a rule of thumb, $\tilde{n} \approx nd$, or even smaller, therefore, the reduction of computation efforts is huge. Mode-combination MCTDH can be used in $\sim 20D$ systems. The limitation of mode-combination MCTDH is that SPFs become multidimensional functions. If one over combines DOFs, the propagation of SPFs will be much more slower and mode-combination MCTDH loses its efficiency. Empirically, 2-mode combination and 3-mode combination are relatively efficient.

MCTDH can propagate multidimensional functions efficiently. Following the spirit of MCTDH, one can use MCTDH type expansion hierarchically to build wave function ansatz for larger size systems. More explicitly, Eq. (2.131) is formally identical to the standard method (FCI type expansion). One can replace the FCI type expansion by the MCTDH type expansion. This can be regarded as adding a new layer between primitive basis and A -vector. One can also treat SPFs $\phi_j^{(\kappa)}(Q_\kappa, t)$ in Eq. (2.129) as “primitive basis sets”, then the FCI type expansion of Eq. (2.129) can be replaced by MCTDH type. To do such operations recursively, the new wave function ansatz can be built. This is so-called multilayer MCTDH (ML-MCTDH) [36–38], which is known as a hierarchical Tucker tensor. ML-MCTDH can be used in hundreds or even thousands DOFs systems.

The application range of MCTDH is not limited to the quantum nuclear propagation dynamics (distinguishable particles). The extension to quantum nuclear propagation with multi-PES electronic DOF is straightforward [181]. The first extension is to add an additional coordinate to describe the electronic DOF

$$\Phi(q_1, q_2, \dots, q_f, \alpha, t) = \sum_{j_1}^{n_1} \dots \sum_{j_f}^{n_f} \sum_s^{n_s} A_{j_1 \dots j_f s}(t) \prod_{\kappa=1}^f \phi_{j_\kappa}^{(\kappa)}(q_\kappa, t) \phi_s^{(f+1)}(\alpha, t), \quad (2.132)$$

where α is discrete and represents the diabatic electronic states. Ordinarily, there are only few PESs that need to be considered. Therefore, the SPF of electronic DOFs is chosen as a complete time independent basis

$$\phi_s^{(f+1)}(\alpha, t) = \delta_{s\alpha}. \quad (2.133)$$

One can re-write Eq. (2.132) as a single-set formalism

$$\Phi(q_1, q_2, \dots, q_f, \alpha, t) = \sum_{j_1}^{n_1} \cdots \sum_{j_f}^{n_f} \sum_s^{n_s} A_{j_1 \dots j_f s}(t) \prod_{\kappa=1}^f \phi_{j_\kappa}^{(\kappa)}(q_\kappa, t) |\alpha\rangle. \quad (2.134)$$

The reason why Eq. (2.134) is called single-set formalism is that different electronic states share the same nuclear SPFs. The Hamiltonian of the system can be expressed as

$$H = \sum_{\alpha, \beta} H^{(\alpha\beta)} |\alpha\rangle \langle \beta| \quad (2.135)$$

A more sophisticated wave function ansatz is multi-set formalism

$$\Phi(q_1, q_2, \dots, q_f, \alpha, t) = \sum_s^{n_s} \Phi^{(\alpha)}(q_1, q_2, \dots, q_f, t) |\alpha\rangle, \quad (2.136)$$

$$\Phi^{(\alpha)}(q_1, q_2, \dots, q_f, \alpha, t) = \sum_{j_1}^{n_1} \cdots \sum_{j_f}^{n_f^\alpha} A_{j_1^\alpha \dots j_f^\alpha}(t) \prod_{\kappa=1}^f \phi_{j_\kappa^\alpha}^{(\kappa, \alpha)}(q_\kappa, t), \quad (2.137)$$

in which different electronic states have different nuclear SPFs. The formalism can represent the wave function more efficiently when the dynamics of in the different diabatic states are quite different. For a given α , SHFs, the gauge constraints, projection operator and density matrix can be defined similar to ordinary MCTDH. The EOMs of multi-set formalism are

$$i\dot{A}_J^{(\alpha)} = \sum_{\beta=1}^{n_s} \sum_L \mathcal{H}_{g; JL}^{(\alpha\beta)} A_L^{(\beta)}, \quad (2.138)$$

$$i\dot{\phi}_j^{(\kappa, \alpha)} = \sum_{l=1}^{n_\kappa^\alpha} g_{jl}^{(\kappa, \alpha)} \phi_l^{(\kappa, \alpha)} + (1 - P^{(\kappa, \alpha)}) \sum_{\beta=1}^{n_s} \sum_{k=1}^{n_\kappa^\alpha} \sum_{l=1}^{n_\kappa^\beta} (\rho^{(\kappa, \alpha)})_{jk}^{-1} \mathcal{H}_{g; kl}^{(\kappa, \alpha\beta)} \phi_l^{(\kappa, \beta)}, \quad (2.139)$$

where

$$H_g^{(\alpha\beta)} = H^{(\alpha\beta)} - \hat{g}^{(\kappa, \alpha)} \delta_{\alpha\beta}, \quad (2.140)$$

$$\mathcal{H}_{g; JL}^{(\alpha\beta)} = \langle \Phi_J^{(\alpha)} | H_g^{(\alpha\beta)} | \Phi_L^{(\beta)} \rangle, \quad (2.141)$$

$$\mathcal{H}_{g; kl}^{(\kappa, \alpha\beta)} = \langle \Phi_k^{(\alpha, \kappa)} | H_g^{(\alpha\beta)} | \Phi_l^{(\beta, \kappa)} \rangle. \quad (2.142)$$

MCTDH can also be used in quantum dynamics of spin chains and indistinguishable particles. Specifically, the particle exchange symmetry must be considered for the application to indistinguishable particles. This can be achieved by either transferring to the second quantization representation (MCTDH-SQR) [182, 183], or using the permanent for bosons (MCTDHB) [184, 185] and slater determinant for fermions (MCTDHF) [184, 185] wave function ansatz in the first quantization representation. With the help of TDVP of mixed state, dissipative dynamics, and relaxation, MCTDH can be extended to these scenarios.

The extension to non-Hermitian Hamiltonians is extremely useful in the scattering problem [33]. Artificial complex absorbing potentials are often added in the non-interaction region to absorb the wave function, which can avoid the long grids (large basis sets). One can also use the MCTDH type wave function ansatz and variational principle to find the eigenstates and eigen energies of the system.

2.3.4 Numerical Implementations

In this subsection, we will briefly review three numerical techniques [33] to improve the numerical efficiency of MCTDH, constant mean-field integration (CMF), DVR [186], and the product form of potential representation. The most expensive operations in MCTDH is to propagate A -vector and the build-up of the mean-fields. In contrast, the propagation of SPFs is rather cheap $\sim sf n N^2$. CMF can reduce the numbers of mean fields build-up. DVR and the product form of potential representation can make mean fields build-up more efficient. All three techniques can improve the efficiency of the propagation of A -vector.

Notice that MCTDH EOMs Eq. (2.121,2.122) are coupled non-linear differential equations. They can be solved by standard integrators such as Runge–Kutta integrator and Adams–Bashforth–Moulton integrator. Due to the fact that $\mathcal{H}_{g;JL}$ and mean fields $\mathcal{H}_{kl}^{(\kappa)}$ must be constructed at each time step, this integration approach is called variable mean-field (VMF) approach. However, the time scale separation between rapidly oscillating A -vectors, SPFs and slowly oscillating $\mathcal{H}_{g;JL}$, $\mathcal{H}_{kl}^{(\kappa)}$ makes VMF inefficient. One way to resolve this problem is to propagate A -vector and SPFs while keeping $\mathcal{H}_{g;JL}$ and $\mathcal{H}_{kl}^{(\kappa)}$ constant during a larger time step τ

$$i\dot{A}_J = \sum_L \bar{\mathcal{H}}_{g;JL} A_L, \quad (2.143)$$

$$i\dot{\phi}_j^{(\kappa)} = \sum_l g_{jl}^{(\kappa)} \phi_l^{(\kappa)} + (1 - P^{(\kappa)}) \sum_l \left\{ \sum_k (\bar{\rho}^{(\kappa)})_{jk}^{-1} \bar{\mathcal{H}}_{kl}^{(\kappa)} - g_{jl}^{(\kappa)} \right\} \phi_l^{(\kappa)}, \quad (2.144)$$

where bars over quantities indicate they are constants during the time step τ . Compared with VMF approach, the EOM of A -vector is linear, which means adapted integrator like Short Iterative Lanczos integrator can be used. On the other hand, $\mathcal{H}_{g;JL}$, $\mathcal{H}_{kl}^{(\kappa)}$ and density matrix need to be built much less than VMF approach. Although the above strategy is simple for the practical numerical simulations, it shows the key idea of CMF approach. More sophisticated higher-order CMF approach is used in practical simulations. We point out that CMF approach violates the energy conservation. If one finds that the energy deviation is unacceptable, a smaller τ must be used.

Both standard method and MCTDH use DVR primitive basis sets. The matrix multiplication operations $\langle \chi_L | H | \chi_J \rangle$ and $\langle \Phi_L | V | \Phi_J \rangle$ are demanded for the propagation of standard method and A -vector in MCTDH, respectively. Hamiltonian can be separated into two parts,

the kinetic operator and potential operator. Potential matrix is diagonal in the DVR basis, therefore, matrix multiplication can speed up drastically by using DVR. In this sense, DVR plays an important role in the standard method, while it has a loose connection to MCTDH. However, a specific type DVR, correlation DVR (CDVR) [187] built by SPFs, is one of the choice to improve the efficiency of propagating A -vector. We will briefly review the role of DVR and CDVR in the standard method and MCTDH, respectively.

Consider the projector onto the subspace \mathcal{S} spanned by the finite basis sets

$$\hat{P} = \sum_{j=1}^N |\varphi_j\rangle \langle \varphi_j| . \quad (2.145)$$

The spectral method approximates the operator T , V and state vector $\langle \Psi|$ as

$$T_{jk}^S = \langle \varphi_j| T | \varphi_k \rangle , \quad (2.146)$$

$$V_{jk}^S = \langle \varphi_j| V | \varphi_k \rangle , \quad (2.147)$$

$$|\Psi\rangle^S = \hat{P} |\Psi\rangle , \quad (2.148)$$

where the superscript S represents the approximation value under the spectral method. VBR (variational basis-set representation) is also used to label them in the other references because the variational methods use these evaluations.

Similar to spectral method, DVR is a scheme to truncate the continuum function to finite basis sets. The key idea of DVR is to approximate the state vector and potential matrix as the values on certain grid points with weights

$$|\Psi\rangle^{\text{DVR}} = \sum_{\alpha=1}^N w_{\alpha}^{1/2} \Psi(x_{\alpha}) |\chi_{\alpha}\rangle , \quad (2.149)$$

$$V_{\alpha\beta}^{\text{DVR}} = V(x_{\alpha}) \delta_{\alpha\beta} , \quad (2.150)$$

where $|\chi_{\alpha}\rangle$ is the DVR basis, and w_{α} are weights on the grid points x_{α} . Eq. (2.150) is the reason why DVR is so intriguing. The potential matrix is diagonal on the DVR basis, which reduces the operations of $\langle \chi_L| V | \chi_J \rangle$ in the standard methods (Eq. (2.95)) per integration step from N^{2f} to N^f .

DVR function behaves like a δ -function in the grid points

$$\langle x_{\alpha} | \chi_{\beta} \rangle = \chi_{\beta}(x_{\alpha}) = w_{\alpha}^{-1/2} \delta_{\alpha\beta} . \quad (2.151)$$

DVR basis is complete in the subspace \mathcal{S}

$$\hat{P} = \sum_{\alpha=1}^N |\chi_{\alpha}\rangle \langle \chi_{\alpha}| , \quad (2.152)$$

and the unitary transformation between DVR basis and basis $|\varphi\rangle_j$ is

$$U_{j\alpha} = \langle \varphi_j | \chi_\alpha \rangle = w_\alpha^{1/2} \varphi_j^*(x_\alpha). \quad (2.153)$$

The matrix elements of kinetic operators in the DVR basis can be evaluated with the help of unitary transformation

$$T_{\alpha\beta}^{\text{DVR}} = T_{\alpha\beta}^{\text{S}} = \sum_{j,k} \langle \chi_\alpha | T | \chi_\beta \rangle = U_{j\alpha}^* T_{jk} U_{k\beta}. \quad (2.154)$$

Generally speaking, the DVR expression and spectral expression do not coincide unless $|\Psi\rangle = \hat{P}|\Psi\rangle \in \mathcal{S}$ and $V = \hat{P}V\hat{P}$. Strictly speaking, the standard method using DVR destroys TDVP. However, it does not mean the truncation error of DVR is larger than spectral method. In fact, DVR truncation error is usually in the same order or smaller than spectral truncation error for smooth potentials and not too few grid points.

It is not always possible to find a DVR which satisfies all above properties. If a DVR does satisfy all above properties, we call it proper DVR. Proper DVR can be generated if the matrix $Q_{jk} = \langle \varphi_j | x | \varphi_k \rangle$ is tri-diagonal. The unitary transformation $U_{j\alpha}$ and grid points x_α are selected as eigenvectors and eigenvalues of Q_{jk} matrix

$$Q_{jk} = \sum_{\alpha=1}^N U_{j\alpha} x_\alpha U_{k\alpha}^*, \quad (2.155)$$

and the weight $w_\alpha^{1/2} = U_{j\alpha}/\varphi_j^*(x_\alpha)$ can be generated by Eq. (2.153), which is independent of j . One can still approximate the potential matrix as its values on the certain grid points without weights if Q_{jk} is not tri-diagonal. This type of DVR is improper DVR.

Notice that $|\Phi_L\rangle$ in MCTDH EOMs Eq. (2.121) is not the primitive basis set, hence the Eq. (2.150) cannot be used directly in MCTDH. Instead, one can use CDVR, and a similar trick as Eq. (2.150) to propagate A -vector. The key idea of CDVR is to build DVR by using SPFs with a modification term that exactly represents the uncorrelated part of the potential. The computational effort of CDVR is $fNn^{f-1} + n^f$. Q_{jk} matrix is time dependent and not tri-diagonal in general. In this sense, CDVR is an improper DVR.

Next we will see how to speed up the matrix multiplication related to $\langle \chi_L | T | \chi_J \rangle$ and $\langle \Phi_L | T | \Phi_J \rangle$ terms with the help of the product form of the kinetic operator. This inspires to approximate the potential operator as a sum of product form operators, which provides another choice to speed up the matrix multiplication related to $\langle \Phi_L | V | \Phi_J \rangle$.

Let us focus on the standard method first. The kinetic operator takes a product form

$$T = \sum_{r=1}^s T^{(1,r)} \dots T^{(f,r)}, \quad (2.156)$$

with $s \approx f$ and lots of $T^{(\kappa,r)}$ are unit. Meanwhile, $T^{(\kappa,r)}$ acts only on the κ -th DOF, which suggests that we can do the matrix multiplication successively

$$\sum_J \langle \chi_L | T | \chi_J \rangle C_J = \sum_{r=1}^s \sum_{j_1} T_{l_1 j_1}^{(1,r)} \cdots \sum_{j_f} T_{l_f j_f}^{(f,r)} C_J, \quad (2.157)$$

where

$$T_{l_\kappa j_\kappa}^{(\kappa,r)} = \langle \chi_{l_\kappa}^{(\kappa)} | T^{(\kappa,r)} | \chi_{j_\kappa}^{(\kappa)} \rangle, \quad (2.158)$$

for $\kappa = 1, 2, \dots, f$. The total effort is sfN^{f+1} , which is much smaller than N^{2f} . This technique can also be used in the kinetic matrix multiplication of A -vector propagation as well as the mean fields build-up, which gives sf^2n^{f+1} . The similar technique can also be used in the potential matrix multiplication of MCTDH. In order to do that, we need to approximate potential operator as a sum of products. This can be done by canonical polyadic decomposition (CPD) [33], multi-grid potfit (MGPF) [188], n -mode representation [189, 190], and Monte Carlo potfit (MCPF) [191].

To summarize, we briefly reviewed the theoretical derivation and numerical implementation of the MCTDH, which is the state-of-the-art numerically converged method for non-adiabatic quantum dynamics. We will also use it as the standard of the benchmarks in the numerical results of Chapter 4.

2.4 Models

Models are essential for chemistry and physics. They are obtained by simplifying real systems while retaining the key physical or chemical features. One advantage of models over the real systems is that the parameters in the models are more flexible, which can help us know the major effects of various phenomena. The sizes of models are usually less than the real systems to render numerical simulations feasible. These two properties are crucial for benchmarking the new approximate numerical methods.

In this section, we will review the common models for the non-adiabatic dynamics, including scattering Tully's models, spin-boson models, linear vibronic coupling models, and atom-in-cavity models. All these models will be used either in chapter 3 for short-time accuracy analysis of phase space methods or in chapter 4 for numerical benchmarks of the GDTWA method.

2.4.1 Tully's models

Tully's models contain three different $1d$ scattering models. The masses of the particles for all three models are 2000 in atomic units. The first model is a single avoided crossing

model, where potential matrix (electronic Hamiltonian in the diabatic basis) is

$$\begin{aligned} V_{11}(x) &= \begin{cases} A(1 - e^{-Bx}), & x > 0 \\ -A(1 - e^{Bx}), & x < 0 \end{cases} \\ V_{22}(x) &= -V_{11}(x) \\ V_{12}(x) &= V_{21}(x) = Ce^{-Dx^2}, \end{aligned} \quad (2.159)$$

where $A = 0.01$, $B = 1.6$, $C = 0.005$, and $D = 1$. All the units in this subsection are in atomic units.

The second model is a dual avoided crossing model, with

$$\begin{aligned} V_{11}(x) &= 0 \\ V_{22}(x) &= E_0 - Ae^{-Bx^2} \\ V_{12}(x) &= H_{21}(x) = Ce^{-Dx^2}, \end{aligned} \quad (2.160)$$

where $A = 0.1$, $B = 0.28$, $C = 0.015$, $D = 0.06$, and $E_0 = 0.05$.

The third model is an extended coupling model, with

$$\begin{aligned} V_{11}(x) &= -V_{22}(x) = A, \\ V_{12}(x) &= \begin{cases} Be^{Cx}, & x > 0 \\ B(2 - e^{-Cx}), & x < 0 \end{cases} \\ V_{21}(x) &= V_{12}(x), \end{aligned} \quad (2.161)$$

where $A = 6 \times 10^{-4}$, $B = 0.10$, $C = 0.90$.

Tully's models I and II are the most commonly used scattering models for linearized phase space methods, while most linearized phase space methods fail in Tully's model III. We will present the theoretical analysis of the short-time accuracy of model I and II for linearized phase space methods in chapter 3. Also, the numerical benchmarks of GDTWA on these two models will be presented in chapter 4.

2.4.2 Spin-boson models

The spin-boson model describes a two-state (spin-1/2) subsystem coupled with a bosonic bath (an infinite set of harmonic oscillators). It has a wide application range including nuclear magnetic resonance (NMR) [171, 192, 193], superconducting quantum interference device (SQUID) rings [171, 192, 193], and a radiationless transition or electron transfer process in a liquid, a solid, a cluster, or a protein [64]. In the language of chemistry, the bosonic bath DOFs are also called as nuclear DOFs, and two spin polarized states of spin-1/2 subsystem are two diabatic states. The Hamiltonian of the spin-boson model is

$$\hat{H} = \frac{1}{2}\Delta\hat{\sigma}_x + \frac{1}{2}\epsilon\hat{\sigma}_z + \sum_j \left(\frac{\hat{p}_j^2}{2m_j} + \frac{1}{2}m_j\omega_j^2x_j^2 + C_j\hat{\sigma}_zx_j \right), \quad (2.162)$$

where $\hat{\sigma}_z$ and $\hat{\sigma}_x$ are Pauli spin matrices, m_j , ω_j , \hat{p}_j and x_j are the mass, frequency, momentum and position for j -th nuclear DOF. C_j are the coupling strengths between j -th nuclear DOF and electronic states. Δ is the tunneling strength between two diabatic states, and ϵ is the energy difference between two diabatic states. Notice that the bath only interacts with diabatic states of the subsystem, rather than assisting in tunneling between diabatic states. This is due to the physical separation of two diabatic states in most of the models. For explicit examples, see the next subsection. Indeed, there are some models that nuclear DOFs play an important role in tunneling between diabatic states. Those models will be discussed in Sec. 2.4.4.

The complete environment information [192] is encapsulated in the initial temperature of the bath, and the spectral function (also named spectral density)

$$J(\omega) = \frac{\pi}{2} \sum_j \frac{C_j^2}{m_j \omega_j} \delta(\omega - \omega_j). \quad (2.163)$$

In the continuum limit, one of the commonly used spectral function is the Ohmic bath with an exponential cut-off

$$J(\omega) = \frac{\xi\pi}{2} \omega e^{-\omega/\omega_c}, \quad (2.164)$$

where ω_c is the cut-off frequency, and ξ is the Kondo parameter. Another commonly used spectral function is Ohmic bath with a Lorentzian cut-off (also called Debye bath or Drude bath)

$$J(\omega) = 2\Lambda \frac{\omega\omega_c}{\omega^2 + \omega_c^2}, \quad (2.165)$$

where Λ is the reorganization energy of the bath, and ω_c is the cut-off frequency. Taking $\omega_c \sim \infty$, Eq. (2.164) reduces to $J(\omega) = \frac{\xi\pi}{2}\omega$ and Eq. (2.165) reduces to $J(\omega) = \frac{2\Lambda}{\omega_c}\omega$.

In practical simulations, spectral function Eq. (2.163) with discrete mode should be used since classical computers can only perform finite numbers of operations. Discrete frequencies and coupling strengths for Eq. (2.164) can be selected as [194, 195]

$$\begin{aligned} \omega_j &= -\omega_c \ln \frac{j}{N+1}, \\ C_j &= \sqrt{\frac{\xi\omega_c}{N+1}} \omega_j, \end{aligned} \quad (2.166)$$

and discrete frequencies and coupling strengths for Eq. (2.165) can be selected as

$$\begin{aligned} \omega_j &= \omega_c \tan\left(\frac{\pi}{2} \frac{j}{N+1}\right), \\ C_j &= \sqrt{\frac{2\Lambda}{N+1}} \omega_j, \end{aligned} \quad (2.167)$$

where N is the number of discrete modes.

2.4.3 Site-exciton Models

In this subsection, we briefly review the Yang, Ishizaki and Fleming's framework [17, 196] on site-to-site energy transfer dynamics in light-harvesting/photosynthetic pigment complexes. Suppose there are n pigments (sites), and each site has a ground state and an excited state $|e_a\rangle$. Different sites are physically separated, and each site interacts with its own bath DOFs x_j^a . The Frenkel exciton Hamiltonian for the one exciton subspace of this system reads as

$$\begin{aligned} \hat{H} = & \sum_{a=1}^n \epsilon_a |e_a\rangle \langle e_a| + \sum_{a>b}^n \sum_{b=1}^n J_{ab} |e_a\rangle \langle e_b| \\ & + \sum_{a=1}^n (\hat{h}_{\text{bath}}^{(a)}(\mathbf{x}^a - \mathbf{d}^a) |e_a\rangle \langle e_a| + \sum_{b \neq a} \hat{h}_{\text{bath}}^{(b)}(\mathbf{x}^b) |e_b\rangle \langle e_b|), \end{aligned} \quad (2.168)$$

$$\hat{h}_{\text{bath}}^{(a)}(\mathbf{x}^a - \mathbf{d}^a) = \sum_{j=1}^{N_a} \left(\frac{(\hat{p}_j^a)^2}{2m_j^a} + \frac{1}{2} m_j^a (\omega_j^a x_j^a - \omega_j^a d_j^a)^2 \right), \quad (2.169)$$

where ϵ_a is the excited energy of a -th site, J_{ab} is the Coulombic interaction between a -th and b -th bath, \mathbf{d}^a is the displacement of the equilibrium geometry of a -th site between the ground and excited electronic state, and N_a is the nuclear DOFs number of the bath of a -th site. The last two terms of Eq. (2.168) can be re-organized as

$$\begin{aligned} & \sum_{a=1}^n (\hat{h}_{\text{bath}}^{(a)}(\mathbf{x}^a - \mathbf{d}^a) |e_a\rangle \langle e_a| + \sum_{b \neq a} \hat{h}_{\text{bath}}^{(b)}(\mathbf{x}^b) |e_b\rangle \langle e_b|) \\ & = \sum_{a=1}^n \sum_{j=1}^{N_a} \left(\frac{(\hat{p}_j^a)^2}{2m_j^a} + \frac{1}{2} m_j^a (\omega_j^a x_j^a)^2 + \frac{1}{2} m_j^a (\omega_j^a d_j^a)^2 |e_a\rangle \langle e_a| - m_j^a (\omega_j^a)^2 d_j^a x_j^a |e_a\rangle \langle e_a| \right). \end{aligned} \quad (2.170)$$

Therefore, $-\sum_{j=1}^{N_a} m_j^a (\omega_j^a)^2 d_j^a x_j^a |e_a\rangle \langle e_a|$ is the interaction term between a -th site and its own bath, and $\sum_{j=1}^{N_a} \frac{1}{2} m_j^a (\omega_j^a d_j^a)^2$ is the reorganization energy of a -th bath.

Similar to spin-boson model, the complete bath information is encoded in the initial temperature and spectral function of each bath. The spectral function for each bath is

$$J^a(\omega) = \frac{\pi}{2} \sum_{j=1}^{N_a} m_j^a \omega_j^a (d_j^a)^2 \delta(\omega - \omega_j^a). \quad (2.171)$$

The spectral function in the continuum limit of each bath is usually chosen as the Debye bath Eq. (2.165). Performing the integration

$$\frac{1}{\pi} \int_0^\infty \frac{J^a(\omega)}{\omega} = \Lambda = \sum_{j=1}^{N_a} \frac{1}{2} m_j^a (\omega_j^a d_j^a)^2. \quad (2.172)$$

That is the reason why parameter Λ in Eq. (2.165) is called reorganization energy.

One of the most commonly used site-exciton models is the two-site exciton model with flexible parameters choice [197, 198]. Apparently, it is a spin-boson model in this scenario. Another commonly used set of models are Fenna–Mathews–Olson (FMO) complex models. The FMO complex, which has eight bacteriochlorophyll-*a* pigments and protein environments [199–201], is found in green sulfur bacteria. Although the seven-site-exciton FMO model is often used due to historical reasons [18, 202–205]. Other well-established light-harvesting/photosynthetic pigment complexes include light harvesting 2 complex of purple bacteria [199, 206–208], and phycobiliproteins of cryptophyte algae [199, 209–212].

In chapter 3, we will present the theoretical analysis for the short-time accuracy of linearized phase space methods on spin-boson models and site-exciton models.

2.4.4 Linear vibronic models

The word vibronic comes from vibrational and electronic, thus vibronic coupling is referred to as the coupling between electronic states and vibrational DOFs. A huge first derivative (gauge vector potential) leads to strong vibronic coupling when adiabatic states are degenerate or nearly degenerate. When excited states are degenerate in the Franck–Condon region, it has a tremendous impact on the observed spectra. One can select the equilibrium geometry of ground state as the reference geometry and expand the Hamiltonian near the reference geometry. The kinetic energy operator and ground state PES can be approximated as

$$\hat{T} = \frac{1}{2} \sum_j \omega_j \hat{p}_j^2, \quad \hat{V}_{\text{GS}} = \frac{1}{2} \sum_j \omega_j x_j^2, \quad (2.173)$$

where x_j is the dimensionless position for the normal vibrational mode j , and $\hat{p}_j = -i\partial_{x_j}$ and ω_j is the corresponding dimensionless momentum and frequency, respectively. Expanding excited diabatic states in the similar way, the Hamiltonian of linear vibronic coupling (LVC) model [2] is given by

$$\hat{H} = \frac{1}{2} \sum_j \omega_j p_j^2 + \sum_{a,b} |a\rangle W_{ab} \langle b|, \quad (2.174a)$$

$$W_{aa} = E_a + \frac{1}{2} \sum_j \omega_j x_j^2 + \sum_j \kappa_j^{(a)} x_j, \quad (2.174b)$$

$$W_{ab} = \sum_j \lambda_j^{(ab)} x_j, \quad a \neq b, \quad (2.174c)$$

where E_a are the vertical excitation energies, and $\kappa_j^{(a)}$ and $\lambda_j^{(ab)}$ are intrastate and interstate vibronic coupling constants, respectively. Relevant vibrational modes are determined by selection rules, and parameters can be obtained by either fitting experimental spectra data or fitting PESs of electronic structure results [128]. One can further reduce the vibrational modes by fitting the experimental spectra data [213–216] or fitting the short time dynamics

[217–219]. We will present the numerical benchmarks of the GDTWA on LVC models in the diabatic representation in chapter 4.

Next we will discuss ADT transformation for LVC Hamiltonian, and show that LVC Hamiltonian can give degenerate PESs and singular gauge vector potential. Furthermore, LVC Hamiltonian shows that real adiabatic states can be no longer single-valued when the adiabatic states are degenerate. The simplest LVC Hamiltonian with degenerate adiabatic states in the diabatic representation is

$$\hat{H} = -\frac{1}{2}\left(\frac{\partial^2}{\partial X^2} + \frac{\partial^2}{\partial Y^2}\right) + \hat{V}^d, \quad (2.175)$$

with the matrix elements of V^d being

$$\begin{aligned} V_{11}^d &= \frac{\omega_1^2}{2}\left(X + \frac{a}{2}\right)^2 + \frac{\omega_2^2}{2}Y^2 + \frac{\Delta}{2}, \\ V_{22}^d &= \frac{\omega_1^2}{2}\left(X - \frac{a}{2}\right)^2 + \frac{\omega_2^2}{2}Y^2 - \frac{\Delta}{2}, \\ V_{12}^d &= V_{21}^d = cY. \end{aligned} \quad (2.176)$$

The real eigenstates [220, 221] of the electronic Hamiltonian V^d in Eq. (2.175) are

$$\begin{aligned} |g\rangle_{\text{adi}} &= -\sin\frac{\theta}{2}|1\rangle_d + \cos\frac{\theta}{2}|2\rangle_d, \\ |e\rangle_{\text{adi}} &= \cos\frac{\theta}{2}|1\rangle_d + \sin\frac{\theta}{2}|2\rangle_d, \end{aligned} \quad (2.177)$$

where $|1\rangle_d$ and $|2\rangle_d$ represent the diabatic basis of V^d , and

$$\theta = \arctan \frac{2V_{12}^d}{V_{11}^d - V_{22}^d}. \quad (2.178)$$

The corresponding eigenenergies are

$$\begin{aligned} V_g &= \frac{V_{11}^d + V_{22}^d}{2} - \sqrt{(V_{12}^d)^2 + \frac{(V_{11}^d - V_{22}^d)^2}{4}}, \\ V_e &= \frac{V_{11}^d + V_{22}^d}{2} + \sqrt{(V_{12}^d)^2 + \frac{(V_{11}^d - V_{22}^d)^2}{4}}. \end{aligned} \quad (2.179)$$

Two adiabatic states are degenerate when $X = Y = 0$. This type of degenerate point is called conical intersection point [101]. It is clear that real basis is not single-valued due to the multi-values of θ . More explicitly, when the eigenstates circle around the conical intersection point, a non-trivial phase factor (-1) in the real adiabatic electronic state should be accumulated. This effect is known as the geometric phase of conical intersections. For this reason, a real adiabatic basis cannot account for the correct geometric phase, and the transformation between the diabatic representation and real adiabatic representation is ill-defined [220, 221]. The numerical results of the MCTDH and gGDTWA approach II for

on-the-fly simulations of LVC models in the adiabatic representation will be presented in chapter 4. Also, we will discuss the effects of the adiabatic basis selections for initial state preparations and EOMs.

A single-valued adiabatic basis should be a complex adiabatic basis which can account for the correct geometric phase. It can be obtained by multiplying a phase factor on the real adiabatic basis [2, 220, 221],

$$\begin{aligned} |g\rangle_g &= e^{i\theta/2} |g\rangle_{\text{adi}} \\ |e\rangle_g &= e^{i\theta/2} |e\rangle_{\text{adi}} . \end{aligned} \quad (2.180)$$

The complex adiabatic basis ensures single-valued initial adiabatic coefficients and a well-defined adiabatic-to-diabatic transformation. The gauge vector potentials for the complex adiabatic basis are given by $\hat{A}_X^g = -\frac{\partial_X \theta}{2}(\hat{I} + \hat{\sigma}_y)$ and $\hat{A}_Y^g = -\frac{\partial_Y \theta}{2}(\hat{I} + \hat{\sigma}_y)$. Similarly, the ‘‘gauge vector potentials’’ for the real adiabatic basis are $\hat{A}_X^a = -\frac{\partial_X \theta}{2}\hat{\sigma}_y$ and $\hat{A}_Y^a = -\frac{\partial_Y \theta}{2}\hat{\sigma}_y$. They are singular when $X \rightarrow 0, Y \rightarrow 0$.

LVC model also has important applications beyond chemistry. In fact, it is an excellent platform to implement artificial gauge theory (also called particles in gauge vector potentials) [222]. Mathematically speaking, we can construct a completely equivalent Hamiltonian by mapping $\hat{p}_x = X, \hat{p}_y = Y, x = i\partial_X$ and $y = i\partial_Y$ of Hamiltonian Eq. (2.175)

$$H = \frac{1}{2}\omega_1(\hat{p}_x - \hat{A}_x)^2 + \frac{1}{2}\omega_2(\hat{p}_y - \hat{A}_y)^2 + \hat{V} , \quad (2.181)$$

where

$$\hat{A}_x = -\frac{a\hat{\sigma}_z}{2} , \quad (2.182)$$

$$\hat{A}_y = -\frac{c\hat{\sigma}_x}{\omega_2^2} , \quad (2.183)$$

$$\hat{V} = \frac{\Delta}{2} + \frac{x^2 + y^2}{2} , \quad (2.184)$$

and unimportant constant terms have been neglected. Eq. (2.181) is the exact form of particles in the gauge potential Eq. (2.13). The gauge curvature of this mapping system is

$$\hat{F}_{xy} = -i[\hat{A}_x, \hat{A}_y] = \frac{ac}{\omega_2^2}\hat{\sigma}_y . \quad (2.185)$$

Nonzero gauge curvature suggests that the non-Abelian gauge potential of the mapping system is nontrivial. For the general LVC Hamiltonian Eq. (2.174), similar mappings can also be constructed, although the explicit form of gauge vector potential would be much more complicated. In chapter 4, we will present explicit expressions of a pyrazine-based three-mode-two-state LVC model as a particle in gauge vector potentials. Moreover, we will compare the numerical results of gGDTWA approach I and gGDTWA approach II for the pyrazine-based LVC model.

2.4.5 Atom-in-cavity models

Light–matter interaction can change the physical and chemical properties of the systems drastically when quantum effects of light play an important role. In this scenario, the electromagnetic (EM) field must be treated quantum mechanically. Consider a stationary atom in a $1d$ lossless cavity, the Hamiltonian [20–28] of the total system is

$$\hat{H} = \hat{H}_A + \hat{H}_{\text{ph}} + \hat{H}_{A-\text{ph}}, \quad (2.186)$$

where \hat{H}_{ph} is the Hamiltonian of the free EM field (photon)

$$\hat{H}_{\text{ph}} = \frac{1}{2} \sum_{j=1}^{N_{\text{p}}} (\hat{p}_j^2 + \omega_j^2 \hat{q}_j^2), \quad (2.187)$$

where N_{ph} is the mode number of photons. \hat{q}_j is proportional to the electric displacement operator, and \hat{p}_j is related to the magnetic field. In principle, there are two polarization DOFs of photons, however, we only consider one polarization here. The atomic Hamiltonian \hat{H}_A is

$$\hat{H}_A = \sum_{n=1}^{N_e} \epsilon_n |a\rangle \langle a|, \quad (2.188)$$

where N_e is the number of energy levels. The last term $\hat{H}_{A-\text{ph}}$ is the interaction term between the atom and photons. In Coulomb gauge, and the dipole approximation, $\hat{H}_{A-\text{ph}}$ reads as

$$\hat{H}_{A-\text{ph}} = \sum_{j=1}^{N_{\text{ph}}} (\omega_j \hat{q}_j (\hat{\mu} \lambda_j) + \frac{1}{2} (\hat{\mu} \lambda_j)^2), \quad (2.189)$$

where λ_j is a coupling strength which is a function of atom position R_s , and $\hat{\mu}$ is the dipole operator of the atom. For the higher dimensional cavity, the multiplication of coupling strength and dipole operator should be replaced by dot product. The last term of $\hat{H}_{A-\text{ph}}$ is a constant when there are only two states.

The frequency and coupling strength in atomic units are given by

$$\omega_j = \frac{j\pi}{\alpha L}, \quad j = 1, 2, \dots, N_{\text{ph}}, \quad (2.190)$$

$$\lambda_j = \sqrt{\frac{8\pi}{L}} \sin\left(\frac{j\pi}{L} R_s\right), \quad (2.191)$$

where α is the fine-structure constant, and L is the length of the cavity. When the atom is in the middle point of the cavity, $R_s = L/2$, all the even modes are decoupled with the atom.

The theoretical analysis for the short-time accuracy of linearized phase space methods on atom-in-cavity models will be discussed in chapter 3.

Part II

Linearized Phase Space Methods for Nonadiabatic Quantum Dynamics

One must introduce approximations to simulate quantum dynamics of large size systems because exponentially growing computational resources are required in numerically “exact” methods. In this part, we will discuss one of the successful approximation methods for nonadiabatic quantum dynamics, linearized phase space methods. To illustrate the idea of linearized phase space methods, we consider the dynamics of nuclei in one PES first. When the quantum effects are weak, nuclei dynamics can be approximated as classical dynamics, and the initial classical phase space distribution is obtained by Wigner transformation of initial density matrix. Such approximation is called linearized semiclassical (LSC) method (also known as truncated Wigner approximation, TWA), which also has been generalized to the multi-PES scenario. The classical dynamics makes the necessary computing resources scale only linearly with the system size, which makes simulations of large size systems possible. One major drawback of the LSC methods is that they cannot capture the nuclear quantum coherence correctly. Nevertheless, this limitation usually does not harm the achieved accuracy too much for the condensed phase systems [223].

When there are multiple PESs, employing the LSC method to such systems requires initial electron phase spaces, which is non-trivial. The original idea to overcome this difficulty is establishing a mapping from electronic DOF onto harmonic oscillators (Meyer–Miller–Stock–Thoss (MMST) mapping harmonic oscillators), and using the phase space of mapping harmonic oscillators. For this reason, LSC methods for nonadiabatic dynamics with multi-PESs is also called mapping approaches. Different mapping approaches are mainly characterized by their electron phase spaces choices, for instance, the phase space of Meyer–Miller–Stock–Thoss (MMST) mapping harmonic oscillators [54–57, 61–74], continuous [75–80] or discrete [47, 48, 95] spin phase space, phase space of angle-action variables [55, 57, 75], constrained phase space [58–60, 96, 224, 225], etc. Here, we will present detailed theoretical analysis for electron phase spaces of various mapping approaches. This part is organized as follows. In chapter 3, we will briefly review several successful mapping approaches, including fully and partially linearized methods as well as symmetrical quasi-classical (SQC) windowing [55, 57, 75, 197, 226, 227]. We also define the intra-electron correlation, and establish rigorous connections between it and the short-time accuracy for fully and partially linearized methods. We also use our theory to explain the accuracy orders in reported numerical benchmarks. In chapter 4, we will introduce generalized discrete truncated Wigner approximation (GDTWA) [47, 48, 52, 95, 228], which is a widely used linearized phase space method in quantum lattices, into chemical nonadiabatic systems. We give detailed theoretical analysis and numerical benchmarks on LVC models. We also develop two new GDTWA for the scenario of particles in gauge vector potentials, which has a close connection to linearized phase space methods in adiabatic representations.

Chapter 3

Linearized phase space methods - review, intra-electron correlation and short time accuracy analysis

This chapter is based on the work “Short-time Accuracy and Intra-electron Correlation for Nonadiabatic Quantum-Classical Mapping Approaches”, in preparation.

Nonadiabatic quantum-classical mapping approaches [43–80] have significantly gained in popularity in the past several decades because they have acceptable accuracy while remaining numerically tractable even for large system sizes. In the recent few years, several novel mapping approaches [55, 57, 59, 62, 63, 74, 77–79, 79, 80, 80, 95] have been developed that display higher accuracy than the traditional Ehrenfest method [2], linearized semiclassical initial value representation (LSC-IVR) [64], and Poisson bracket mapping equation (PBME) [65, 66, 229] approaches, but without seriously increasing the additional computation efforts. The reason is that these methods choose more suitable electronic phase spaces as compared to the traditional methods. While various benchmarks have already demonstrated the advantages and limitations of those methods, rigorous theoretical justifications of the connections between electron phase space properties and their short-time accuracy are still demanded.

In this chapter, the connection between electron phase space properties and short-time accuracy is established with the help of intra-electron correlation [48, 95, 230]. Intra-electron correlation is a measure of the statistical feature of the electronic phase space that has first been formally proposed in the context of the generalized discrete truncated Wigner approximation (GDTWA). In the original GDTWA paper [48], the correct intra-electron correlation sampling states that the statistical average of the quadratic electronic (spin) phase space variables should be identical to the quantum expectation values of the symmetrized product of the corresponding electronic operators, see also Eq. (4.8) in the next chapter. A similar

idea [230] was also developed by Golosov and Reichman for two-level spin-boson models. We remind the readers that intra-electron correlation is distinguished from the static and dynamical correlation in quantum electronic structure, or the correlation between nuclei and electron [95]. We generalize the concept of intra-electron correlation to both fully linearized mapping approaches and partially linearized mapping approaches. The fully and partially linearized methods considered in this chapter are Ehrenfest [2], LSC-IVR [64], PBME [65, 66, 229], four different traceless MMST (also called modified LSC, (mLSC)) [62, 63], spin linearized semiclassical method (Spin-LSC) with both full sampling and focus sampling [79, 80], partially linearized density matrix method [67, 68] (PLDM), and spin partially linearized density matrix method [77, 78] (Spin-PLDM) with both full sampling and focus sampling. For each approach, we give either a proof that it correctly samples the intra-electron correlation or provide an explicit violation example. We also prove that the correct intra-electron correlation can improve the short-time accuracy in various chemical motivated models. Specifically, we give the explanations of the following short-time accuracy orders, which are reported in references: 1. There are no short-time accuracy improvements of advanced mapping approaches in scattering models [223]; 2. mLSC/ $\phi^1\phi^1$ have higher accuracy than mLSC/ $\phi^1\phi^2$ and mLSC/ $\phi^2\phi^2$ for cavity-modified molecular dynamics of three-level systems [27]; 3. mLSC/ $\phi^1\phi^1$, PLDM, spin-PLDM are more accurate than mLSC/ $\phi^2\phi^2$, Ehrenfest, PBME, LSC-IVR and spin-LSC [62, 63, 77, 79, 80] on the FMO model. Our theoretical analysis provides a measure for the short-time accuracy of mapping approaches.

This chapter is organized as follows. In the first section, we briefly review the LSC method for nuclear dynamics in one PES. In the second section, we present several successful extension of the LSC method, including SQC windowing [55, 57, 75, 197, 226, 227], fully linearized methods, and partially linearized methods, to the nuclear dynamics in multi-PES. In the third section, we rewrite fully linearized methods and partially linearized methods as a unified formalism, and establish the rigorous connection between intra-electron correlations and short-time accuracy. Also, we use the analysis to explain the accuracy of previous numerical benchmarks including Tully models, spin-boson models, and cavity-modified molecular dynamics. In the fourth section, we give a detailed analysis of the intra-electron correlation for these methods. For the methods with correct and wrong intra-electron correlations, we give the proof and explicit violation examples, respectively. In the last section, we summarize our results.

3.1 Linearized Semiclassical Method for Nuclear Dynamics in one PES

Consider a Hamiltonian of nuclei in one spatial dimension moving on one PES,

$$\hat{H} = \frac{\hat{p}^2}{2m} + U(\hat{x}), \quad (3.1)$$

where m is the mass of the particle, and \hat{x} and \hat{p} are the nuclear position and momentum operators, respectively. Assuming the density matrix of the initial state is $\rho_{\text{nuc}}(0)$, the initial nuclei phase space distribution can be expressed as the Wigner function of the density matrix (up to a prefactor) [43, 46, 231],

$$\begin{aligned} W_{\text{nuc}}(x_0, p_0) &= \frac{1}{2\pi} (\rho_{\text{nuc}}(0))_W(x_0, p_0), \\ (\rho_{\text{nuc}}(0))_W(x_0, p_0) &:= \int d\eta \left\langle x - \frac{\eta}{2} \left| \rho_{\text{nuc}}(0) \right| x + \frac{\eta}{2} \right\rangle e^{i p \eta}, \end{aligned} \quad (3.2)$$

where we set $\hbar = 1$. The generalization to multidimensional systems is straightforward by replacing x, p, η by the corresponding vectors and the pre-factor $(2\pi)^{-1}$ by $(2\pi)^{-d}$, where d is the dimension of the system. The quantum expectation value of an arbitrary nuclei observable $\langle \hat{O}_{\text{nuc}} \rangle$ is identical to the statistical average of its Wigner function $O_{w,\text{nuc}}(x_0, p_0) := (\hat{O}_{\text{nuc}})_W(x_0, p_0)$ over the Wigner distribution,

$$\begin{aligned} \langle \hat{O}_{\text{nuc}} \rangle &= \text{Tr} \left\{ \rho(0) \hat{O}_{\text{nuc}} \right\}_{\text{q}} = \frac{1}{2\pi} \int dx_0 dp_0 (\rho_{\text{nuc}}(0))_W(x_0, p_0) (\hat{O}_{\text{nuc}})_W(x_0, p_0) \\ &= \int dx_0 dp_0 W_{\text{nuc}}(x_0, p_0) O_{w,\text{nuc}}(x_0, p_0), \end{aligned} \quad (3.3)$$

where $\text{Tr} \{ \}_{\text{q}}$ represents the trace over all quantum DOFs. Specifically, for any scalar function g , the Wigner transformation gives

$$\begin{aligned} g(x) &= (g(\hat{x}))_W(x, p), \\ g(p) &= (g(\hat{p}))_W(x, p), \\ p g(x) &= \left(\frac{\hat{p} g(\hat{x}) + g(\hat{x}) \hat{p}}{2} \right)_W(x, p), \\ p^2 g(x) &= \left(\frac{\hat{p}^2 g(\hat{x}) + g(\hat{x}) \hat{p}^2 + 2 \hat{p} g(\hat{x}) \hat{p}}{4} \right)_W(x, p). \end{aligned} \quad (3.4)$$

Wigner function of the density matrix and observables reduce to the classical phase space distribution and classical observables in the classical limit $\hbar \rightarrow 0$.

The time dependent observable can also be calculated by statistical average over phase space distribution rigorously,

$$\langle \hat{O}_{\text{nuc}}(t) \rangle = \text{Tr} \left\{ \rho(0) \hat{O}_{\text{nuc}}(t) \right\}_{\text{q}} = \frac{1}{2\pi} \int dx_0 dp_0 (\rho_{\text{nuc}}(0))_W(x_0, p_0) (\hat{O}_{\text{nuc}}(t))_W(x_0, p_0), \quad (3.5)$$

where $\hat{O}_{\text{nuc}}(t) = e^{i\hat{H}t}\hat{O}_{\text{nuc}}e^{-i\hat{H}t}$. However, the simulation of $(\hat{O}_{\text{nuc}}(t))_W(x_0, p_0)$ rigorously is not less difficult than solving the time dependent Schrödinger equation. One must introduce approximations for large size system simulations. A straightforward way is to approximate the equations of motions (EOMs) of phase space variables x and p as classical EOMs,

$$\dot{x}_t = \frac{p_t}{m}, \quad (3.6a)$$

$$\dot{p}_t = -\frac{\partial U(x_t)}{\partial x_t}. \quad (3.6b)$$

The time dependent observable evaluation can be expressed as

$$\langle \hat{O}_{\text{nuc}}(t) \rangle \approx \langle \hat{O}_{\text{nuc}}(t) \rangle_{\text{m}} = \frac{1}{2\pi} \int dx_0 dp_0 (\rho_{\text{nuc}}(0))_W(x_0, p_0) (\hat{O}_{\text{nuc}})_W(x_t, p_t), \quad (3.7)$$

where we denote the statistical average of approximate time dependent observables over Wigner phase distribution as $\langle \quad \rangle_{\text{m}}$. In practical simulations, we sample the initial phase space variables via the Wigner function Eq. (3.2), then evolve these variables as Eq. (3.6). The time dependent observables are evaluated as statistical average of phase space trajectories according to Eq. (3.7).

Above approximations are so called the linearized semiclassical (LSC) method (also known as truncated Wigner approximation (TWA)), which can be derived in various ways, for instance, truncating Moyal bracket, path integral, or Heisenberg EOMs. Here, we present the derivation of truncating Heisenberg EOMs,

$$\dot{\hat{x}}_t = \frac{\hat{p}_t}{m}, \quad (3.8a)$$

$$\dot{\hat{p}}_t = -\frac{\partial U(\hat{x}_t)}{\partial \hat{x}_t}. \quad (3.8b)$$

The only difference between Eq. (3.6) and Eq. (3.8) is whether the arguments are c -numbers or operators. In this sense, the LSC method takes the mean-field form of the Heisenberg EOMs in each single trajectory, which effectively truncates the order of the EOMs up to the classical level. We stress that LSC is still a method beyond the mean-field theory because the quantum fluctuations are partially accounted for in the initial statistical distributions of the phase space variables. LSC is exact for short time limit $\mathcal{O}(t^2)$ as well as harmonic oscillators, and asymptotically exact in the classical limit. In principle, LSC method is only qualitatively correct to the Ehrenfest time scale $\mathcal{O}(-\ln \hbar)$, however, numerical benchmarks suggest that it can still be correct for the long time limit for certain models [48, 50, 232, 233].

3.2 Linearized Semiclassical Method for Nuclear Dynamics in Multi-PES

In this section, we will discuss how to apply the LSC method to nuclear dynamics in multi-PES. We consider a non-adiabatic Hamiltonian in the diabatic representation of nuclei in one spatial dimension coupled to S electronic states,

$$\hat{H} = \frac{\hat{p}^2}{2m} + U(\hat{x}) + \hat{V}(\hat{x}), \quad (3.9)$$

$$\hat{V}(\hat{x}) = \sum_{kl} |k\rangle V_{kl}(\hat{x}) \langle l|, \quad (3.10)$$

where $\hat{V}(\hat{x})$ is a traceless potential. Different from the nuclei DOF, the electronic subsystem is discrete. A more severe problem is that the electronic DOF does not have an immediate expression in position and momentum operators. Various different mapping approaches are developed to resolve this problem. The basic idea of those methods are similar, i.e., to find the proper phase space to describe the electronic subsystem. Successful attempts include the $SU(S)$ Schwinger boson (MMST harmonic oscillator) phase space [54–57, 61–74], Stratonovich–Weyl (SW) spin phase space [77–80, 234], Wootters’ spin discrete phase space [48, 95, 235], action-angle phase space [55, 57], etc. In this chapter, we mainly focus on $SU(S)$ Schwinger boson (harmonic oscillator) phase space, Stratonovich–Weyl spin phase space, and action-angle phase space. The results based on Wootters’ spin discrete phase space will be presented in the next chapter.

We prepare the initial product states in the form $\rho(0) = \rho_{\text{nuc}}(0) \otimes \rho_{\text{el}}(0)$ and $\rho_{\text{el}}(0) = |r\rangle \langle r|$. These initial states can appear, e.g., in molecular systems with only one populated electronic state, such as the ground electronic state, or electronically excited systems prepared by a laser pulse shorter than the time-scale for nuclear displacements. For the explicit examples that demonstrate a wrong intra-electron correlation sampling, we set $r = 1$. We point out that the initial product state selection and pure diagonal electronic state selection are not restrictions for the mapping approaches. Any pure electronic states with off-diagonal terms can be converted to $|r\rangle \langle r|$ by unitary transformations while any non-product nuclei-electron initial state and initial mixed electronic states can be expressed as linear combinations of the selected state. We will briefly review fully linearized methods, partially linearized methods and SQC windowing in this section. All methods suppose that the quantum dynamics can be approximated as the classical dynamics in the classical phase space. For fully linearized methods and partially linearized methods, we will also discuss their short-time accuracy analysis in the next section. We denote the collection of electronic phase space variables by Γ . The equations of motions (EOMs) of nuclear classical phase

space variables for all methods considered in this chapter are

$$\begin{aligned}\dot{x}_t &= p_t/m, \\ \dot{p}_t &= -\partial_{x_t}U(x_t) + F(\Gamma_t, x_t),\end{aligned}\tag{3.11}$$

where $F(\Gamma_t, x_t)$, as a Γ_t, x_t -dependent function, is the electron back-action force to the nuclei. Specifically, for the methods considered in this chapter, $F(\Gamma_t, x_t)$ can be expressed as

$$F(\Gamma_t, x_t) = -\text{Tr}\left\{\frac{\partial\hat{V}(x_t)}{\partial x_t}\hat{F}(\Gamma_t)\right\},\tag{3.12}$$

where, depending on the situation, $\text{Tr}\{\}$ represents the trace over the electronic DOFs or the usual matrix trace. The explicit form of $\hat{F}(\Gamma_t)$, the EOMs of Γ_t , and the way to evaluate observables will be given in the following three subsections.

3.2.1 Fully linearized methods

For the fully linearized methods considered in this chapter, the electronic phase space variables are the positions and momenta of S fictitious particles [62–65, 79, 80], $\Gamma_t = (X_t, P_t) = (X_1(t), X_2(t), \dots, X_S(t), P_1(t), P_2(t), \dots, P_S(t))$. In these methods, the treatment of the electronic DOFs is similar in spirit to the TWA for pure nuclei DOFs [46]. The initial electronic phase space distribution, $W_{\text{el}}(\Gamma_0)$, is generated according to $\rho_{\text{el}}(0)$, then the phase space variables are sampled according to the initial phase space distribution and propagated. The expectation of any traceless electronic observable \hat{O} is evaluated as the statistical average of the corresponding phase space expression over the phase space trajectories $\langle\hat{O}(t)\rangle_{\text{m}}$. For convenience, we define the matrix $\hat{K}(X_t, P_t)$

$$K_{mn}(X_t, P_t) = \frac{(X_m(t) + iP_m(t))(X_n(t) - iP_n(t))}{2}.\tag{3.13}$$

Then, the explicit forms of $\hat{F}(\Gamma_t)$, and the EOMs of Γ_t and $\hat{K}(X_t, P_t)$ are

$$\hat{F}_f(\Gamma_t) = \hat{K}(X_t, P_t)\tag{3.14}$$

$$\dot{X}_m(t) = \sum_n V_{mn}(x_t)P_n(t)\tag{3.15}$$

$$\dot{P}_m(t) = -\sum_n V_{mn}(x_t)X_n(t)\tag{3.16}$$

$$\frac{d}{dt}\hat{K}(X_t, P_t) = i[\hat{K}(X_t, P_t), \hat{V}(x_t)].\tag{3.17}$$

The corresponding phase space expression of \hat{O} is given by the replacement

$$\hat{O} \rightarrow \text{Tr}\left\{\hat{O}\hat{K}(X, P)\right\},\tag{3.18}$$

and the time dependent expectation value $\langle \hat{O}(t) \rangle$ is approximated as

$$\langle \hat{O}(t) \rangle \approx \langle \hat{O}(t) \rangle_m = \int dx_0 dp_0 d\Gamma_0 W_{\text{nuc}}(x_0, p_0) W_{\text{el}}(\Gamma_0) \text{Tr} \left\{ \hat{O} \hat{K}(X_t, P_t) \right\}. \quad (3.19)$$

Different fully linearized methods choose different initial electronic phase space distributions $W_{\text{el}}(\Gamma_0)$. We also use the notation $f(\Gamma_0)$ to represent the electron phase space distribution $W_{\text{el}}(\Gamma_0)$ for the convenience of the discussion of intra-electron correlation, which will be presented in the next section. The explicit expression of $f(\Gamma_0)$ and phase space choices for each method will be discussed in the following.

Ehrenfest method

The Ehrenfest method [2] is the simplest MMST mapping approach, in which the initial electronic DOFs is always the single electronic state $|r\rangle$. In each single trajectory, the nuclei are classical particles, and move on the mean field of PESs, and the electronic state $|\Psi(t)\rangle_{\text{Eh}}$ evolves under the Hamiltonian $\hat{V}(x_t)$. Equivalently, one can use the transformation,

$$\begin{aligned} X_n(t) + iP_n(t) &= \sqrt{2} \langle n | \Psi(t) \rangle_{\text{Eh}}, \\ \sum_n X_n(t)^2 + P_n(t)^2 &= 2, \end{aligned} \quad (3.20)$$

to transfer the electronic states to mapping variables. It is straightforward to check that the mapping variables satisfy the EOMs Eq. (3.15) and (3.16), and the initial electron phase space can be expressed as [2]

$$f_{\text{Ehrenfest}}(\Gamma) = \frac{1}{\pi^S} \delta(X_r^2 + P_r^2 - 2) \prod_{n \neq r} \delta(X_n^2 + P_n^2). \quad (3.21)$$

In this sense, a set of mapping variables are equivalent to an electronic state in each single trajectory.

LSC-IVR and PBME

Other more sophisticated MMST approaches [62–65] map the electronic system onto S harmonic oscillators within the singly-excited harmonic oscillators (SEO) subspace ($SU(S)$ Schwinger bosons). The electronic state $|m\rangle$ maps onto $|M\rangle$ which represents the m -th oscillator being on the first excited state. The projector on the SEO subspace is defined as $\hat{\Pi} = \sum_M |M\rangle \langle M|$. The creation, annihilation, position, and momentum operators for the m -th oscillator are defined as \hat{a}_m^\dagger , \hat{a}_m , $\hat{X}_m = (\hat{a}_m^\dagger + \hat{a}_m)/\sqrt{2}$, and $\hat{P}_m = i(\hat{a}_m^\dagger - \hat{a}_m)/\sqrt{2}$, respectively.

The mapping of $|m\rangle \langle n|$ (as an operator; notice that it can also be a term in the density matrix) can take two forms: it can either be a pure creation-annihilation term [65] $\hat{a}_m^\dagger \hat{a}_n$ or

a creation-annihilation term projected onto the SEO subspace $|M\rangle\langle N|$ [64]. The relation between the two different mappings is

$$|M\rangle\langle N| = \hat{a}_m^\dagger \hat{a}_n \hat{\Pi}. \quad (3.22)$$

It is straightforward to verify the following Wigner transformations

$$(\hat{a}_m^\dagger \hat{a}_n)_W(X, P) = \frac{(X_m - iP_m)(X_n + iP_n) - \delta_{mn}}{2}, \quad (3.23a)$$

$$(|M\rangle\langle N|)_W(X, P) = \frac{(X_m - iP_m)(X_n + iP_n) - \delta_{mn}/2}{2}\phi, \quad (3.23b)$$

where

$$\phi = 2^{(S+2)} \exp\left\{-\sum_{m=1}^S (X_m^2 + P_m^2)\right\} \quad (3.24)$$

is a conserved quantity.

In fact, EOMs of fully linearized methods Eq. (3.11), (3.14), (3.15), (3.16) can be derived from the classical EOMs of mapping Hamiltonian obtained from Eq. (3.9),

$$\frac{\hat{p}^2}{2m} + U(\hat{x}) + \hat{V}(\hat{x}) \rightarrow \frac{p^2}{2m} + U(x) + \sum_{m,n} V_{mn}(x) (\hat{a}_m^\dagger \hat{a}_n)_W(X, P), \quad (3.25)$$

The zero-point energy term $-\frac{\delta_{mn}}{2}$ in the mapping Eq. (3.23a) does not appear explicitly in Eq. (3.25) since we split the nuclei-electrons coupling term to traceless part $\hat{V}(\hat{x})$ and state-independent part $U(\hat{x})$. In the other mapping approaches, the mapping relation Eq. (3.23a) can be modified as

$$(\hat{a}_m^\dagger \hat{a}_n)_W(X, P) = \frac{(X_m - iP_m)(X_n + iP_n) - \gamma\delta_{mn}}{2}, \quad (3.26)$$

where γ is the ZPE parameter. We will discuss more on it in the Spin-LSC method of this subsection, the last subsection of this section, as well as the next chapter.

Both PBME [65] and LSC-IVR [64] use $(|R\rangle\langle R|)_W$ as the initial electronic phase space. The major difference between the two methods is in the mapping procedure of observables. PBME maps the electronic observable onto pure creation-annihilation terms, which yields (for a traceless observable \hat{O})

$$f_{\text{PBME}}(\Gamma) = \frac{1}{2(2\pi)^S} (X_r^2 + P_r^2 - \frac{1}{2})\phi, \quad (3.27)$$

while LSC-IVR maps the observables onto a creation-annihilation term projected onto the SEO subspace, which yields an effective sampling (for a traceless observable \hat{O})

$$f_{\text{LSC-IVR}}(\Gamma) = \frac{1}{2(2\pi)^S} (X_r^2 + P_r^2 - \frac{1}{2})\phi^2. \quad (3.28)$$

One major problem of LSC-IVR and PBME is the zero-point energy (ZPE) leakage, which arises from the fact that the ZPE can flow between different electronic states, and causes the time dependent electron phase space to no longer be the SEO subspace.

Modified LSC

In recent years, mLSC methods [62, 63] have been developed to improve the accuracy of MMST mappings. The basic idea of mLSC methods is to separate the initial state into identity and traceless parts,

$$|r\rangle\langle r| = \frac{1}{S}(\hat{I} + \hat{Q}_r), \quad (3.29)$$

$$\hat{Q}_r = S|r\rangle\langle r| - \hat{I} = (S-1)|r\rangle\langle r| - \sum_{m \neq r}^S |m\rangle\langle m|, \quad (3.30)$$

and calculate their contribution to the expectation value separately,

$$\text{Tr}\left\{\rho_{\text{nuc}} \otimes \hat{I} e^{i\hat{H}t} \hat{O} e^{-i\hat{H}t}\right\}_{\text{q}} \approx \frac{1}{(2\pi)^S} \int dx_0 dp_0 d\Gamma_0 W_{\text{nuc}}(x_0, p_0) \phi^a \text{Tr}\left\{\hat{K}(X_t, P_t) \hat{O}\right\}, \quad (3.31)$$

$$\begin{aligned} \text{Tr}\left\{\rho_{\text{nuc}} \otimes \hat{Q}_r e^{i\hat{H}t} \hat{O} e^{-i\hat{H}t}\right\}_{\text{q}} &\approx \frac{1}{(2\pi)^S} \int dx_0 dp_0 d\Gamma_0 W_{\text{nuc}}(x_0, p_0) \phi^b \\ &\times \text{Tr}\left\{\hat{K}(X_0, P_0) \hat{Q}_r\right\} \text{Tr}\left\{\hat{K}(X_t, P_t) \hat{O}\right\}, \end{aligned} \quad (3.32)$$

where $a, b = 1, 2$. The different a, b combinations give different mLSC/ $\phi^a \phi^b$ methods [223]. In this sense, mLSC methods are also called traceless MMST methods. For completeness, we list the explicit form of $f(\Gamma)$ for mLSC/ $\phi^a \phi^b$,

$$f_{\text{mLSC}/\phi^a \phi^b}(\Gamma) = \frac{1}{S(2\pi)^S} \left\{ \phi^a + \frac{\phi^b}{2} [S(X_r^2 + P_r^2) - \sum_m^S (X_m^2 + P_m^2)] \right\}. \quad (3.33)$$

Spin-LSC

The spin-LSC based on SW representation uses the initial electronic phase space, which is a more “natural” phase space for electronic DOFs, instead of the phase space of the $SU(S)$ Schwinger bosons. For this reason, the ZPE-leakage problem is much more mitigated. There are three different common SW representations [79, 80], Glauber-P representation, Husimi-Q representation, and Wigner-W representation. Spin-LSC based on Wigner-W representation is the most robust and accurate one [79, 80]. Thus, we only consider Spin-LSC based on Wigner-W representation, and unless we specify otherwise mean the Wigner-W representation when we mention SW representation.

The SW representation in Cartesian variables for the spin system is

$$\text{Tr}\left\{\hat{B}\hat{C}\right\} = \int dX dP \rho_{\text{full}}(X, P) \text{Tr}\left\{\hat{W}_{\text{scs}}(X, P) \hat{B}\right\} \text{Tr}\left\{\hat{W}_{\text{scs}}(X, P) \hat{C}\right\}, \quad (3.34)$$

where \hat{B} and \hat{C} are arbitrary electronic operators, and $\text{Tr}\left\{\hat{W}_{\text{scs}}(X, P) \hat{B}\right\}$ and $\text{Tr}\left\{\hat{W}_{\text{scs}}(X, P) \hat{C}\right\}$ are their SW transformations. The definitions of the full sampling integration weight $\rho_{\text{full}}(X, P)$

and the SW transformation kernel $\hat{W}_{\text{scs}}(X, P)$ are

$$\begin{aligned}\rho_{\text{full}}(X, P) &= \frac{S!R}{\pi^S} \delta\left(\sum_{m=1}^S (X_m^2 + P_m^2) - R^2\right), \\ \hat{W}_{\text{scs}}(X, P) &:= \hat{K}(X, P) - \frac{\gamma}{2},\end{aligned}\quad (3.35)$$

where the sampling radius and ZPE parameter [79, 80] are

$$R^2 = 2\sqrt{S+1}, \quad (3.36)$$

$$\gamma = \frac{R^2 - 2}{S} = \frac{2\sqrt{S+1} - 2}{S}, \quad (3.37)$$

which are level-dependent. We use the subscript ‘‘scs’’ since $\hat{W}_{\text{scs}}(X, P)$ has a close connection to the spin coherent state [77, 78]. One can use the kernel and full sampling integration weight to express the ‘‘closure relation’’ and arbitrary electronic operator

$$\hat{I} = \int dX dP \rho_{\text{full}}(X, P) \hat{W}_{\text{scs}}(X, P), \quad (3.38)$$

$$\hat{B} = \int dX dP \rho_{\text{full}}(X, P) \hat{W}_{\text{scs}}(X, P) \text{Tr}\left\{\hat{W}_{\text{scs}}(X, P) \hat{B}\right\}. \quad (3.39)$$

The similarity between Eq. (3.34) and Eq. (3.3) suggests that $\text{Tr}\left\{\hat{W}_{\text{scs}}(X, P) |r\rangle \langle r|\right\}$ can be regarded as a phase space distribution of initial state $|r\rangle \langle r|$. For this reason, the full sampling Spin-LSC method approximates the initial phase space distribution as the product of the full sampling integration weight times the SW transformation of $|r\rangle \langle r|$, which yields

$$f_{\text{Spin-LSC,full}}(\Gamma) = \frac{1}{2}(X_r^2 + P_r^2 - \gamma)\rho_{\text{full}}(X, P). \quad (3.40)$$

One of the advantage of the spin-LSC is that the identity operator and traceless operators are treated uniformly. One can check that momentum EOM in Eq. (3.11) is equivalent with

$$\dot{p}_t = -\text{Tr}\left\{\frac{\partial(\hat{V}(x_t) + U(x_t))}{\partial x_t} \hat{W}_{\text{scs}}(X_t, P_t)\right\}, \quad (3.41)$$

however, one cannot absorb the $U(x_t)$ into the trace in PBME and LSC-IVR methods. The reduced and level-dependent ZPE parameter and uniform treatment of identity and traceless operators are the main features of the spin phase space, which are tremendously different from mapping harmonic oscillators.

There exists another initial sampling strategy that can also express the trace of two electronic operators, ‘‘closure relation’’ and arbitrary electronic operator, named focus sam-

pling [77–80],

$$\rho_{\text{foc}}^{(m)}(X, P) = \frac{1}{\pi S} \delta(X_m^2 + P_m^2 - \gamma - 2) \prod_{n \neq m} \delta(X_n^2 + P_n^2 - \gamma), \quad (3.42)$$

$$\text{Tr}\{\hat{B}\hat{C}\} = \sum_m \int dX dP \rho_{\text{foc}}^{(m)}(X, P) \text{Tr}\{\hat{W}_{\text{scs}}(X, P)\hat{B}\} \text{Tr}\{\hat{W}_{\text{scs}}(X, P)\hat{C}\}, \quad (3.43)$$

$$\hat{I} = \sum_m \int dX dP \rho_{\text{foc}}^{(m)}(X, P) \hat{W}_{\text{scs}}(X, P), \quad (3.44)$$

$$\hat{B} = \sum_m \int dX dP \rho_{\text{foc}}^{(m)}(X, P) \hat{W}_{\text{scs}}(X, P) \text{Tr}\{\hat{W}_{\text{scs}}(X, P)\hat{B}\}. \quad (3.45)$$

The focus sampling Spin-LSC also samples the initial electronic phase space variables on several circles of the same hypersphere surface as full sampling, rather than the entire hypersphere surface, which gives

$$f_{\text{Spin-LSC, foc}}(\Gamma) = \rho_{\text{foc}}^{(r)}(X, P). \quad (3.46)$$

3.2.2 Partially linearized methods

In the partially linearized methods, the initial electronic phase space sampling is achieved by inserting the ‘‘closure relation’’ of either coherent state [67, 69] (Eq. (3.52) for PLDM) or spin coherent state [77, 78] (Eq. (3.38,3.44) for Spin-PLDM) between $\rho_{\text{el}}(0)$ and forward/backward propagator $e^{-i\hat{H}t}/e^{i\hat{H}t}$. Therefore, two sets of electronic phase space variables $\hat{\Gamma} = (X, P, X', P')$ are required. We suppose that (X_t, P_t) is used to represent the forward propagator and (X'_t, P'_t) is used to represent the backward propagator. The forward and backward propagator in each single phase space trajectory are approximated as $\hat{W}(X_0, P_0, t)$ and $\hat{W}^\dagger(X'_0, P'_0, t)$, and they satisfy the following initial conditions and EOMs,

$$\begin{aligned} \hat{W}(X_0, P_0, 0) &= \hat{K}(X_0, P_0) - \frac{\gamma \hat{I}}{2}, \\ \frac{d}{dt} \hat{W}(X_0, P_0, t) &= -i\hat{V}(x_t) \hat{W}(X_0, P_0, t), \end{aligned} \quad (3.47)$$

and analogously for $\hat{W}^\dagger(X'_0, P'_0, t)$ by taking the hermitian conjugate and replacing X_0, P_0 by X'_0, P'_0 . Here, γ is the zero-point energy (ZPE) parameter and differs in PLDM and Spin-PLDM. Furthermore, each set of electronic phase space variables has the same form of EOMs as the fully linearized scenario, i.e., Eqs. (3.15) and (3.16).

The nuclear DOF moves along the mean force of forward and backward electronic phase space variables, which leads to

$$\hat{F}_{\text{p}}(\Gamma_t) = \frac{\hat{K}(X_t, P_t) + \hat{K}(X'_t, P'_t)}{2}. \quad (3.48)$$

The expectation value of a traceless operator \hat{O} reads as

$$\begin{aligned} \langle \hat{O}(t) \rangle_m &= \int dx_0 dp_0 d\Gamma_0 W_{\text{nuc}}(x_0, p_0) h(X_0, P_0) \\ &\times h(X'_0, P'_0) \text{Tr} \left\{ \hat{W}(X_0, P_0, t) \rho_{\text{el}}(0) \hat{W}^\dagger(X'_0, P'_0, t) \hat{O} \right\}, \end{aligned} \quad (3.49)$$

where $h(X_0, P_0)$ and $h(X'_0, P'_0)$ are method-dependent sampling weights that appear in the “closure relations.”, which will be presented lately in this subsection. Fully linearized approaches can be regarded as approximations of partially linearized approaches [77, 78, 236]. Usually, the partially linearized approaches provide more accurate results than the fully linearized approaches.

PLDM

PLDM and PBME treat the initial electron density matrix and observable in the same fashion, i.e., mapping the initial electron density matrix and observable onto the excited state of fictitious harmonic oscillators and the pure creation–annihilation operator, respectively. In PLDM [67, 69], the inserted identity is the “closure relation” of the coherent state of the harmonic oscillators. The “closure relation” and related properties of the coherent states are

$$\Phi(X, P) = \frac{\exp \left\{ - \sum_{m=1}^S \frac{1}{2} (X_m^2 + P_m^2) \right\}}{(2\pi)^S}, \quad (3.50)$$

$$\hat{W}_{\text{cs}}(X, P) = \hat{K}(X, P), \quad (3.51)$$

$$\hat{I} = \int dX dP \Phi(X, P) \hat{W}_{\text{cs}}(X, P), \quad (3.52)$$

$$\hat{O} = \int dX dP \Phi(X, P) \hat{W} \text{Tr} \left\{ \hat{W}_{\text{cs}}(X, P) \hat{O} \right\}, \quad (3.53)$$

which corresponds to the zero ZPE parameter of Eq. (3.47). Therefore, the initial sampling of PLDM is given by

$$h_{\text{PLDM}}(X_0, P_0) = \Phi(X, P). \quad (3.54)$$

Spin-PLDM

The relation between spin-PLDM and spin-LSC is similar to the relation between PLDM and PBME. Therefore, spin-PLDM [77, 78] inserts the “closure relation” based on the SW transformation kernel Eq. (3.38, 3.44), which yields

$$h_{\text{Spin-PLDM,full}}(X_0, P_0) = \rho_{\text{full}}(X_0, P_0) \quad (3.55)$$

$$h_{\text{Spin-PLDM,foc}}(X_0, P_0) = \sum_m \rho_{\text{foc}}^{(m)}(X, P). \quad (3.56)$$

The two versions of “closure relation” give the full sampling Spin-PLDM and focus sampling Spin-PLDM, respectively. The sampling radius and ZPE parameter are identical to Eq. (3.36, 3.37).

3.2.3 Symmetrical quasi-classical windowing

SQC windowing method uses the angle-action phase space [55, 57, 75, 197, 227], and the transformation between angle-action variables n_k, φ_k and position-momentum variables P_k, X_k is given by

$$n_k = \frac{X_k^2 + P_k^2 - \gamma}{2}, \quad (3.57)$$

$$\varphi_k = -\tan^{-1} \frac{P_k}{X_k}, \quad (3.58)$$

$$P_k = -\sqrt{2n_k + \gamma} \sin \varphi_k, \quad (3.59)$$

$$X_k = \sqrt{2n_k + \gamma} \cos \varphi_k, \quad (3.60)$$

where γ is the ZPE parameter, and the EOMs of position-momentum variables in SQC windowing are identical to them in fully linearized methods Eq. (3.16,3.15). We point out that the ZPE parameter of SQC windowing in this thesis is different from its definition in the references by an additional factor 1/2 for matching the ZPE parameter definitions of fully linearized and partially linearized methods. The initial action-angle phase space can be expressed as

$$W_{\text{aa}}^r(n, \varphi) = \delta(n_r - 1) \prod_{k \neq r} \delta(n_k), \quad (3.61)$$

In fact, Eq. (3.61) with $\gamma = 0$ is the phase space of the Ehrenfest method. For other fully linearized methods using angle-action phase space, γ is usually chosen as $0 < \gamma < 1$ to mitigate the ZPE-leakage problem [72, 73]. The ZPE parameter can even be chosen as negative values in constrained phase space methods [237].

Unlike fully linearized methods with action-angle phase space using delta functions, the idea of SQC windowing is replacing delta function in Eq. (3.61) by “pre-limit” delta functions, i.e., the quasi-classical “window” functions centered about the appropriate values of the action variables. The first proposed window function [55,57] is the histogram function, which is given by choosing “pre-limit” delta function $w(x)$,

$$\delta(x) \rightarrow \frac{1}{\gamma} w\left(\frac{\gamma}{2} - |x|\right), \quad (3.62)$$

where

$$w(x) = \begin{cases} 0, & x < 0, \\ 1, & x \geq 0, \end{cases} \quad (3.63)$$

and the ZPE-parameter in n_l of the arguments of w function is selected as 0 for all $l = 1, 2, \dots, S$. Hence, the ZPE-parameter only determines the width of the window, rather than the center. The SQC windowing phase space distribution of the histogram window can be expressed as

$$W_{\text{aa,his}}^r(n, \varphi) = \frac{1}{\gamma^S} w\left(\frac{\gamma}{2} - |n_r - 1|\right) \prod_{k \neq r} w\left(\frac{\gamma}{2} - |n_k|\right). \quad (3.64)$$

The raw transition probability from $|r\rangle$ to $|k\rangle$ in SQC windowing can be approximated as

$$\tilde{P}_{|r\rangle\rightarrow|k\rangle}(t) \approx \frac{1}{(2\pi)^S} \int dx_0 dp_0 dn_0 d\varphi_0 W_{\text{nuc}}(x_0, p_0) W_{\text{aa,his}}^r(n_0, \varphi_0) W_{\text{aa,his}}^k(n_t, \varphi_t), \quad (3.65)$$

and the transition probability is obtained by renormalizing them

$$P_{|r\rangle\rightarrow|k\rangle}(t) = \tilde{P}_{|r\rangle\rightarrow|k\rangle}(t) / \sum_l \tilde{P}_{|r\rangle\rightarrow|l\rangle}(t) \quad (3.66)$$

SQC windowing can also be used in off-diagonal elements calculations [226]. The Wigner transformation of $|k\rangle \langle l|$ in the action-angle way can be expressed as

$$W_{\text{aa}}^{kl}(n, \varphi) = e^{i(\varphi_k - \varphi_l)} \delta(n_k - \frac{1}{2}) \delta(n_l - \frac{1}{2}) \prod_{j \neq k, l} \delta(n_j), \quad (3.67)$$

and the histogram window function is given by

$$W_{\text{aa,his}}^{kl}(n, \varphi) = \frac{1}{\gamma^S} e^{i(\varphi_k - \varphi_l)} w(\frac{\gamma}{2} - |n_k - \frac{1}{2}|) w(\frac{\gamma}{2} - |n_l - \frac{1}{2}|) \prod_{j \neq k, l} w(\frac{\gamma}{2} - |n_j|). \quad (3.68)$$

The time dependent evaluation can be approximated as

$$\langle |k\rangle \langle l| (t) \rangle \approx \frac{1}{(2\pi)^S} \int dx_0 dp_0 dn_0 d\varphi_0 W_{\text{nuc}}(x_0, p_0) W_{\text{aa,his}}^r(n_0, \varphi_0) W_{\text{aa,his}}^{kl}(n_t, \varphi_t). \quad (3.69)$$

Eq. (3.64) and Eq. (3.65) suggest that the ZPE parameter does have an impact on the initial sampling and observable evaluations in SQC windowing, although it does not have an effect on the EOMs when we separate the Hamiltonian operator as state-dependent part and traceless part. We stress that the windowing function and ZPE parameter choices are empirical, and highly rely on the numerical benchmarks on typical models. One of the successful choice is the histogram window with $\gamma = \sqrt{3} - 1$ (also known as the standard histogram window) since it is nearly optimal in various models. For the weak coupling between nuclei and electrons scenario, the standard triangle window function [238] is more often used. The SQC windowing phase space distribution of the triangle window for diagonal and off-diagonal operators of a two-level system are given by

$$W_{\text{aa,tri}}^1(n, \varphi) = 2w(n_1 + \frac{\gamma}{2} - 1)w(n_2 + \frac{\gamma}{2})w(2 - \gamma - n_1 - n_2), \quad (3.70)$$

$$W_{\text{aa,tri}}^{12}(n, \varphi) = 2e^{i(\varphi_1 - \varphi_2)} w(n_1 + \frac{\gamma}{2} - \frac{1}{2})w(n_2 + \frac{\gamma}{2} - \frac{1}{2})w(2 - \gamma - n_1 - n_2), \quad (3.71)$$

where the ZPE parameter is chosen as $\gamma = \frac{1}{3}$, and $W_{\text{aa,tri}}^2(n, \varphi)$ as well as $W_{\text{aa,tri}}^{21}(n, \varphi)$ can be obtained by swapping n_1, φ_1 and n_2, φ_2 . The standard triangle window function has been generalized to higher-level systems, for the details, see Ref. [227].

So far we have reviewed fully and partially linearized methods as well as SQC windowing. In the next section, we will do the detailed short-time accuracy analysis for fully and partially linearized methods.

3.3 Intra-electron Correlation and Short-time Accuracy

As we have shown above, fully and partially linearized methods have similar EOMs of nuclear and mapping variables. In the following, we will further rewrite fully and partially linearized methods in a unified expression. With the help of such a re-formulation, we will establish a rigorous connection between short-time accuracy and intra-electron correlation.

3.3.1 Unified expression of linearized phase space methods

The expectation value $\langle \hat{O}(t) \rangle_m$ of the fully and partially linearized methods can be expressed through the following unified form

$$\begin{aligned} \langle \hat{O}(t) \rangle_m &= \int dx_0 dp_0 W_{\text{nuc}}(x_0, p_0) \langle\langle \text{Tr} \{ \hat{J}(\Gamma_0, t) \hat{O} \} \rangle\rangle \\ &:= \int dx_0 dp_0 d\Gamma_0 W_{\text{nuc}}(x_0, p_0) f(\Gamma_0) \text{Tr} \{ \hat{J}(\Gamma_0, t) \hat{O} \}, \end{aligned} \quad (3.72)$$

where $\hat{J}(\Gamma_0, t)$ and $f(\Gamma_0)$ are method-dependent and initial state-dependent quantities, and the double angle bracket means the integration over the weight factor $f(\Gamma_0)$. For the fully linearized approaches,

$$f(\Gamma_0) = W_{\text{el}}(X_0, P_0), \quad (3.73)$$

$$\hat{J}(\Gamma_0, 0) = \hat{K}(X_0, P_0), \quad (3.74)$$

while for the partially linearized approaches,

$$f(\Gamma_0) = h(X_0, P_0) h(X'_0, P'_0), \quad (3.75)$$

$$\hat{J}(\Gamma_0, 0) = \hat{W}(X_0, P_0, 0) \rho_{\text{el}}(0) \hat{W}^\dagger(X'_0, P'_0, 0). \quad (3.76)$$

The EOM of $\hat{J}(\Gamma_0, t)$ in Eq. (3.72) and \hat{F} in Eq. (3.12) are unified

$$\frac{d}{dt} \hat{J}(\Gamma_0, t) = i[\hat{J}(\Gamma_0, t), \hat{V}(x_t)], \quad (3.77)$$

$$\frac{d}{dt} \hat{F}(\Gamma_t) = i[\hat{F}(\Gamma_t), \hat{V}(x_t)]. \quad (3.78)$$

3.3.2 Definition of the intra-electron correlation

With the help of the unified form Eq. (3.72), it becomes apparent that the first as well as second time derivatives of $\langle \hat{O}(t) \rangle_m$ and $\langle \hat{O}(t) \rangle$ at $t = 0$ coincide. The difference between

the third time derivatives at $t = 0$ is (the individual expressions are reported in Appendix)

$$\begin{aligned} \frac{d^3}{dt^3} \langle \hat{O}(t) \rangle_m |_{t=0} - \frac{d^3}{dt^3} \langle \hat{O}(t) \rangle |_{t=0} &= -i \frac{1}{2m} \langle [\hat{O}, \frac{\partial \hat{V}(\hat{x}_0)}{\partial \hat{x}_0}] \frac{\partial \hat{V}(\hat{x}_0)}{\partial \hat{x}_0} + \frac{\partial \hat{V}(\hat{x}_0)}{\partial \hat{x}_0} [\hat{O}, \frac{\partial \hat{V}(\hat{x}_0)}{\partial \hat{x}_0}] \rangle \\ &+ i \int dx_0 dp_0 W_{\text{nuc}}(x_0, p_0) \langle \langle \text{Tr} \left\{ \hat{J}(\Gamma_0, 0) [\hat{O}, \frac{\partial \hat{V}(x_0)}{\partial x_0}] \right\} \text{Tr} \left\{ \frac{\partial \hat{V}(x_0)}{\partial x_0} \hat{F}(\Gamma_0) \right\} \frac{1}{m} \rangle \rangle. \end{aligned} \quad (3.79)$$

After integrating out the nuclear DOF, the vanishing of Eq. (3.79) requires

$$\text{Tr} \left\{ \rho_{\text{el}}(0) \frac{\hat{O}_1 \hat{O}_2 + \hat{O}_2 \hat{O}_1}{2} \right\} = \langle \langle \text{Tr} \left\{ \hat{J}(\Gamma_0, 0) \hat{O}_1 \right\} \text{Tr} \left\{ \hat{F}(\Gamma_0) \hat{O}_2 \right\} \rangle \rangle, \quad (3.80)$$

where \hat{O}_1 and \hat{O}_2 are two arbitrary traceless electron operators, or equivalently, they are arbitrary generalized Gell-Mann matrices [239]. Thus, Eq. (3.80) is the definition of the methods with correct intra-electron correlation sampling, which generically have a higher short-time accuracy than the methods with wrong intra-electron correlations. We stress that the $\mathcal{O}(t^3)/\mathcal{O}(t^2)$ accuracy for the methods with/without correct intra-electron correlations can be improved when the Hamiltonian \hat{H} and evaluation observable \hat{O} have specific forms. Detailed discussions can be found in the Sec. 3.3.4.

The intra-electron correlation can be written more explicitly, for the fully linearized methods,

$$\text{Tr} \left\{ \rho_{\text{el}}(0) \frac{\hat{O}_1 \hat{O}_2 + \hat{O}_2 \hat{O}_1}{2} \right\} = \langle \langle \text{Tr} \left\{ \hat{K}(X_0, P_0) \hat{O}_1 \right\} \text{Tr} \left\{ \hat{K}(X_0, P_0) \hat{O}_2 \right\} \rangle \rangle, \quad (3.81)$$

and for the partially linearized methods,

$$\begin{aligned} &\text{Tr} \left\{ \rho_{\text{el}}(0) \frac{\hat{O}_1 \hat{O}_2 + \hat{O}_2 \hat{O}_1}{2} \right\} \\ &= \langle \langle \text{Tr} \left\{ \hat{W}(X_0, P_0, 0) \rho_{\text{el}}(0) \hat{W}^\dagger(X'_0, P'_0, 0) \hat{O}_1 \right\} \text{Tr} \left\{ \frac{\hat{K}(X_0, P_0) + \hat{K}(X'_0, P'_0)}{2} \hat{O}_2 \right\} \rangle \rangle. \end{aligned} \quad (3.82)$$

The intra-electron correlation for the fully linearized methods considered in this chapter is identical to its original definition [48, 95]. However, modifications are required for the partially linearized methods. Interestingly, the definition of intra-electron correlation for the partially linearized methods looks asymmetric. In fact, such asymmetry represents the different roles of \hat{O}_1 and \hat{O}_2 in the partially linearized methods. The term $\text{Tr} \left\{ \frac{\hat{K}(X_0, P_0) + \hat{K}(X'_0, P'_0)}{2} \hat{O}_2 \right\}$ represents the back-action force and $\text{Tr} \left\{ \hat{W}(X_0, P_0, 0) \rho_{\text{el}}(0) \hat{W}^\dagger(X'_0, P'_0, 0) \hat{O}_1 \right\}$ represents the observable evaluations. As a comparison, the back-action force representations and the observable evaluations for the fully linearized methods considered in this chapter are symmetrical.

3.3.3 Classification of linearized phase space methods

Before moving to the detailed discussions on the short-time accuracy, we briefly give the classification of fully linearized and partially linearized methods. Those methods can be classified into three categories according to the intra-electron correlation, namely, wrong intra-electron correlation, correct intra-electron correlation only for 2-level systems, and correct intra-electron correlation. Three traditional methods, Ehrenfest, PBME, and LSC-IVR fall into the first category. mLSC/ $\phi^1\phi^2$, mLSC/ $\phi^2\phi^2$, full spin-LSC, and focus spin-LSC fall into the second category. mLSC/ $\phi^1\phi^1$, mLSC/ $\phi^2\phi^1$, full spin-PLDM, focus spin-PLMD, and PLDM fall into the third category. Readers who are interested in the proof of the respective classifications or explicit violation examples can check the next section.

3.3.4 Short-time analysis for general Hamiltonians

From this subsection to the end of this section, we further investigate the connection between intra-electron correlation and the short-time accuracy of population dynamics for a selection of chemical motivated models. In particular, this allows us to explain the order of short-time accuracy that has been observed in previous numerical benchmarks. The correct intra-electron correlations can improve the short-time accuracy of population dynamics from $\mathcal{O}(t^2)$ to $\mathcal{O}(t^3)$ for a general Hamiltonian with both real and imaginary off-diagonal matrix elements, from $\mathcal{O}(t^3)$ to $\mathcal{O}(t^4)$ for the atom-in-cavity models, and from $\mathcal{O}(t^5)$ to $\mathcal{O}(t^6)$ for spin-boson models. However, the correct intra-electron correlation cannot improve the short-time accuracy for scattering models, as methods with correct and wrong intra-electron correlations are both accurate up to $\mathcal{O}(t^3)$.

We choose \hat{O}_1 and \hat{O}_2 as two generalized Gell-Mann matrices. The generalized Gell-Mann matrices $\hat{\Lambda}_\mu$ can be divided into three classes [48, 95], the diagonal class $\hat{\Lambda}_D$, the real off-diagonal class $\hat{\Lambda}_R$, and the imaginary off-diagonal class $\hat{\Lambda}_I$

$$\hat{\Lambda}_\mu = \begin{cases} \frac{1}{\sqrt{2}}(|m\rangle\langle n| + |n\rangle\langle m|) \in \hat{\Lambda}_R & \text{for } 1 \leq \mu \leq S(S-1)/2, \quad 1 \leq n < m \leq S, \\ \frac{1}{\sqrt{2}i}(|n\rangle\langle m| - |m\rangle\langle n|) \in \hat{\Lambda}_I & \\ \text{for } S(S-1)/2 < \mu \leq S(S-1), \quad 1 \leq n < m \leq S, \\ \frac{1}{\sqrt{m(m+1)}} \sum_{n=1}^m (|n\rangle\langle n| - m|m+1\rangle\langle m+1|) \in \hat{\Lambda}_D & \\ \text{for } S(S-1) < \mu \leq S^2-1, \quad 1 \leq m < S. & \end{cases} \quad (3.83)$$

With the help of the classification of generalized Gell-Mann matrices, the commutation

relations have the following properties

$$\begin{aligned}
[\hat{\Lambda}_D, \hat{\Lambda}_R] &\Rightarrow \hat{\Lambda}_I \\
[\hat{\Lambda}_D, \hat{\Lambda}_I] &\Rightarrow \hat{\Lambda}_R \\
[\hat{\Lambda}_R, \hat{\Lambda}_R] &\Rightarrow \hat{\Lambda}_I \\
[\hat{\Lambda}_I, \hat{\Lambda}_I] &\Rightarrow \hat{\Lambda}_R \\
[\hat{\Lambda}_R, \hat{\Lambda}_I] &\Rightarrow \hat{\Lambda}_R + \hat{\Lambda}_D,
\end{aligned} \tag{3.84}$$

where $[\hat{\Lambda}_R, \hat{\Lambda}_I] \Rightarrow \hat{\Lambda}_R + \hat{\Lambda}_D$ means that the commutator between an operator spanned by $\hat{\Lambda}_R$ and an operator spanned by $\hat{\Lambda}_I$ is spanned by $\hat{\Lambda}_D$ and $\hat{\Lambda}_R$.

We always choose $\hat{O} \in \hat{\Lambda}_D$ because it is connected with the population dynamics. Because of symmetry, when \hat{O}_1 and \hat{O}_2 belong to different classes of generalized Gell-Mann matrices, Eq. (3.80) always holds (l.h.s. = r.h.s. = 0) for fully and partially linearized methods. Similarly, Eq. (3.80) also holds (l.h.s. = r.h.s. = 0) when $\hat{O}_1 \neq \hat{O}_2$, and \hat{O}_1, \hat{O}_2 belong to $\hat{\Lambda}_R$ or $\hat{\Lambda}_I$ simultaneously.

In the usual chemical motivated models, \hat{V} and thus $\frac{\partial \hat{V}(\hat{x}_0)}{\partial \hat{x}_0}$ are spanned by $\hat{\Lambda}_D$ and $\hat{\Lambda}_R$, and hence $[\hat{O}, \frac{\partial \hat{V}(\hat{x}_0)}{\partial \hat{x}_0}]$ is spanned by $\hat{\Lambda}_I$. Therefore, Eq. (3.79) equals to zero and all the considered methods are accurate up to $\mathcal{O}(t^3)$ in these scenarios. However, there do exist certain cases in which \hat{V} is spanned by all three types of generalized Gell-Mann matrices, for instance, systems with light induced conical intersections [240, 241] and systems with magnetic forces [242–244]. In these cases, the methods with correct intra-electron correlation have higher short-time accuracy than the wrong one.

3.3.5 Short-time analysis for scattering models

In this subsection, we consider the most common \hat{V} spanned by $\hat{\Lambda}_D$ and $\hat{\Lambda}_R$. In order to see the role of intra-electron correlation, the fourth order time derivative of $\langle \hat{O}(t) \rangle_m - \langle \hat{O}(t) \rangle$, and the time derivative of $F(\Gamma_t, x_t)$ are required,

$$\frac{d}{dt} F(\Gamma_t, x_t) = i \operatorname{Tr} \left\{ \hat{F}(\Gamma_t) \left[\frac{\partial \hat{V}(x_t)}{\partial x_t}, \hat{V}(x_t) \right] \right\} - \operatorname{Tr} \left\{ \frac{\partial^2 \hat{V}(x_t)}{\partial x_t^2} \frac{p_t}{m} \hat{F}(\Gamma_t) \right\}, \tag{3.85}$$

$$\begin{aligned}
& \frac{d^4}{dt^4} \langle \hat{O}(t) \rangle_m |_{t=0} - \frac{d^4}{dt^4} \langle \hat{O}(t) \rangle |_{t=0} = - \langle \frac{1}{4m^2} [[\hat{O}(0), \frac{\partial^2 \hat{V}(0)}{\partial \hat{x}_0^2}], \frac{\partial^2 \hat{V}(0)}{\partial \hat{x}_0^2}] \rangle \\
& - 2 \langle [[\hat{O}(0), \frac{\partial \hat{V}(0)}{\partial \hat{x}_0}], \hat{V}(0)] \frac{\partial \hat{V}(0)}{\partial \hat{x}_0} \rangle \frac{1}{2m} - \langle [[\hat{O}(0), \hat{V}(0)], \frac{\partial \hat{V}(0)}{\partial \hat{x}_0}] \frac{\partial \hat{V}(0)}{\partial \hat{x}_0} \rangle \frac{1}{2m} \\
& - 2 \langle \frac{\partial \hat{V}(0)}{\partial \hat{x}_0} [[\hat{O}(0), \frac{\partial \hat{V}(0)}{\partial \hat{x}_0}], \hat{V}(0)] \rangle \frac{1}{2m} - \langle \frac{\partial \hat{V}(0)}{\partial \hat{x}_0} [[\hat{O}(0), \hat{V}(0)], \frac{\partial \hat{V}(0)}{\partial \hat{x}_0}] \rangle \frac{1}{2m} \\
& - \langle \frac{1}{2m} [\hat{O}(0), \frac{\partial \hat{V}(0)}{\partial \hat{x}_0}] [\frac{\partial \hat{V}(0)}{\partial \hat{x}_0}, \hat{V}(0)] \rangle - \langle \frac{1}{2m} [\frac{\partial \hat{V}(0)}{\partial \hat{x}_0}, \hat{V}(0)] [\hat{O}(0), \frac{\partial \hat{V}(0)}{\partial \hat{x}_0}] \rangle \quad (3.86) \\
& + \frac{1}{m} \int dx_0 dp_0 W_{\text{nuc}}(x_0, p_0) \langle \langle \text{Tr} \left\{ \hat{J}(\Gamma_0, 0) \left\{ \text{Tr} \left\{ \hat{F}(\Gamma_0) \frac{\partial \hat{V}(x_0)}{\partial x_0} \right\} \right\} \right. \\
& \times \left. \left\{ 2 [[\hat{O}, \frac{\partial \hat{V}(x_0)}{\partial x_0}], \hat{V}(x_0)] + [[\hat{O}, \hat{V}(x_0)], \frac{\partial \hat{V}(x_0)}{\partial x_0}] \right\} \right. \\
& \left. \left. + [\hat{O}, \frac{\partial \hat{V}(x_0)}{\partial x_0}] \text{Tr} \left\{ \hat{F}(\Gamma_0) [\frac{\partial \hat{V}(x_0)}{\partial x_0}, \hat{V}(x_0)] \right\} \right\} \right\rangle,
\end{aligned}$$

where we already ignored the trivial canceling terms at $t = 0$, such as the expectation of single electronic operator and intra-electron correlation terms for \hat{O}_1, \hat{O}_2 spanned by different generalized Gell-Mann matrices classes. The explicit time derivative expressions of $\langle \hat{O}(t) \rangle$ and $\langle \hat{O}(t) \rangle_m$ are listed in the Appendix. The notation $\hat{V}(0) = \hat{V}(t = 0)$ is equivalent to $\hat{V}(\hat{x}_0)$. The additional term $-\frac{1}{4m^2} [[\hat{O}(0), \frac{\partial^2 \hat{V}(0)}{\partial \hat{x}_0^2}], \frac{\partial^2 \hat{V}(0)}{\partial \hat{x}_0^2}]$ in the first line of Eq. (3.86) tells us that the correct intra-electron correlation cannot improve the short-time accuracy. This phenomenon has already been observed in the short-time population dynamics of Tully's models in Ref. [223].

3.3.6 Short-time analysis for cavity-modified molecular dynamics

Unlike the scattering models, atom-in-cavity models [27] have vanishing $\frac{\partial^2 \hat{V}(\hat{x})}{\partial \hat{x}^2}$, which means the methods with correct intra-electron correlation are accurate up to at least $\mathcal{O}(t^4)$, while the methods with wrong intra-electron correlation are only accurate up to $\mathcal{O}(t^3)$. This corollary is confirmed in Ref. [27], in which Saller *et al.* reported that mLSC methods have tremendous improvement over Ehrenfest, PBME, and LSC-IVR. Specifically, mLSC/ $\phi^1 \phi^1$ (correct intra-electron correlation) outperforms mLSC/ $\phi^2 \phi^2$ and mLSC/ $\phi^1 \phi^2$ (wrong intra-electron correlation) in the three-level systems. We also expect that similar phenomena can be observed in the LVC models, which also have vanishing $\frac{\partial^2 \hat{V}(\hat{x})}{\partial \hat{x}^2}$.

3.3.7 Short-time analysis for spin-boson models

For simplicity, we consider one $1d$ boson bath in this subsection. The generalization to multi-dimensional multi-bosons bath is straightforward. For the spin-boson models [192, 193],

$U(\hat{x})$ is a quadratic polynomial of \hat{x} . $\hat{V}(\hat{x})$ depends on \hat{x} linearly, and $\frac{\partial \hat{V}}{\partial \hat{x}}$ is a diagonal position-independent operator. The above conditions give the following relations

$$\begin{aligned} [\hat{O}(t), \frac{\partial \hat{V}(t)}{\partial \hat{x}_t}] &= 0, \\ \frac{\partial^m \hat{V}(t)}{\partial \hat{x}_t^m} &= 0, \quad m > 1, \\ \frac{\partial^m U(t)}{\partial \hat{x}_t^m} &= 0, \quad m > 2. \end{aligned} \tag{3.87}$$

These specific properties make the higher order derivative of $\langle \hat{O}(t) \rangle$ and $\langle \hat{O}(t) \rangle_m$ simplified drastically. The fourth order and fifth order time derivatives of $\langle \hat{O}(t) \rangle$ and $\langle \hat{O}(t) \rangle_m$ at $t = 0$ coincide, and the difference of the sixth time derivative vanishes when the method can capture the correct intra-electron correlations. For the explicit time derivatives, see the Appendix. Therefore, the methods with correct intra-electron correlations are accurate up to at least $\mathcal{O}(t^6)$ for the population dynamics of the spin-boson models, while the methods with wrong intra-electron correlations are only accurate up to $\mathcal{O}(t^5)$. This conclusion is not limited to spin-boson models. The time scale analysis also works on the site-excitation models which have the property Eq. (3.87), for instance, FMO model [62, 63, 77, 79, 80, 245, 246] and Frenkel biexciton model [223, 245]. Our theoretical analyses in this subsection give an explanation to the previous numerical observations [62, 63, 77, 79, 80] that FMO models, i.e., Spin-PLDM, PLDM, and mLSC/ $\phi^1 \phi^1$ sampling, give better short-time results than Ehrenfest, PBME, LSC-IVR, Spin-LSC, and mLSC/ $\phi^2 \phi^2$.

3.4 Proof of classifications of linearized phase space methods

In this section, we report the proof of the classification of intra-electron correlations for fully and partially linearized methods presented in the previous section. The readers who are not interested in the proof can skip this section.

3.4.1 Ehrenfest method, PBME and LSC-IVR

Neither of Ehrenfest nor PBME or LSC-IVR is able to correctly sample the intra-electron correlation, even for a two-level system. As an explicit violation example, consider $\hat{O}_1 = \hat{O}_2 = |1\rangle \langle 2| + |2\rangle \langle 1|$. Then,

$$\left\langle \frac{\hat{O}_1 \hat{O}_2 + \hat{O}_2 \hat{O}_1}{2} \right\rangle = 1, \tag{3.88}$$

while

$$\begin{aligned}
\langle\langle \text{Tr}\{\hat{K}(X_0, P_0)\hat{O}_1\} \text{Tr}\{\hat{K}(X_0, P_0)\hat{O}_2\} \rangle\rangle_{\text{Ehrenfest}} &= 0, \\
\langle\langle \text{Tr}\{\hat{K}(X_0, P_0)\hat{O}_1\} \text{Tr}\{\hat{K}(X_0, P_0)\hat{O}_2\} \rangle\rangle_{\text{LSC-IVR}} &= \frac{1}{2}, \\
\langle\langle \text{Tr}\{\hat{K}(X_0, P_0)\hat{O}_1\} \text{Tr}\{\hat{K}(X_0, P_0)\hat{O}_2\} \rangle\rangle_{\text{PBME}} &= \frac{3}{2}.
\end{aligned} \tag{3.89}$$

3.4.2 mLSC

For mLSC methods, it is insightful to examine the intra-electron correlation for the identity operator and traceless operator separately. For the identity operator, both $a = 1, 2$ samplings hold the intra-electron correlation

$$\text{Tr}\{\hat{O}_1\hat{O}_2\} = \frac{1}{(2\pi)^S} \int d\Gamma_0 \phi^a \text{Tr}\{\hat{K}(X_0, P_0)\hat{O}_1\} \text{Tr}\{\hat{K}(X_0, P_0)\hat{O}_2\}. \tag{3.90}$$

In order to prove this relation, we need the following Wigner transformation

$$\begin{aligned}
\sum_{m,n} O_{1,mn}(\hat{a}_m^\dagger \hat{a}_n)_W(X_0, P_0) &= \text{Tr}\{\hat{O}_1 \hat{K}(X_0, P_0)\}, \\
\sum_{m,n} (\delta_{mM} \delta_{nN} O_{1,mn} |M\rangle \langle N|)_W(X_0, P_0) &= \text{Tr}\{\hat{O}_1 \hat{K}(X_0, P_0)\} \phi,
\end{aligned} \tag{3.91}$$

and the expectation identity relation between electronic system and the fictitious harmonic oscillator system

$$\begin{aligned}
\text{Tr}\{\hat{O}_1\hat{O}_2\} &= \frac{1}{(2\pi)^S} \int d\Gamma_0 \sum_{m,n} O_{1,mn}(\hat{a}_m^\dagger \hat{a}_n)_W(X_0, P_0) \sum_{k,l} (\delta_{kK} \delta_{lL} O_{2,kl} |K\rangle \langle L|)_W(X_0, P_0) \\
&= \frac{1}{(2\pi)^S} \int d\Gamma_0 \sum_{m,n} (\delta_{mM} \delta_{nN} O_{1,kl} |M\rangle \langle N|)_W(X_0, P_0) \sum_{k,l} (\delta_{kK} \delta_{lL} O_{2,kl} |K\rangle \langle L|)_W(X_0, P_0).
\end{aligned} \tag{3.92}$$

Combining Eqs. (3.3), (3.91), and (3.92), Eq. (3.90) can be obtained immediately.

For the traceless operator, only the approach with $b = 1$ can faithfully sample the intra-electron correlation for systems with arbitrary S ,

$$\begin{aligned}
\text{Tr}\left\{\hat{Q}_r \frac{\hat{O}_1\hat{O}_2 + \hat{O}_1\hat{O}_2}{2}\right\} &= \frac{1}{(2\pi)^S} \int d\Gamma_0 \phi^b \\
&\times \text{Tr}\{\hat{K}(X_0, P_0)\hat{Q}_r\} \text{Tr}\{\hat{K}(X_0, P_0)\hat{O}_1\} \text{Tr}\{\hat{K}(X_0, P_0)\hat{O}_2\}.
\end{aligned} \tag{3.93}$$

The proof of Eq. (3.93) is quite similar to the proof of the intra-electron correlation for the identity operator Eq. (3.90). The Wigner transformation and the expectation identity relation

between electronic system and the fictitious harmonic oscillator system we need additionally are

$$\begin{aligned} & \sum_{m,n,k,l} \left(\frac{O_{1,mn} O_{2,kl} (\hat{a}_m^\dagger \hat{a}_n \hat{a}_k^\dagger \hat{a}_l + \hat{a}_k^\dagger \hat{a}_l \hat{a}_m^\dagger \hat{a}_n)}{2} \right)_W(X_0, P_0) \\ &= \text{Tr} \left\{ \hat{O}_1 \hat{K}(X_0, P_0) \right\} \text{Tr} \left\{ \hat{O}_2 \hat{K}(X_0, P_0) \right\} - \frac{\text{Tr} \left\{ \hat{O}_1 \hat{O}_2 \right\}}{4}, \end{aligned} \quad (3.94)$$

$$\begin{aligned} & \text{Tr} \left\{ \hat{Q}_r \frac{\hat{O}_1 \hat{O}_2 + \hat{O}_1 \hat{O}_2}{2} \right\} = \frac{1}{(2\pi)^S} \int d\Gamma_0 \sum_{u,v} Q_{r,uv} (\delta_{uU} \delta_{vV} |U\rangle \langle V|)_W(X_0, P_0) \\ & \times \sum_{m,n,k,l} \left(\frac{O_{1,mn} O_{2,kl} (\hat{a}_m^\dagger \hat{a}_n \hat{a}_k^\dagger \hat{a}_l + \hat{a}_k^\dagger \hat{a}_l \hat{a}_m^\dagger \hat{a}_n)}{2} \right)_W(X_0, P_0). \end{aligned} \quad (3.95)$$

Combining Eqs. (3.3), (3.91), (3.94), and (3.95), Eq. (3.93) can also be obtained immediately.

We also give an explicit violation example to show how the approach with $b = 2$ fails to sample the intra-electron correlation for a traceless operator in a S -level system, where $S > 2$. Consider $\hat{O}_1 = \hat{O}_2 = |2\rangle \langle 3| + |3\rangle \langle 2|$. Then,

$$\text{Tr} \left\{ \hat{Q}_r \frac{\hat{O}_1 \hat{O}_2 + \hat{O}_2 \hat{O}_1}{2} \right\} = -2,$$

while

$$\frac{1}{(2\pi)^S} \int dX dP \frac{1}{2} [S(X_1^2 + P_1^2) - \sum_m^S (X_m^2 + P_m^2)] \phi^2 (X_2 X_3 + P_2 P_3)^2 = -1. \quad (3.96)$$

We stress that the $b = 2$ approach for traceless operator samples the intra-electron correlation perfectly for two-level system. For two level system, the traceless operators \hat{O}_1 and \hat{O}_2 can only take the form

$$\begin{aligned} \hat{O}_1 &= s_{1,x} \hat{\sigma}_x + s_{1,y} \hat{\sigma}_y + s_{1,z} \hat{\sigma}_z, \\ \hat{O}_2 &= s_{2,x} \hat{\sigma}_x + s_{2,y} \hat{\sigma}_y + s_{2,z} \hat{\sigma}_z \end{aligned} \quad (3.97)$$

where all the coefficients of Pauli matrices are complex numbers. Using the algebra of the Pauli matrices and performing the integral in Eq. (3.93), one can immediately obtain

$$\begin{aligned} & \text{Tr} \left\{ \hat{Q}_r \frac{\hat{O}_1 \hat{O}_2 + \hat{O}_2 \hat{O}_1}{2} \right\} \equiv 0, \\ & \frac{1}{(2\pi)^S} \int d\Gamma_0 \phi^2 \text{Tr} \left\{ \hat{K}(X_0, P_0) \hat{Q}_r \right\} \text{Tr} \left\{ \hat{K}(X_0, P_0) \hat{O}_1 \right\} \text{Tr} \left\{ \hat{K}(X_0, P_0) \hat{O}_2 \right\} \equiv 0, \end{aligned} \quad (3.98)$$

which means ϕ^2 approach for the traceless operator can sample the intra-electron correlation faithfully for 2-level systems.

3.4.3 Spin-LSC

In general, Spin-LSC cannot sample the intra-electron correlation correctly except for the two-level systems. Here, we list an explicit example with wrong intra-electron correlation for any $S > 2$ systems. Considering $\hat{O}_1 = \hat{O}_2 = |2\rangle\langle 3| + |3\rangle\langle 2|$, one has

$$\begin{aligned}
& \left\langle \frac{\hat{O}_1 \hat{O}_2 + \hat{O}_2 \hat{O}_1}{2} \right\rangle = 0, \\
& \left\langle \left\langle \text{Tr} \left\{ \hat{O}_1 \hat{K}(X_0, P_0) \right\} \text{Tr} \left\{ \hat{O}_2 \hat{K}(X_0, P_0) \right\} \right\rangle \right\rangle_{\text{Spin-LSC(full)}} \\
& = \frac{R^4}{4(S+1)} \left(\frac{R^2}{S+2} - \gamma \right) = \frac{2\sqrt{S+1}}{S+2} - \frac{2}{S} (\sqrt{S+1} - 1), \\
& \left\langle \left\langle \text{Tr} \left\{ \hat{O}_1 \hat{K}(X_0, P_0) \right\} \text{Tr} \left\{ \hat{O}_2 \hat{K}(X_0, P_0) \right\} \right\rangle \right\rangle_{\text{Spin-LSC(focus)}} \\
& = \frac{\gamma^2}{2} = 2 \frac{S+2 - 2\sqrt{S+1}}{S^2}. \tag{3.99}
\end{aligned}$$

The proof of correct intra-electron correlation for spin-LSC is similar to the proof for traceless ϕ^2 approach. It is straightforward to verify that

$$\begin{aligned}
& \text{Tr} \left\{ |r\rangle\langle r| \frac{\hat{O}_1 \hat{O}_2 + \hat{O}_2 \hat{O}_1}{2} \right\} \equiv s_{1,x} s_{2,x} + s_{1,y} s_{2,y} + s_{1,z} s_{2,z}, \\
& \int d\Gamma_0 \frac{1}{2} (X_r^2 + P_r^2 - \gamma) \rho_{\text{full}}(X, P) \text{Tr} \left\{ \hat{K}(X_0, P_0) \hat{O}_1 \right\} \text{Tr} \left\{ \hat{K}(X_0, P_0) \hat{O}_2 \right\} \\
& \equiv s_{1,x} s_{2,x} + s_{1,y} s_{2,y} + s_{1,z} s_{2,z}, \\
& \int d\Gamma_0 \rho_{\text{foc}}^{(r)}(X, P) \text{Tr} \left\{ \hat{K}(X_0, P_0) \hat{O}_1 \right\} \text{Tr} \left\{ \hat{K}(X_0, P_0) \hat{O}_2 \right\} \\
& \equiv s_{1,x} s_{2,x} + s_{1,y} s_{2,y} + s_{1,z} s_{2,z}, \tag{3.100}
\end{aligned}$$

where \hat{O}_1 and \hat{O}_2 are identical to Eq. (3.97). Therefore, both full sampling and focus sampling can successfully capture the intra-electron correlation for 2-level systems.

3.4.4 Spin-PLDM and PLDM

The proof of Spin-PLDM full sampling, Spin-PLDM focus sampling, and PLDM satisfying the intra-electron correlation is straightforward. Using the property of ‘‘closure relation’’ Eq. (3.38/3.44/3.52) and the operator expression via $\hat{W}_{\text{scs}}(X, P)/\hat{W}_{\text{cs}}(X, P)$ Eq. (3.39/3.45/3.53) in the right-hand side of Eq. (3.82), we can immediately obtain the left-hand side of Eq. (3.82).

3.5 Conclusions

In this chapter, we have generalized the concept of intra-electron correlation, which has first been introduced in the context of the GDTWA [48, 95], to various mapping approaches. We

have established rigorous connections between short-time accuracy and intra-electron correlation for various models. The correct intra-electron correlation can improve the short-time accuracy for Hamiltonians with both real and imaginary matrix elements, atom-in-cavity models, and spin-boson models, while it cannot for scattering models. We analytically prove that the Ehrenfest method, LSC-IVR, and PBME fail to correctly sample the intra-electron correlation even for two-level systems. Spin-PLDM, PLDM, traceless MMST with both ϕ and ϕ^2 sampling for initial identity operator, and traceless MMST with ϕ^2 sampling for initial traceless operators can sample the intra-electron correlation faithfully for arbitrary S -level systems. While traceless MMST with ϕ sampling for initial traceless operators and Spin-LSC successfully sample the intra-electron correlation for two-level systems, they cannot sample the intra-electron correlation for S -level systems with $S > 2$.

Our theoretical analyses give explanations for various previous numerical observations [27, 62, 63, 77, 79, 80, 223] and they may provide a guideline for the development of future mapping approaches with increased accuracy. They also suggest that the benchmark results in Ref. [223] on the two-level systems, which showed that $\text{mLSC}/\phi^1\phi^1$, $\text{mLSC}/\phi^1\phi^2$, and $\text{mLSC}/\phi^2\phi^2$ have similar accuracy, might be difficult to generalize to higher level systems. According to our analysis, $\text{mLSC}/\phi^1\phi^1$ and $\text{mLSC}/\phi^2\phi^1$ should be more accurate than $\text{mLSC}/\phi^1\phi^2$ and $\text{mLSC}/\phi^2\phi^2$ for higher-level systems in the short-time dynamics. Finally, we stress that the intra-electron correlation is only a measure for the accuracy of short-time dynamics, and methods that violate intra-electron correlations can outperform methods with correct intra-electron correlations in simulations of the long-time behavior. For instance, Spin-LSC, which incorrectly samples intra-electron correlations, has the best long-time accuracy among the methods considered in this chapter on FMO models [77, 78].

Chapter 4

Generalized discrete truncated Wigner approximation for nonadiabatic dynamics

This chapter is based on the work “Generalized Discrete Truncated Wigner Approximation for Nonadiabatic Quantum-Classical Dynamics”, *The Journal of Chemical Physics* 155 (2), 024111, and “Generalized Discrete Truncated Wigner Approximation for Nonadiabatic Dynamics of Particles in Synthetic Non-Abelian Gauge Fields”, submitted to PRA, in revision.

In the last chapter, we reviewed the framework of mapping approaches, and several successful methods to mitigate the ZPE-leakage problem, including splitting the initial state to traceless and identity parts, continuous spin phase space, and using the reduced ZPE parameter. In this chapter, we will introduce a linearized semiclassical method, the generalized discrete truncated Wigner approximation (GDTWA) [47, 48, 52, 95], which is well-established in the context of quantum spin lattice systems, into the arena of chemical nonadiabatic systems. GDTWA samples the initial electron DOFs in the Wootters’ discrete spin phase space with correct intra-electron correlations. Physically, the discreteness of Wootters’ phase space is motivated by the discreteness of possible measurement results for spin degrees of freedom. GDTWA can capture the revivals and entanglement dynamics in quantum spin lattice systems up to an astoundingly long time [47]. Motivated by trapped-ion experiments, it has also been shown that DTWA is applicable to spin-boson models under the rotating wave approximation [52]. We will present the detailed theoretical analysis and numerical benchmarks of GDTWA for typical relevant chemical systems, for instance, the nuclei in scattering potentials [247], and one spin coupled to few nuclei with non-trivial conical intersection [2].

Our theoretical analysis shows that such discrete initial sampling can account for an effective reduced ZPE without an explicit ZPE parameter, and for two effective electronic

states in each single simulation trajectory [95]. For this reason, GDTWA can be regarded as a fully-partially hybrid method. As numerical benchmarks on two Linear Vibronic Coupling models and Tully's models show, GDTWA has a satisfactory accuracy in a wide parameter regime, independently of whether the dynamics is dominated by relaxation or by coherent interactions. It achieves an accuracy at least as good as existing state-of-the-art mapping approaches, and outperforms them in some of the selected applications in this chapter. Our results suggest that the discrete phase space used in GDTWA is tailor-made to treat the discrete space of electronic states in molecules, and the method can be very adequate to treat challenging nonadiabatic dynamics problems in chemistry and related fields.

We also develop two new GDTWA for particles in the gauge vector potentials (gGDTWA approach I and approach II), which has a close relation to the non-adiabatic on-the-fly simulations in the adiabatic representations when the gauge curvature is zero, for details, see Sec. 2.1.2. We use the terminology diabatic Hamiltonian for systems with vanishing gauge curvature and zero gauge vector potentials because of this connection. When the gauge curvature is not zero, a large variety of intriguing phenomena, such as spin Hall effect, conical intersections, *Zitterbewegung*, and more, have close connections with non-Abelian gauge fields [222,248,249], which can be implemented in LVC models, for details, see Sec. 2.4.4. Other experimental platforms realizing particles in the gauge vector potentials include cold atoms, trapped ions, and so on. [102,222]. The dynamics of particles in the gauge vector potentials face the same problem as nonadiabatic quantum dynamics, i.e., the computational efforts grow exponentially with the system sizes. Therefore, linearized semiclassical methods are also useful tools for their large system sizes simulations. The theoretical analysis and numerical benchmarks show that the Approach I, based on canonical momentum, is similar to the ordinary GDTWA and more suitable for particles in synthetic non-Abelian gauge fields, while approach II, based on kinematic momentum, is more suitable for on-the-fly simulations.

This chapter is organized as follows. Sec. 4.1 and 4.2 present GDTWA and gGDTWA, respectively. Sec. 4.1 contains two subsections. In Sec. 4.1.1, we present the theoretical analysis of GDTWA, including the original formalism, an equivalent rewriting in the unified expression proposed in the last chapter, ZPE analysis, and comparison with other mapping approaches. In Sec. 4.1.2, we present numerical benchmark results on Tully's model I and II, as well as two LVC models. Sec. 4.2 also contains two subsections. In Sec. 4.2.1, we present the derivation of Approach I and Approach II as well as the theoretical analysis of favorable applications of two approaches. In Sec. 4.2.2, we present numerical benchmark results on a neutral ultracold atom in an optical lattice, LVC model as a synthetic gauge field theory, and on-the-fly simulations of LVC models. Sec. 4.3 contains our conclusions.

4.1 Generalized Discrete Truncated Wigner Approximation

In this section, we will present the theoretical analysis as well as numerical benchmarks of GDTWA.

4.1.1 Theory

In this subsection, We first give the original form of the GDTWA. We then derive an equivalent form in analogous form to traditional mapping methods, which is exactly identical to the unified expression established in the last chapter. This pedagogical rewriting allows us not only to implement the simulations with a lower computational cost, it also permits us to reveal special advantages of GDTWA, including the effective non-zero reduced ZPE and the mitigation of physical space leakage. We also present the comparisons with fully and partially linearized methods.

Basics of GDTWA

Identical to the last chapter, we also consider the non-adiabatic Hamiltonian Eq. (3.9) describing S electronic states, $|1\rangle, |2\rangle, \dots, |S\rangle$, coupled to a nuclear DOF (the generalization to several nuclear DOFs is straightforward). In this section, we focus on initial product states of the form $\rho(0) = \rho_{\text{nuc}}(0) \otimes \rho_{\text{el}}(0)$.

The density matrix of the electronic DOFs and the nuclei-electron interaction $\hat{V}(\hat{x})$ are matrices with $\mathcal{D} = S \times S$ elements. We can define \mathcal{D} Hermitian operators $\hat{\Lambda}_\mu$, using the Generalized Gell-Mann Matrices for $SU(S)$ Eq. (3.83) and the identity matrix $\hat{\Lambda}_{\mathcal{D}} = \frac{1}{\sqrt{S}}\hat{I}$ as a complete basis for the electron DOF. Such basis elements are orthonormal, $\text{tr} \hat{\Lambda}_\mu \hat{\Lambda}_\nu = \delta_{\mu\nu}$ with the commutation relation $[\hat{\Lambda}_\mu, \hat{\Lambda}_\nu] = i f_{\mu\nu\xi} \hat{\Lambda}_\xi$, where $f_{\mu\nu\xi}$ are the structure constants,

$$i f_{\mu\nu\xi} = \text{tr}(\hat{\Lambda}_\xi [\hat{\Lambda}_\mu, \hat{\Lambda}_\nu]), \quad (4.1)$$

and the Einstein notation has been used. We are going to use these basis elements to derive a semiclassical description.

Any operator \hat{O}_{el} acting on the electron DOF can be expanded as $\sum_\mu c_\mu \hat{\Lambda}_\mu$ with $c_\mu = \text{tr} \hat{O}_{\text{el}} \hat{\Lambda}_\mu$. Then, the Hamiltonian in Eq. (3.9) can be expressed as

$$\hat{H} = \frac{\hat{p}^2}{2m} \sqrt{S} \hat{\Lambda}_{\mathcal{D}} + V_\mu(\hat{x}) \hat{\Lambda}_\mu, \quad (4.2)$$

with $V_\mu(\hat{x}) = \text{tr} \hat{V}(\hat{x}) \hat{\Lambda}_\mu$ for $0 < \mu < \mathcal{D}$, and $V_{\mathcal{D}}(\hat{x}) = \sqrt{S} U(\hat{x})$. The Heisenberg EOMs of

the operators are

$$\begin{aligned}\dot{\hat{x}}_t &= \hat{p}_t/m, \\ \dot{\hat{p}}_t &= -\partial_{\hat{x}_t} V_\mu(\hat{x}_t) \hat{\Lambda}_\mu(t), \\ \dot{\hat{\Lambda}}_\mu(t) &= f_{\mu\nu\xi} V_\nu(\hat{x}_t) \hat{\Lambda}_\xi(t).\end{aligned}\quad (4.3)$$

As in the usual fully linearized methods, GDTWA approximates the observables as statistical averages over trajectories of the phase space variables whose equations of motion are classical and formally identical to the quantum Heisenberg EOMs. Define x_t , p_t , and $\lambda_\mu(t)$ as the time dependent classical phase variables for \hat{x} , \hat{p} , and $\hat{\Lambda}_\mu$, respectively. Then, their EOMs are

$$\begin{aligned}\dot{x}_t &= p_t/m, \\ \dot{p}_t &= -\partial_{x_t} V_\mu(x_t) \lambda_\mu(t), \\ \dot{\lambda}_\mu(t) &= f_{\mu\nu\xi} V_\nu(x_t) \lambda_\xi(t),\end{aligned}\quad (4.4)$$

with initial condition $x_{t=0} = x_0$ and $p_{t=0} = p_0$. Similar to other LSC methods [43–80], GDTWA is a method beyond the mean-field theory because the quantum fluctuations are partially accounted for in the initial statistical distributions of the phase space variables.

The sampling of GDTWA for the initial nuclear phase variables are identical to the ordinary LSC methods Eq. (3.2), and the novelty of GDTWA is to sample the initial λ_μ as a discrete distribution. The details are as follows. First, $\hat{\Lambda}_\mu$ can be decomposed as $\hat{\Lambda}_\mu = \sum_{a_\mu} a_\mu |a_\mu\rangle \langle a_\mu|$, where $|a_\mu\rangle$ are the eigenvectors of $\hat{\Lambda}_\mu$. Then, the initial distribution of $\lambda_\mu(0)$ is $\lambda_\mu(0) \in \{a_\mu\}$ with probabilities

$$p(\lambda_\mu(0) = a_\mu) = \text{tr}[\hat{\rho}_{el}(0) |a_\mu\rangle \langle a_\mu|]. \quad (4.5)$$

This distribution can represent arbitrary quantum expectation values exactly as a statistical average,

$$\langle \hat{O}_{el} \rangle = \sum_\mu c_\mu \langle \hat{\Lambda}_\mu \rangle = \sum_{\mu, a_\mu} c_\mu p(\lambda_\mu(0) = a_\mu) a_\mu. \quad (4.6)$$

Follow the spirit of fully linearized methods, the formula to evaluate arbitrary observables $\hat{O} = \hat{O}_{\text{nuc}} \otimes \hat{O}_{\text{el}}$ under the GDTWA framework can be expressed as,

$$\langle \hat{O}(t) \rangle \approx \sum_{\mu, a_\mu} \int dx_0 dp_0 W_{\text{nuc}}(x_0, p_0) O_{w, \text{nuc}}(x_t, p_t) c_\mu p(\lambda_\mu(0) = a_\mu) \lambda_\mu(t), \quad (4.7)$$

where $\hat{O}_{\text{nuc}} = (\hat{O}_{\text{nuc}})_W(x, p)$, is the Wigner transformation of the operator \hat{O}_{nuc} . The connection with Wootters' phase space will be discussed in the next subsection.

The above sampling for electronic DOFs can be applied to arbitrary electronic initial states with the accuracy $\mathcal{O}(t^2)$. However, as we discussed in the last chapter, an increased accuracy can be achieved for initial states for which the statistical sampling reproduces the

initial intra-correlation [48] of the electron states, i.e., for the observables

$$\begin{aligned} \langle \frac{\hat{\Lambda}_\mu \hat{\Lambda}_\nu + \hat{\Lambda}_\nu \hat{\Lambda}_\mu}{2} \rangle &= \sum_{a_\mu, a_\nu} p(\lambda_\mu(0) = a_\mu) p(\lambda_\nu(0) = a_\nu) a_\mu a_\nu \quad \text{for } \mu \neq \nu, \\ \langle \hat{\Lambda}_\mu^2 \rangle &= \sum_{a_\mu} p(\lambda_\mu(0) = a_\mu) a_\mu^2. \end{aligned} \quad (4.8)$$

Generally, it has been proven that the GDTWA sampling distribution can reproduce the intra-electron correlation for the diagonal states [48] $|m\rangle \langle m|$, $1 \leq m \leq S$. For convenience, we only consider the initial state $|1\rangle \langle 1|$ in this chapter. As we discussed in the last chapter, this initial state selection is not atypical, i.e., all the other initial pure states can be expressed by this state by either unitary transformations for pure states, or the summation over of pure states for mixed states. An explicit wrong intra-electron correlation sampling of GDTWA for non-diagonal initial state is the following. Consider the state $|\Psi\rangle = (|1\rangle + e^{i\chi} |2\rangle)/\sqrt{2}$ for a two-level system, where the discrete sampling gives the probability distribution

$$\begin{aligned} p(\lambda_1 = \pm \frac{1}{\sqrt{2}}) &= \frac{1 \pm \cos \chi}{2}, \\ p(\lambda_2 = \pm \frac{1}{\sqrt{2}}) &= \frac{1 \pm \sin \chi}{2}, \\ p(\lambda_3 = \pm \frac{1}{\sqrt{2}}) &= \frac{1}{2}. \end{aligned} \quad (4.9)$$

With an explicit calculation, we obtain $\frac{\hat{\Lambda}_1 \hat{\Lambda}_2 + \hat{\Lambda}_2 \hat{\Lambda}_1}{2} = 0$, while

$$\sum_{a_1, a_2} p(\lambda_1 = a_1) p(\lambda_2 = a_2) a_1 a_2 = \frac{\sin 2\chi}{4}, \quad (4.10)$$

which means the discrete sampling of this state is faithful for the intra-electron correlation only if $\chi = 0, \pi$, or $\pm\pi/2$.

Re-formulation of GDTWA in the language of mapping approaches & Comparison with partially linearized methods

In the following, we re-write the GDTWA in completely equivalent forms, which take the form of the unified expression Eq. (3.72). Such re-writing not only reduces the computational cost by reducing the classical DOFs used to describe the electronic subsystem [50] from $S^2 - 1$ to $4S$, but also reveals important concepts such as ZPE, thus enabling a direct comparison to the formalism of linearized semiclassical methods. We also compare GDTWA and partially linearized methods in this subsection, and the comparison with fully linearized methods will be presented in the next subsection.

At the core of GDTWA lies a sampling over trajectories. In the original formulation of GDTWA, this is achieved via sampling over the continuous initial phase space of the nuclear

degree of freedom as well as the discrete electronic initial phase space variables $\lambda_\mu^{(\alpha)}(0)$, where we used the index α to label the diverse electronic initial conditions in the discrete phase space. In the formulation we are developing here, the role of $\lambda_\mu^{(\alpha)}(0)$ is assumed by the so-called discrete quasi-phase point operators $\hat{J}_\alpha(0)$, which are used to describe the electronic DOFs using the transformation

$$\begin{aligned}\hat{J}_\alpha(t) &= \sum_\mu \lambda_\mu^{(\alpha)}(t) \hat{\Lambda}_\mu \\ \lambda_\mu^{(\alpha)}(t) &= \text{tr} \hat{J}_\alpha(t) \hat{\Lambda}_\mu.\end{aligned}\quad (4.11)$$

For convenience, we will use the notation \hat{J}_α to express $\hat{J}_\alpha(t)$ in this chapter when there is no ambiguity.

The sampling of the initial condition $\hat{J}_\alpha(0)$ is achieved via a sampling of the initial $\rho_{\text{el}}(0)$ as in Eq. (4.5), which using the transformation Eq. (4.11) translates into

$$\hat{J}_\alpha(0) = \begin{pmatrix} 1 & \frac{\delta_2 - i\sigma_2}{2} & \dots & \frac{\delta_S - i\sigma_S}{2} \\ \frac{\delta_2 + i\sigma_2}{2} & 0 & \dots & 0 \\ \vdots & \vdots & \ddots & \vdots \\ \frac{\delta_S + i\sigma_S}{2} & 0 & \dots & 0 \end{pmatrix}, \quad (4.12)$$

with $\delta_i, \sigma_i = \pm 1$ being independent and identically distributed discrete uniform variables on the integers ± 1 . The initial density matrix of the electron subsystem is expanded as $\rho_{\text{el}}(0) = |1\rangle\langle 1| = \sum_\alpha w_\alpha \hat{J}_\alpha(0)$, where $w_\alpha = 2^{-2(S-1)}$ for all α . The GDTWA sampling strategy for the electron subsystem is converted to generating the initial discrete phase points by sampling δ_i and σ_i accordingly. In fact, $\hat{J}_\alpha(0)$ is nothing but the quasi-phase point operator in the Wootters' discrete phase space representation [235, 250]. Here, we call $\hat{J}_\alpha(0)$ discrete quasi-phase point operator because it plays the same role as the discrete phase point operator in the Wootters' discrete phase space representation but without the orthogonality $\text{Tr} \{ \hat{J}_\alpha(0) \hat{J}_\beta(0) \} \propto \delta_{\alpha\beta}$. Physically, the discrete sampling of the electronic DOFs is motivated by the fact that a measurement of the observable $\hat{\Lambda}_\mu$ will yield only discrete results. This property is faithfully represented by the discrete phase space and is fundamentally different from the mapping approaches where electronic DOFs are described by the continuous phase variables of harmonic oscillators. It is also different from focused-sampling approaches, where sampling of a continuous phase space is restricted to some parameter regions for computational convenience [74]. Instead, GDTWA faithfully samples a discrete phase space that is physically motivated from the discreteness of possible eigenvalues of spin degrees of freedom.

The ansatz of GDTWA in this form is that the Wigner function is evolved along the classical stationary trajectories

$$W(x, p, J, t) \approx \sum_\alpha \int dx_0 dp_0 w_\alpha W_{\text{nuc}}(x_0, p_0) \delta(x - x_t) \delta(p - p_t) \otimes \hat{J}_\alpha(t), \quad (4.13)$$

where the EOMs of the variables are

$$\begin{aligned}\dot{x}_t &= p_t/m, \\ \dot{p}_t &= -\partial_{x_t} \text{Tr} \left\{ \hat{J}_\alpha(t) (\hat{V}(x_t) + U(x_t)) \right\}, \\ \dot{\hat{J}}_\alpha(t) &= i[\hat{J}_\alpha(t), \hat{V}(x_t)],\end{aligned}\tag{4.14}$$

with initial condition $x_{t=0} = x_0$ and $p_{t=0} = p_0$. Any observable $\hat{O} = \hat{O}_{\text{nuc}} \otimes \hat{O}_{\text{el}}$ can be evaluated as

$$\begin{aligned}\langle \hat{O}(t) \rangle &\approx \text{tr} \int dx dp W(x, p, J, t) O_{w, \text{nuc}}(x, p) \otimes \hat{O}_{\text{el}} \\ &= \sum_\alpha \int dx_0 dp_0 w_\alpha W_{\text{nuc}}(x_0, p_0) O_{w, \text{nuc}}(x_t, p_t) \text{Tr} \left\{ \hat{J}_\alpha(t) \hat{O}_{\text{el}} \right\},\end{aligned}\tag{4.15}$$

Again, we point out that the product structure in the ansatz only appears in each single trajectory. The summation over index α already accounts for nontrivial quantum fluctuations beyond Ehrenfest theory. In fact, Eq. (4.15) is a variant of the unified expression Eq. (3.72), where the label α and probability distribution w_α play the role of Γ and $f(\Gamma_0)$, respectively. Meanwhile, $\hat{J}_\alpha(t)$ in GDTWA plays the role of both the operator $\hat{F}(\Gamma_t)$ in the general force expression Eq. (3.12) and the operator $\hat{J}(\Gamma_0, t)$ in the unified expression Eq. (3.72). It is straightforward to check that the EOM of $\hat{J}_\alpha(t)$, Eq. (4.14), is identical to the general expressions of EOMs of $\hat{J}(\Gamma_0, t)$ and $\hat{F}(\Gamma_t)$, Eq. (3.77) and (3.78). Therefore, the intra-electron correlation of GDTWA, Eq. (3.79), should coincide with the general intra-electron correlation definition, Eq. (4.8). More explicitly, the following relationship should hold,

$$\begin{aligned}\sum_\alpha w_\alpha \text{Tr} \left\{ \hat{J}_\alpha \hat{\Lambda}_\mu \right\} \text{Tr} \left\{ \hat{J}_\alpha \hat{\Lambda}_\nu \right\} &= \sum_{a_\mu, a_\nu} p(\lambda_\mu(0) = a_\mu) p(\lambda_\nu(0) = a_\nu) a_\mu a_\nu \quad \text{for } \mu \neq \nu, \\ \sum_\alpha w_\alpha \text{Tr} \left\{ \hat{J}_\alpha \hat{\Lambda}_\mu \right\}^2 &= \sum_{a_\mu} p(\lambda_\mu(0) = a_\mu) a_\mu^2.\end{aligned}\tag{4.16}$$

The proof is the following. Using the transformation relation Eq. (4.11), R.H.S.s of above equations become $\sum_\alpha \lambda_\mu^{(\alpha)} \lambda_\nu^{(\alpha)}$ for $\mu \neq \nu$, and $\sum_\alpha (\lambda_\mu^{(\alpha)})^2$ for $\mu = \nu$, which are identical to the L.H.S.s.

To implement the simulation, we require the spectral decomposition for the quasi-phase point operator \hat{J}_α . It is easy to check that the spectral decomposition of Eq. (4.12) is $\hat{J}_\alpha(0) = \lambda_+ |\Psi_+^\alpha(0)\rangle \langle \Psi_+^\alpha(0)| + \lambda_- |\Psi_-^\alpha(0)\rangle \langle \Psi_-^\alpha(0)|$, where the eigenvalues are

$$\lambda_\pm = \frac{1 \pm \sqrt{2S - 1}}{2},\tag{4.17}$$

with the amplitudes of the associated eigenvectors

$$\begin{aligned}\langle 1|\Psi_{\pm}^{\alpha}(0)\rangle &= \sqrt{\frac{\lambda_{\pm}^2}{\lambda_{\pm}^2 + (S-1)/2}}, \\ \langle j|\Psi_{\pm}^{\alpha}(0)\rangle &= \sqrt{\frac{\lambda_{\pm}^2}{\lambda_{\pm}^2 + (S-1)/2}} \frac{\delta_j + i\sigma_j}{2\lambda_{\pm}} \quad \forall j > 1.\end{aligned}\quad (4.18)$$

The eigenvalues of the quasi-phase point operator can be interpreted as quasi-probabilities, since $\lambda_+ + \lambda_- = 1$, $\lambda_+ > 0$ and $\lambda_- < 0$. Such quasi-probabilities constitute the spectrum of \hat{J}_{α} , and are conserved during the propagation. We can propagate $|\Psi_{\pm}^{\alpha}(t)\rangle$ rather than $\hat{J}_{\alpha}(t)$ using the EOMs

$$i\frac{d}{dt}|\Psi_{\pm}^{\alpha}(t)\rangle = \hat{V}(x_t)|\Psi_{\pm}^{\alpha}(t)\rangle \quad (4.19)$$

and $\hat{J}_{\alpha}(t) = \lambda_+|\Psi_+^{\alpha}(t)\rangle\langle\Psi_+^{\alpha}(t)| + \lambda_-|\Psi_-^{\alpha}(t)\rangle\langle\Psi_-^{\alpha}(t)|$. One can also transform the such two electronic states to two sets of mapping variables via the transformation in the same spirit in the Ehrenfest method Eq. (3.20),

$$\begin{aligned}X_n^{\pm}(t) + iP_n^{\pm}(t) &= \sqrt{2\lambda_{\pm}}\langle n|\Psi_{\pm}^{\alpha}(t)\rangle, \\ \sum_n X_n^{\pm}(t)^2 + P_n^{\pm}(t)^2 &= 2\lambda_{\pm},\end{aligned}\quad (4.20)$$

where we neglect the label α in mapping variables. The mapping variables of GDTWA also satisfy the EOMs in the general expressions Eq. (3.15) and (3.16). With the help of Eq. (4.20), one can express $f(\Gamma_0)$, $\hat{F}(\Gamma_t)$, and $\hat{J}(\Gamma_0, t)$ with the mapping variables arguments as

$$\begin{aligned}f(\Gamma_0) &= 2^{-2(S-1)} \prod_{\tau=\pm} \delta(X_1^{\tau}(0) - \sqrt{2\lambda_{\tau}}\sqrt{\frac{\lambda_{\tau}^2}{\lambda_{\tau}^2 + (S-1)/2}})\delta(P_1^{\tau}(0)) \\ &\times \prod_{j>1} \sum_{\sigma_j, \delta_j} \delta(X_j^{\tau}(0) - \sqrt{\frac{\lambda_{\tau}^2}{\lambda_{\tau}^2 + (S-1)/2}} \frac{\delta_j}{\sqrt{2\lambda_{\tau}}})\delta(P_j^{\tau}(0) - \sqrt{\frac{\lambda_{\tau}^2}{\lambda_{\tau}^2 + (S-1)/2}} \frac{\sigma_j}{\sqrt{2\lambda_{\tau}}}),\end{aligned}\quad (4.21)$$

$$J_{mn}(\Gamma_0, t) = F_{mn}(\Gamma_t) = K_{mn}(X^+(t), P^+(t)) + K_{mn}(X^-(t), P^-(t)). \quad (4.22)$$

Clearly, the nuclei in both GDTWA and partially linearized methods move on a mean-field potential, which is the average potential of two effective electronic states, in each single trajectory. Nevertheless, GDTWA has a significantly different logic from traditional partially linearized methods, as we illustrate with the help of Eq. (4.21) and (4.22). In partially linearized methods, two electronic states (sets of mapping variables) are sampled via the inserting the ‘‘closure relation’’ between $\rho_{\text{el}}(0)$ and forward/backward propagator $e^{-i\hat{H}t}/e^{i\hat{H}t}$. Therefore, they must be sampled independently, and yield a non-Hermitian $\hat{J}(\Gamma_0, t)$. As a comparison, there is no forward and backward electronic trajectories concept in GDTWA.

The two electronic wavefunctions for GDTWA are the spectral decomposition of the quasi-phase point operator. The initial conditions for two electronic states in GDTWA in a single trajectory are necessarily correlated. More explicitly, the samplings of (X^+, P^+) and (X^-, P^-) depend on δ_j, σ_j simultaneously, which means they are dependent variables, and re-writing as the product structure such as Eq. (3.75) in the partially linearized methods is impossible for the GDTWA. The sampling philosophy of the GDTWA is more close to fully linearized methods, i.e., sample mapping variables as the electron phase space distribution. In this sense, the GDTWA is a fully-partially hybrid linearized method.

To summarize, the above completely equivalent reformulations reduce the number of electronic subsystem DOFs from $S^2 - 1$ to $4S$. Although, GDTWA use same numbers of mapping variables as partially linearized methods, their sampling logic are completely different. These re-writings also help us compare GDTWA with fully linearized methods, which will be discussed in the following.

ZPE treatment within the GDTWA approach & comparison with fully linearized methods

In this subsection, we will compare GDTWA with fully linearized methods. Except for different numbers of mapping variables (electronic states) in each single trajectory, GDTWA accounts for a non-zero effective reduced ZPE without introducing an explicit ZPE parameter because of the discrete sampling. GDTWA also treats identity operator and traceless operators in a unified way. These features show that the discrete spin phase space is a tailor-made phase space for molecular systems.

As we discussed in the last chapter, both full ZPE (approaches based on MMST mapping without empirical ZPE parameters) and zero ZPE (Ehrenfest method) are harmful for numerical accuracy [72, 73]. One possible solution is splitting the initial state to the identity operator and traceless operators, and sampling them separately, which is used in mLSC methods. However, such operations are unnecessary in GDTWA, which automatically treats the identity operator and traceless operators in the equal footing via Eq. (4.5). The other possible solution to this problem is to introduce an adjusted ZPE-parameter to make the classical dynamics and phase space of the mapping variables of the harmonic oscillators of the electronic DOFs mimic the spin as much as possible [72, 73, 79, 80], for instance, spin-LSC, fully linearized methods with action-angle variables, and SQC windowing. GDTWA solves this problem with a fundamentally different logic, i.e., GDTWA never introduces such a parameter but tames the ZPE only through a judiciously designed initial sampling procedure.

To illustrate how GDTWA accounts for an effective non-zero reduced ZPE, it is convenient to first review how fully linearized methods with action-angle variables [72, 73] and

spin-LSC [79, 80], account for the ZPE. We introduce the following transformation, which is similar to the transformations in the Ehrenfest method Eq. (3.20) and GDTWA Eq. (4.20),

$$\begin{aligned}\hat{L}_\alpha(t) &= \frac{R_\alpha^2}{2} |\Psi_\alpha(t)\rangle \langle \Psi_\alpha(t)| - \frac{\gamma}{2} \hat{I}, \\ X_n(t) + iP_n(t) &= R_\alpha \langle n | \Psi_\alpha(t) \rangle, \\ \sum_n X_n(t)^2 + P_n(t)^2 &= R_\alpha^2,\end{aligned}\tag{4.23}$$

where R_α is the square root of the radius of the mapping variables, and $|\Psi_\alpha(t)\rangle$ the normalized electronic wave function. With the help of this transformation, the EOMs of fully such fully linearized methods Eq. (3.11), (3.15) and (3.16) can also be written in the form of Eq. (4.14),

$$\begin{aligned}\dot{x}_t &= p_t/m, \\ \dot{p}_t &= -\partial_{x_t} \text{Tr} \left\{ L_\alpha(t) (\hat{V}(x_t) + U(x_t)) \right\}, \\ \dot{\hat{L}}_\alpha(t) &= i[\hat{L}_\alpha(t), \hat{V}(x_t)].\end{aligned}\tag{4.24}$$

R_α and γ are conserved during the evolution and the EOM of $|\Psi_\alpha(t)\rangle$ is

$$i \frac{d}{dt} |\Psi_\alpha(t)\rangle = \hat{V}(x_t) |\Psi_\alpha(t)\rangle.\tag{4.25}$$

For each single trajectory, $\hat{L}_\alpha(t)$ has one non-degenerate eigenvalue $R_\alpha^2/2 - \gamma/2$ and $S - 1$ degenerate eigenvalues $-\gamma/2$, as can be seen immediately from the definition of $\hat{L}_\alpha(t)$ in Eq. (4.23). In this sense, the ZPE parameter in the traditional fully linearized method is a negative diagonal energy correction term for the nuclei-electron interactions. The nuclei always see a modified average potential energy during the evolution in each single trajectory, whence mapping approaches with a non-zero ZPE parameter already account for some quantum effects in their EOMs.

Though Eq. (4.24) and Eq. (4.14) are formally identical, it is impossible to express \hat{L}_α in the form $\frac{R_\alpha^2}{2} |\Psi_\alpha(t)\rangle \langle \Psi_\alpha(t)| - \frac{\gamma}{2} \hat{I}$, and thus to construct the ZPE-parameter, except for the case of $S = 2$, in which case, $\gamma = \sqrt{3} - 1$. We can also understand the difference from the viewpoint of the numbers of mapping variables, i.e., fully linearized methods have one set of mapping variables, while GDTWA has two. We can nevertheless identify an effective ZPE-parameter governing the evolution of \hat{J}_α . Namely, the ZPE-parameter in the traditional fully linearized methods can also be constructed by the following strategy. Notice that $\text{tr}(\hat{L}_\alpha) = R_\alpha^2/2 - \frac{\gamma}{2}S$ and $\text{tr}(\hat{L}_\alpha^2) = R_\alpha^4/4 - \gamma R_\alpha^2/2 + \frac{\gamma^2}{4}S$ only depend on R_α and γ . Hence, the ZPE-parameter in the traditional fully linearized methods can be expressed as

$$\gamma = \frac{2\sqrt{S \text{tr}(\hat{L}_\alpha^2) - (\text{tr} \hat{L}_\alpha)^2}}{S\sqrt{S-1}} - \frac{2 \text{tr} \hat{L}_\alpha}{S}\tag{4.26}$$

By formally replacing \hat{L}_α with \hat{J}_α in Eq. (4.26), we obtain an effective ZPE-parameter for the GDTWA,

$$\gamma_{\text{eff}} = \frac{2\sqrt{S+1} - 2}{S}. \quad (4.27)$$

Interestingly, this reduced effective ZPE coincides with the ZPE in spin-LSC methods [77–80]. The reason of such identical ZPE is that both GDTWA and spin-LSC start from the phase space of the electronic DOFs, rather than the phase space of Schwinger bosons. The ZPE of spin-LSC and GDTWA can, however, be different when the Hamiltonian is block diagonal. Consider a simple $N \times N$ Hamiltonian with the elements $H_{kl} = 0$ for $M < k \leq N$, $1 \leq l \leq M$ and $1 \leq k \leq M$, $M < l \leq N$. The first M diabatic states are decoupled from the other $N - M$ states. Again, we only consider the initial state $|1\rangle \langle 1|$. As before, we denote the electron phase space variable of the $N \times N$ full electron system as $\hat{J}_\alpha(t)$ and $\hat{L}_\alpha(t)$ while the submatrix $\hat{J}_\alpha(t)[1, 2, \dots, M; 1, 2, \dots, M]$ is indicated as $\hat{J}_\alpha^M(t)$ (and analogously for \hat{L}_α).

Since the first M diabatic states are decoupled from the others, it is also possible to sample the $M \times M$ subsystem directly. We use $\tilde{\hat{J}}_\alpha^M(t)$ and $\tilde{\hat{L}}_\alpha^M(t)$ to represent the electron phase space variables obtained by sampling from the $M \times M$ subsystem. It is easy to check that the initial distributions of $\hat{J}_\alpha^M(0)$ and $\tilde{\hat{J}}_\alpha^M(0)$ are identical. Moreover, the classical trajectories satisfy $\hat{J}_\alpha^M(t) = \tilde{\hat{J}}_\alpha^M(t)$ if their initial conditions are the same. Thanks to the implicit ZPE parameter of GDTWA, all the physical quantities are invariant independent of whether we use the $N \times N$ full electron system or the $M \times M$ subsystem.

The above arguments become much more subtle for the spin-LSC methods with the dimension dependent ZPE parameter. The initial distribution of $\hat{L}_\alpha^M(0)$ and $\tilde{\hat{L}}_\alpha^M(0)$ become different, as do the classical trajectories, even when the same initial conditions are applied. This difference may affect the observables, though it is difficult to give a general statement under which circumstances this is the case.

Another advantage related to the spin phase space of GDTWA is that the method does not suffer from the severe physical space leakage problem of the electronic subsystem [72, 73], and thus eliminates the additional projection that is necessary in the LSC-IVR and PBME approaches [55, 57, 64, 70]. The EOMs and initial sampling constructions ensure that the $\hat{J}_\alpha(t)$ trajectories are almost trapped in this tailor-made electronic phase space, similarly to what is achieved for $\hat{L}_\alpha(t)$ in the recently spin-LSC methods [77–80], although they do not fully exclude an unphysical negative population in general.

To summarize, GDTWA treats the traceless and identity operators of electronic states in a unified way. It does not have a ZPE parameter because of the specific structure of \hat{J}_α . However, it can account for an effective reduced ZPE without an explicit ZPE parameter. The ZPE-leakage problem is mitigated by the initial discrete spin phase space choice.

4.1.2 Numerical Results

In this subsection, we benchmark the GDTWA presented in the previous section by numerical calculations for prototypical non-adiabatic dynamics problems in chemistry, including Tully’s models and LVC models. Since each GDTWA trajectory evolves the classical nuclei and two coupled electronic time-dependent states, its numerical complexity is close to the partially linearized approach and slightly larger than the fully linearized mapping approach. We may thus expect that GDTWA should be considered as an alternative approach to partially linearized methods, which is indeed confirmed by the numerics reported in this subsection.

Tully’s models

Already in the second chapter, we presented the standard scattering benchmarks for the semi-classical methods, Tully’s models [247]. It is well-known that all the popular mapping approaches [223] can capture the final populations of Tully’s single avoided crossing model 1 and Tully’s dual avoided crossing model 2 quantitatively in the high momentum region and qualitatively in the low momentum region, but fail for the Tully’s extended coupling model 3. GDTWA, as a linearized mapping approach, also fails when the quantum tunneling and interference are crucial. Therefore, we present the transmission probabilities of Tully’s single avoided crossing model 1, Eq. (2.159), and Tully’s dual avoided crossing model 2, Eq. (2.160). GDTWA results in this subsection are obtained by the statistical average of 10^4 trajectories. Both initial states for the two models are prepared as $\exp(iP_0x) \exp[-(x - x_0)^2/\sigma^2] |1\rangle$ with $x_0 = -20$ and $\sigma = 20/P_0$, where P_0 is the initial nuclear momentum.

Figure 4.1 represents the transmission probabilities to the upper surface T_{11} (dashed line) and the lower surface T_{12} (solid line) of Tully’s model 1, calculated by GDTWA (blue) and quantum results [247] (black), respectively. It becomes apparent that GDTWA is accurate in the high momentum region $P_0 > 10$ and has a fair performance in the low momentum region $P_0 < 10$, which coincides with the previous observations on the other mapping approaches [223].

Figure 4.2 displays the transmission probabilities to the lower surface T_{11} (dashed line) and the upper surface T_{12} (solid line) of Tully’s model 2, calculated by GDTWA (blue) and quantum results [247] (black), respectively. This model is more challenging than the Tully’s model 1 because of Stückelberg oscillations. GDTWA can describe such phenomenon quite well, at least qualitatively. There is only a slight mismatch in the low energy region $\log E = \log P_0^2/2m < -1$. Again, it is not a surprising result since all the popular mapping approaches can achieve such accuracy [223]. GDTWA has a fair accuracy for these two

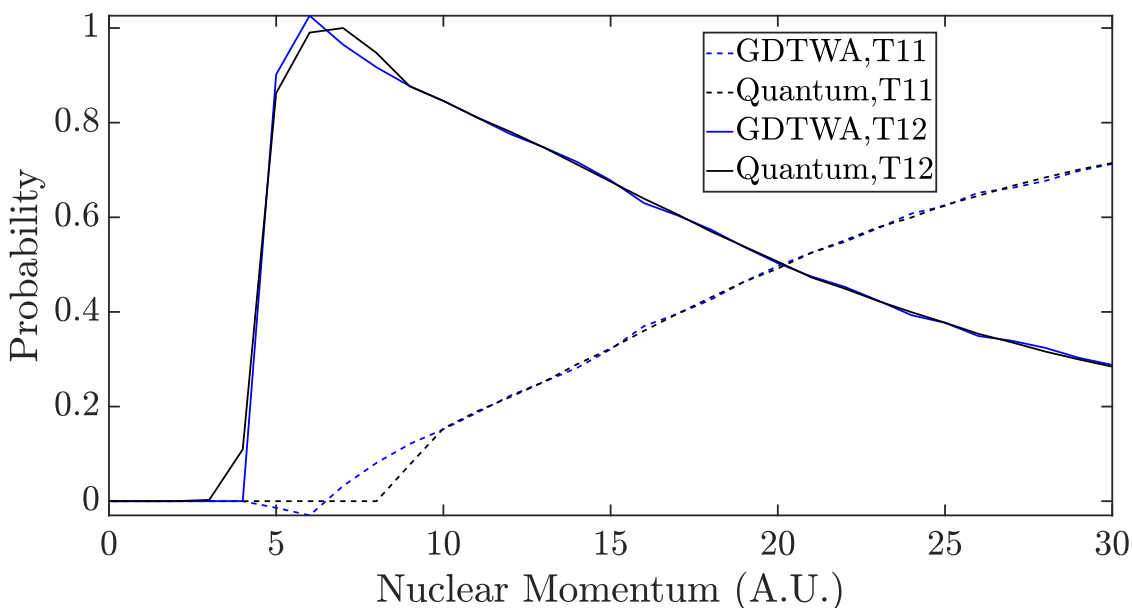


Figure 4.1. Transmission probabilities to the upper surface $T11$ (dashed line) and the lower surface $T12$ (solid line) for the Tully's single avoided crossing model 1. GDTWA (blue) fits the quantum results (black) nearly perfect in the high momentum region ($P_0 > 10$), and is qualitatively correct in the low momentum region.

scattering benchmarks. Finally, we point out that there are unphysical negative populations in the extremely low energy region, though the violations are very small.

Linear vibronic coupling models

In this subsection, we present the population dynamics of diabatic state, tuning coordinates, and second-order correlations of the tuning coordinates of two LVC models, where the Hamiltonian form of them Eq. (2.174) is already presented in the second chapter. The parameters are given in the Tables 4.1 and 4.2. Model I is a three-modes two-states model based on Pyrazine. It includes two tuning coordinates x_1 and x_{6a} , and one coupling coordinate x_{10a} , and the initial electron wave function is prepared in the second diabatic state $|2\rangle$ [2], which is the experimentally most relevant initial state (though the method can capture also other initial conditions, see discussion in Sec. 4.1.1). Model II is a five-modes three-states model based on Benzene radical cation. It includes three tuning coordinates x_2 , x_{16} , and x_{18} , and two coupling coordinates x_8 and x_{19} , and the electron wave function is initialized in the third diabatic state $|3\rangle$ [2].

We focus on the time dependence of observables for the initial product state of the vibrational ground state $\Psi = \prod_j \frac{1}{\pi^{1/4}} \exp\{-x_j^2/2\}$ and the excited electronic state, which is a typical setup of femtochemistry experiments. The selected mapping approaches to

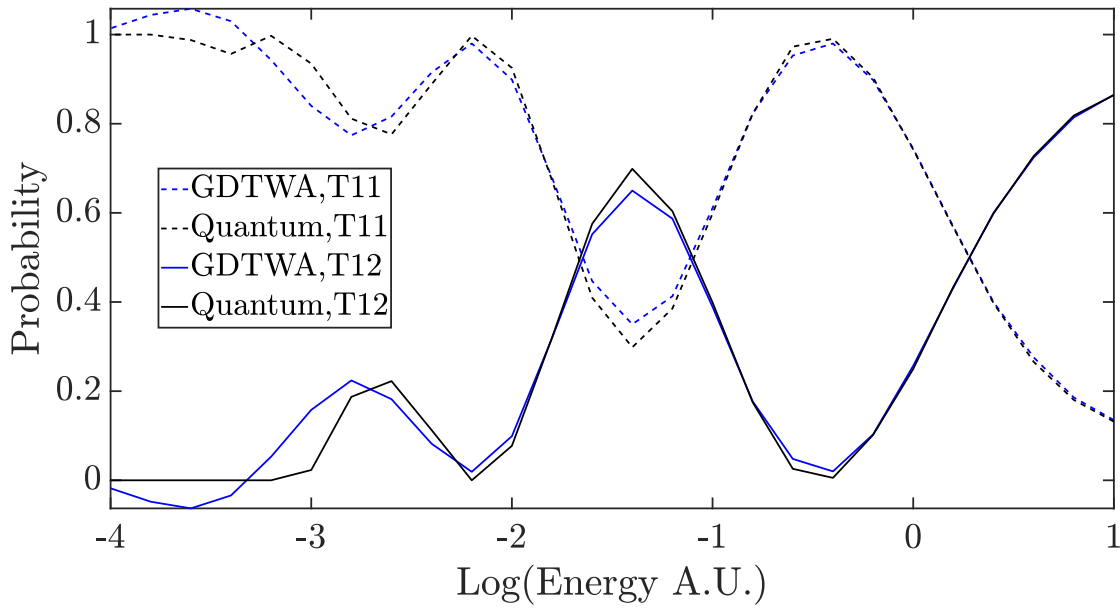


Figure 4.2. Transmission probabilities to the lower surface T_{11} (dashed line) and the upper surface T_{12} (solid line) for the Tully's dual avoided crossing model 1. GDTWA (blue) fits the quantum results (black) nearly perfect in the high energy region, and is qualitatively correct in the low energy region.

	E_k	ω_1	$\kappa_1^{(k)}$	ω_{6a}	$\kappa_{6a}^{(k)}$	ω_{10a}	λ
1⟩	3.94	0.126	0.037	0.074	-0.105	0.118	0.262
2⟩	4.84	0.126	-0.254	0.074	0.149	0.118	

Table 4.1. Parameters of Model I that is based on Pyrazine. All quantities are given in eV.

which we compare are PLDM [67], Spin-PLDM [77, 78], and the Ehrenfest [2] method. Specifically, we consider PLDM and Spin-PLDM without focused sampling since they are at least as accurate than the focused sampling variants [74, 77, 78] and thus provide better benchmarks for GDTWA. For all the methods we run 10^6 trajectories to ensure convergence, though GDTWA starts to converge already with 10^4 trajectories, a number comparable with the Ehrenfest method. We will show numerical benchmarks for two LVC models [2, 213, 214, 216], comparing the selected linearized semiclassical methods with numerically converged Multi-configuration time-dependent Hartree (MCTDH) calculations [33, 34, 251].

Due to symmetry, all the off-diagonal elements of the electron density matrix of the two models vanish. In Fig. 4.3, we show the population of the second diabatic state of

	E_k	ω_2	$\kappa_2^{(k)}$	ω_{16}	$\kappa_{16}^{(k)}$	ω_{18}	$\kappa_{18}^{(k)}$	ω_8	$\lambda_8^{(12)}$	ω_{19}	$\lambda_{19}^{(23)}$
1⟩	9.75	0.123	-0.042	0.198	-0.246	0.075	-0.125	0.088		0.12	
									0.164		
2⟩	11.84	0.123	-0.042	0.198	0.242	0.075	0.1	0.088		0.12	
											0.154
3⟩	12.44	0.123	-0.301	0.198	0	0.075	0	0.088		0.12	

Table 4.2. Parameters of Model II based on Benzene radical cation. All quantities are given in eV.

Model I. The GDTWA result compares fairly well to the exact quantum dynamics. It seems to underestimate the amplitude of oscillations around the mean, and reaches a long-time average that lies slightly below the exact value. The functional form seems to be better reproduced than with the Ehrenfest method, and the curve lies closer to the exact result than the curve computed using the Spin-PLDM method. Finally, the PLDM methods produces the best estimate of the long-time average, but considerably overestimates the damping of the oscillations. GDTWA fits the quantum result rather well at short times and has a fair performance at longer times, though it does not outperform the other approaches in this regime.

Figure 4.4 shows the dynamics of the two tuning coordinates, $\langle x_1 \rangle$ and $\langle x_{6a} \rangle$. Though GDTWA does not entirely capture the correct amplitude, it does match very well the frequency of the occurring oscillation. This behavior is similar to the Spin-PLDM method, while PLDM significantly underestimates the oscillation amplitude and the Ehrenfest method loses half a period within about five to ten oscillations. We have also computed the propagation of $\langle x_1^2 \rangle$, $\langle x_{6a}^2 \rangle$, and $\langle x_{10a}^2 \rangle$, see Fig. 4.5. In general, we should not expect the linearized semi-classical methods to work reliably for such higher-order correlations. As the numerical results suggest, Spin-PLDM and GDTWA nevertheless still give qualitatively satisfactory results, while PLDM and the Ehrenfest method rather quickly accumulate uncontrolled errors.

The relaxation dynamics of the more complex Model II is considerably more challenging for the linearized semi-classical methods because several states are involved simultaneously in the relaxation dynamics. GDTWA is the only one among the selected semi-classical methods to qualitatively correctly capture the relaxation dynamics, as seen in the diabatic populations in Figure 4.6. In Figures 4.7, we show the populations of the tuning coordinates. The results of diagonal second-order correlations of the tuning coordinates and the coupling coordinates are listed in Figs. (4.8) and (4.9). For nuclear observables including first and second order correlations, PLDM and the Ehrenfest method with zero ZPE display

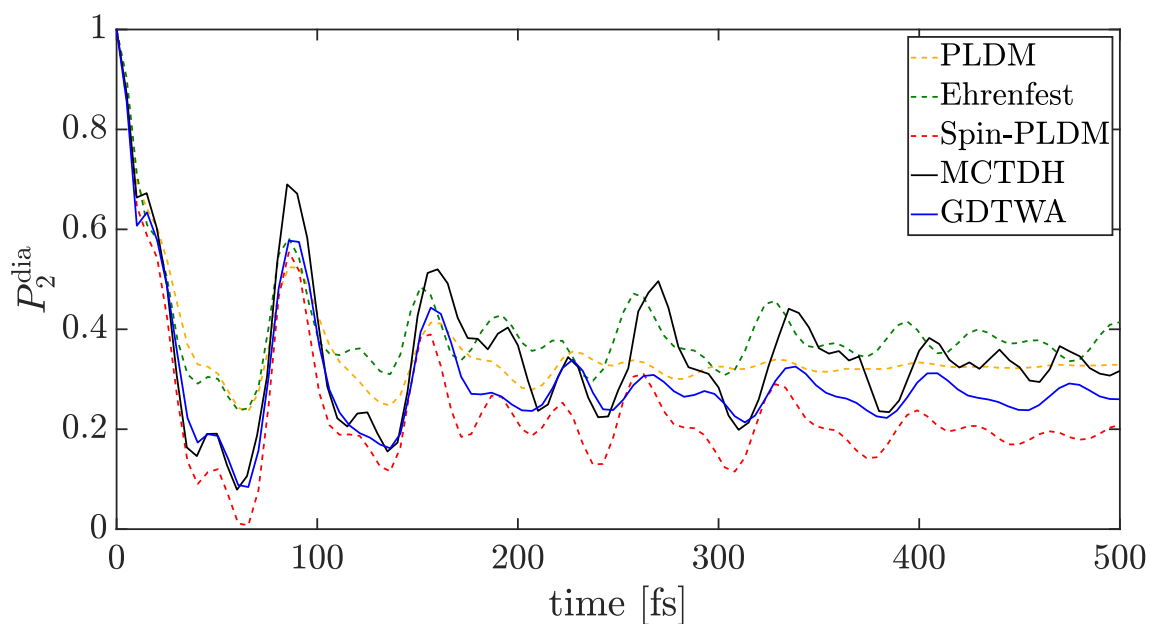


Figure 4.3. Second diabatic state population of a three-modes two-states model based on Pyrazine (see table 4.1), computed using different methods. The GDTWA result (blue solid line) compares fairly well to the exact quantum dynamics (black solid). While GDTWA and, even more so, the Spin-PLDM method (red dashed) underestimate the mean value reached at long times, the Ehrenfest method (green dashed) overestimates it. The PLDM methods (yellow dashed) considerably overestimates the damping of the oscillations.

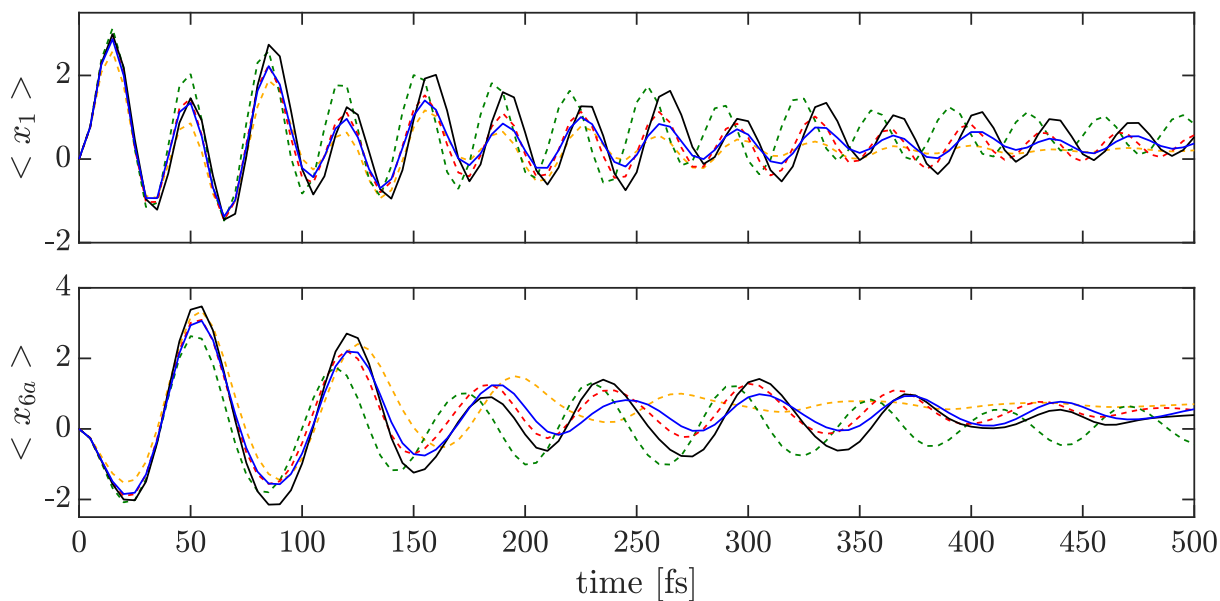


Figure 4.4. Populations of the tuning coordinates $\langle x_1 \rangle$ and $\langle x_{6a} \rangle$ of the Pyrazine-based Model I. The GDTWA (blue solid line) and Spin-PLDM (red dashed) results fail to capture the oscillation amplitudes, but still give a qualitatively fair description on the frequency. In contrast, the Ehrenfest (green dashed) and PLDM methods (yellow dashed) mismatch the oscillation pattern of the exact quantum results (black dashed) after a few periods.

significant deviations from the exact dynamics. In contrast, GDTWA yields surprisingly accurate predictions, for some observables even slightly but noticeably better than Spin-PLDM. In summary, GDTWA has a good performance on both electronic populations and nuclear populations and correlations in this challenging model.

To summarize, we have introduced a recently developed method from the TWA family, GDTWA, to chemical non-adiabatic systems in this section. The novelty and strength of GDTWA is to sample the electron DOF in a discrete phase space. GDTWA with the faithful sampling of the initial electronic conditions can yield a higher accuracy, and can be applied to any initial states, including pure and mixed states. We have also re-written the GDTWA in the unified expression proposed in the last chapter, with the aim of showcasing similarities and differences to more conventional methods. Formally, the EOMs of GDTWA are identical to fully linearized mapping approaches. By the spectral decomposition of the electron EOM, we demonstrate that the fundamental difference between GDTWA and traditional approaches is that GDTWA has two coupled correlated electron states in each single classical trajectory, and hence can be regarded as a partially linearized approach. GDTWA also accounts for an effective ZPE without an explicit ZPE parameter. Numerical benchmarks show the validity of GDTWA for non-adiabatic systems. For the two Tully's models,

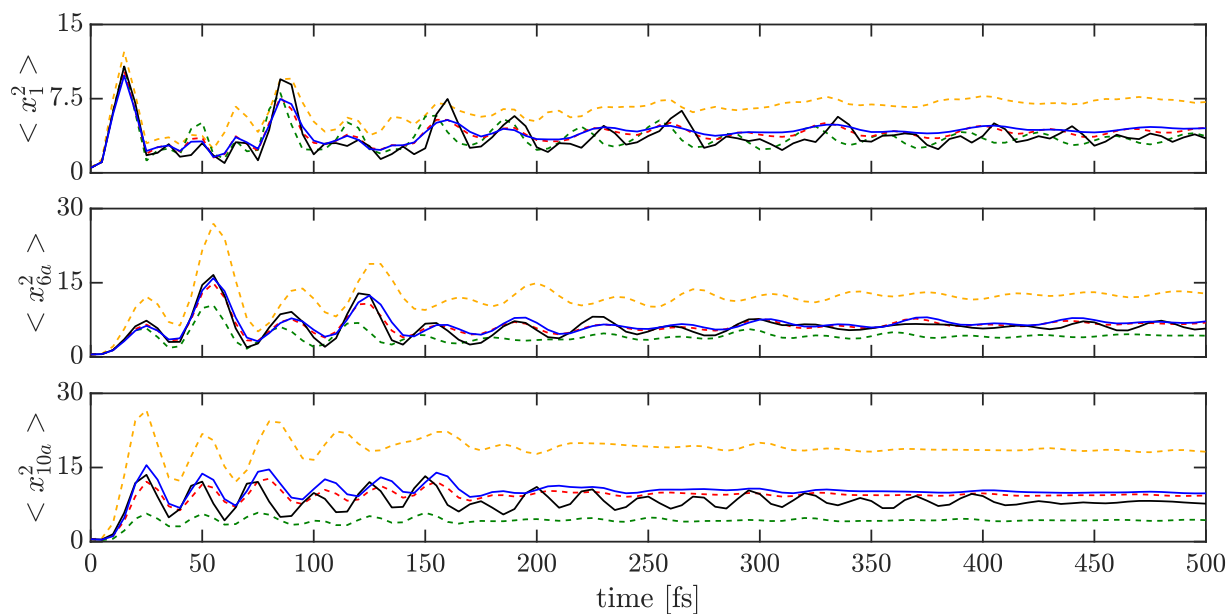


Figure 4.5. Expectation values of second-order correlations of the tuning coordinates $\langle x_1^2 \rangle$ and $\langle x_{6a}^2 \rangle$, and the coupling coordinate $\langle x_{10a}^2 \rangle$ of the Pyrazine-based Model I. The color notations are identical to Fig. 4.3. The GDTWA (blue solid line) and Spin-PLDM (red dashed) results qualitatively predict the ideal higher-order correlation, while the Ehrenfest (green dashed) and PLDM methods (yellow dashed) deviate significantly from the exact quantum results (black dashed).

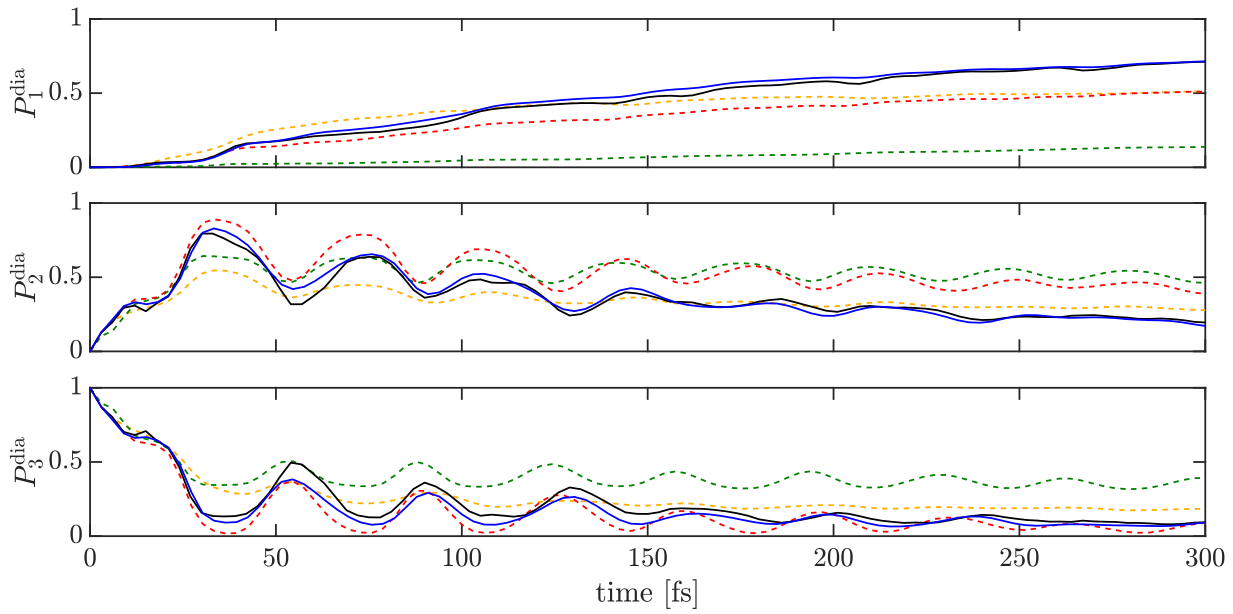


Figure 4.6. Populations of all three diabatic states of a five-modes three-states model based on Benzene radical cation (see table 4.2), computed using different semiclassical techniques. The GDTWA result (blue solid line) compares fairly well to the exact quantum dynamics (black solid) for all the three diabatic states populations, while all the other methods considered fail to describe the long time populations.

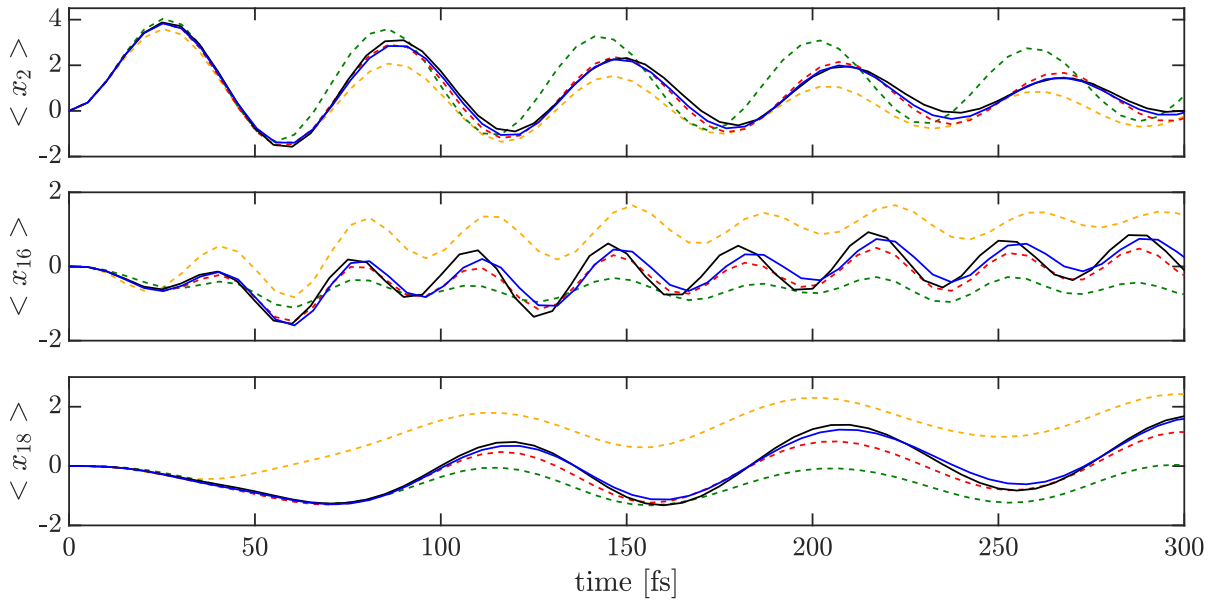


Figure 4.7. Populations of tuning coordinates $\langle x_2 \rangle$, $\langle x_{16} \rangle$, and $\langle x_{18} \rangle$ of the Model II that is based on Benzene radical cation. The GDTWA result (blue solid line) matches the exact quantum dynamics (black solid) best and slightly outperforms the Spin-PLDM result (red dashed).

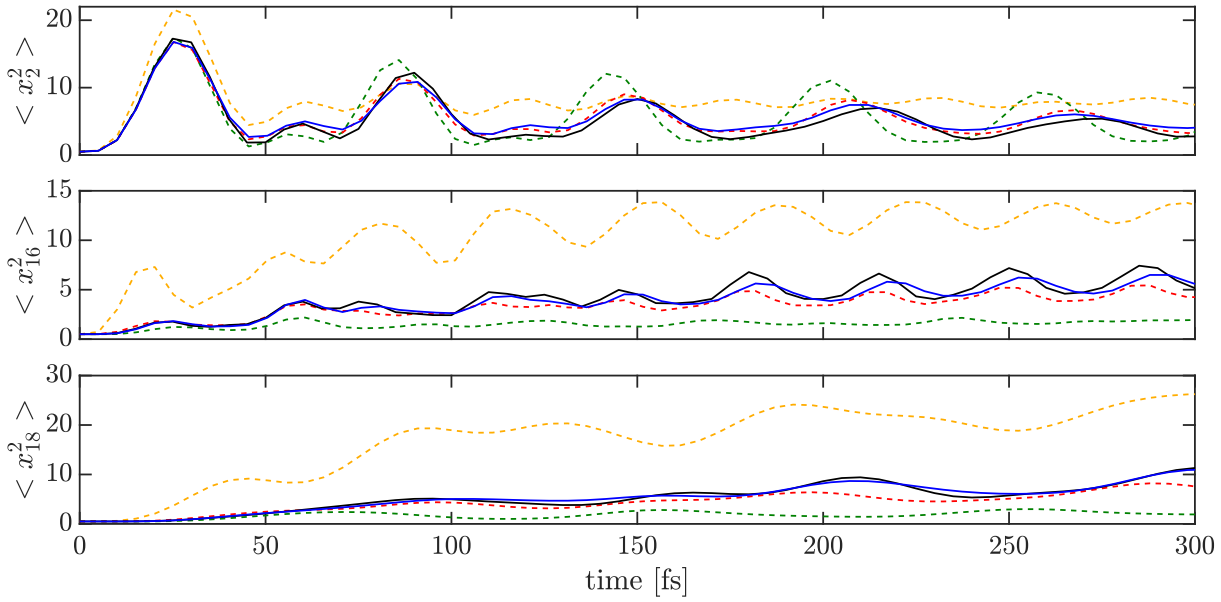


Figure 4.8. The second-order correlations of the tuning coordinates $\langle x_2^2 \rangle$, $\langle x_{16}^2 \rangle$, and $\langle x_{18}^2 \rangle$ of Model II. Both GDTWA (blue solid line) and Spin-PLDM (red dashed) match the exact quantum results (black solid) for the dynamics of $\langle x_2^2 \rangle$. GDTWA slightly outperforms the Spin-PLDM result (red dashed) for the dynamics of $\langle x_{16}^2 \rangle$, while GDTWA is noticeably more accurate than all the other methods for the dynamics of $\langle x_{18}^2 \rangle$.

GDTWA shows reasonable accuracy, in line with other mapping approaches. For the two benchmark LVC models considered, GDTWA displays qualitative and quantitative accuracy compared to the fully quantum description. For one of the considered models, it even outperforms the Spin-PLDM, which is the only other of the considered methods to display an at least qualitative agreement for most of the considered situations.

4.2 GDTWA for particles in the gauge vector potentials

In this section, we develop two different GDTWA (gGDTWA approach I and approach II) methods for particles in gauge vector potentials (i.e., without backaction of the particle to the field). In the first subsection, we present the theoretical analysis of two gGDTWA methods. In the second subsection, we present the numerical benchmarks of two methods.

4.2.1 Theory

In this subsection, we derive two different candidates for a gGDTWA formalism by truncating the Heisenberg equations with canonical momentum and kinematic momentum, respectively. We also analyze the favorable applications of two approaches in this subsection.

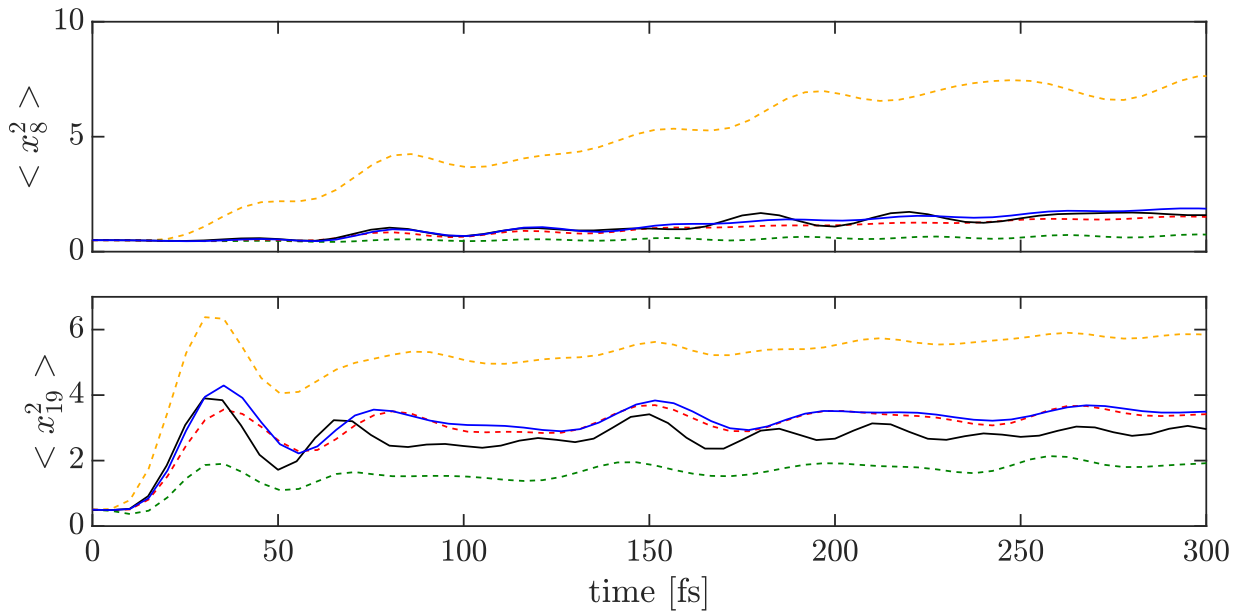


Figure 4.9. Second-order correlations of the coupling coordinates $\langle x_8^2 \rangle$ and $\langle x_{19}^2 \rangle$ of Model II. For the dynamics of $\langle x_8^2 \rangle$, both GDTWA (blue solid line) and Spin-PLDM (red dashed) match the exact quantum results (black solid), with GDTWA slightly outperforming the Spin-PLDM result. For $\langle x_{19}^2 \rangle$, both methods reproduce qualitative features of the exact evolution better than the other considered semiclassical techniques.

Approach I

The first derivation of gGDTWA (Approach I) proceeds from the gauge Hamiltonian (Eq. (2.13)) directly to the Heisenberg equations of motion (EOMs) of the position, canonical momentum, and electronic operators,

$$\begin{aligned}
 \dot{\hat{x}}_j(t) &= \frac{\hat{p}_{\text{can},j}(t)}{m_j} - \frac{A_{j,\mu}\hat{\Lambda}_\mu(t)}{m_j}, \\
 \dot{\hat{p}}_{\text{can},j}(t) &= -\partial_j V_\mu \hat{\Lambda}_\mu - \partial_j B_\mu \hat{\Lambda}_\mu + \sum_k \frac{\hat{p}_{\text{can},k}(t) \partial_k A_{j,\mu} \hat{\Lambda}_\mu(t) + \text{H.c.}}{2m_k}, \\
 \dot{\hat{\Lambda}}_\mu(t) &= f_{\mu\nu\xi} [V_\nu + B_\nu - \sum_j \frac{\hat{p}_{\text{can},j}(t) A_{j,\nu} + \text{H.c.}}{2m_j}] \hat{\Lambda}_\xi(t).
 \end{aligned} \tag{4.28}$$

Subsequently the dynamics of the expectation value of observables $\hat{x}_j(t)$, $\hat{p}_{\text{can},j}(t)$, and $\hat{\Lambda}_\mu(t)$ (and functions thereof) is approximated as the statistical average of the classical correspondence of the quantum observables, which are functions of classical phase space variables $x_j(t)$, $p_{\text{can},j}(t)$, and $\lambda_\mu(t)$. The EOMs of such classical phase space variables take the same form as the Heisenberg EOMs in each single phase space trajectory of the classical ensemble,

$$\begin{aligned}
\dot{x}_j(t) &= \frac{p_{\text{can},j}(t)}{m_j} - \frac{A_{j,\mu}\lambda_\mu(t)}{m_j}, \\
\dot{p}_{\text{can},j}(t) &= -\partial_j V_\mu \lambda_\mu - \partial_j B_\mu \lambda_\mu + \sum_k \frac{p_{\text{can},k}(t) \partial_k A_{j,\mu} \lambda_\mu(t)}{m_k}, \\
\dot{\lambda}_\mu(t) &= f_{\mu\nu\xi} [V_\nu + B_\nu - \sum_j \frac{p_{\text{can},j}(t) A_{j,\nu}}{m_j}] \lambda_\xi(t),
\end{aligned} \tag{4.29}$$

which truncates the quantum correlations to the classical order.

For the experimentally relevant initial adiabatic product state $|\Psi(\mathbf{x}, 0)\rangle = \chi_1(\mathbf{x}) |1(\mathbf{x})\rangle$, the initial distribution of the classical phase space variables $\mathbf{x}(t)$ and $\mathbf{p}_{\text{can}}(t)$ are generated by the Wigner transformation

$$W_{\text{nuc}}(\mathbf{x}(0), \mathbf{p}_{\text{can}}(0)) = \frac{1}{(2\pi)^d} \int d\mathbf{y} \chi_1(\mathbf{x}(0) - \frac{\mathbf{y}}{2}) \chi_1^*(\mathbf{x}(0) + \frac{\mathbf{y}}{2}) e^{i\mathbf{p}_{\text{can}}(0) \cdot \mathbf{y}}, \tag{4.30}$$

and the initial distribution of $\lambda_\mu(0)$ is given by $p(\lambda_\mu(0) = a_\mu) = |\langle 1(\mathbf{x}) | a_\mu \rangle|^2$, where $|a_\mu\rangle$ are the eigenvectors of $\hat{\Lambda}_\mu$ with eigenvalue a_μ , which is identical to the sampling procedure of GDTWA.

An (arbitrary) observable of the system $\hat{O} = \hat{O}_{\text{nuc}} \otimes \hat{O}_{\text{el}}$ under the gGDTWA Approach I is evaluated as

$$\langle \hat{O}(t) \rangle \approx \sum_{\mu, a_\mu} \int d\mathbf{x}(0) d\mathbf{p}_{\text{can}}(0) W_{\text{nuc}}(\mathbf{x}(0), \mathbf{p}_{\text{can}}(0)) O_{w,\text{nuc}}(\mathbf{x}(t), \mathbf{p}_{\text{can}}(t)) c_\mu p(\lambda_\mu(0) = a_\mu) \lambda_\mu(t), \tag{4.31}$$

which is also identical to the GDTWA, Eq. (4.7).

The reducing computational efforts technique discussed in the last subsection, using quasi-phase point operators, of GDTWA can also be used in the Approach I, which yields the following EOMs

$$\begin{aligned}
\dot{x}_j(t) &= \frac{p_{\text{can},j}(t)}{m_j} - \frac{\text{tr}\{\hat{A}_j \hat{J}_\alpha(t)\}}{m_j}, \\
\dot{p}_{\text{can},j}(t) &= -\partial_j \text{tr}\{\hat{V} \hat{J}_\alpha(t)\} - \partial_j \text{tr}\{\hat{B} \hat{J}_\alpha(t)\} + \sum_k \frac{p_{\text{can},k}(t) \partial_k \text{tr}\{\hat{A}_j \hat{J}_\alpha(t)\}}{m_k}, \\
\dot{J}_\alpha(t) &= i[J_\alpha(t), \hat{V} + \hat{B} - \sum_j \frac{p_{\text{can},j}(t) \hat{A}_j}{m_j}], \\
i\hbar \frac{d}{dt} |\Psi_\pm^\alpha(t)\rangle &= (\hat{V} + \hat{B} - \sum_j \frac{p_{\text{can},j}(t) \hat{A}_j}{m_j}) |\Psi_\pm^\alpha(t)\rangle,
\end{aligned} \tag{4.32}$$

where the parameter notations are identical to the GDTWA. Also, the observables evaluations can be expressed as

$$\langle \hat{O}(t) \rangle \approx \sum_\alpha \int d\mathbf{x}(0) d\mathbf{p}_{\text{kin}}(0) w_\alpha W_{\text{nuc}}(\mathbf{x}(0), \mathbf{p}_{\text{kin}}(0)) O_{w,\text{nuc}}(\mathbf{x}(t), \mathbf{p}_{\text{kin}}(t)) \text{Tr}\{\hat{J}_\alpha(t) \hat{O}_{\text{el}}\}. \tag{4.33}$$

The approach I is not gauge invariant because the canonical momentum is not gauge covariant. For simplicity, we consider the vanishing gauge curvature scenario. The representation transformation from the adiabatic representation to the diabatic representation can be expressed as $\hat{U}(x)$ with the matrix elements $U_{ab}(x) = \langle a'|b \rangle$, where $|a'\rangle$ is the diabatic basis and $|b\rangle$ is the adiabatic basis. The algebraic properties of \hat{U} are $\partial_j \hat{U} = -i\hat{U}\hat{A}_j$ and $\partial_j \hat{U}^\dagger = i\hat{A}_j \hat{U}^\dagger$. In the diabatic representation, $\hat{V}^d = \hat{U}\hat{V}\hat{U}^\dagger$, $\hat{J}_\alpha^d = \hat{U}\hat{J}_\alpha\hat{U}^\dagger$, $\hat{A}_j^d = 0$, and $\hat{B}^d = 0$. Replacing respectively \hat{J}_α , \hat{V} , and \hat{A}_j with \hat{J}_α^d , \hat{V}^d , and \hat{A}_j^d in Eq. (4.32), we can verify that the equality of $\hat{J}_\alpha(t)$ holds if

$$i[\hat{J}_\alpha, \hat{B} - \sum_j \frac{\hat{A}_j \text{tr}\{\hat{A}_j \hat{J}_\alpha\}}{m_j}] \equiv 0, \quad (4.34)$$

which is not satisfied in general. Therefore, Approach I is not a gauge invariant method.

Approach II

Approach II consists in truncating the Heisenberg equation of $\hat{p}_{\text{kin},j}$, \hat{x}_j , and $\hat{\Lambda}_\mu$ to the classical order, and replace them with classical phase space variables x_j , $p_{\text{kin},j}$, and λ_μ . In contrast to the canonical momentum $\hat{p}_{\text{can},j}$ used in Approach I, the kinematic momentum $\hat{p}_{\text{kin},j}$ is gauge co-variant. Such variable choice is also widely used in the context of semiclassical theories, for instance, quantum chromodynamics plasmas [252], superconductors [253], topological matter [254], and chemical non-adiabatic systems [54, 76, 255, 256]. The corresponding Heisenberg EOMs are

$$\begin{aligned} \dot{\hat{x}}_j(t) &= \hat{p}_{\text{kin},j}(t)/m_j, \\ \dot{\hat{p}}_{\text{kin},j}(t) &= -\partial_j V_\mu \hat{\Lambda}_\mu(t) - f_{\mu\nu\xi} A_{j,\mu} V_\nu \hat{\Lambda}_\xi(t) + \sum_k \frac{\hat{p}_{\text{kin},k}(t) F_{jk,\mu} \hat{\Lambda}_\mu(t) + \text{H.c.}}{2m_k}, \\ \dot{\hat{\Lambda}}_\mu(t) &= f_{\mu\nu\xi} \left[\frac{V_\nu}{2} - \frac{\hat{p}_{\text{kin},j}(t) A_{j,\nu}}{2m_j} \right] \hat{\Lambda}_\xi(t) + \text{H.c.}, \end{aligned} \quad (4.35)$$

where $F_{jk,\mu}$ is the gauge curvature Eq. (2.15).

Similar to ordinary GDTWA, in the gGDTWA Approach II the EOMs of phase space variables $x_j(t)$, $p_{\text{kin},j}(t)$, and $\lambda_\mu(t)$ in each single trajectory assume the same form of the EOMs of the operators $\hat{x}_j(t)$, $\hat{p}_{\text{kin},j}(t)$, and $\hat{\Lambda}_\mu(t)$,

$$\begin{aligned} \dot{x}_j(t) &= p_{\text{kin},j}(t)/m_j, \\ \dot{p}_{\text{kin},j}(t) &= -\partial_j V_\mu \lambda_\mu(t) - f_{\mu\nu\xi} A_{j,\mu} V_\nu \lambda_\xi(t) + \sum_k \frac{p_{\text{kin},k}(t) F_{jk,\mu} \lambda_\mu(t)}{m_k}, \\ \dot{\lambda}_\mu(t) &= f_{\mu\nu\xi} \left[V_\nu - \frac{p_{\text{kin},j}(t) A_{j,\nu}}{m_j} \right] \lambda_\xi(t). \end{aligned} \quad (4.36)$$

Though \mathbf{x} and \mathbf{p}_{kin} are not canonical variables, the phase space volumes in Approach II are invariant during the propagation. The sufficient and necessary condition of time independent phase space volume elements is $\nabla_{z_t} \cdot \dot{z}_t = 0$ [254], where z_t is the collection of

phase space variables, $\vec{z}_t = \{\mathbf{x}(t), \mathbf{p}(t), \lambda_1(t), \dots, \lambda_{N^2}(t)\}$. It is straightforward to verify that $\nabla_{\vec{z}_t} \cdot \dot{\vec{z}}_t = 0$ for Eq. (4.36) in the Approach II. Therefore, the phase space volume of Approach II is time independent.

The initial sampling of $\mathbf{x}(0)$, $\mathbf{p}_{\text{kin}}(0)$, and $\lambda_\mu(0)$ for the initial adiabatic product state is generated in a two-step procedure. The first step is to generate the initial distribution of $\mathbf{x}(0)$, $\mathbf{p}_{\text{can}}(0)$, and $\lambda_\mu(0)$ by the method in Approach I. The second step is to compute $\mathbf{p}_{\text{kin}}(0)$ according to $\mathbf{p}_{\text{can}}(0)$,

$$\mathbf{p}_{\text{kin}}(0) = \mathbf{p}_{\text{can}}(0) - \mathbf{A}_\mu \lambda_\mu(0). \quad (4.37)$$

The observables \hat{O} can be evaluated as

$$\langle \hat{O}(t) \rangle \approx \sum_{\mu, a_\mu} \int d\mathbf{x}(0) d\mathbf{p}_{\text{kin}}(0) \tilde{W}_{\text{nuc}}(\mathbf{x}(0), \mathbf{p}_{\text{kin}}(0)) \tilde{O}_{w,\text{nuc}}(\mathbf{x}(t), \mathbf{p}_{\text{kin}}(t)) c_\mu p(\lambda_\mu(0) = a_\mu) \lambda_\mu(t), \quad (4.38)$$

where $\tilde{O}_{w,\text{nuc}}(\mathbf{x}, \mathbf{p}_{\text{kin},j}) = O_{w,\text{nuc}}(\mathbf{x}, \mathbf{p}_{\text{kin},j} + \mathbf{A}_\mu \lambda_\mu)$, i.e., Wigner transformation with shifted momentum. The function $\tilde{W}_{\text{nuc}}(\mathbf{x}(0), \mathbf{p}_{\text{kin}}(0))$ denotes the initial distribution of phase space variables. Numerically, we found that $\tilde{W}_{\text{nuc}}(\mathbf{x}(0), \mathbf{p}_{\text{can}}(0))$ can be well approximated by $W_{\text{nuc}}(\mathbf{x}(0), \mathbf{p}_{\text{can}}(0))$ as given by Eq. (4.30) when the initial wave packet center is not close to the conical intersection point for on-the-fly simulation. That is, the momentum shift in the second step in the procedure for the generation of $\mathbf{p}_{\text{kin}}(0)$ can be neglected, at least for the benchmark models considered in this chapter. Similar to the Approach I, the technique to transfer the variables to the discrete quasi-phase point operators used in the GDTWA can still be applied here, which yields the following EOMs and observables evaluations,

$$\begin{aligned} \dot{x}_j(t) &= \frac{p_{\text{kin},j}(t)}{m_j}, \\ \dot{p}_{\text{kin},j}(t) &= -\partial_j \text{tr}\{\hat{V} \hat{J}_\alpha(t)\} + i \text{tr}\{[\hat{A}_j, \hat{V}] \hat{J}_\alpha(t)\} + \sum_k \frac{\text{tr}\{\hat{F}_{jk} \mathcal{J}_\alpha(t)\} p_{\text{kin},k}(t)}{m_k}, \\ \dot{J}_\alpha(t) &= i[\hat{J}_\alpha(t), \hat{V} - \sum_j \frac{p_{\text{kin},j}(t) \hat{A}_j}{m_j}], \\ i\hbar \frac{d}{dt} |\Psi_\pm^\alpha(t)\rangle &= (\hat{V} - \sum_k \frac{p_{\text{kin},k}(t) \hat{A}_k}{m_k}) |\Psi_\pm^\alpha(t)\rangle, \end{aligned} \quad (4.39)$$

$$\langle \hat{O}(t) \rangle \approx \sum_\alpha \int d\mathbf{x}(0) d\mathbf{p}_{\text{kin}}(0) w_\alpha \tilde{W}_{\text{nuc}}(\mathbf{x}(0), \mathbf{p}_{\text{kin}}(0)) \tilde{O}_{w,\text{nuc}}(\mathbf{x}(t), \mathbf{p}_{\text{kin}}(t)) \text{Tr}\{\hat{J}_\alpha(t) \hat{O}_{\text{el}}\}. \quad (4.40)$$

A major difference between the approach I and II is that approach II is gauge invariant because of the gauge covariance of the kinematic momentum. For convenience, we use

the quasi-phase point operator technique. It is straightforward to verify that Eq. (4.39) is invariant under the following transformation

$$\begin{aligned}
x'_j &= x_j, \\
p'_{\text{kin},j} &= p_{\text{kin},j}, \\
\hat{J}'_\alpha &= \hat{U} \hat{J}_\alpha \hat{U}^\dagger, \\
\hat{V}' &= \hat{U} \hat{V}' \hat{U}^\dagger, \\
\hat{A}'_j &= \hat{U} \hat{A}_j \hat{U}^\dagger - i(\partial_j \hat{U}) \hat{U}^\dagger, \\
\hat{F}'_{jk} &= \partial_j \hat{A}'_k - \partial_k \hat{A}'_j - i[\hat{A}'_j, \hat{A}'_k].
\end{aligned} \tag{4.41}$$

where \hat{U} is an arbitrary unitary transformation. In fact, this transformation is identical to the transformation Eq. (2.16) except that all operators are replaced by phase space variables.

Discussion

In this subsection, the differences between Approach I and II are analyzed detail, and we highlight the different preferred scenario for the two approaches. We also discuss how the gGDTWA construction differs from common adiabatic mapping approaches in quantum chemistry.

We stress that the gGDTWA Approaches I and II are different methods, even though they share the same initial sampling and start from equivalent Heisenberg equations. If we replace $\mathbf{p}_{\text{can}}(t)$, $\mathbf{x}(t)$, and $\lambda_\mu(t)$ in Eq. (4.29) with $\mathbf{p}_{\text{kin}}(t) = \mathbf{p}_{\text{can}}(t) - \mathbf{A}_\mu \lambda_\mu(t)$, Eq. (4.36) will not be obtained. Formally, the differences arise from the different $\hat{\Lambda}_\mu$ -dependent relation in Eq. (4.28) and Eq. (4.35). Both Eq. (4.28) and Eq. (4.35) are formally linear $\hat{\Lambda}_\mu$ -dependent. However, among the variables in Eq. (4.35), $\hat{\mathbf{p}}_{\text{kin}}$ also depends linearly on $\hat{\Lambda}_\mu$, which leads to a quadratic $\hat{\Lambda}_\mu$ dependence in Eq. (4.35). In contrast, all variables $\hat{\mathbf{x}}$, $\hat{\mathbf{p}}_{\text{can}}$, and $\hat{\Lambda}_\mu$ in Eq. (4.28) are independent, and therefore only a linear dependence on $\hat{\Lambda}_\mu$ appears in Eq. (4.28).

At first sight, it seems plausible that the Approach I should be the preferred route since the corresponding Heisenberg EOMs Eq. (4.28) have an apparent linear dependence on $\hat{\Lambda}_\mu$ and the truncation variables [257] are the canonical variables. Indeed, Approach I is identical to the ordinary GDTWA, which displays excellent performance in several common experimentally relevant spin-boson coupled models [52, 95]. However, there are two main drawbacks of Approach I. First, Approach I is not gauge invariant. Second, it still requires the knowledge of higher order derivatives of the gauge vector potential $\hat{\mathbf{A}}$ when the gauge curvature is vanishing, which is highly non-trivial for electronic structure calculations. Moreover, the higher order derivative of the gauge vector potential could also cause numerical instabilities when the gauge vector potential itself is singular. These drawbacks make Approach

I unsuitable for semi-classical on-the-fly dynamics simulations. Approach II overcomes these shortcomings of Approach I. First, when the gauge curvature vanishes, Approach II only uses the potential, its gradient, and first-order derivative coupling, which are the direct outputs of electronic structure computations. Second, all the variables are gauge invariant or gauge co-variant. The above advantages are crucial for numerical as well as theoretical aspects. Numerically, $\hat{\mathbf{A}}$ is singular near conical intersections in the adiabatic representation. Hence, simulations in this representation may present numerical instabilities close to conical intersections and may require impractically small time steps. However, such numerical problems can be alleviated by introducing a local quasi-diabatic basis [258–262]. These numerical tricks are possible within Approach II because of its gauge independence, and could be used to improve its numerical efficiency. The quadratic $\hat{\Lambda}_\mu$ dependence in Eq. (4.35) does not harm the accuracy too much since the first-order derivatives are usually small except in the region near the conical intersection points. To summarize, Approach I is suitable for ordinary synthetic gauge field models, while Approach II is more convenient for chemical on-the-fly simulations, in which the gauge curvature can be approximated as zero and where the adiabatic electron basis is used. For this reason, we also call the Approach II with vanishing gauge curvature as adiabatic GDTWA (aGDTWA).

Another interesting difference between the two approaches is that Approach II has a well-defined classical limit while Approach I does not. In the classical limit, the nuclear DOFs are classical particles with an internal DOF (spin DOF). The description of the classical particles should be independent from the gauge choice of the internal DOF. Approach II is consistent with this construction principle, whereas Approach I is not. In fact, common qualitatively semi-classical analysis of non-Abelian gauge theory usually use the kinematic momentum.

Finally, it is useful to discuss the difference between the approaches to construct the semi-classical theory pursued in this chapter and the common approach for semi-classical molecular dynamics on-the-fly simulation in the adiabatic representation (implying vanishing gauge curvature). The EOMs of Approach II are obtained by truncating the quantum EOMs with kinematic momentum, which is marked as red arrows in Fig. 4.10. The black arrow in Fig. 4.10 represents the Approach I, in which we perform the de-quantization with canonical momentum. The common way to construct the semi-classical theory for on-the-fly simulations is illustrated as the blue arrows in Fig. 4.10. The starting point is the diabatic quantum Hamiltonian (gauge vector potentials are zero). The classical diabatic Hamiltonian is obtained by de-quantization directly. One can perform the canonical transformation to obtain the classical adiabatic Hamiltonian as well as the EOMs. The canonical momentum coincides with the kinematic momentum in the diabatic basis. However, EOMs are different when we perform de-quantization with kinematic/canonical momentum in the adiabatic

basis. This difference implies that the operations of de-quantization and canonical transformation do not commute with each other [263], and explains for the case of vanishing gauge curvature why Approach I and Approach II yield inequivalent theories.

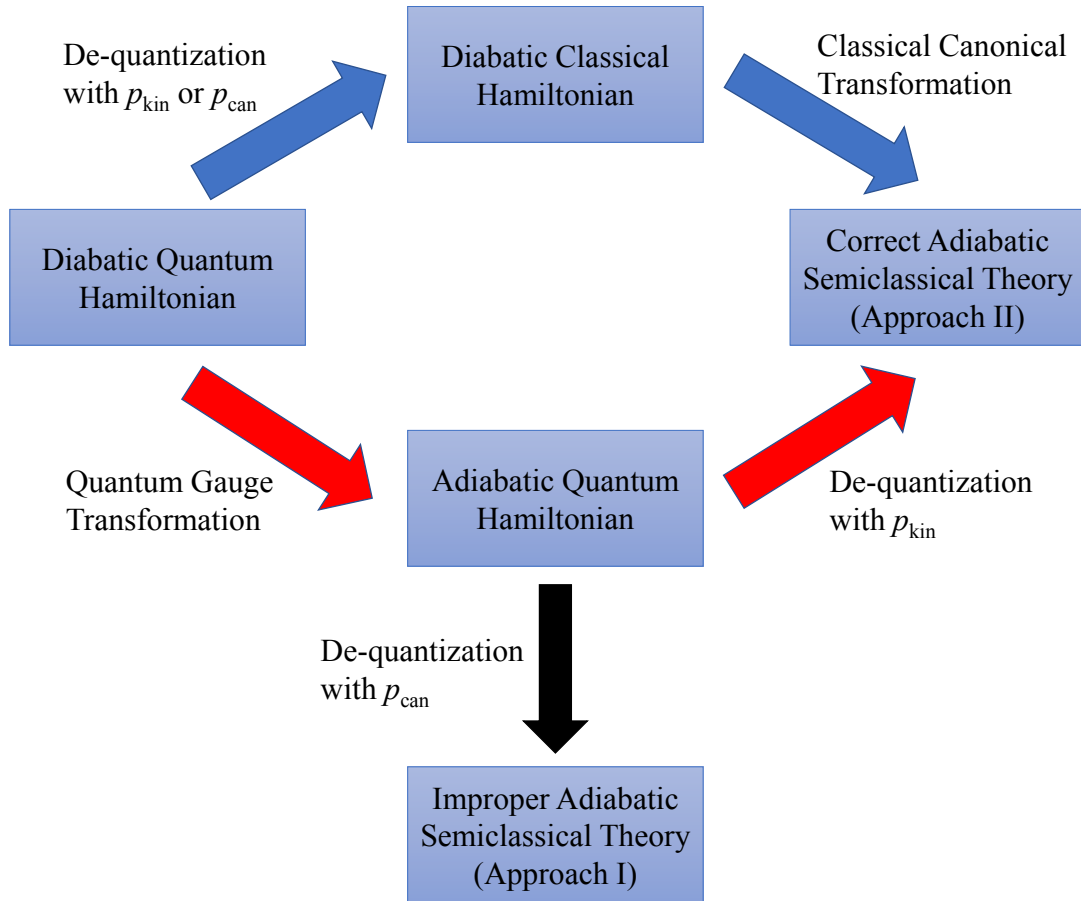


Figure 4.10. The conceptual diagram of constructing the semiclassical theory in the adiabatic representation (vanishing gauge curvature). Inequivalent results can be obtained because de-quantization and canonical transformation are not commuting operations. The blue arrows represent de-quantization then canonical transformation, which leads to the correct semiclassical theory for on-the-fly simulations. Gauge transformation then de-quantization with p_{kin} (Approach II, red arrows) also gives the correct semiclassical theory, while gauge transformation then de-quantization with p_{can} (Approach I, black arrow) cannot. We stress that “improper” and “correct” refers only to the adiabatic representation such as required for on-the-fly simulations. In other scenarios, Approach I may provide better simulation results than Approach II.

To summarize, we established two different gGDTWA, approach I and approach II truncating canonical and kinematic momentum, respectively. The approach I is more similar to the GDTWA, and more suitable for synthetic gauge field theory simulations, while the approach II is gauge invariant and more suitable for on-the-fly simulations.

4.2.2 Numerical results

In this subsection, we present numerical benchmarks of the gGDTWA approaches derived above. In the first two subsections, the comparison between Approach I and II for particles in a synthetic gauge field is presented. In the third subsection, we present the results of Approach II as well as other popular semi-classical methods for the quantum chemistry on-the-fly simulations.

Atom in synthetic gauge field

As first example, we consider a neutral ultracold atom in an optical lattice. This is an excellent experimental platform to observe, e.g., *Zitterbewegung* (ZB) and spin Hall effect (SHE) [222, 248, 249]. The system Hamiltonian is

$$H = \frac{1}{2m}(\hat{p}_y - \hbar k_0 \epsilon_R \hat{\sigma}_z)^2 + \frac{1}{2m}(\hat{p}_x + \hbar k_0 \epsilon_R \hat{\sigma}_y)^2 + \frac{\hbar^2 k_0^2}{m} \epsilon_R \hat{\sigma}_z, \quad (4.42)$$

where $\epsilon_R = \sqrt{2} - 1$, $k_0 = 2\pi/820\text{nm}^{-1}$ is the wavenumber of the lattice laser, and m is the mass of the atoms, which we assume to be ^{87}Rb . The initial state is prepared as the Gaussian wave packet

$$\Psi(x, y, t = 0) = \frac{d}{\sqrt{2\pi}} \int dk_x dk_y e^{ik_y y + ik_x x} e^{-(k_y d)^2/2 - (k_x d)^2/2} \begin{pmatrix} 1 \\ 1 \end{pmatrix}, \quad (4.43)$$

where $k_0 d = 16.2$.

The system is exactly solvable. The eigenstates of the Hamiltonian Eq. (4.42) are the momentum eigenstates,

$$\begin{aligned} \phi_{\mathbf{k},+}(x, y) &= e^{ik_y y + ik_x x} \begin{pmatrix} \cos \frac{\theta_{\mathbf{k}}}{2} \\ i \sin \frac{\theta_{\mathbf{k}}}{2} \end{pmatrix} \\ \phi_{\mathbf{k},-}(x, y) &= e^{ik_y y + ik_x x} \begin{pmatrix} \sin \frac{\theta_{\mathbf{k}}}{2} \\ -i \cos \frac{\theta_{\mathbf{k}}}{2} \end{pmatrix}, \end{aligned} \quad (4.44)$$

where

$$\begin{aligned} \cos \theta_{\mathbf{k}} &= \frac{k_0 - k_y}{\sqrt{(k_0 - k_y)^2 + k_x^2}}, \\ \sin \theta_{\mathbf{k}} &= \frac{k_x}{\sqrt{(k_0 - k_y)^2 + k_x^2}}, \end{aligned} \quad (4.45)$$

and the corresponding eigenvalues are

$$\begin{aligned} E(\mathbf{k}, +) &= \frac{\hbar^2 k_x^2 + \hbar^2 k_y^2}{2m} + \epsilon_{\mathbf{k}} \\ E(\mathbf{k}, -) &= \frac{\hbar^2 k_x^2 + \hbar^2 k_y^2}{2m} - \epsilon_{\mathbf{k}}, \end{aligned} \quad (4.46)$$

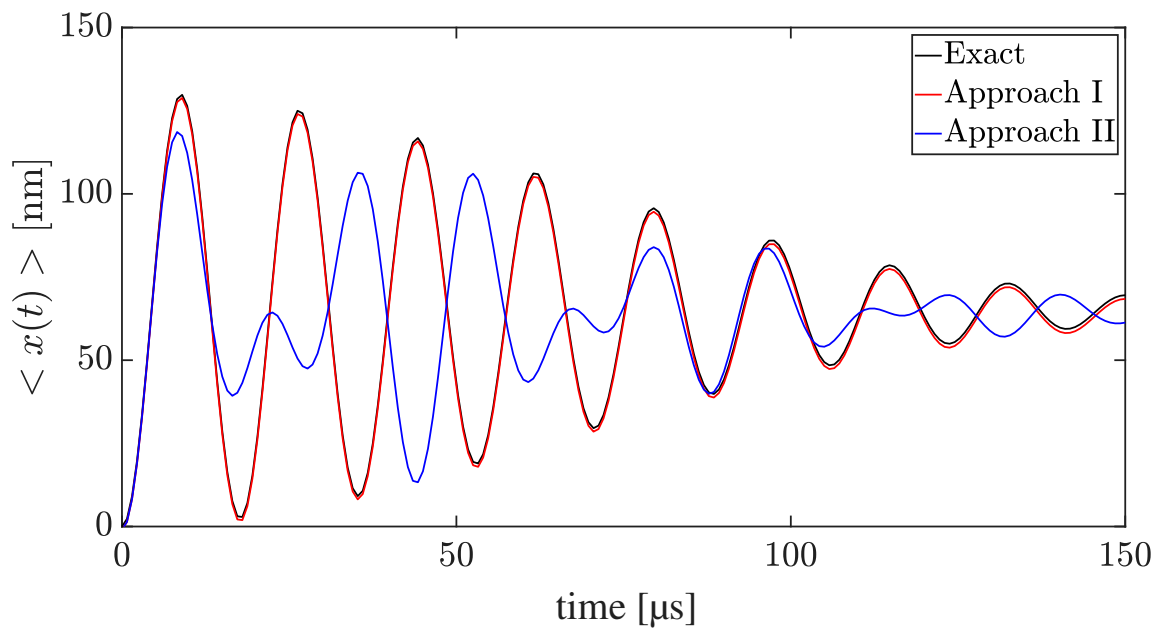


Figure 4.11. Population of $\langle x(t) \rangle$. Approach I (red solid) fits the exact result (black solid), however, Approach II (blue solid) has a huge mismatch with exact result.

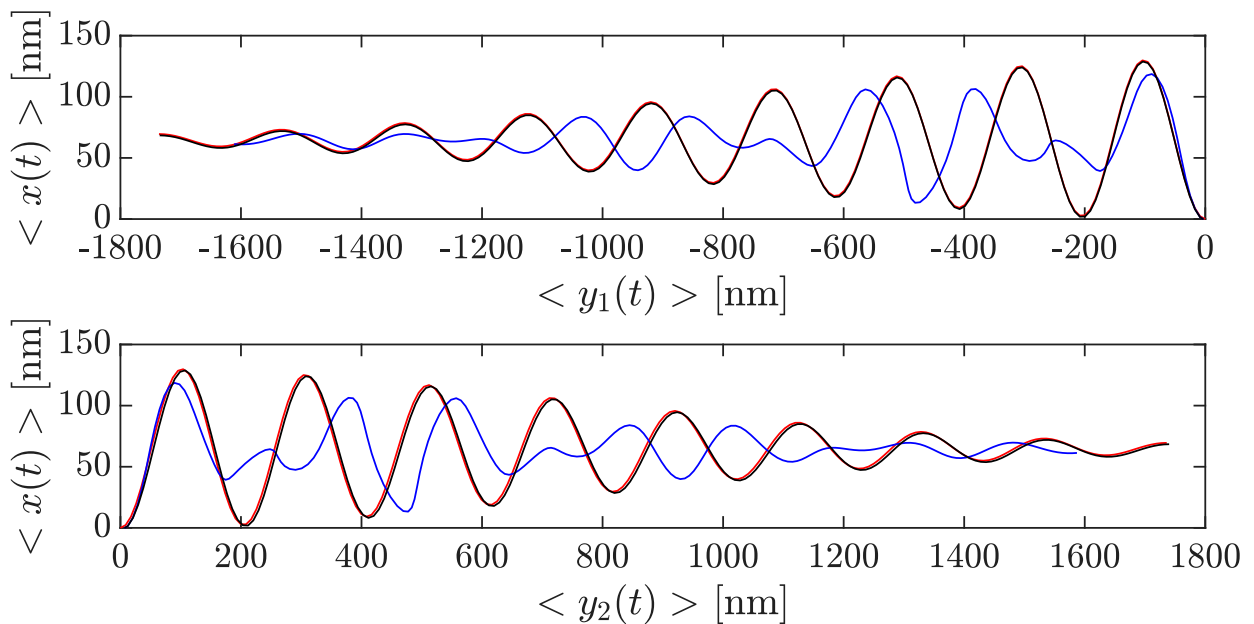


Figure 4.12. Trajectories of the expectation value of $\langle y_{1,2}(t) \rangle - \langle x(t) \rangle$. Both Approach I (red solid) and Approach II (blue solid) show the separation of the projected expectation value by spin state. However, Approach II fails to reproduce the exact solution while Approach I is also quantitatively correct.

where

$$\epsilon_{\mathbf{k}} = \frac{\hbar^2 k_0}{m} \epsilon_R \sqrt{(k_0 - k_y)^2 + k_x^2} \quad (4.47)$$

The time-dependent wave function solution of Eq. (17) can then be obtained explicitly as

$$\Psi(x, y, t) = \frac{d}{\sqrt{\pi}} \int dk_x dk_y e^{-(k_y y d)^2/2 - (k_x x d)^2/2} e^{ik_y y + ik_x x} e^{-i \frac{\hbar^2 k_x^2 + \hbar^2 k_y^2}{2m} t} \Phi(k_x, k_y, t), \quad (4.48)$$

where

$$\Phi(k_x, k_y, t) = \frac{1}{\sqrt{2}} \cos \epsilon_{\mathbf{k}} t \begin{pmatrix} 1 \\ 1 \end{pmatrix} - \frac{1}{\sqrt{2}} i e^{-i\theta_{\mathbf{k}}} \sin \epsilon_{\mathbf{k}} t \begin{pmatrix} 1 \\ -1 \end{pmatrix}. \quad (4.49)$$

In Fig. 4.11, we compare the dynamics of $\langle x(t) \rangle$ for the exact solution, Approach I, and Approach II. Both approaches are averaged over 10^6 trajectories (although convergence is not fully reached, this value is sufficient to show the salient features of the two methods). The oscillation of $\langle x(t) \rangle$ is the typical feature of the phenomenon of ZB. Approach I fits the exact solution almost perfectly, while Approach II has a considerable mismatch. Another typical feature of ZB is the wave packet separation by spin state, also known as spin Hall effect. In Fig. 4.12, we plot the spin separation, i.e., the expectation value of $\langle y_{1,2}(t) \rangle = \langle y(1 \pm \hat{\sigma}_z(t))/2 \rangle$. Although both Approach I and Approach II show a clear separation, Approach I outperforms Approach II significantly in its quantitative agreement with the exact solution.

Linear vibronic coupling model as a synthetic gauge field theory

As we presented in the second chapter, the LVC model is an excellent platform for synthetic gauge field implementation [222] via mapping $Q_j = -p_j$ and $P_j = x_j$. In this subsection, we also consider the three-mode-two-state pyrazine-based model, which is used in GDTWA benchmarking. For the parameters and initial state preparation, see the Sec. 4.1.2. The gauge Hamiltonian (after mapping with the spirit of Eq. (2.181)) of the model is

$$H = \frac{1}{2} \sum_j \omega_j (P_j - A_j)^2 + V, \quad (4.50)$$

where

$$V = \frac{1}{2} \sum_j \omega_j Q_j^2 + \frac{\sqrt{2}}{2} (E_1 - E_2 - \frac{(\kappa_1^{(1)})^2 - (\kappa_1^{(2)})^2}{2\omega_1} - \frac{(\kappa_{6a}^{(1)})^2 - (\kappa_{6a}^{(2)})^2}{2\omega_{6a}}) \hat{\Lambda}_3, \quad (4.51)$$

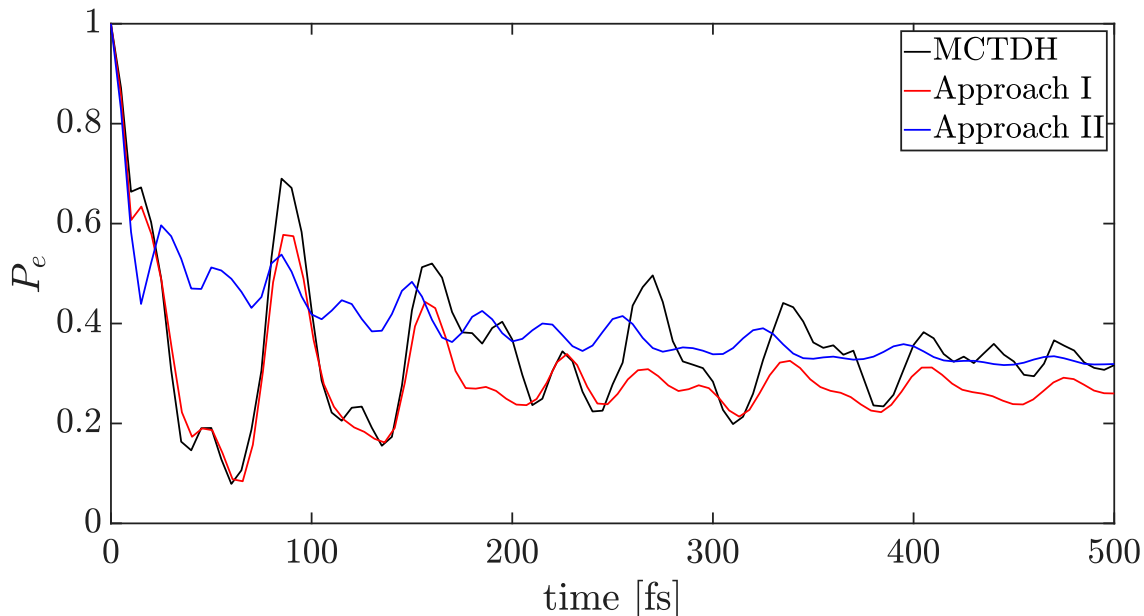


Figure 4.13. Population of the diabatic excited state of a three-modes two-states model based on pyrazine. Results are obtained by Approach I (red solid), Approach II (blue solid line), and MCTDH (black solid). While both semiclassical approximations qualitatively describe the long-time relaxation, Approach II completely fails to capture the oscillations in the short to medium time dynamics.

and

$$\begin{aligned}
 A_1 &= -\frac{\kappa_1^{(1)} + \kappa_1^{(2)}}{2\omega_1} - \sqrt{2} \frac{\kappa_1^{(1)} - \kappa_1^{(2)}}{2\omega_1} \hat{\Lambda}_3, \\
 A_{6a} &= -\frac{\kappa_{6a}^{(1)} + \kappa_{6a}^{(2)}}{2\omega_{6a}} - \sqrt{2} \frac{\kappa_{6a}^{(1)} - \kappa_{6a}^{(2)}}{2\omega_{6a}} \hat{\Lambda}_3, \\
 A_{10a} &= -\sqrt{2} \frac{\lambda_{10a}^{(12)}}{\omega_{10a}} \hat{\Lambda}_1.
 \end{aligned} \tag{4.52}$$

We focus on the diabatic excited state population P_e dynamics rather than the nuclei observables. In Fig. 4.13, we compare the population of P_e for numerically converged Multi-configuration time-dependent Hartree (MCTDH) calculations [33, 34, 251], which provide the exact benchmark, as well as Approach I and Approach II. Both Approach I and II are averaged over 10^6 trajectories. For this model, Approach I is identical to the ordinary GDTWA method. As the Fig. 4.13 shows, Approach I captures both the short time dynamics as well as the long time relaxation with a satisfying accuracy. Approach II has some better quantitative agreement as regards the value of the long-time relaxation, but completely fails to describe the oscillations in the short to medium time behavior.

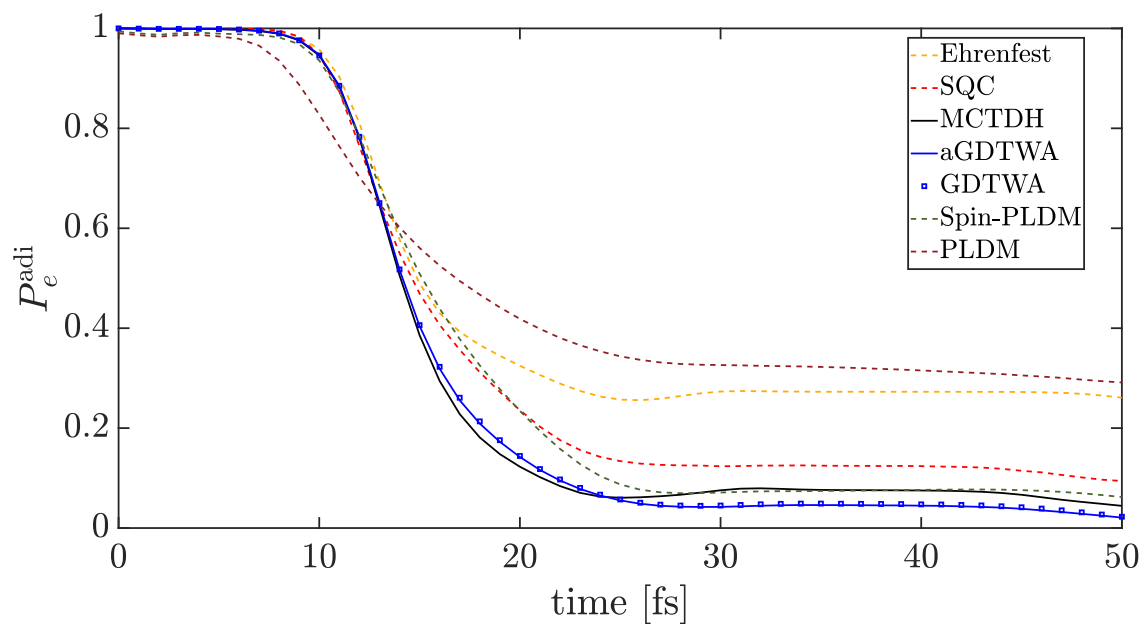


Figure 4.14. Population of the excited adiabatic state of a two-modes two-states model based on pyrazine. Results are obtained by aGDTWA (blue solid line), Ehrenfest method (yellow dashed line), SQC (red dashed), GDTWA in the diabatic representation (blue rectangles), PLDM (brown dashed), Spin-PLDM (green dashed) and MCTDH (black solid). All the semiclassical methods considered capture the dynamics qualitatively, but to different levels of quantitative agreement, with GDTWA being among the top-performing methods. Model parameters: $\omega_1 = 3.650 \times 10^{-3}$, $\omega_2 = 4.186 \times 10^{-3}$, $a = 48.45$, $c = 4.946 \times 10^{-4}$ and $\Delta = 0.02757$.

On-the-fly simulation for linear vibronic coupling models

In this subsection, we consider the on-the-fly simulation for two-modes two-states LVC models [2, 264] with a tuning coordinate X and a coupling coordinate Y . The Hamiltonian is selected as Eq. (2.175). The corresponding adiabatic states are already discussed in the second chapter. We consider three models, Pyrazine molecule, bis(methylene) adamantyl (BMA), and Butatriene cation [220, 221], corresponding to the model parameters listed below the respective figure (Fig. 4.14 to 4.16). We prepare the initial electronic state as the excited adiabatic state with correct geometric phase $|e\rangle_g$ (for details, see Sec. 2.4.4), and the nuclear state as

$$\Psi(X, Y) = \frac{(\omega_1\omega_2)^{1/4}}{\pi^{1/2}} \exp\left\{-\frac{\omega_1}{2}\left(X - \frac{a}{2}\right)^2 - \frac{\omega_2}{2}Y^2\right\}. \quad (4.53)$$

We compare the population of excited adiabatic states as obtained by numerically converged Multi-configuration time-dependent Hartree (MCTDH) calculations [33, 34, 251], which provide the exact benchmark, the Ehrenfest method [2], the symmetrical windowing quasi-classical (SQC) method [55, 57, 75] with the standard triangle window, partially linearized density matrix (PLDM) [67, 68], spin partially linearized density matrix (Spin-PLDM) [77, 78], aGDTWA, and GDTWA in the diabatic representation. Spin-PLDM is averaged over 5×10^5 trajectories and all the other semi-classical methods are averaged over 10^5 trajectories to ensure convergence. As Figs. 4.14, 4.15, and 4.16 show, aGDTWA as well as the other semi-classical methods capture the dynamics qualitatively well. SQC and aGDTWA predict the best agreement with the exact results for all models, and aGDTWA slightly outperforms SQC in the pyrazine model. Interestingly, compared with SQC and GDTWA, Spin-PLDM gives a promising result for the pyrazine model (better than SQC), but performs slightly worse than SQC and aGDTWA in the BMA and butatriene models. aGDTWA and GDTWA in the diabatic representation coincide perfectly in all three models. In Figs. 4.17, 4.18, and 4.19, the position $\langle X \rangle$ and kinematic momentum $\langle P_X \rangle$ of the three models are presented. All the semiclassical methods capture the dynamics qualitatively, with aGDTWA, SQC, and Spin-PLDM demonstrating the best performance out of the chosen methods. Figures 4.20, 4.21, and 4.22 provide the benchmarks of the adiabatic ground state-specific position $\langle X \rangle_g$ and the adiabatic excited state-specific position $\langle X \rangle_e$ for the three models. The position expectation averaged on each adiabatic surface are correlations of higher order, and thus are challenging for the linearized semi-classical methods. However, SQC, Spin-PLDM, and GDTWA still provide qualitatively correct results. Specifically, GDTWA overestimates the coherent dynamics of $\langle X \rangle_e$ in Figs. 4.20 and 4.22 but it still has a satisfactory accuracy for those two models, especially for the region 0-25 fs of the pyrazine model in Fig. 4.20. As these results illustrate, aGDTWA provides a competitive and numerically tractable method to treat non-adiabatic chemical systems.

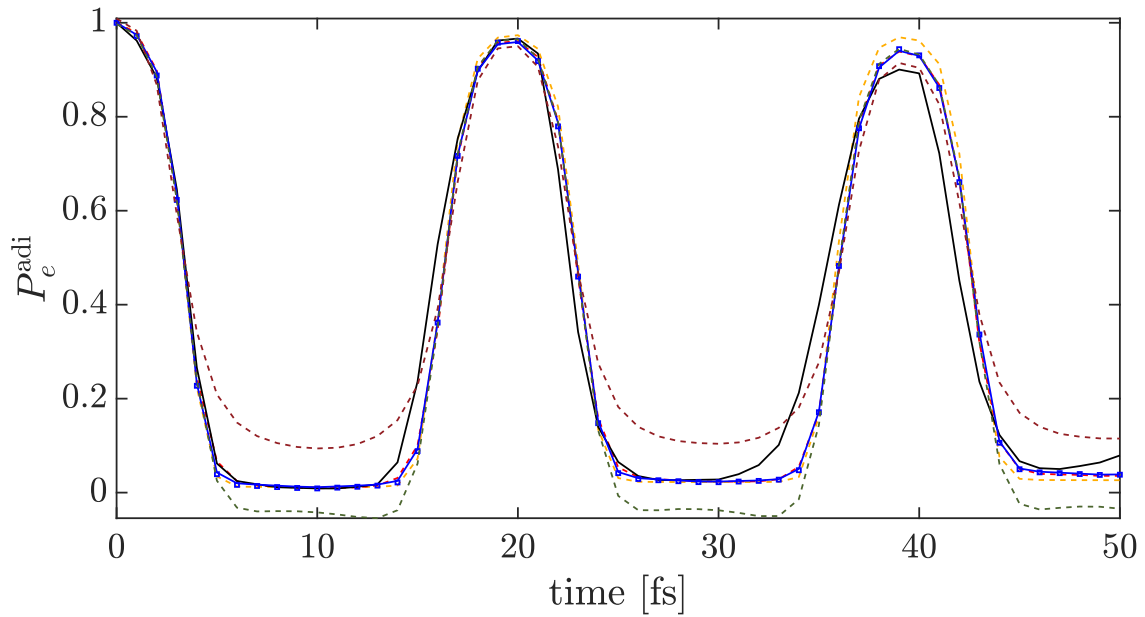


Figure 4.15. Similar to Fig. (4.14), but for BMA-based model. All the methods capture the dynamics qualitatively. Model parameters: $\omega_1 = 7.743 \times 10^{-3}$, $\omega_2 = 6.680 \times 10^{-3}$, $a = 31.05$, $c = 8.092 \times 10^{-5}$, and $\Delta = 0.00000$.

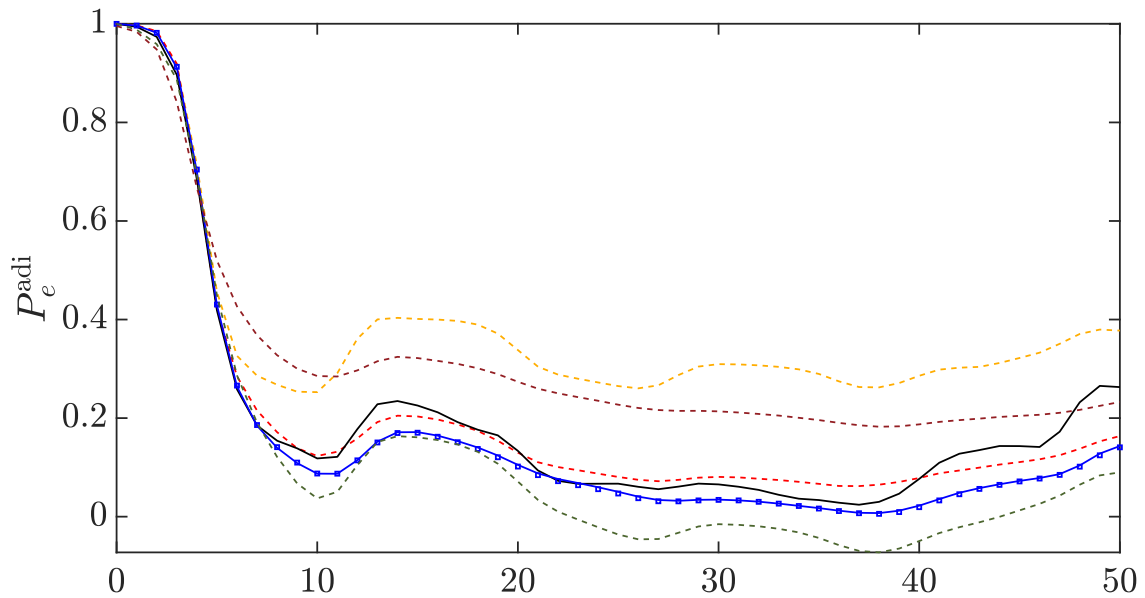


Figure 4.16. Similar to Fig. (4.14), but for Butatriene-based model. All the methods capture the dynamics qualitatively. Model parameters: $\omega_1 = 9.557 \times 10^{-3}$, $\omega_2 = 3.3515 \times 10^{-3}$, $a = 20.07$, $c = 6.127 \times 10^{-4}$, and $\Delta = 0.01984$.

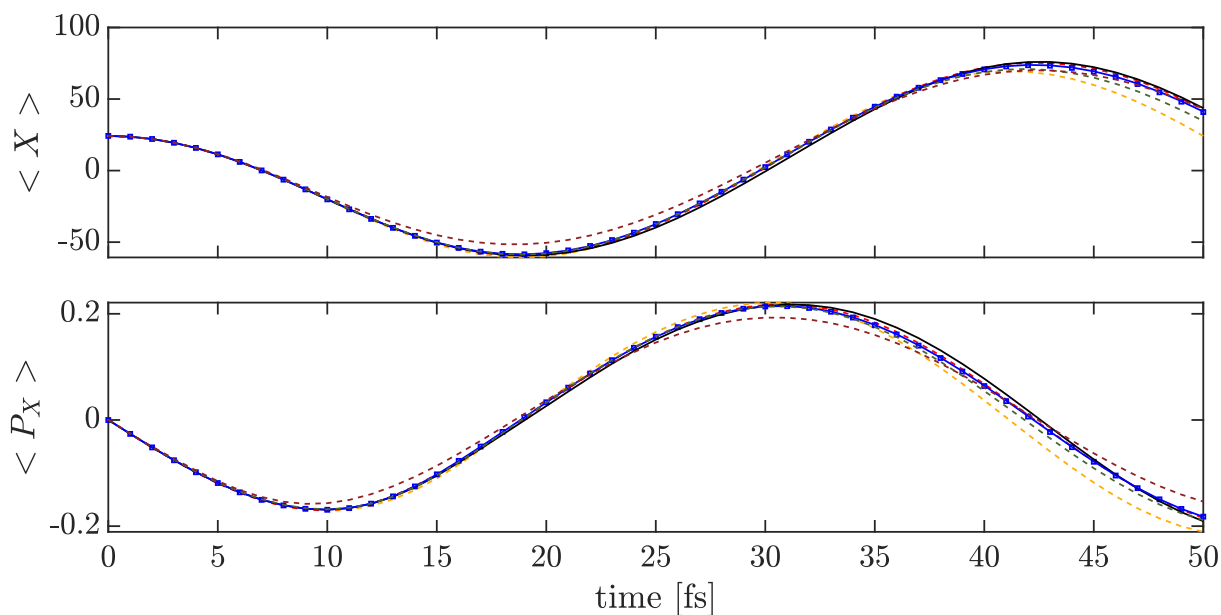


Figure 4.17. Population of position $\langle X \rangle$ and kinematic momentum $\langle P_X \rangle$ of a two-modes two-states model based on pyrazine. Results are obtained by aGDTWA (blue solid line), Ehrenfest method (yellow dashed line), SQC (red dashed), GDTWA in the diabatic representation (blue rectangles), PLDM (brown dashed), Spin-PLDM (green dashed), and MCTDH (black solid). All the methods capture the dynamics qualitatively and even quantitatively, especially in the case of aGDTWA and SQC.

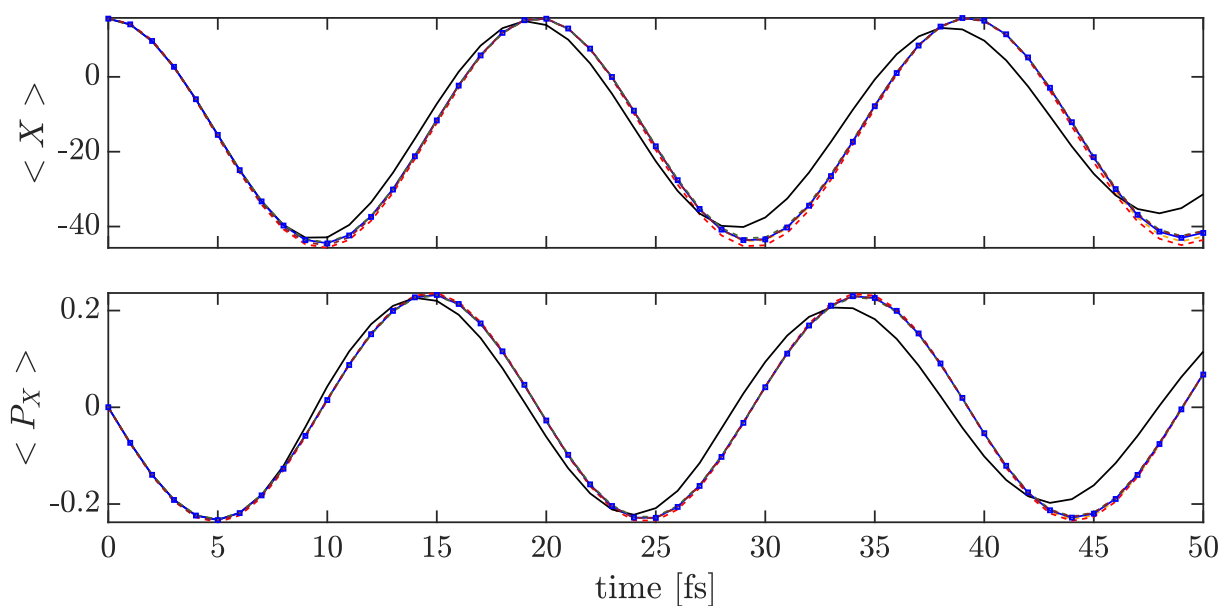


Figure 4.18. Similar to Fig. (4.17), but for BMA-based model. All the methods capture the dynamics qualitatively.

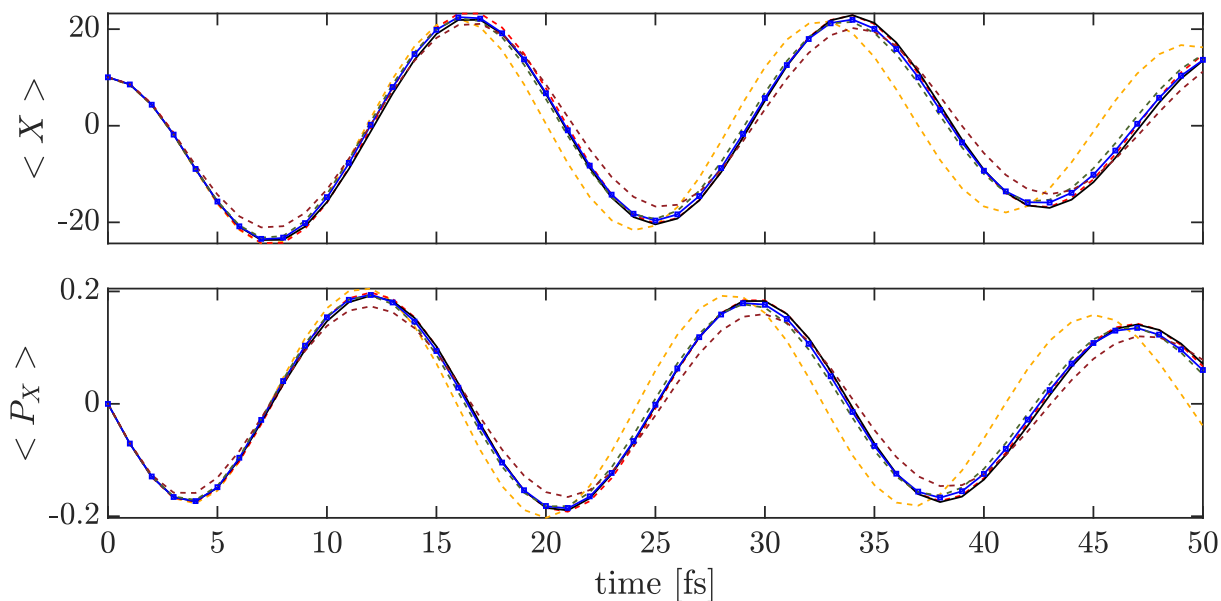


Figure 4.19. Similar to Fig. (4.17), but for Butatriene-based model. All the methods capture the dynamics qualitatively, Spin-PLDM, SQC and aGDTWA even quantitatively.

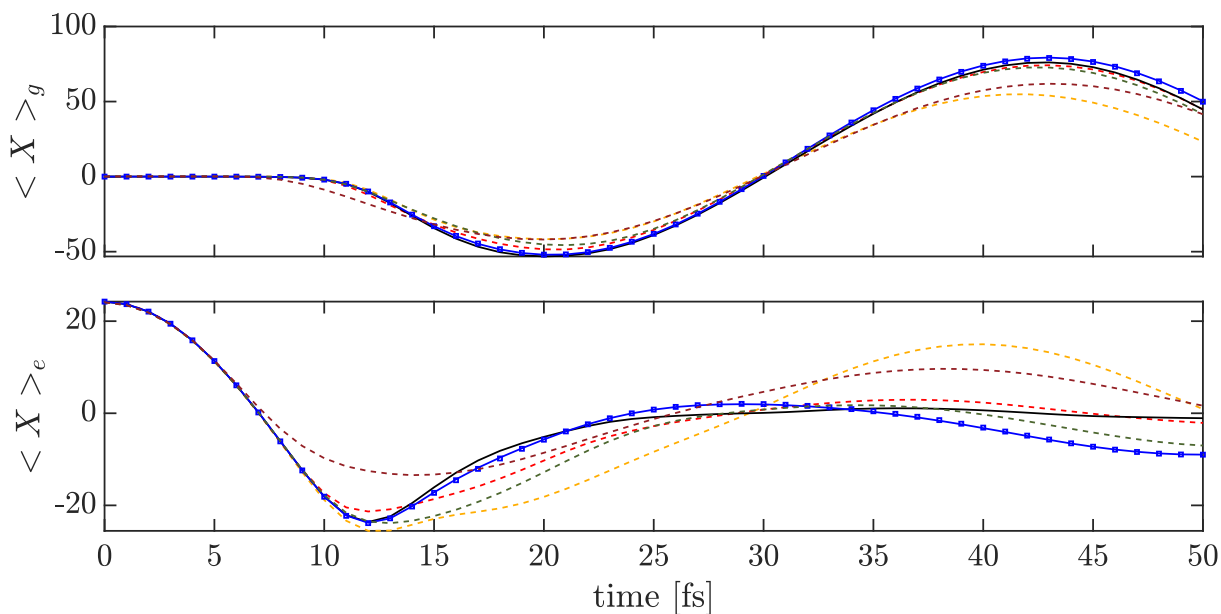


Figure 4.20. Population of the adiabatic ground state-specific position $\langle X \rangle_g$ and the adiabatic excited state-specific position $\langle X \rangle_e$ of a two-modes two-states model based on pyrazine. Results are obtained by aGDTWA (blue solid line), Ehrenfest method (yellow dashed line), SQC (red dashed), GDTWA in the diabatic representation (blue rectangle), PLDM (brown dashed), Spin-PLDM (green dashed), and MCTDH (black solid). All the methods capture the dynamics qualitatively.

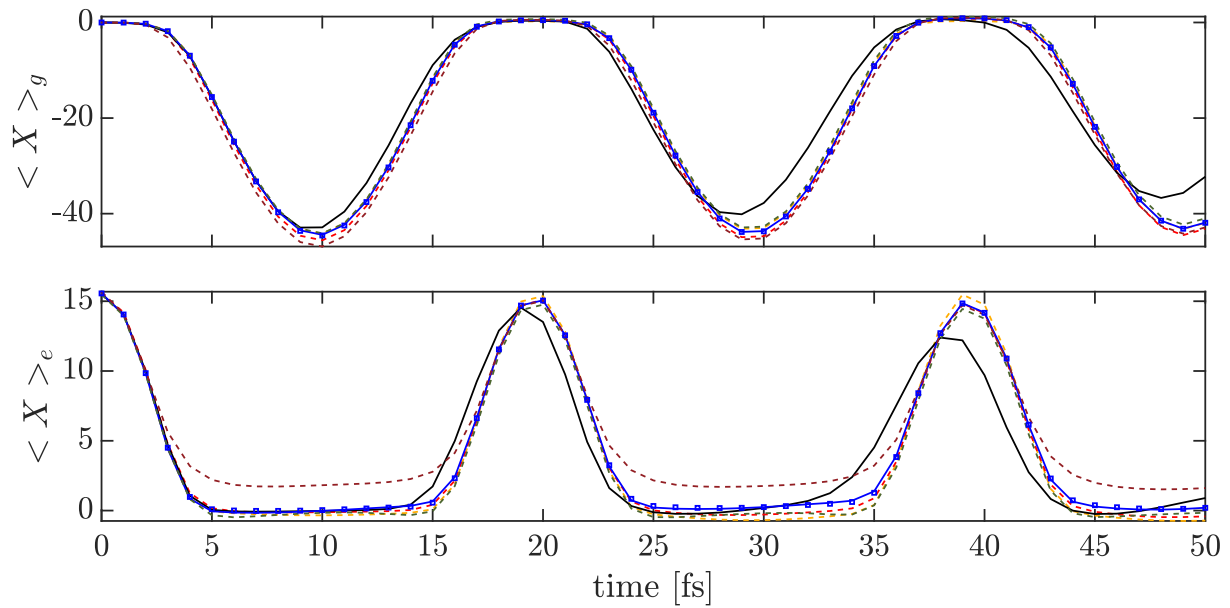


Figure 4.21. Similar to Fig. (4.20), but for BMA-based model. All the methods capture the dynamics qualitatively.

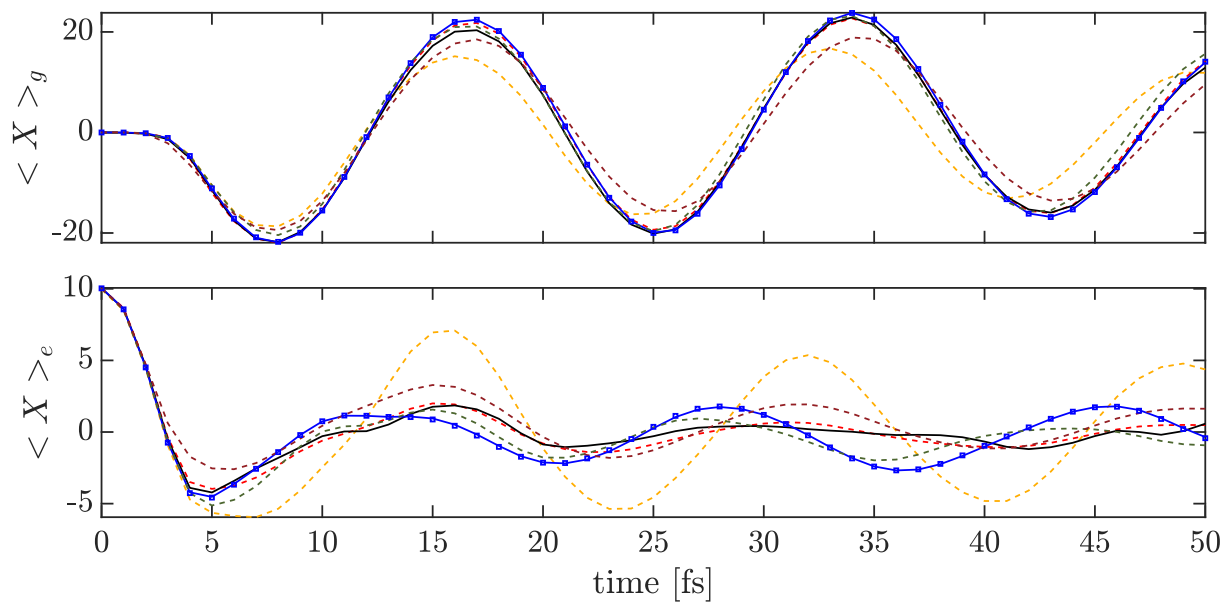


Figure 4.22. Similar to Fig. (4.20), but for Butatriene-based model. All the methods capture the $\langle X \rangle_g$ dynamics qualitatively, while $\langle X \rangle_e$ dynamics is challenging for them except SQC.

Let us finally comment on the role of the geometric phase in both aGDTWA and numerically “exact” methods, which in the adiabatic representation is introduced by the singularity generated by the conical intersection. As we discussed in the Sec. 2.4.4, to account for it, we employ complex-rotated adiabatic states rather than real adiabatic states [221]. For the full quantum mechanical reference simulations, which are performed in the diabatic representation, the complex adiabatic basis results in a consistent adiabatic-to-diabatic transformation of the initial adiabatic state $\Psi(X, Y) \otimes |e\rangle_g$. In contrast, the choice of adiabatic basis has no significant influence on the aGDTWA computations, which for the investigated model yield almost indistinguishable results with and without the complex rotation (data not shown). Notice that $\hat{A}_X^g = -\frac{\partial_X \theta}{2}(\hat{I} + \hat{\sigma}_y)$ and $\hat{A}_Y^g = -\frac{\partial_Y \theta}{2}(\hat{I} + \hat{\sigma}_y)$ for complex basis, as well as $\hat{A}_X^g = -\frac{\partial_X \theta}{2}\hat{\sigma}_y$ and $\hat{A}_Y^g = -\frac{\partial_Y \theta}{2}\hat{\sigma}_y$ for real basis, only difference between them is proportional to the identity operator. Therefore, the EOMs using either a complex or a real basis are identical, and the only difference lies in the shift of the initial nuclear momentum when using Eq. (4.37), which can be neglected for the considered benchmark models. These results indicate that the linearized semiclassical method with normal real adiabatic basis can capture geometric phase effects for the dynamics when the initial state is prepared in the excited state, which coincides with the findings of Ref. [221].

To summarize, in this subsection we have introduced two gGDTWA. The approach I, obtained by truncating canonical momentum, is more similar to the GDTWA, and has a better performance for synthetic gauge field models. The approach II, obtained by truncating kinematic momentum, is gauge invariant and more suitable for on-the-fly simulations.

4.3 Conclusions

In this chapter, we have introduced a recently developed linearized semiclassical method for quantum lattice systems, GDTWA, to chemical non-adiabatic systems with detailed theoretical analysis and numerical benchmarks. We re-wrote GDTWA in the unified expression proposed in the last chapter. Such re-writing can not only reduce the computational efforts, but also provide the convenience of comparison with other mapping approaches. GDTWA can be regarded as a fully-partially linearized method, which has two coupled electronic states in one trajectory, and the initial electronic DOFs are sampled via discrete electronic phase space. Such sampling also accounts for a reduced ZPE without an explicit ZPE parameter. For the initial diagonal states, GDTWA can sample the correct intra-electron correlations. Numerical benchmarks show that GDTWA is reliable for various chemical models, including scattering models and LVC models.

We also developed two gGDTWA, which establishes the foundation for treating particles in non-Abelian gauge fields using the GDTWA formalism. The Approach I, using

canonical momentum, presents very promising results for the synthetic gauge fields, while the gauge-invariance property of Approach II, using kinematic momentum, provides the freedom of representation choice required in quantum chemistry for on-the-fly simulations. Thus, Approach II can be combined with popular diabaticization approaches to avoid issues with possible singularities. We also discussed the sampling of the initial adiabatic product state, and showed that the two-step sampling procedure can be approximated by a single step for on-the-fly simulations. We believe the gGDTWA will provide a powerful tool for the simulation of systems with synthetic gauge fields [102] and on-the-fly semiclassical simulations.

Part III

Quantum Simulations for Quantum Dynamics of Chemical Systems

The main difficulty of simulating nonadiabatic quantum dynamics as well as other quantum phenomena arises from the incompatibility between classical computers and quantum effects, i.e., the exponential growth of Hilbert space makes the demanded computational resources blow up. Already in the last two parts, we presented numerically “exact” methods (mainly MCTDH) and linearized phase space methods to mitigate this problem. However, both of them have their own limitations. MCTDH tries to account for quantum effects as much as possible, but suffers from the exponential growth of computational efforts. Additionally, the efficient representation of MCTDH wave function ansatz relies on the entanglement of the system, which prohibits its application to the long time dynamics [33]. Linearized phase space methods account for the quantum effects of initial states while approximating the dynamics classically. They are qualitatively correct only for systems with negligible quantum coherence [96, 225].

Is it possible to simulate an arbitrary quantum system quantitatively without exponential resources? The answer is yes! In 1982, Richard Feynman [83] proposed the concept of quantum simulators: “Let the computer itself be built of quantum mechanical elements which obey quantum mechanical laws.” Although we are still far away from large scale quantum simulations, research on the field is extremely active and numerous progresses have been achieved [265]. This part includes the discussion of quantum simulations as computationally cheap and reliable methods for nonadiabatic quantum dynamics. In chapter 5, we will present the background knowledge of quantum simulations. In chapter 6, we will present a simple but efficient scheme to protect the symmetry in quantum simulations. We will also show how this scheme works in lattice gauge theory (LGT) and hydrogen molecules. Specifically, quantum simulations of $U(1)$ LGT and hydrogen molecule with linear penalties have potential applications in atom-in-cavity models and nonadiabatic quantum dynamics under a novel framework [86, 87], respectively. Additionally, digital quantum simulations of hydrogen molecules with linear penalties can also be used in the quantum cooling algorithm [266] for electronic structure computing.

Chapter 5

Background on Quantum Simulators

Simulations are the mimics of real world systems by conducting experiments with model systems, which are approximations of real systems, on either silicon chips, or physical objects. As we stated in Chapter 2, models are approximations of real systems while retaining key characteristics. Strictly speaking, almost all of numerics on computers are simulations because all known physical laws are only valid in certain energy scales. When people talk about simulations, they overwhelmingly mean computer simulations because of the power of modern computers. However, there do exist simulations performed on physical objects when the problem is too complicated for computers. An explicit example is the usage of wind tunnels in aerodynamics. Navier–Stokes equations of fluid dynamics are hard for computers, therefore, wind tunnels are often used in aerodynamics. Similar to fluid dynamics, quantum dynamics is challenging for classical computers. As an alternative compute paradigm that is currently emerging, it has been proposed to use quantum devices to perform simulations for quantum systems [81–83]. Such quantum devices are so called quantum simulators (Qs). This type of processes is known as quantum simulation. There are two conceptually different Qs [84, 85] (and corresponding quantum simulations), digital Qs (DQs) and analog Qs (AQs). Several theoretical and experimental achievements of quantum simulations on chemistry have been made in recent years, for instance, analog [267] and digital [268, 269] quantum simulation of nonadiabatic dynamics, analog simulation of electronic structure [270], which will be discussed in the corresponding sections.

This chapter is organized as follows. DQs, which are closely related to quantum computers, will be covered in Sec. 5.1. We will also discuss successful quantum algorithms and their applications on chemistry in this section. In Sec. 5.2, we will discuss AQs.

5.1 Digital quantum simulator

The DQS is one specific application of circuit models of quantum computations. In the first subsection, we will briefly review the circuit models of quantum computations, and quantum algorithms. In the second subsection, we will discuss the implementations of digital quantum simulations. Quantum error correction (QEC) and fault-tolerant quantum computation will be reviewed in the third subsection. In the fourth subsection, we will discuss quantum error mitigation (QEM) and noisy intermediate-scale quantum era.

5.1.1 Basics of circuit models of quantum computations

There are some other models of quantum computations, for instance, quantum walk [271] and adiabatic quantum computing [272], however, for simplicity, quantum computations in this thesis are referred to as circuit models of quantum computations if not specified otherwise. Before discussing how quantum computers work, it is beneficial to review the functioning of classical computers. In classical computers, all algorithms are transferred to logical gate operations (AND gate, OR gate, NOT gate, etc.) on classical bits in a register, and outputs of algorithms are obtained by measurement results of classical bits. Similarly, in quantum computers, quantum algorithms are transferred to quantum logical gate operations on qubits in a quantum register, and outputs of algorithms are obtained by measurement results of qubits. Next, we will introduce these new concepts in detail [81].

A qubit is the quantum version of a classical bit. Unlike the classical bit characterized by two statuses 0 and 1, a qubit is a two-state quantum system

$$|\Psi\rangle = \alpha|0\rangle + \beta|1\rangle, \quad (5.1)$$

where α and β are arbitrary complex numbers. A quantum register comprises multiple qubits. Therefore, the Hilbert space of a quantum register grows exponentially with the number of qubits. Quantum logical gates are unitary transformations which act on quantum registers. In this sense, quantum computers are devices which obey quantum mechanics rigorously. That is the reason why DQSs can simulate quantum dynamics efficiently.

In the circuit diagram [273], a qubit is represented by a line, and quantum logic gates are represented by rectangles on the line. Here, we list several commonly used quantum gates and their notations in the circuit diagram.

Single qubit gates are unitary operations which only act on a single qubit. They do not generate quantum entanglement between different qubits. The Pauli gates (X,Y,Z) are three single qubit gates, and they are identical to the corresponding Pauli matrices,

$$\text{---} \boxed{X} \text{---}, \quad X = \begin{pmatrix} 0 & 1 \\ 1 & 0 \end{pmatrix}, \quad (5.2)$$

$$\text{---} \boxed{Y} \text{---} , \quad Y = \begin{pmatrix} 0 & -i \\ i & 0 \end{pmatrix}, \quad (5.3)$$

$$\text{---} \boxed{Z} \text{---} , \quad Z = \begin{pmatrix} 1 & 0 \\ 0 & -1 \end{pmatrix}. \quad (5.4)$$

Specifically, X gate is also called NOT gate since it flips a qubit. Therefore, it is a quantum version of classical NOT gate. One can also define the square root of the NOT gate,

$$\text{---} \boxed{\sqrt{\text{NOT}}} \text{---} , \quad \sqrt{\text{NOT}} = \frac{1}{2} \begin{pmatrix} 1+i & 1-i \\ 1-i & 1+i \end{pmatrix}. \quad (5.5)$$

It is not hard to verify that $(\sqrt{\text{NOT}})^2 = \text{NOT}$.

The phase shift gate is a family of single qubit gates, which adds an additional phase factor on state $|1\rangle$,

$$\text{---} \boxed{P(\varphi)} \text{---} , \quad P(\varphi) = \begin{pmatrix} 1 & 0 \\ 0 & e^{i\varphi} \end{pmatrix}. \quad (5.6)$$

There are several commonly used phase shift gates, $P(\pi) = Z$, $P(\frac{\pi}{2}) = S = \sqrt{Z}$, and $P(\frac{\pi}{4}) = T = \sqrt{S}$.

The rotation gates are defined as the rotation operators on a single qubit,

$$\text{---} \boxed{R_x(\theta)} \text{---} , \quad R_x(\theta) = \begin{pmatrix} \cos \frac{\theta}{2} & -i \sin \frac{\theta}{2} \\ -i \sin \frac{\theta}{2} & \cos \frac{\theta}{2} \end{pmatrix}, \quad (5.7)$$

$$\text{---} \boxed{R_y(\theta)} \text{---} , \quad R_y(\theta) = \begin{pmatrix} \cos \frac{\theta}{2} & -\sin \frac{\theta}{2} \\ \sin \frac{\theta}{2} & \cos \frac{\theta}{2} \end{pmatrix}, \quad (5.8)$$

$$\text{---} \boxed{R_z(\theta)} \text{---} , \quad R_z(\theta) = \begin{pmatrix} \exp(-i\frac{\theta}{2}) & 0 \\ 0 & \exp(i\frac{\theta}{2}) \end{pmatrix}. \quad (5.9)$$

Any arbitrary single qubit gate can be expressed as the product of three or less rotation gates.

The Hadamard gate maps z -polarized states $|0\rangle, |1\rangle$ to x -polarized states $\frac{1}{\sqrt{2}}(|0\rangle + |1\rangle)$ and $\frac{1}{\sqrt{2}}(|0\rangle - |1\rangle)$,

$$\text{---} \boxed{H} \text{---} , \quad H = \frac{1}{\sqrt{2}} \begin{pmatrix} 1 & 1 \\ 1 & -1 \end{pmatrix}. \quad (5.10)$$

Two-qubit gates act on two qubits, and thus can generate non-trivial quantum entanglement. One of the most used two-qubit gate is controlled- U gate,

$$\begin{array}{c} \text{---} \bullet \text{---} \\ | \\ \text{---} \boxed{U} \text{---} \end{array} , \quad CU = |0\rangle \langle 0| \otimes |1\rangle \langle 1| + |1\rangle \langle 1| \otimes U, \quad (5.11)$$

where the upper line represents the control qubit, and the lower line represents the target qubit. U gate acts on the target qubit gate if and only if the control qubit is $|1\rangle$. The CNOT and CZ gates are the most commonly used controlled U gates. In fact, CNOT (CX) gate and CZ gate have their own notations

$$\begin{array}{c} \bullet \\ \text{---} \\ | \\ \oplus \\ \text{---} \end{array}, \quad \text{CNOT} = \begin{pmatrix} 1 & 0 & 0 & 0 \\ 0 & 1 & 0 & 0 \\ 0 & 0 & 0 & 1 \\ 0 & 0 & 1 & 0 \end{pmatrix}, \quad (5.12)$$

$$\begin{array}{c} \bullet \\ \text{---} \\ | \\ \bullet \\ \text{---} \end{array}, \quad \text{CZ} = \begin{pmatrix} 1 & 0 & 0 & 0 \\ 0 & 1 & 0 & 0 \\ 0 & 0 & 1 & 0 \\ 0 & 0 & 0 & -1 \end{pmatrix}. \quad (5.13)$$

Notice that CZ gate does not have a unique target qubit due to the fact CZ gate only maps $|11\rangle$ to $-|11\rangle$ while other states remain unchanged, and is thus symmetric.

SWAP gate and $\sqrt{\text{SWAP}}$ gate are also commonly used two-qubit gates,

$$\begin{array}{c} \times \\ \text{---} \\ | \\ \times \\ \text{---} \end{array}, \quad \text{SWAP} = \begin{pmatrix} 1 & 0 & 0 & 0 \\ 0 & 0 & 1 & 0 \\ 0 & 1 & 0 & 0 \\ 0 & 0 & 0 & 0 \end{pmatrix}, \quad (5.14)$$

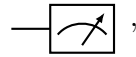
$$\begin{array}{c} \text{---} \\ \boxed{\sqrt{\text{SWAP}}} \\ \text{---} \end{array}, \quad \sqrt{\text{SWAP}} = \begin{pmatrix} 1 & 0 & 0 & 0 \\ 0 & \frac{1}{2}(1+i) & \frac{1}{2}(1-i) & 0 \\ 0 & \frac{1}{2}(1-i) & \frac{1}{2}(1+i) & 0 \\ 0 & 0 & 0 & 1 \end{pmatrix}, \quad (5.15)$$

and the relation $(\sqrt{\text{SWAP}})^2 = \text{SWAP}$ holds.

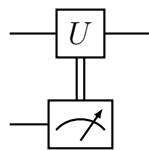
A key concept of quantum gates is the universal quantum gate set. An arbitrary unitary operator can be expressed by a set of universal quantum gates. Universal quantum gates are also useful in the initial state preparation procedure, as any initial states can be prepared by applying the gate operations to the state $|0\rangle^{\otimes n}$ with the help of universal quantum gates. One of a set of universal quantum gates is rotation gates R_x, R_y, R_z , phase shift gate $P(\varphi)$, and CNOT gate, which can be replaced by $\sqrt{\text{SWAP}}$ gate.

The readout of quantum algorithms is determined by quantum measurements. The measurement basis set is usually chosen as $\{|0\rangle, |1\rangle\}$. According to the Copenhagen interpretation, quantum measurement on qubits makes the wave function of the quantum register

collapse, and the outputs of measurement results are determined by Born's rule. Generally, one needs to run the circuit multiple times and obtain the probability distribution on measurement basis sets. In the circuit diagram, the measurement is represented by



where the line terminates at the end of measurement meaning the operation on the qubit ends after measuring. Indeed, one can also use the gate to operate the qubit after measuring. In this scenario, one just needs to add a line after measurement in the graph notations. Sometimes we need to operate other qubits according to the measurement output. It is a measurement version of controlled- U gate, and this can be represented by



This notation means that applying U gate to the upper qubit if the measurement output of lower is $|1\rangle$, otherwise do nothing. Here, the double-line between the measurement and the U gate represents the classical information, which is different from the single-line in the CU gate.

Already, we have introduced the basic concepts of quantum computations. To build up a quantum computer, one needs physical realizations of scalable qubits, to manipulate interactions between qubits to implement a set of universal quantum gates, to prepare simple initial states such as the product state $|0\rangle^{\otimes n}$, and measure the qubits. In practical situations, there always exists interactions between quantum computers and environments, which causes decoherence. Therefore, the decoherence times of quantum computers must be long enough to support finishing manipulations and measurements. These conditions are the so called DiVincenzo's criteria [274]. The most attractive experimental schemes of universal quantum computers to date are trapped ion quantum computers [275–277] and superconducting quantum computers [278,279], but there are also many other platforms, for instance, NMR [280], Rydberg array [281], quantum dots [282], photons [283], etc [284].

In the end of this subsection, we will briefly review the other important application of quantum computations: quantum algorithms. Heuristically speaking, gate operations on a quantum register can be regarded as parallelism computing because of the quantum superposition. Therefore, one could expect that quantum algorithms have the speedup over classical algorithms, in which quantum features, such as quantum entanglement and quantum superposition, play important roles. Another tremendous difference between quantum algorithms and classical algorithms is that most of quantum algorithms are probabilistic algorithms, because the outputs of quantum measurements are probability distributions. Here, we will list

several famous quantum algorithms [285]. One of the most commonly used quantum algorithm is quantum Fourier transform, which has an exponential speedup ($\mathcal{O}(N^2)$) compared with classical Fourier transformation ($\mathcal{O}(Ne^N)$), where N is the number of qubits. Lots of quantum algorithms are based on Quantum Fourier transform, for instance, quantum phase estimation algorithm [286] for estimating eigenvalues of a matrix, HHL algorithm for solving linear systems of equations [287], Shor's algorithm [288] for finding the prime factors of an integer. Specifically, there have been experimental realizations of the quantum phase estimation algorithm for electronic structure computations [289,290]. Another commonly used quantum algorithm is the Grover's algorithm [291] for searching unstructured databases, which only has a quadratic speedup (from $\mathcal{O}(N)$ to $\mathcal{O}(\sqrt{N})$), where N is the number of elements in the unstructured databases. Although it is not as efficient as quantum Fourier transform, we still gain a lot when N is huge.

5.1.2 Digital quantum simulation

Next, we will review how to use a quantum computer to perform digital quantum simulations. The resources of digital quantum simulation grows linearly with system size, rather than exponentially as in classical computers. Assume the system Hamiltonian and initial state are \hat{H}_{sys} and $|\Psi(0)\rangle_{\text{sys}}$, respectively. When the basis of the Hamiltonian \hat{H}_{sys} is finite, one can always map the system Hamiltonian \hat{H}_{sys} as well as the corresponding Hilbert space onto the Hamiltonian of a quantum register \hat{H} and its Hilbert space [84]. We denote the mapping initial wave state as $|\Psi(0)\rangle$. Then the time dependent state can be expressed as

$$|\Psi(t)\rangle = \hat{U}(t) |\Psi(0)\rangle = e^{-i\hat{H}t} |\Psi(0)\rangle, \quad (5.16)$$

where $\hat{U}(t) = e^{-i\hat{H}t}$ is the unitary time evolution operator. In principle, one can construct $\hat{U}(t)$ by a set of universal quantum gates. However, the construction can in general be highly non-trivial. Instead, researchers commonly use the Trotterization strategy to construct the unitary time evolution operator. Suppose the Hamiltonian can be expressed as

$$\hat{H} = \sum_{l=1}^M \hat{H}_l. \quad (5.17)$$

According to the Suzuki-Trotter formula, the evolution operator can be approximated as [292]

$$\hat{U}(t) = \hat{U}\left(\frac{t}{n}\right)^n \approx \left[\prod_l \hat{U}_l\left(\frac{t}{n}\right) \right]^n + \frac{t^2}{n} \sum_{l>m=1}^M [\hat{H}_l, \hat{H}_m], \quad (5.18)$$

where $\hat{U}_l\left(\frac{t}{n}\right) = e^{-i\hat{H}_l \frac{t}{n}}$, and n is the number of time slices. $\frac{t}{n}$ is also known as Trotter step size. There are two important ideas behind Eq. (5.18). First, each unitary operator $\hat{U}_l\left(\frac{t}{n}\right)$ can be constructed efficiently by a set of universal quantum gates, which requires that

the form of \hat{H}_l should be simple enough, for instance, the summations of few product of Pauli operators. Second, the unitary evolution operator $\hat{U}(\frac{t}{n})$ can be well approximated by $\prod_l \hat{U}_l(\frac{t}{n})$.

The error of the approximation Eq. (5.19) is given by

$$\hat{U}(t) - [\prod_l \hat{U}_l(\frac{t}{n})]^n = \frac{t^2}{n} \sum_{l>m=1}^M [\hat{H}_l, \hat{H}_m] + o(\frac{t^3}{n^2}). \quad (5.19)$$

The higher order decomposition can also be constructed, while it increases the number of gates in each time slices. Eq. (5.19) suggests that the bounded error requires that the number of total gates should grow quadratically with time $n \sim t^2$. Fortunately, it has been observed that $t \sim n$, i.e., fixed Trotter step size regardless how long evolution time, is sufficient to make error of local observables bounded for local Hamiltonians [293, 294]. The last step of digital quantum simulations is to measure observables of time dependent states. If the decoherence of DQs is weak enough, digital quantum simulations can give quantitative predictions for quantum dynamics with only linearly increasing qubit numbers with system sizes, which are much less than exponentially increasing bit numbers in classical algorithms. We also point out there is already a successful theoretical proposal for digital quantum simulations of nonadiabatic quantum dynamics [295].

5.1.3 Fault-tolerant quantum computation

In engineering, a system is fault-tolerant if it can still work properly when parts of the system have failures. In this subsection, we will briefly review error corrections in classical and quantum computers. We will also discuss the resources of errors in quantum computers [296, 297].

First, we will illustrate the idea of repetition code for error correction in classical computers. Suppose each bit has a probability $p \ll 1$ of flipping (an additional undesired NOT gate) in each gate operation. The simplest strategy to detect and correct this error is the repetition code, of which the key idea is employing redundancy. One can group three physical bits to one logical bit. The status 000 and 111 of physical bits represent status 0_L and 1_L , respectively. One can apply the same gate three times individually to all physical bits, and measure the statuses of them. The measurement output of logical bits are called syndrome, which tells us the possible error in logical bits. If all three bits have the same statuses, we think no errors has occurred in the gate operation. If one single bit has a different status, we think a flip error has happened on that bit, and apply a NOT gate on that bit to correct it. The above repetition code rules out all single bit-flip errors, and the probability of the error reduces from p to $3(1-p)p^2 + p^3 = 3p^2 - 2p^3$. It can be improved by further redundancy.

Next we will briefly review the origin of errors in quantum computers. Such errors can be classified into two categories, coherent errors and incoherent errors [296]. Coherent errors, which include all errors that make quantum gates deviate from a perfect implementation while keeping the dynamics of quantum registers still unitary, arise from the imperfect knowledge or control of Hamiltonians of quantum registers. In contrast, incoherent errors, which include all errors that make the evolution of quantum registers non-unitary, can be further classified into three subclasses, decoherence, loss, and leakage. Decoherence errors, which have been discussed in Sec. 5.1.1, are caused by the interaction between environments and quantum registers. Sometimes, some qubits in quantum registers could be intractable, i.e., we cannot manipulate or measure them, and such errors are called loss errors. Qubits are often implemented by two-level subspaces of particles, for instance, the Hilbert space of a superconducting qubit is spanned by the ground state and first excited state of an anharmonic oscillator. Errors such that particles escape from two-level subspaces are referred to as leakage errors. It has been shown that evolution of quantum registers with errors can be efficiently represented by quantum channels. Furthermore, most decoherence and coherent errors can be efficiently represented by applying additional X gates (bit-flip error) and Z (phase-flip error) gates stochastically after each gate operations [296], which can be efficiently corrected by quantum error correction (QEC) codes, for the details, see the following discussions. QECs for leakage and loss are much more complicated. The readers who are interested in details of these QECs can check Ref. [296].

Now we are in the position to discuss QEC. Similar to error correction in classical computers, QEC codes also use redundancy. Generally, $[[n, k, d]]$ QEC code represents that n physical qubits group to k logical qubits with a distance d between basis states. Here, the distance means the minimal number (larger than zero) of Pauli gate operations which makes logical qubit invariant; for an explicit example, see the following. The simplest QEC code is the $[[3, 1, 2]]$ code for bit-flip errors [296]. The logical states are encoded as

$$|0\rangle \rightarrow |0\rangle_L = |000\rangle, \quad |1\rangle \rightarrow |1\rangle_L = |111\rangle, \quad (5.20)$$

$$\alpha |0\rangle_L + \beta |1\rangle_L \rightarrow \alpha |000\rangle + \beta |111\rangle, \quad (5.21)$$

where $|0\rangle_L$ and $|1\rangle_L$ mean basis states of logical qubits. The distance of this code is 2 since the logical qubit is invariant under $Z_1 Z_2$, which contains two Z gates. Already, we see a huge difference between QEC code and classical repetition code, i.e., different physical qubits in one logical qubit must be manipulated non-individually. To be more explicit, Pauli \bar{X} and \bar{Z} gates for the logical qubit are

$$\bar{X} = X^{\otimes 3}, \quad \bar{Z} = Z^{\otimes 3}, \quad (5.22)$$

which are repetition operations of single qubit gates. However, the gate $\frac{1}{2}(Z + X)$ for the

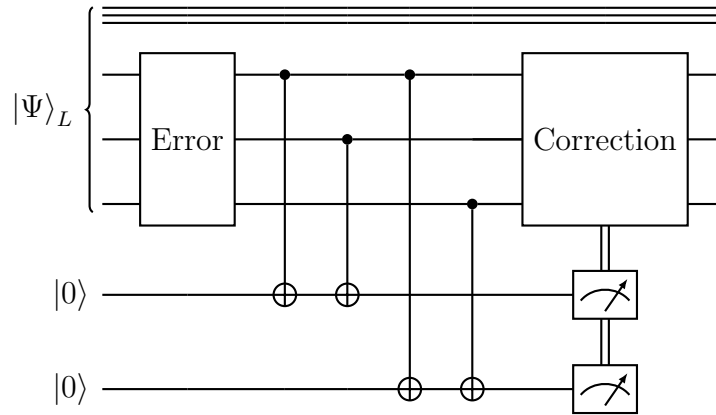


Figure 5.1. Circuit diagram of $[[3,1,2]]$ QEC code for detection and correction of single qubit error. The three-line bundle represents the other qubits in the quantum register, three physical qubits encode the logical qubit, and two additional ancilla qubits are introduced.

logical qubit is $\frac{1}{2}(\bar{Z} + \bar{X})$, which cannot be obtained by operating three physical qubits individually.

Another huge difference between classical repetition codes and QEC codes arises from the destructiveness of quantum measurements. For this reason, one has to use ancilla qubits to extract syndrome information. Figure (5.1) shows the circuit diagram for error detection and correction of the $[[3,1,2]]$ QEC code. The input state of the whole quantum register $|\Psi\rangle_L$ is prepared as

$$|\Psi\rangle_L = \alpha |q_0\rangle |000\rangle + \beta |q_1\rangle |111\rangle, \quad (5.23)$$

where $|q_0\rangle$ and $|q_1\rangle$ represent normalized vectors of other qubits in the quantum register. The final states before measurements and corresponding correct gates are listed in the Table.5.1. Ancilla qubits are always eigenstates of measurement basis, hence, quantum measurements on ancilla qubits do not cause destructiveness of quantum states. When there is only one single qubit error on the logical qubit, $[[3,1,2]]$ QEC code can recognize and correct all single bit-flip errors. However, it cannot correct phase-flip errors and multi-bit-flip errors. In an ideal device with no Z gate errors and low enough probability of X gate errors, $[[3,1,2]]$ QEC code can work efficiently.

More sophisticated QEC codes can be constructed by stabilizer codes with the knowledge of group theory, for instance, Shor's code [298], $[[5,1,3]]$ code [299], $[[7,1,3]]$ code [300], surface codes, etc. Fault-tolerant quantum computations can be implemented with the help of QEC codes and good enough devices. Specifically, small scale fault-tolerant quantum computations have been realized in experiments [301, 302], however, we are still far away from large scale fault-tolerant quantum computations for practical simulations.

Error gate	Final state, $ \text{Other}\rangle \text{Logical}\rangle \text{Ancilla}\rangle$	Correction gate
No error	$(\alpha q_0\rangle 000\rangle + \beta q_1\rangle 111\rangle) 00\rangle$	None
bit-flip error on qubit 1	$(\alpha q_0\rangle 100\rangle + \beta q_1\rangle 011\rangle) 11\rangle$	X gate on qubit 1
bit-flip error on qubit 2	$(\alpha q_0\rangle 010\rangle + \beta q_1\rangle 101\rangle) 10\rangle$	X gate on qubit 2
bit-flip error on qubit 3	$(\alpha q_0\rangle 001\rangle + \beta q_1\rangle 110\rangle) 01\rangle$	X gate on qubit 3
bit-flip error on qubit 1, 2	$(\alpha q_0\rangle 110\rangle + \beta q_1\rangle 001\rangle) 01\rangle$	X gate on qubit 3
bit-flip error on qubit 2, 3	$(\alpha q_0\rangle 011\rangle + \beta q_1\rangle 100\rangle) 11\rangle$	X gate on qubit 1
bit-flip error on qubit 1, 3	$(\alpha q_0\rangle 101\rangle + \beta q_1\rangle 010\rangle) 10\rangle$	X gate on qubit 2
three bit-flip errors	$(\alpha q_0\rangle 111\rangle + \beta q_1\rangle 000\rangle) 01\rangle$	None
one phase-flip error	$(\alpha q_0\rangle 000\rangle - \beta q_1\rangle 111\rangle) 00\rangle$	None
two phase-flip error	$(\alpha q_0\rangle 000\rangle + \beta q_1\rangle 111\rangle) 00\rangle$	None
three phase-flip error	$(\alpha q_0\rangle 000\rangle - \beta q_1\rangle 111\rangle) 00\rangle$	None

Table 5.1. Error gate, final state before measurements and correct gate circuit diagram of $[[3,1,2]]$ QEC code. Although the phase-flip errors cannot be corrected by the $[[3,1,2]]$ QEC code, it can still be efficient when bit-flip errors dominate.

5.1.4 Noisy intermediate-scale quantum era

In 2018, John Preskill coined a new word, NISQ [265], which stands for Noisy Intermediate Scale Quantum, for the current and impending quantum computation era. “Intermediate-scale” is referred to as the number of available qubits ranging from 50 to few hundreds, and “noisy” emphasizes that the control of each quantum qubit is imperfect. Most importantly, the error probabilities are not low enough to support fault-tolerant quantum computations. We stress that NISQ technologies also include AQSs, which will be presented in the next subsection.

We cannot expect that NISQ devices are suitable for standard quantum algorithms such as Quantum Fourier transformation and Grover’s search. Instead, lots of quantum algorithms for NISQ devices, which are called NISQ algorithms have been developed. One of the most successful NISQ algorithms is the Variational Quantum Eigensolver (VQE) algorithm [303, 304]. An explicit example is the UCC method for ground state calculations of molecules. For convenience, we consider a closed-shell molecule. As we discussed in Sec. 2.2.2, the UCC wave function ansatz is

$$|\Psi_0\rangle_{\text{UCC}} = \exp(\hat{T} - \hat{T}^\dagger) |\Psi_0\rangle_{\text{HF}}, \quad (5.24)$$

where \hat{T} is chosen as Eq. (2.84) with suitable truncations, and the Hartree–Fock wave function is given by Eq. (2.57). The eigenstates and eigenenergies are determined by the varia-

tional principle

$$\min_{\hat{T}} \langle \Psi_0 | H_{el} | \Psi_0 \rangle_{UCC} . \quad (5.25)$$

The VQE algorithm is a hybrid quantum-classical iteration algorithm. In each iteration, the UCC wave function is prepared in a quantum processor, and all the physical quantities which a classical optimizer requires are obtained by quantum measurements. The new parameters of the quantum state for next iteration are determined by a classical optimizer. The above procedure is repeated until the convergence is reached. As a comparison, wave function and energy in the ordinary CC are determined by projection CC ansatz wave function into ground and excited configurations due to the fact that the variational UCC method is hard to solve in classical computers. The above hybrid quantum-classical optimization approach is not limited in the VQE algorithm. When the similar procedure is applied into classical optimization problems, it is so called Quantum Approximate Optimization Algorithm (QAOA) [303, 304]. Other interesting applications of NISQ technologies include quantum annealing [305], quantum deep learning [306], quantum simulation [84], etc.

There are two important questions on NISQ technologies: 1. can we get quantum a speed up on NISQ devices? 2. Can we trust results based on NISQ devices? The answer of the first question is yes! In fact, many experiments have demonstrated that NISQ technologies can outperform state-of-the-art classical computers in certain problems [278, 279, 283]. The answer of the second question is very subtle. In principle, one cannot trust any results without error corrections. In practice, we do trust them in some certain cases [85, 284]. For instance, we only need good enough approximations of optimization problems, which means the deviation due to the noise in quantum devices for QAOA might be acceptable. The scenario for quantum simulations are more complicated. When the numerical simulations on classical computers are feasible, one can benchmark AQSs by classical computers. For the systems beyond classical computers, the way to justify the results of quantum simulations is to extract universal information, i.e., to run quantum simulations on different types of QSSs and find the common features.

Although QEC is not possible for NISQ processors, one can use quantum error mitigation (QEM) techniques to reduce the error effects. Similar to QEC codes, QEM techniques, which do not group several physical qubits into one logical qubit, are mainly developed for quantum computers and DQSs. Commonly used QEM techniques include zero-noise extrapolation [307, 308], randomization methods [307], subspace expansions [309, 310], and so on. In NISQ devices, minimal levels of noise are unavoidable, however, one can increase the strength of noise controllably. The idea of zero-noise extrapolation is performing simulations or algorithms with different noise strengths and doing extrapolation to obtain the results on zero-noise [307, 308]. In randomization methods [307], one represents the ideal circuit as a quasi-probabilistic mixture of noisy ones, and zero-noise results are obtained

by statistical average of noisy results. Subspace expansions is the most similar QEM technique to QEC codes. If the symmetries of the system are known, one can check whether the symmetries of quantum states are correct or not, and correct them if the symmetries are wrong [309].

5.2 Analog quantum simulator

Unlike DQSs employing discrete quantum gates, all operations in AQSs are implemented continuously. In analog quantum simulations, one needs to map the system Hamiltonian \hat{H}_{sys} into an experimentally realizable mapping Hamiltonian \hat{H} , and let the AQSs evolve under the Hamiltonian \hat{H} . Similar to digital quantum simulations, information about the evolution of observables under the dynamics generated by \hat{H}_{sys} can then be extracted by measurements on the constituents of the AQS. To establish the mapping, often suitable energy penalties need to be engineered in order to obtain a low-energy theory that controllably approximates \hat{H}_{sys} , see also the next chapter. The Hilbert space of \hat{H} can be infinite, for instance, one can use phonons and photons to simulate harmonic oscillators [84]. In fact, Feynman's initial proposal on quantum simulators is the AQS: "...there is to be an exact simulation, that the computer will do exactly the same as nature."

It seems that analog quantum simulations are more straightforward than digital quantum simulations. However, to find experimentally realizable mapping Hamiltonians is not trivial. Successful analog quantum simulations (experiments and theoretical proposals) include black hole simulations in photon and phonon systems [311], Dirac equation simulations in trapped ions systems [312], CoI simulations in trapped ions [313] and Rydberg atoms systems [314], electronic structure simulations in Rydberg atoms [270], lattice gauge dynamics in cold atoms [92], nonadiabatic quantum dynamics in trapped ions systems [267], and so on.

Several QEM techniques have been developed for AQSs [315], however, there are still no known QEC methods of analog quantum simulations currently. The lack of QEC methods suggests that we cannot fully trust AQSs even if the devices are sufficiently accurate. This is the major drawback of analog quantum simulations. The way to justify the results of analog quantum simulations is similar to NISQ technologies, i.e., we can only trust the universal information of analog quantum simulations, which has been discussed in the previous subsection.

To summarize, we briefly reviewed the basic concepts of quantum computers and QSs in this chapter. We also discussed quantum algorithms, QEC and QEM. Specifically, we briefly reviewed several successful quantum algorithms and quantum simulations for chemical systems, including VQE and quantum phase estimation for electronic structure compu-

tations, digital and analog quantum simulations for nonadiabatic quantum dynamics, and analog quantum simulation for electronic structure computations. In the next chapter, a specific QEM technique based on the quantum Zeno effect (QZE) and its application on lattice gauge theory and quantum chemistry will be presented.

Chapter 6

Symmetry protected quantum simulators for quantum dynamics

Penalty methods have been widely used in constrained optimization problems. Consider a Hamiltonian \hat{H} with a complete set of commuting observables \hat{K}_j ,

$$[\hat{H}_0, \hat{K}_j] = 0, \quad [\hat{K}_i, \hat{K}_j] = 0 \quad \text{for } i, j = 1, 2, \dots, r. \quad (6.1)$$

For convenience, we define the coefficients vector for penalties and symmetry sector as $\mathbf{c} = (c_1, c_2, \dots, c_r)^T$ and $\mathbf{K} = (K_1, K_2, \dots, K_r)^T$, respectively. We also define the projector on the symmetry sector \mathbf{K} as $\hat{P}_{\mathbf{K}}$, which will be used in the Sec. 6.1. In principle, one can choose arbitrary positive coefficients for quadratic penalty methods. The approximate ground state $\Phi(\theta)$ in the symmetry sector \mathbf{K}^* can be obtained by the variational method [316] with quadratic penalty

$$\min_{\theta} \langle \Phi(\theta) | [\hat{H}_0 + V \sum_j c_j (\hat{K}_j - K_j^*)^2] | \Phi(\theta) \rangle, \quad (6.2)$$

where Vc_j are strengths of penalties. It has been shown that the $|\Phi(\theta)\rangle$ approximately lies in the symmetry sector \mathbf{K}^* if Vc_j are strong enough. Quadratic penalty methods can also be applied in dynamical systems. Even small symmetry breaking terms can change the simulation results drastically due to the fact these terms drive the system out of the symmetry sectors. Therefore, symmetry protections are crucial for quantum simulations, which—being NISQ devices—will always be plagued by at least some level of errors, see Chapter 5. Supposing an additional symmetry-violation error Hamiltonian \hat{H}_1 is generated during the implementation of \hat{H}_0 in an AQS, such error can be suppressed with the help of quadratic penalties [88]

$$i\partial_t |\Psi\rangle = [\hat{H}_0 + \hat{H}_1 + V \sum_j c_j (\hat{K}_j - K_j^*)^2] |\Psi\rangle, \quad (6.3)$$

where the initial state $|\Psi(0)\rangle$ is prepared in the symmetry sector \mathbf{K}^* . Penalty methods can also be regarded as a QEM technique for AQSs, which will be discussed in the Sec. 6.1.

The major problem of quadratic penalty methods is that experimental implementation of quadratic penalty terms are generally challenging, as K_j^2 typically represents fine-tuned interaction terms. In this chapter, we will present an experimentally feasible linear penalty method, which is based on the quantum Zeno effect (QZE), for suppressing coherent quantum errors in both AQSs and DQSs [89]. This chapter is organized as follows. In Sec. 6.1, we will briefly review the mathematical formalism of QZE, and the related symmetry protection scheme. In Sec. 6.2, we will show how this scheme applies to LGTs. In Sec. 6.3, we will present the application of this scheme in Hydrogen molecule. Sec. 6.1 and 6.2 are based on the work ‘‘Gauge-symmetry protection using single-body terms’’, PRX Quantum 2 (4), 040311, and Sec. 6.3 is a part of the ongoing research project, digital quantum simulation of quench dynamics in molecular systems with linear penalties. (All figures and numerical results of Sec. 6.2 are made by collaborators Dr. Jad C. Halimeh and Julius Mildenerberger. The author only contributed to the theoretical and analytical aspects of this section.)

6.1 Protection scheme based on quantum Zeno effect

6.1.1 Continuous quantum Zeno effect

Quantum measurements can change the properties of quantum systems drastically. One example is the quantum Zeno effect (QZE) [317, 318], i.e., quantum systems can be frozen under certain measurements. Mathematically speaking, continuous measurement processes [97, 319] can be formulated as the time evolution under the Hamiltonian \hat{H}_V

$$\hat{H}_V = \hat{H} + V\hat{H}_{\text{meas}}, \quad (6.4)$$

where \hat{H} is the Hamiltonian of the system, and $V\hat{H}_{\text{meas}}$ is the coupling term between the apparatus and the system, and V is the coupling strength. Assuming that the spectral decomposition of \hat{H}_{meas} is

$$\hat{H}_{\text{meas}} = \sum_n E_n \hat{\Pi}_n, \quad (6.5)$$

where E_n is the eigenenergy and $\hat{\Pi}_n$ is the corresponding projector. For convenience, we assume the spectral gap of \hat{H}_{meas} is order $\mathcal{O}(1)$. When V is sufficiently large, the time evolution operator can be approximated as

$$e^{-it\hat{H}_V} \approx e^{-it(V\hat{H}_{\text{meas}} + \sum_n \hat{\Pi}_n \hat{H} \hat{\Pi}_n)} = \sum_n e^{-it(V E_n + \hat{\Pi}_n \hat{H} \hat{\Pi}_n)} \hat{\Pi}_n, \quad (6.6)$$

with a residual term $\mathcal{O}(\|\hat{H}\|^2 t/V)$. Therefore, such approximation is valid up to time scale $t \sim V/\|\hat{H}\|^2$. If we prepare an initial state $|\phi(0)\rangle$ in the eigensector m ,

$$\hat{\Pi}_m |\phi(0)\rangle = |\phi(0)\rangle, \quad (6.7)$$

Eq. (6.6) suggests that the time dependent state can be approximated as

$$|\phi(t)\rangle \approx e^{-it(\hat{\Pi}_m \hat{H} \hat{\Pi}_m + V E_m)} |\phi(0)\rangle . \quad (6.8)$$

Therefore, the system can be prevented from exploring undesired sectors $m' \neq m$ with the assistance of quantum measurements, which is the interpretation of QZE.

6.1.2 Linear penalty method for AQSs

The quadratic penalty method Eq. (6.3) can be interpreted in the framework of QZE. The quadratic penalty term $V \sum_j c_j (\hat{K}_j - K_j^*)^2$, and the summation of implementation Hamiltonian and error Hamiltonian $\hat{H}_0 + \hat{H}_1$ in Eq. (6.3) play the role of coupling term $V \hat{H}_{\text{meas}}$ and system Hamiltonian \hat{H} in Eq. (6.4, respectively. With the help of Eq. (6.6) and (6.8), the effective Hamiltonian in Eq. (6.3) can be expressed as

$$\hat{H}_{\text{eff}} = \hat{H}_0 + \hat{\Pi}_0 \hat{H}_1 \hat{\Pi}_0 , \quad (6.9)$$

where $\hat{\Pi}_0$ represents the projector on the eigenstate with zero eigenvalue of the quadratic penalty $V \sum_j c_j (\hat{K}_j - K_j^*)^2$, which is identical to the projector $\hat{P}_{\mathbf{K}^*}$. Such effective Hamiltonian commutes with all symmetries in the complete set of commuting observables,

$$[\hat{H}_{\text{eff}}, \hat{K}_j] = 0 , \quad j = 1, 2, \dots, n . \quad (6.10)$$

Therefore, the effective dynamics preserves the symmetry. Furthermore, when $\hat{\Pi}_0 \hat{H}_1 \hat{\Pi}_0 = 0$, the effective Hamiltonian is the exact Hamiltonian we want to implement.

The idea of linear penalty protection scheme is quite similar to the quadratic penalty method for dynamics. For an initial state which is in the symmetry sector \mathbf{K}^* , an additional linear penalty term $V \sum_j c_j (\hat{K}_j - K_j^*)$ is added in the Hamiltonian

$$i\partial_t |\Psi\rangle = [\hat{H}_0 + \hat{H}_1 + V \sum_j c_j (\hat{K}_j - K_j^*)] |\Psi\rangle , \quad (6.11)$$

where the interpretations of all operators and physical parameters in Eq. (6.11) are identical to Eq. (6.3). The effective Hamiltonian for Eq. (6.11) reads as Eq. (6.9), where the interpretation of $\hat{\Pi}_0$ is the projector on the eigenstate with zero eigenvalue of the linear penalty $V \sum_j c_j (\hat{K}_j - K_j^*)$. Notice that the major difference between the effective Hamiltonian for the linear penalty method and the quadratic penalty method is that the projector $\hat{\Pi}_0$ in the linear penalty method can contain projectors other than the desired symmetry sector, i.e., the relation $\hat{\Pi}_0 = \hat{P}_{\mathbf{K}^*}$ does not always hold.

There are two scenarios where linear penalty can promise symmetry protected dynamics up to a timescale $t \sim V/||\hat{H}||^2$, with a controlled violation of $\mathcal{O}(||\hat{H}||^2/V)$. In the first scenario, the eigenstate with zero eigenvalue of $V \sum_j c_j (\hat{K}_j - K_j^*)$ is non-degenerate, which

means the projector $\hat{\Pi}_0 = \hat{P}_{\mathbf{K}^*}$. Specifically, for a general \hat{H}_1 , the symmetries are protected when the c_j are sufficiently incommensurate, i.e.,

$$\mathbf{c}^T \cdot (\mathbf{K} - \mathbf{K}^*) = 0, \quad \text{iff } \mathbf{K} = \mathbf{K}^*. \quad (6.12)$$

This condition can be easily satisfied when c_j are random numbers or irrational numbers, or even fine-tuned integers.

In the second scenario, \hat{H}_1 cannot spilt up the degeneracy of $\hat{\Pi}_0$ in the first order perturbation theory. In this case, one has

$$\hat{\Pi}_0 \hat{H}_1 \hat{\Pi}_0 = \sum_{\substack{\mathbf{K} \in \{\mathbf{K} | \mathbf{c}^T \cdot \mathbf{K} = \mathbf{c}^T \cdot \mathbf{K}^*\} \\ \mathbf{K}' \in \{\mathbf{K}' | \mathbf{c}^T \cdot \mathbf{K}' = \mathbf{c}^T \cdot \mathbf{K}^*\}}} \hat{P}_{\mathbf{K}} \hat{H}_1 \hat{P}_{\mathbf{K}'} = \sum_{\mathbf{K} \in \{\mathbf{K} | \mathbf{c}^T \cdot \mathbf{K} = \mathbf{c}^T \cdot \mathbf{K}^*\}} \hat{P}_{\mathbf{K}} \hat{H}_1 \hat{P}_{\mathbf{K}}, \quad (6.13)$$

which is still different from $\hat{P}_{\mathbf{K}^*} \hat{H}_1 \hat{P}_{\mathbf{K}^*}$. However, such difference does not yield different effective dynamics for arbitrary initial states in the sector \mathbf{K}^* ,

$$\begin{aligned} |\Psi(t)\rangle &\approx e^{-i\hat{H}_{\text{eff}}t} |\Psi(0)\rangle = \exp\left(-i(\hat{H}_0 + \sum_{\mathbf{K} \in \{\mathbf{K} | \mathbf{c}^T \cdot \mathbf{K} = \mathbf{c}^T \cdot \mathbf{K}^*\}} \hat{P}_{\mathbf{K}} \hat{H}_1 \hat{P}_{\mathbf{K}})t\right) |\Psi(0)\rangle \\ &= e^{-i(\hat{H}_0 + \hat{P}_{\mathbf{K}^*} \hat{H}_1 \hat{P}_{\mathbf{K}^*})t} |\Psi(0)\rangle. \end{aligned} \quad (6.14)$$

Compared with the first scenario, the second scenario has its own advantages and disadvantages. Condition Eq. (6.13) suggests that the error information must be known. However, the sequences c_j based on the second scenario are usually much simpler than the first; for explicit examples, see the next section. When the error Hamiltonian \hat{H}_1 satisfies $\hat{P}_{\mathbf{K}^*} \hat{H}_1 \hat{P}_{\mathbf{K}^*} = 0$, both the first scheme and second scheme can yield the exact Hamiltonian \hat{H}_0 . Specifically, one can reduce the penalty terms with the help of the knowledge of \hat{H}_1 ; for an explicit example, see Sec. 6.3. For this reason, the linear penalty method can also be regarded as a QEM technique. We stress that the error suppression schemes of both traditional penalty methods and linear penalty methods only require $\|\hat{H}\| \ll \|\hat{H}_{\text{meas}}\|$ instead of $\|\hat{H}_1\| \ll \|\hat{H}_0\|$. In this sense, the continuous QZE is an example of strong perturbation theory. In fact, adding additional penalty terms can also be used in the implementation of Hamiltonians with specific symmetries in Qs [92, 320], in which case one could not expect $\|\hat{H}_1\| \ll \|\hat{H}_0\|$ holds generally.

The linear penalty protection scheme can be also used when the initial state is prepared as a superposition state of different symmetry sectors (for applications of the superposition initial states, see refs. [321–323].), and the total Hamiltonian reads as

$$\hat{H}_V = \hat{H}_0 + \hat{H}_1 + V \sum_j c_j \hat{K}_j, \quad (6.15)$$

where we ignore the constant energy shift term. The effective Hamiltonian must be written as

$$\hat{H}_{\text{eff}} = V \sum_j c_j \hat{K}_j + \hat{H}_0 + \sum_n \hat{\Pi}_n \hat{H}_1 \hat{\Pi}_n. \quad (6.16)$$

The extension of coefficients is straightforward. One only needs to let the conditions of c_j hold for all sectors rather than one specific sector \mathbf{K}^* , i.e., Eq. (6.12) and (6.13) become the followings respectively,

$$\forall \mathbf{K}, \mathbf{K}', \quad \mathbf{c}^T \cdot (\mathbf{K} - \mathbf{K}') = 0, \quad \text{iff} \quad \mathbf{K} = \mathbf{K}', \quad (6.17)$$

$$\forall n, \quad \hat{\Pi}_n \hat{H}_1 \hat{\Pi}_n = \sum_{\substack{\mathbf{K} \in \{\mathbf{K} | \mathbf{c}^T \cdot \mathbf{K} = E_n\} \\ \mathbf{K}' \in \{\mathbf{K}' | \mathbf{c}^T \cdot \mathbf{K}' = E_n\}}} \hat{P}_{\mathbf{K}} \hat{H}_1 \hat{P}_{\mathbf{K}'} = \sum_{\mathbf{K} \in \{\mathbf{K} | \mathbf{c}^T \cdot \mathbf{K} = E_n\}} \hat{P}_{\mathbf{K}} \hat{H}_1 \hat{P}_{\mathbf{K}}. \quad (6.18)$$

If either of the two conditions is satisfied, one can protect the symmetries of the system for any initial state.

6.1.3 Unitary kicks version of the quantum Zeno effect

Consider the implementation of Eq. (6.4) on a DQS. The approximated unitary evolution operator can be expressed as

$$\hat{U}_N(t) = [\hat{U}_{\text{kick}} \hat{U}(t/N)]^N, \quad (6.19)$$

where $\hat{U}(t/N)$ is the time evolution operator of the system Hamiltonian in one period

$$\hat{U}(t/N) = e^{-it(\hat{H}_0 + \hat{H}_1)/N}, \quad (6.20)$$

which is often further approximated as Trotterization, and \hat{U}_{kick} is the unitary evolution operator for coupling term

$$\hat{U}_{\text{kick}} = e^{-iVt\hat{H}_{\text{meas}}/N}. \quad (6.21)$$

In the $N \rightarrow \infty$ and finite V/N limit,

$$\hat{U}_N(t) \approx \exp\left(-it \sum_m (V\hat{\Pi}_m E_m + \hat{\Pi}_m \hat{H} \hat{\Pi}_m)\right), \quad (6.22)$$

which is known as the unitary kicks version of the QZE, and identical to the continuous QZE Eq. (6.6).

With the help of the unitary kicks version of QZE, one can directly apply both linear and quadratic penalty methods to DQSs without changes of penalty coefficients. In practical simulations, $\hat{U}(t/N)$ is approximated as Trotterization, and \hat{U}_{kick} can be expressed as

$$\hat{U}_{\text{kick}} = \prod_j e^{-itVc_j(\hat{K}_j - K_j^*)/N}, \quad (6.23)$$

for the linear penalty method, and

$$\hat{U}_{\text{kick}} = \prod_j e^{-itVc_j(\hat{K}_j - K_j^*)^2/N}, \quad (6.24)$$

for the quadratic penalty method. Similar to the applications of penalty methods in the AQSs, the implementation of linear penalties $e^{-itVc_j(\hat{K}_j - K_j^*)/N}$ is much simpler than quadratic penalties $e^{-itVc_j(\hat{K}_j - K_j^*)^2/N}$.

To summarize this section, we have established the rigorous theoretical formalism of penalty methods for QSs under the framework of the QZE. Compared with quadratic penalty methods, the major advantage of linear penalty methods is experimentally favorable, and the drawback is that penalty coefficients in linear penalty methods are complicated. With the knowledge of error Hamiltonian, such complications can be simplified drastically. We have also discussed the connections between penalty methods and QEM technique. In next two sections, we will represent numerical results of LGT and hydrogen molecule, respectively.

6.2 Application: lattice gauge theory

Gauge theories, which are the language of the standard model [324], are field theories with gauge invariance (invariance under local unitary transformations), which is accounted for by gauge fields. They also have important applications in condensed matter physics [325] and nuclear physics [326]. When the gauge fields are static, gauge theories are reduced to the particles in gauge vector potentials, which have been discussed in chapters 2 and 3. To perform computations on modern computers, gauge field theories are often discretized on lattices [327], which is known as lattice gauge theory (LGT). The local gauge invariance under the discretizations translates into an extensive number of symmetries of the system, and LGT is thus an excellent testbed for the linear penalty method. In this section, we will present the numerical benchmarks of the linear penalty method on $U(1)$ LGT.

6.2.1 Basics of $U(1)$ lattice gauge theory

The $U(1)$ gauge theory is the mathematical language of quantum electrodynamics (QED), which describes the matter–light interactions. Although in most cases on the chemistry energy scale, semiclassical electromagnetic fields are sufficient, there do exist certain circumstances that electromagnetic fields must be treated quantumly. Two explicit examples are 1. atom-in-cavity models [20–28] which have been discussed in chapters 2 and 3; 2. electronic structure computations for heavy elements with high atomic numbers [328].

Consider a $(1+1)d$ $U(1)$ LGT in the so-called quantum link model formulation [329],

$$H_0 = \sum_{j=1}^L \left[J(\sigma_j^- \tau_{j,j+1}^+ \sigma_{j+1}^- + \text{H.c.}) + \frac{\mu}{2} \sigma_j^z \right]. \quad (6.25)$$

Here, we drop the hats of operators for simplicity. The matter fields σ , which are hard core bosons, and gauge fields τ , which are non-compact electric fields, place on the sites

and links, respectively. Specifically, Pauli ladder operators σ_j^\pm ($\tau_{j,j+1}^\pm$) represent the creation/annihilation (gauge flipping) operators of the matter (gauge) fields at site j [link $(j, j+1)$], and σ_j^z ($\tau_{j,j+1}^z$) is a mass-density (electric-field) operator at site j [link $(j, j+1)$]. The matter–gauge coupling strength is given by J , the matter rest mass is μ , and the number of matter sites is L . All of our numerical results in this subsection use the periodic boundary conditions, and we checked that other boundary conditions do not change the conclusions. We stress that particle statistics of matter fields do not have an effect on our results for two reasons. First, bosons in Hamiltonian Eq. (6.25) can be straightforwardly transferred to fermions by a Jordan–Wigner transformation on the matter fields. Second, penalty methods Eq. (6.3) and (6.11) based on QZE are independent of the particle statistics.

There are two major conceptual differences between the present $U(1)$ LGT and atom-in-cavity models discussed in the second chapter. First, $U(1)$ LGT Eq. (6.25) is a relativistic theory with electron–positron production and annihilation, while atom-in-cavity models are non-relativistic. Second, the discretization of $U(1)$ LGT is in the real space while atom-in-cavity models are naturally discrete because of the bounds of cavities. Nonetheless, one could expect that the linear penalty method can be used in atom-in-cavity models if the LGT formalism is employed since both atom-in-cavity models and $U(1)$ LGT describe light–matter interactions. We also point out that gauge fields are dynamical variables in LGT, which has a huge difference from particles in gauge vector potentials discussed in Chapters 2 and 4.

Hamiltonian Eq. (6.25) is invariant under gauge transformations $e^{i\sum_j \alpha_j G_j}$, where G_j are local Gauss-law (local-symmetry) generators on site j ,

$$G_j = \frac{(-1)^j}{2} (\sigma_j^z + \tau_{j-1,j}^z + \tau_{j,j+1}^z + 1), \quad (6.26)$$

$$[G_j, H_0] = 0, \quad \forall j, \quad (6.27)$$

and α_j are arbitrary real numbers. All G_j commute with each other, $[G_j, G_l] = 0, \forall j, k$, hence $U(1)$ LGT is an Abelian gauge theory. Here, G_j plays the role of \hat{K}_j in Eq. (6.1). Meanwhile, we use $\mathbf{g} = (g_1, g_2, \dots, g_L)$ to label the gauge sectors, which is similar to \mathbf{K} to label symmetry sectors in previous discussions. The restriction $g_j = 0$ is a discretized and truncated version of the Gauss law $\nabla E = \rho$, where E is the electric field and ρ is the charge density. For a non-Abelian gauge theory, different local-gauge generators could not commute with each other. Strictly speaking, gauge symmetry is a rendering rather than a symmetry, because gauge symmetries are never spontaneously broken, and different gauge sectors are equivalent. However, in practical implementations of gauge symmetries in QSSs could unavoidably generate coherent gauge violation errors, except for implementations of Hamiltonians obtained by integrating out matter or gauge fields [93, 94]. We denote such errors as λH_1 , where $[H_1, G_j] \neq 0$, and λ controls the strengths of errors. Usually, H_1 is

dominated by unassisted matter coupling and gauge flipping [90–92]. Here, we model these undesired terms by

$$H_1 = \sum_j (\tau_{j,j+1}^x + \sigma_j^+ \sigma_{j+1}^+ + \sigma_j^- \sigma_{j+1}^-). \quad (6.28)$$

As we discussed in the beginning of this chapter, λH_1 are non-negligible even if they are small, due to the fact they drive the Qs out of gauge-invariant subspace. This $U(1)$ LGT model is an excellent platform to test linear penalty methods because of the following two reasons. First, all terms in Hamiltonians and symmetries are local, which makes it experimentally feasible. Second, extensive numbers (L) of symmetries makes the Hilbert space highly restricted, which suggests that good performance of linear penalty methods on $U(1)$ LGT model could be transferable to other systems.

6.2.2 Numerical results of AQs

We prepare the initial state as staggered gauge field and empty matter field state on a $L = 6$ lattice, which is in the gauge sector $\mathbf{g} = \mathbf{0}$ (also called “physical subspace”), for the explicit diagram, see Fig. (6.1). We use the following linear penalties to protect gauge symmetries

$$V H_G = V \sum_j c_j G_j, \quad (6.29)$$

where we set $\max_j |c_j| = 1$ to ensure that V is the typical energy scale of the protection term. Therefore, the total Hamiltonian is

$$H = H_0 + \lambda H_1 + V H_G. \quad (6.30)$$

Before discussing coefficients selections for linear penalty methods, we will first analyze the allowed gauge sectors of the Hamiltonian Eq. (6.25). Possible eigenvalues of the Gauss’s-law generators of the $U(1)$ LGT given in Eq. (6.26) are 2, 1, 0, -1 for every matter site j up to a factor of $(-1)^j$. However, physically allowed eigenvalue combinations are restricted. Up to a factor of $(-1)^j$, assuming matter site j with gauge-generator eigenvalue 2, the matter site j and field links $j - 1, j$ and $j, j + 1$ have to be spin up, which forbids the gauge-generator eigenvalue -1 for its two neighbors. Therefore, there are no “2, -1 ” or “ $-1, 2$ ” combinations up to a factor of $(-1)^j$ in any of the allowed gauge sectors.

With the knowledge of allowed gauge sectors information, we design the following four sequences for testing the performance of the linear penalty method. The first sequence is given by $\mathbf{c}^T = (-115, 116, -118, 122, -130, 146)/146$, which satisfies Eq. (6.12) and belongs to the first scenario of the linear penalty method. The second sequence is obtained by slightly modification of the first sequence, $\mathbf{c}^T = (-115, 116, -118, 122, -130, 145)/145$,

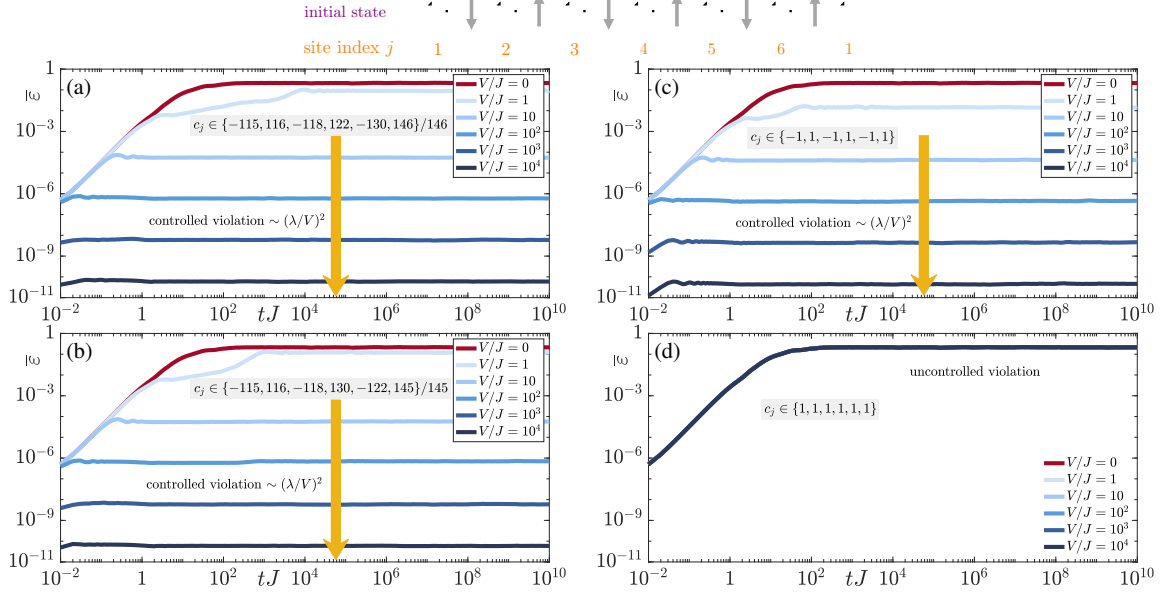


Figure 6.1. Time averaged gauge violation of H_0 at $\mu = 0.5J$, with the error $H_1 = \sum_j (\tau_{j,j+1}^x + \sigma_j^+ \sigma_{j+1}^+ + \sigma_j^- \sigma_{j+1}^-)$ at $\lambda = 0.05J$, under the linear penalty Eq. (6.29). The initial state is drawn on top, where the circle represents the sites are empty. As expected, sequences in (a), (b), and (c) can provide promising protection, keeping gauge-symmetry violations on a level $\sim (\lambda/V)^2$. Surprisingly, they work up to all the numerically accessible time. (d) A simple sequence completely fails to protect symmetries.

which satisfies Eq. (6.13) rather than Eq. (6.12) and belongs to the second scenario of the linear penalty method. The third sequence, $\mathbf{c}^T = (-1, 1, -1, 1, -1, 1)$, is experimentally favorable, and belongs to the second scenario. The fourth sequence is also experimentally favorable, $\mathbf{c}^T = (1, 1, 1, 1, 1, 1)$, however, it does not protect against gauge symmetry violations. The first three sequences satisfy the relation $\hat{\Pi}_0 H_1 \hat{\Pi}_0 = 0$, hence, we can expect that the effective dynamics of the faulty theory Eq. (6.30) is approximately identical to the ideal gauge theory H_0 . In Fig. (6.1), we present V/J scanning results of the time average gauge violations $\bar{\varepsilon}(t)$,

$$\varepsilon(t) = \frac{1}{L} \sum_{j=1}^L \langle \psi(t) | G_j^2 | \psi(t) \rangle, \quad (6.31)$$

$$\bar{\varepsilon}(t) = \int_0^t ds \varepsilon(s)/t, \quad (6.32)$$

for these four sequences with parameters $\lambda = 0.05J$ and $\mu = 0.5J$. All numerical results in this subsection are obtained by our own in-house exact diagonalization code (analog), which we have benchmarked with QuTiP [330, 331]. As we expect, first three sequences can protect the gauge symmetry but the fourth sequence cannot. Surprisingly, all first three sequences can protect the gauge symmetries up to the time scale $10^{10}/J$, which is much longer than prediction from the QZE $t \sim V/(JL)^2 \sim 300/J$ for $V/J = 10^4$.

We also investigate the protection performance of linear penalty method on local observables, such as the electric flux E and matter occupation n

$$E = \frac{1}{L} \sum_{j=1}^L (-1)^j \langle \psi(t) | \tau_{j,j+1}^z | \psi(t) \rangle, \quad (6.33)$$

$$n = \frac{1}{2} + \frac{1}{2L} \sum_{j=1}^L \langle \psi(t) | \sigma_j^z | \psi(t) \rangle. \quad (6.34)$$

The coefficients sequence is selected as the experimentally favorable $c_j = (-1)^j$. In Fig. (6.2), we present the comparison of time averaged local observables \bar{E} and \bar{n} between ideal-theory dynamics (dynamics under H_0) and linear penalty results. Results of the ideal theory and the linear penalty method coincide up to the time scale $\propto V/J^2$. Meanwhile, the insets suggest that the errors of local observables are suppressed as $1/V$ and grows linearly in time. These behaviors fit the prediction of the QZE in Sec. 6.1 perfectly. Thus, the penalty protection method not only restores the correct symmetry, but also the correct dynamics of local observables.

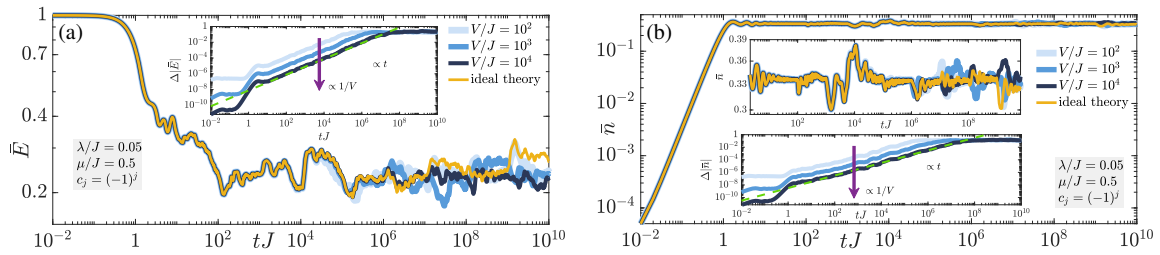


Figure 6.2. The dynamics of time averaged (a) electric field and (b) matter occupation of faulty gauge theory $H = H_0 + \lambda H_1 + V \sum_j (-1)^j G_j$ as well as the ideal gauge theory H_0 . As predicted by the QZE, linear penalty terms make the faulty dynamics coincide with the ideal dynamics up to a timescale $\propto 1/V$. Meanwhile, the differences between the ideal-theory and the faulty-theory dynamics are suppressed by V and grows linearly in time, which are shown in the insets.

6.2.3 Numerical results of DQSs

In this subsection, we will focus on the gauge violation dynamics of the linear penalty method on DQSs. the initial state is identical to the initial state in Sec. 6.2.2, and the sequence is selected as the first sequence $\mathbf{c}^T = (-115, 116, -118, 122, -130, 146)/146$. Similar to analog quantum simulations, we use an additional term $e^{-i\delta t \lambda H_1}$ in each Trotter step to mimic the errors in DQSs. The diagram representation of the implementation of digital quantum simulations in one Trotter step δt is implemented as $e^{-i\delta t H_J} e^{-i\delta t \lambda H_1} e^{-i\delta t V H_G} e^{-i\delta t H_m}$,

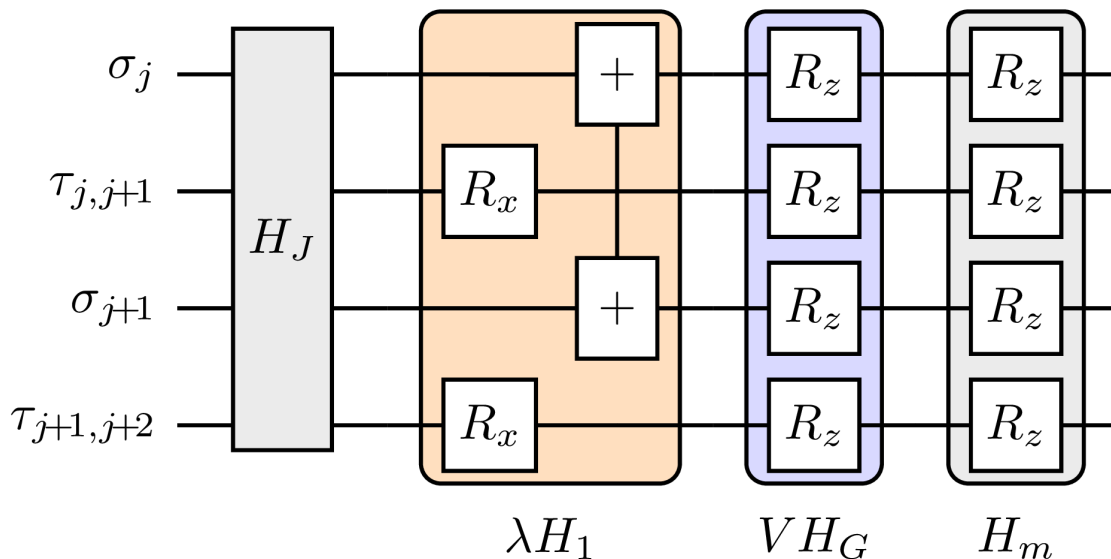


Figure 6.3. Elementary unit for one Trotter step of the quantum circuit. σ_j ($\tau_{j,j+1}$) denotes a qubit representing a matter (gauge) field at matter site j [gauge link $(j, j + 1)$]. The implementation of H_J can be obtained by Cirq [332]. R_x and R_z denote the x -rotation and z -rotation gates, respectively. The angles of them are determined by the Trotter step and Hamiltonian parameters. “+” denotes the unitary gate $\exp[-i(\sigma_j^+ \sigma_{j+1}^+ + \text{H.c.})\lambda\delta t]$ with Trotter time step δt .

and presented in Fig. (6.3), where we divide H_0 into two parts,

$$H_J = \sum_{j=1}^L J(\sigma_j^- \tau_{j,j+1}^+ \sigma_{j+1}^- + \text{H.c.}), \quad (6.35)$$

$$H_m = \sum_{j=1}^L \frac{\mu}{2} \sigma_j^z. \quad (6.36)$$

The gate decomposition of $e^{-iJ(\sigma_j^- \tau_{j,j+1}^+ \sigma_{j+1}^- + \text{H.c.})t}$, which is the component of the Trotterization of $e^{-iH_J \delta t}$, can be obtained by the software Cirq [332]. Both $e^{-iV H_G \delta t}$ and $e^{-iH_m \delta t}$ are the product of z -rotation gates, hence can be combined. The local gauge violation term $e^{-i\lambda H_1 \delta t}$ can be split into single qubit x -rotation gate $e^{-i\delta t \lambda \tau_j^x}$ and two qubit gate $e^{-i\delta t \lambda (\sigma_j^- \sigma_{j+1}^- + \sigma_j^+ \sigma_{j+1}^+)}$.

Fig. (6.4a) shows that time averaged gauge violations ε can be suppressed efficiently up to $t \sim 20/J$ by the linear penalty method. The parameters of Hamiltonian are identical to the parameters in the last subsection. In Fig. (6.4b), we present the final time $t_f = 20/J$ violation of digital quantum simulations for different Trotter steps and analog quantum simulations. It shows that the controlled-violation scales as λ/V^2 . Moreover, there is an optimal protection strength V_{ideal} . For the protection strength smaller than V_{ideal} but in the controlled-violation region, digital quantum simulation errors coincide with analog quantum simulation errors. While for the protection strength larger than V_{ideal} , the protection

becomes worse. The ideal protection strength is given by

$$V_{\text{ideal}} \approx \frac{\pi}{2\bar{c}\delta t} - \xi, \quad (6.37)$$

where $\bar{c} = \sum_j |c_j|/L$, and ξ is a non-universal constant determined by microscopic details of the model, and $\xi = 0.58J$ for the considered model. Intuitively, the first term of the universal relation Eq. (6.37) is z -rotation angle of the qubits on the Bloch sphere of the protection term. When the protection strength is larger than V_{ideal} , protection per Trotter step becomes weaker. The fitting results of Eq. (6.37) is presented in Fig. (6.4c). The universal behavior Eq. (6.37) is also confirmed in Fig. (6.4d), in which curves collapsing around V_{ideal} is observed by rescaling the time averaged violation $\bar{\varepsilon} \rightarrow \bar{\varepsilon}/(J\delta t)^2$, and the protection strength $V \rightarrow V\delta t$. Although the best protection needs experimental fine tuning, V with small deviations near V_{ideal} still gives reasonable protection, which suggests neither Trotter steps nor protection strength requires fine tuning.

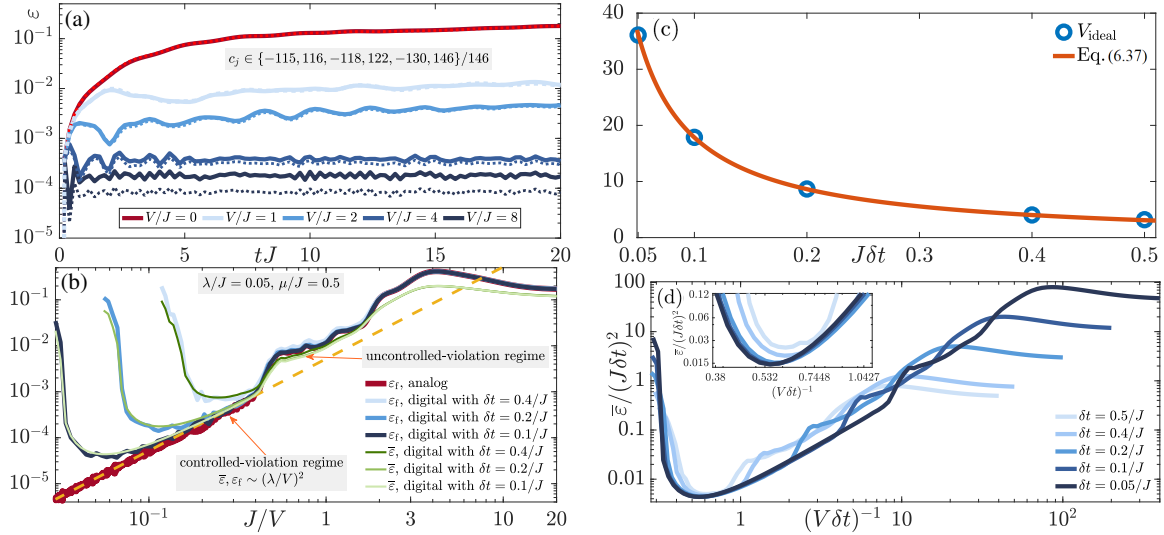


Figure 6.4. Numerical benchmarks of gauge violation dynamics in a DQS, at various values of gauge-protection strength V , with $\mu/J = 0.5$, $\lambda/J = 0.05$, and $L = 6$ matter sites. (a) Violation ε dynamics for a Trotter time step $\delta t = 0.2/J$ (solid lines), and the corresponding numerical data for the AQS are shown in dotted lines of the same color. (b) The gauge violation at final time $t_f = 20/J$ in the AQS and in the DQS for various Trotter time steps (see legend). The gauge violation reaches a broad minimum around the ideal protection strength of $V_{\text{ideal}} \approx \pi/(2\bar{c}\delta t) - \xi$, see Eq. (6.37). (c) Ideal protection strength V_{ideal} that provides the minimal time averaged gauge violation $\bar{\varepsilon}$. Blue diamonds are numerically extracted data points, and the red line is given by Eq. (6.37) with $\xi = 0.58J$. (d) Rescaled mean gauge violation depending on protection strength for various Trotter time steps δt . The results collapse around their minimum, which suggests a universal behavior.

To summarize this section, we tested the performance of linear penalty methods on the

$U(1)$ LGT. Promising protections can be reached in both AQSs and DQSs. As stated in Sec. 6.2.1, we could expect that such good performance would be transferable to other systems.

6.3 Application: Hydrogen molecule

The linear penalty method can also be applied to digital quantum simulations of quench dynamics with explicit electronic DOFs because a general electronic Hamiltonian always has a complete set of observables including the total spin, spin z -component, and total electron numbers, for the detailed discussion, see Sec. 2.2.1. Such quench dynamics have at least two potential applications 1. pure electronic quench dynamics, which can be used in quantum cooling algorithms [266] for electronic structure computing; 2. nonadiabatic quantum dynamics with unified treatments of nuclear and electronic DOFs, which is a novel framework [86, 86] established recently.

In this section, we will present the quench dynamics of a hydrogen molecule in the minimal basis with imperfect implementation errors and linear penalties on DQSs as a prototype. The second quantization representation of hydrogen molecule Hamiltonian in the minimal basis [310, 333–335] is

$$\begin{aligned}
 H = & h_{11}(a_1^\dagger a_1 + a_2^\dagger a_2) + h_{33}(a_3^\dagger a_3 + a_4^\dagger a_4) + g_{1212}a_1^\dagger a_2^\dagger a_2 a_1 + g_{3434}a_3^\dagger a_4^\dagger a_4 a_3 \\
 & + g_{1313}(a_1^\dagger a_4^\dagger a_4 a_1 + a_2^\dagger a_3^\dagger a_3 a_2) + (g_{1313} - g_{1331})(a_1^\dagger a_3^\dagger a_3 a_1 + a_2^\dagger a_4^\dagger a_4 a_2) \\
 & + g_{1331}(a_1^\dagger a_4^\dagger a_2 a_3 + a_3^\dagger a_2^\dagger a_4 a_1 + a_1^\dagger a_2^\dagger a_4 a_3 + a_3^\dagger a_4^\dagger a_2 a_1).
 \end{aligned} \tag{6.38}$$

Here, we use the notation of the second quantization form of a general molecule Hamiltonian Eq. (2.39), and merge terms having different coefficient parameter notations but same parameter values. a_1 , a_2 , a_3 , and a_4 are annihilation operators of Hartree–Fock orbitals $|\varphi_g\rangle|\uparrow\rangle$, $|\varphi_g\rangle|\downarrow\rangle$, $|\varphi_u\rangle|\uparrow\rangle$, and $|\varphi_u\rangle|\downarrow\rangle$. The definition of parameters are Eq. (2.40) and (2.41), and their values are $h_{11} = -1.252477$, $h_{33} = -0.475934$, $g_{1212} = 0.674493$, $g_{3434} = 0.697397$, $g_{1313} = 0.663472$, and $g_{1331} = 0.181287$ in atomic units. A complete set of observables of general molecule Hamiltonian includes the total spin, spin z -component, and total electron numbers, for the detailed discussion, see Sec. 2.2.1. We prepare the initial state as the Hartree–Fock ground state $|1100\rangle_f$ in the fermionic basis, then let it evolve under Hamiltonian H . In fact, the exact time dependent wave function can be solved analytically due to the symmetry of Eq. (6.38),

$$|\Psi(t)\rangle_{\text{ex}} = \cos(g_{1331}t) |1100\rangle_f - i \sin(g_{1331}t) |0011\rangle_f. \tag{6.39}$$

In order to perform quantum simulations of fermionic Hamiltonian Eq. (6.38) in DQSs,

one needs the Jordan–Wigner transformation to map it onto the qubit Hamiltonian,

$$a_j = \frac{1}{2}(X_j + iY_j) \prod_{k=j+1}^4 \otimes Z_k, \quad (6.40)$$

$$a_j^\dagger = \frac{1}{2}(X_j - iY_j) \prod_{k=j+1}^4 \otimes Z_k,$$

where X , Y , and Z are Pauli gates, and the upper limit of product can be replaced by the number of qubits for a general fermionic Hamiltonian. With the help of Eq. (6.40), the qubit Hamiltonian of the hydrogen molecule can be expressed as,

$$H = H^{(0)} + H^{(1)} + H^{(2)} + H^{(3)}, \quad (6.41)$$

$$H^{(0)} = h_{11} + h_{33} + \frac{g_{1212} + g_{3434}}{4} + \frac{2g_{1313} - g_{1331}}{2}, \quad (6.42)$$

$$H^{(1)} = \left(\frac{h_{11}}{2} + \frac{g_{1212} + 2g_{1313} - g_{1331}}{4} \right) (Z_1 + Z_2) \quad (6.43)$$

$$+ \left(\frac{h_{33}}{2} + \frac{g_{3434} + 2g_{1313} - g_{1331}}{4} \right) (Z_3 + Z_4),$$

$$H^{(2)} = \frac{g_{1313}}{4} (Z_1 Z_4 + Z_2 Z_3) + \frac{g_{1313} - g_{1331}}{4} (Z_1 Z_3 + Z_2 Z_4) + \frac{g_{1212}}{4} Z_1 Z_2 + \frac{g_{3434}}{4} Z_3 Z_4, \quad (6.44)$$

$$H^{(3)} = \frac{g_{1331}}{4} (X_1 Y_2 Y_3 X_4 + Y_1 X_2 X_3 Y_4 - X_1 X_2 Y_3 Y_4 - Y_1 Y_2 X_3 X_4). \quad (6.45)$$

In each Trotter step, $e^{-i\delta t H}$ can be approximated as $e^{-i\delta t H^{(0)}} e^{-i\delta t H^{(1)}} e^{-i\delta t H^{(2)}} e^{-i\delta t H^{(3)}}$. The first term $e^{-i\delta t H^{(0)}}$ is a global phase shift, and the second term $e^{-i\delta t H^{(1)}}$ can be implemented as z -rotation gates. Implementations of the third $e^{-i\delta t H^{(2)}}$ and the fourth term $e^{-i\delta t H^{(3)}}$ can be obtained by Cirq [332]. The Trotter step in this section is selected as $\delta t = 0.1$ a.u. in this subsection. The initial state is also transferred to $|0011\rangle_q$ in the qubit basis.

Similar to previous section, we model the coherent error as additional quantum gates $e^{-i\delta t \lambda H_1}$ in each Trotter step, where

$$H_1 = X_1 + X_2 + X_3 + X_4, \quad (6.46)$$

and such additional quantum gates can be implemented via x -rotation gates. We set $\lambda = 0.1$ a.u. in this subsection. The linear penalty $e^{-i\delta t V H_N}$ with only particle number symmetry

$$H_N = Z_1 + Z_2 + Z_3 + Z_4, \quad (6.47)$$

is sufficient to suppress this specific error. Similar to the protection in previous subsection, $e^{-i\delta t V H_N}$ are the product of z -rotation gates, hence can be combined with $e^{-i\delta t H^{(1)}}$ in practical simulations. Therefore, $e^{-i\delta t H^{(0)}} e^{-i\delta t H^{(1)}} e^{-i\delta t V H_N} e^{-i\delta t H^{(2)}} e^{-i\delta t H^{(3)}} e^{-i\delta t \lambda H_1}$ is the overall implementation in each Trotter step.

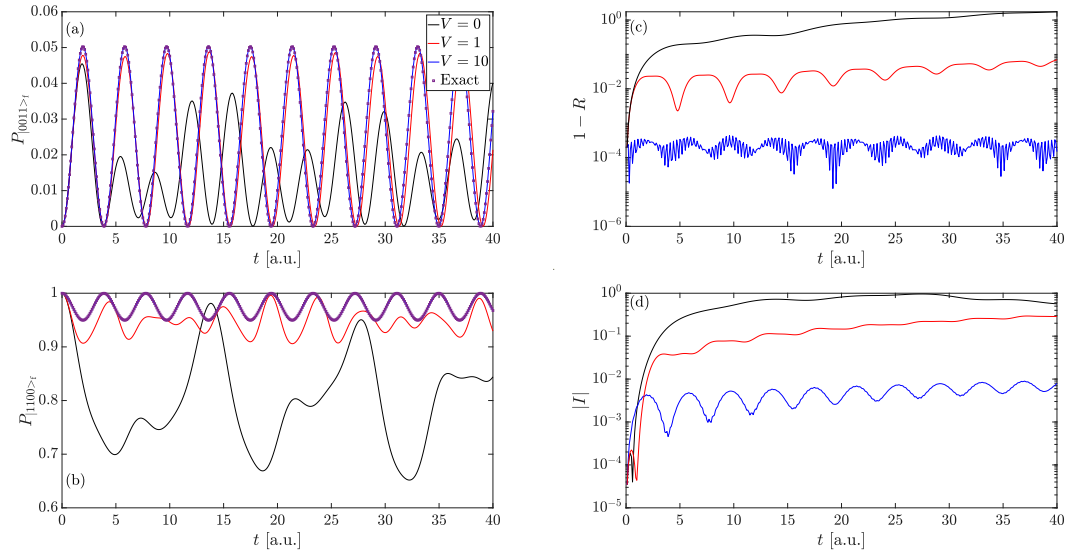


Figure 6.5. Quench dynamics of population and overlap of a hydrogen molecule in the minimal basis for various protection strength (See legends of (a)). (a) Population of state $|0011\rangle_f$ for various protection strength. While the dynamics of zero protection (black solid) is qualitatively wrong, a moderate protection strength $V = 1$ can already yield qualitatively correct dynamics, and it is almost indistinguishable for the results of $V = 10$ (blue solid) and the exact results (purple square). (b) Similar to (a), but for the state $|1100\rangle_f$. (c,d) Dynamics of the real and imaginary part of the overlap, respectively. $1 - R \sim 10^{-4}$, and $|I| \sim 10^{-3}$ for protection strength $V = 10$ suggests a promising protection on the wave function.

In Fig. (6.5), we present the population of states $|0011\rangle_q$ ($|1100\rangle_{fm}$) and $|1100\rangle_q$ ($|0011\rangle_{fm}$), as well as the overlap between the exact wave function and the wave function on a DQS, ${}_{\text{DQS}}\langle\Psi(t)|\Psi(t)\rangle_{\text{ex}} = R + iI$, where R and I are the real part and imaginary part of the overlap respectively, for various protection strengths up to 40 a.u. (near 1 fs). As we see, $V = 10$ a.u. provides quite promising protections not only for observables, but also for the wave function itself.

6.4 Conclusion

Dynamics of molecules are often overwhelmingly determined by quantum effects, which is extremely challenging for classical computers. One of the potential techniques to overcome this difficulty is the quantum computer. However, we will be in the NISQ era for quite a long time, and the reliability of quantum simulation results on near-term NISQ devices are subtle. In this chapter, we have proposed a novel linear penalty method, which can be regarded as a QEM technique for coherent errors, for symmetry protections in both analog and digital quantum simulations under the framework of the QZE. Compared with traditional

quadratic penalty methods, the new method is more experimentally feasible. The method can even remove the errors completely (in the sense of effective Hamiltonian) for specific errors. Our numerical results on $U(1)$ LGT and hydrogen molecule in the minimal basis show that the novel linear penalty method can provide extremely promising protections for both observables and wave functions. Our method can improve the reliability of general quantum simulations beyond the systems considered in this chapter, for instance, $U(1)$ LGT in the thermodynamic limit [336], and non-Abelian $U(2)$ LGT [337], in near-term NISQ devices. We believe it will be widely used in future quantum simulations.

Chapter 7

Conclusions and Outlook

In this thesis, we investigated two possible routines of computing quantum dynamics of systems with large DOFs, linearized phase space methods and quantum simulations. Both methods can overcome the difficulty of exponentially increasing computational efforts. However, they also have their own limitations. Linearized phase space methods are qualitatively correct when quantum coherence and interference of systems are negligible. Therefore, the knowledge of the reliability of linearized phase space methods are often obtained by numerical benchmarks on typical model systems. Quantum simulations mainly suffer from the imperfect controls of quantum devices, which might cause fatal errors to make simulations unreliable. For both methods, we presented rigorous theoretical analysis for their accuracy and reliability. Specifically, we established a rigorous measure for short-time accuracy of linearized phase space methods, intra-electron correlation, which is based on the initial sampling and the force expression. We also rigorously proved that the linear penalty terms can protect the dynamics of quantum simulators. Moreover, we introduced a well-known linearized phase space method for quantum lattice models, GDTWA, to chemical systems. Also, we developed two gGDTWA methods, approach I and approach II, for particles in gauge vector potentials, which have close connections to LVC models and on-the-fly simulations.

To establish the intra-electron correlation, we first rewrote fully and partially linearized methods as a unified expression with the same forms of EOMs and observables evaluations. Different methods are characterized by the numbers of mapping variables, initial sampling functions, and force expressions. With the help of such unified expression, we performed the Taylor expansion for the difference of expectations of observables between exact quantum results and mapping approaches results, and the intra-electron correlation is defined by matching the third order derivatives. Therefore, methods with correct intra-electron correlations have higher short-time accuracy than methods with a wrong one for general Hamiltonians and observables. For chemical motivated models with specific form

of Hamiltonians, the short-time accuracy of populations can be improved. We found that the correct short-time accuracy can yield higher short-time accuracy except for scattering models. We also classified popular mapping approaches into three classes, correct intra-electron correlation sampling, wrong intra-electron correlation sampling, and correct intra-electron sampling only for 2-level systems. For each method we considered, either a proof or an explicit violation example was reported. Our theoretical analysis gave the explanations of short-time accuracy order reported in previous references. Moreover, correct intra-electron correlation can also be a guideline for possible future mapping approaches.

GDTWA was introduced to chemical systems with detailed theoretical and numerical analysis. We reformulate GDTWA to the unified expression of mapping approaches. The number of mapping variables of GDTWA is identical to partially linearized methods, however, the initial sampling is more similar to fully linearized methods. In this sense, GDTWA is a fully-partially hybrid linearized method. GDTWA can sample the intra-electron correlation correctly for initial diagonal states. Our theoretical analysis also shows that the discrete initial sampling of GDTWA can account for a reduced ZPE but without an explicit ZPE parameter. Numerical benchmarks on Tully's models and LVC models suggests that GDTWA has a competitive accuracy with state-of-the-art phase space methods. Then, we further developed two gGDTWA for particles in gauge vector potentials. The approach I, using canonical momentum, is more similar to GDTWA, and more suitable for synthetic gauge field systems. The approach II, using kinematic momentum, is more similar to mapping approaches in adiabatic representation, and more suitable for on-the-fly simulations. Numerical benchmarks on ultracold atoms, LVC models as a synthetic gauge field theory, and on-the-fly simulations of LVC models confirm our analysis. We believe that GDTWA as well as gGDTWA are good candidates for large size systems simulations.

We also discussed another attractive route for this aim, quantum simulations. However, errors in NISQ devices may cause serious mistakes on simulation results, especially for the scenario that errors violate the symmetry of the system. We developed a linear penalty method based on the quantum Zeno effect to protect the dynamics of symmetries. Compared with traditional quadratic penalty methods, the linear penalty method is more experimentally feasible. For the physical errors with simple enough forms, the linear penalty can even protect the dynamics. Numerical results of lattice gauge theory shows that the linear penalty method can protect symmetries as well as local observables efficiently for extensive symmetries restrictions. Numerical results of the hydrogen molecule shows that the linear penalty method can also protect the wave function. Our proposals have already been implemented in experiments.

We hope our works can inspire future investigations on quantum dynamics of systems with large DOF. Interesting questions for the future are 1. A rigorous measure of linearized

phase space methods for the accuracy of spectroscopy simulations; 2. A partially linearized version of GDTWA; 3. Linear penalty methods for VQE and TDVP; 4. QEC for analog simulations, etc.

Bibliography

- [1] Lorenz S Cederbaum. Born–oppenheimer approximation and beyond for time-dependent electronic processes. *The Journal of chemical physics*, 128(12):124101, 2008.
- [2] Wolfgang Domcke, David Yarkony, and Horst Köppel. *Conical intersections: electronic structure, dynamics & spectroscopy*, volume 15. World Scientific, 2004.
- [3] RK Nesbet. Configuration interaction in orbital theories. *Proceedings of the Royal Society of London. Series A. Mathematical and Physical Sciences*, 230(1182):312–321, 1955.
- [4] Rodney J Bartlett and Monika Musiał. Coupled-cluster theory in quantum chemistry. *Reviews of Modern Physics*, 79(1):291, 2007.
- [5] Garnet Kin-Lic Chan and Sandeep Sharma. The density matrix renormalization group in quantum chemistry. *Annual review of physical chemistry*, 62(1):465–481, 2011.
- [6] Steven R White. Density matrix formulation for quantum renormalization groups. *Physical review letters*, 69(19):2863, 1992.
- [7] Steven R White. Density-matrix algorithms for quantum renormalization groups. *Physical review b*, 48(14):10345, 1993.
- [8] David Perez-Garcia, Frank Verstraete, Michael M Wolf, and J Ignacio Cirac. Matrix product state representations. *arXiv preprint quant-ph/0608197*, 2006.
- [9] Sebastian Keller, Michele Dolfi, Matthias Troyer, and Markus Reiher. An efficient matrix product operator representation of the quantum chemical hamiltonian. *The Journal of chemical physics*, 143(24):244118, 2015.
- [10] Brian M Austin, Dmitry Yu Zubarev, and William A Lester Jr. Quantum monte carlo and related approaches. *Chemical reviews*, 112(1):263–288, 2012.
- [11] Peter J Reynolds, David M Ceperley, Berni J Alder, and William A Lester Jr. Fixed-node quantum monte carlo for molecules a) b). *The Journal of Chemical Physics*, 77(11):5593–5603, 1982.

- [12] Aron J Cohen, Paula Mori-Sánchez, and Weitao Yang. Challenges for density functional theory. *Chemical reviews*, 112(1):289–320, 2012.
- [13] Walter Kohn. Density functional theory. *Introductory Quantum Mechanics with MATLAB: For Atoms, Molecules, Clusters, and Nanocrystals*, 2019.
- [14] Miquel Huix-Rotllant, Nicolas Ferré, and Mario Barbatti. Time-dependent density functional theory. *Quantum Chemistry and Dynamics of Excited States: Methods and Applications*, pages 13–46, 2020.
- [15] Kieron Burke, Jan Werschnik, and EKV Gross. Time-dependent density functional theory: Past, present, and future. *The Journal of chemical physics*, 123(6):062206, 2005.
- [16] Lachlan P Lindoy, Benedikt Kloss, and David R Reichman. Time evolution of ml-mctdh wavefunctions. i. gauge conditions, basis functions, and singularities. *The Journal of Chemical Physics*, 155(17):174108, 2021.
- [17] Mino Yang and Graham R Fleming. Influence of phonons on exciton transfer dynamics: comparison of the redfield, förster, and modified redfield equations. *Chemical physics*, 282(1):163–180, 2002.
- [18] Akihito Ishizaki and Graham R Fleming. Theoretical examination of quantum coherence in a photosynthetic system at physiological temperature. *Proceedings of the National Academy of Sciences*, 106(41):17255–17260, 2009.
- [19] Kaijun Yuan, Richard N Dixon, and Xueming Yang. Photochemistry of the water molecule: adiabatic versus nonadiabatic dynamics. *Accounts of Chemical Research*, 44(5):369–378, 2011.
- [20] Johannes Flick, Michael Ruggenthaler, Heiko Appel, and Angel Rubio. Atoms and molecules in cavities, from weak to strong coupling in quantum-electrodynamics (qed) chemistry. *Proceedings of the National Academy of Sciences*, 114(12):3026–3034, 2017.
- [21] V Bužek, G Drobný, Min Gyu Kim, M Havukainen, and PL Knight. Numerical simulations of atomic decay in cavities and material media. *Physical Review A*, 60(1):582, 1999.
- [22] Q Su and JH Eberly. Model atom for multiphoton physics. *Physical Review A*, 44(9):5997, 1991.
- [23] Michael Ruggenthaler, Nicolas Tancogne-Dejean, Johannes Flick, Heiko Appel, and Angel Rubio. From a quantum-electrodynamical light-matter description to novel spectroscopies. *Nature Reviews Chemistry*, 2(3):1–16, 2018.

- [24] Ilya V Tokatly. Time-dependent density functional theory for many-electron systems interacting with cavity photons. *Physical review letters*, 110(23):233001, 2013.
- [25] Norah M Hoffmann, Christian Schäfer, Niko Säkkinen, Angel Rubio, Heiko Appel, and Aaron Kelly. Benchmarking semiclassical and perturbative methods for real-time simulations of cavity-bound emission and interference. *The Journal of Chemical Physics*, 151(24):244113, 2019.
- [26] Johannes Flick, Michael Ruggenthaler, Heiko Appel, and Angel Rubio. Kohn–sham approach to quantum electrodynamical density-functional theory: Exact time-dependent effective potentials in real space. *Proceedings of the National Academy of Sciences*, 112(50):15285–15290, 2015.
- [27] Maximilian AC Saller, Aaron Kelly, and Eitan Geva. Benchmarking quasiclassical mapping hamiltonian methods for simulating cavity-modified molecular dynamics. *The Journal of Physical Chemistry Letters*, 12(12):3163–3170, 2021.
- [28] Norah M Hoffmann, Christian Schäfer, Angel Rubio, Aaron Kelly, and Heiko Appel. Capturing vacuum fluctuations and photon correlations in cavity quantum electrodynamics with multitrajjectory ehrenfest dynamics. *Physical Review A*, 99(6):063819, 2019.
- [29] Tian-Shu Chu, Yan Zhang, and Ke-Li Han. The time-dependent quantum wave packet approach to the electronically nonadiabatic processes in chemical reactions. *International Reviews in Physical Chemistry*, 25(1-2):201–235, 2006.
- [30] Ahmed H Zewail. Femtochemistry. *The Journal of Physical Chemistry*, 97(48):12427–12446, 1993.
- [31] Basile FE Curchod and Todd J Martínez. Ab initio nonadiabatic quantum molecular dynamics. *Chemical reviews*, 118(7):3305–3336, 2018.
- [32] Rachel Crespo-Otero and Mario Barbatti. Recent advances and perspectives on nonadiabatic mixed quantum–classical dynamics. *Chemical reviews*, 118(15):7026–7068, 2018.
- [33] Michael H Beck, Andreas Jäckle, Graham A Worth, and H-D Meyer. The multiconfiguration time-dependent hartree (mctdh) method: a highly efficient algorithm for propagating wavepackets. *Physics reports*, 324(1):1–105, 2000.
- [34] H-D Meyer, Uwe Manthe, and Lorenz S Cederbaum. The multi-configurational time-dependent hartree approach. *Chemical Physics Letters*, 165(1):73–78, 1990.
- [35] Hans-Dieter Meyer, Fabien Gatti, and Graham A Worth. *Multidimensional quantum dynamics: MCTDH theory and applications*. John Wiley & Sons, 2009.

- [36] Haobin Wang and Michael Thoss. Multilayer formulation of the multiconfiguration time-dependent hartree theory. *The Journal of chemical physics*, 119(3):1289–1299, 2003.
- [37] Uwe Manthe. A multilayer multiconfigurational time-dependent hartree approach for quantum dynamics on general potential energy surfaces. *The Journal of chemical physics*, 128(16):164116, 2008.
- [38] Oriol Vendrell and Hans-Dieter Meyer. Multilayer multiconfiguration time-dependent hartree method: Implementation and applications to a henon–heiles hamiltonian and to pyrazine. *The Journal of Chemical Physics*, 134(4):044135, 2011.
- [39] Alberto Baiardi, Christopher J Stein, Vincenzo Barone, and Markus Reiher. Vibrational density matrix renormalization group. *Journal of Chemical Theory and Computation*, 13(8):3764–3777, 2017.
- [40] Alberto Baiardi and Markus Reiher. Large-scale quantum dynamics with matrix product states. *Journal of chemical theory and computation*, 15(6):3481–3498, 2019.
- [41] Hsing-Ta Chen, Guy Cohen, and David R Reichman. Inchworm monte carlo for exact non-adiabatic dynamics. i. theory and algorithms. *The Journal of chemical physics*, 146(5):054105, 2017.
- [42] Hsing-Ta Chen, Guy Cohen, and David R Reichman. Inchworm monte carlo for exact non-adiabatic dynamics. ii. benchmarks and comparison with established methods. *The Journal of chemical physics*, 146(5):054106, 2017.
- [43] MOSM Hillery, Robert F O’Connell, Marlan O Scully, and Eugene P Wigner. Distribution functions in physics: fundamentals. *Physics Reports*, 106(3):121–167, 1984.
- [44] MJ Steel, MK Olsen, LI Plimak, PD Drummond, SM Tan, MJ Collett, DF Walls, and R Graham. Dynamical quantum noise in trapped bose-einstein condensates. *Physical Review A*, 58(6):4824, 1998.
- [45] P Blair Blakie, AS Bradley, MJ Davis, RJ Ballagh, and CW Gardiner. Dynamics and statistical mechanics of ultra-cold bose gases using c-field techniques. *Advances in Physics*, 57(5):363–455, 2008.
- [46] Anatoli Polkovnikov. Phase space representation of quantum dynamics. *Annals of Physics*, 325(8):1790–1852, 2010.
- [47] Johannes Schachenmayer, Alexander Pikovski, and Ana Maria Rey. Many-body quantum spin dynamics with monte carlo trajectories on a discrete phase space. *Physical Review X*, 5(1):011022, 2015.

- [48] Bihui Zhu, Ana Maria Rey, and Johannes Schachenmayer. A generalized phase space approach for solving quantum spin dynamics. *New Journal of Physics*, 21(8):082001, 2019.
- [49] Shainen M Davidson and Anatoli Polkovnikov. $Su(3)$ semiclassical representation of quantum dynamics of interacting spins. *Physical Review Letters*, 114(4):045701, 2015.
- [50] Jonathan Wurtz, Anatoli Polkovnikov, and Dries Sels. Cluster truncated wigner approximation in strongly interacting systems. *Annals of Physics*, 395:341–365, 2018.
- [51] Anatoli Polkovnikov. Quantum corrections to the dynamics of interacting bosons: Beyond the truncated wigner approximation. *Physical Review A*, 68(5):053604, 2003.
- [52] Asier Piñeiro Orioli, Arghavan Safavi-Naini, Michael L Wall, and Ana Maria Rey. Nonequilibrium dynamics of spin-boson models from phase-space methods. *Physical Review A*, 96(3):033607, 2017.
- [53] Lorenzo Pucci, Analabha Roy, and Michael Kastner. Simulation of quantum spin dynamics by phase space sampling of bogoliubov-born-green-kirkwood-yvon trajectories. *Physical Review B*, 93(17):174302, 2016.
- [54] Hans-Dieter Meyer and William H Miller. A classical analog for electronic degrees of freedom in nonadiabatic collision processes. *The Journal of Chemical Physics*, 70(7):3214–3223, 1979.
- [55] Stephen J Cotton and William H Miller. Symmetrical windowing for quantum states in quasi-classical trajectory simulations: Application to electronically non-adiabatic processes. *The Journal of Chemical Physics*, 139(23):234112, 2013.
- [56] Gerhard Stock and Michael Thoss. Semiclassical description of nonadiabatic quantum dynamics. *Physical Review Letters*, 78(4):578, 1997.
- [57] Stephen J Cotton and William H Miller. Symmetrical windowing for quantum states in quasi-classical trajectory simulations. *The Journal of Physical Chemistry A*, 117(32):7190–7194, 2013.
- [58] Jian Liu. Isomorphism between the multi-state hamiltonian and the second-quantized many-electron hamiltonian with only 1-electron interactions. *The Journal of Chemical Physics*, 146(2):024110, 2017.
- [59] Xin He and Jian Liu. A new perspective for nonadiabatic dynamics with phase space mapping models. *The Journal of Chemical Physics*, 151(2):024105, 2019.
- [60] Jian Liu. A unified theoretical framework for mapping models for the multi-state hamiltonian. *The Journal of Chemical Physics*, 145(20):204105, 2016.

- [61] William H Miller and Stephen J Cotton. Classical molecular dynamics simulation of electronically non-adiabatic processes. *Faraday Discussions*, 195:9–30, 2017.
- [62] Maximilian AC Saller, Aaron Kelly, and Jeremy O Richardson. On the identity of the identity operator in nonadiabatic linearized semiclassical dynamics. *The Journal of Chemical Physics*, 150(7):071101, 2019.
- [63] Maximilian AC Saller, Aaron Kelly, and Jeremy O Richardson. Improved population operators for multi-state nonadiabatic dynamics with the mixed quantum-classical mapping approach. *Faraday Discussions*, 221:150–167, 2019.
- [64] Xiong Sun, Haobin Wang, and William H Miller. Semiclassical theory of electronically nonadiabatic dynamics: Results of a linearized approximation to the initial value representation. *The Journal of Chemical Physics*, 109(17):7064–7074, 1998.
- [65] Hyojoon Kim, Ali Nassimi, and Raymond Kapral. Quantum-classical liouville dynamics in the mapping basis. *The Journal of Chemical Physics*, 129(8):084102, 2008.
- [66] Aaron Kelly, Ramses van Zon, Jeremy Schofield, and Raymond Kapral. Mapping quantum-classical liouville equation: Projectors and trajectories. *The Journal of Chemical Physics*, 136(8):084101, 2012.
- [67] Pengfei Huo and David F Coker. Communication: Partial linearized density matrix dynamics for dissipative, non-adiabatic quantum evolution. *The Journal of Chemical Physics*, 135(8):201101, 2011.
- [68] Pengfei Huo, Thomas F Miller III, and David F Coker. Communication: Predictive partial linearized path integral simulation of condensed phase electron transfer dynamics. *The Journal of Chemical Physics*, 139(8):151103, 2013.
- [69] Chang-Yu Hsieh and Raymond Kapral. Nonadiabatic dynamics in open quantum-classical systems: Forward-backward trajectory solution. *The Journal of Chemical Physics*, 137(22):22A507, 2012.
- [70] Chang-Yu Hsieh and Raymond Kapral. Analysis of the forward-backward trajectory solution for the mixed quantum-classical liouville equation. *The Journal of Chemical Physics*, 138(13):134110, 2013.
- [71] Raymond Kapral and Giovanni Ciccotti. Mixed quantum-classical dynamics. *The Journal of Chemical Physics*, 110(18):8919–8929, 1999.
- [72] Gerhard Stock and Uwe Müller. Flow of zero-point energy and exploration of phase space in classical simulations of quantum relaxation dynamics. *The Journal of Chemical Physics*, 111(1):65–76, 1999.

- [73] Uwe Müller and Gerhard Stock. Flow of zero-point energy and exploration of phase space in classical simulations of quantum relaxation dynamics. ii. application to non-adiabatic processes. *The Journal of Chemical Physics*, 111(1):77–88, 1999.
- [74] Pengfei Huo and David F Coker. Consistent schemes for non-adiabatic dynamics derived from partial linearized density matrix propagation. *The Journal of Chemical Physics*, 137(22):22A535, 2012.
- [75] Stephen J Cotton and William H Miller. A symmetrical quasi-classical spin-mapping model for the electronic degrees of freedom in non-adiabatic processes. *The Journal of Physical Chemistry A*, 119(50):12138–12145, 2015.
- [76] Hans-Dieter Meyer and William H Miller. Classical models for electronic degrees of freedom: Derivation via spin analogy and application to $f^* + h_2 \rightarrow f + h_2$. *The Journal of Chemical Physics*, 71(5):2156–2169, 1979.
- [77] Jonathan R Mannouch and Jeremy O Richardson. A partially linearized spin-mapping approach for nonadiabatic dynamics. i. derivation of the theory. *The Journal of Chemical Physics*, 153(19):194109, 2020.
- [78] Jonathan R Mannouch and Jeremy O Richardson. A partially linearized spin-mapping approach for nonadiabatic dynamics. ii. analysis and comparison with related approaches. *The Journal of Chemical Physics*, 153(19):194110, 2020.
- [79] Johan E Runeson and Jeremy O Richardson. Spin-mapping approach for nonadiabatic molecular dynamics. *The Journal of Chemical Physics*, 151(4):044119, 2019.
- [80] Johan E Runeson and Jeremy O Richardson. Generalized spin mapping for quantum-classical dynamics. *The Journal of Chemical Physics*, 152(8):084110, 2020.
- [81] Michael A Nielsen and Isaac Chuang. Quantum computation and quantum information, 2002.
- [82] IU I Manin. *Vychislimoe i nevychislimoe*. Sov. radio,, 1980.
- [83] Richard P Feynman. Simulating physics with computers. In *Feynman and computation*, pages 133–153. CRC Press, 2018.
- [84] Iulia M Georgescu, Sahel Ashhab, and Franco Nori. Quantum simulation. *Reviews of Modern Physics*, 86(1):153, 2014.
- [85] Philipp Hauke, Fernando M Cucchietti, Luca Tagliacozzo, Ivan Deutsch, and Maciej Lewenstein. Can one trust quantum simulators? *Reports on Progress in Physics*, 75(8):082401, jul 2012.

- [86] Sudip Sasmal and Oriol Vendrell. Non-adiabatic quantum dynamics without potential energy surfaces based on second-quantized electrons: Application within the framework of the mctdh method. *The Journal of Chemical Physics*, 153(15):154110, 2020.
- [87] Sudip Sasmal and Oriol Vendrell. Sum-of-products form of the molecular electronic hamiltonian and application within the mctdh method. *The Journal of Chemical Physics*, 2022.
- [88] Jad C. Halimeh and Philipp Hauke. Reliability of lattice gauge theories. *Phys. Rev. Lett.*, 125:030503, Jul 2020.
- [89] Jad C Halimeh, Haifeng Lang, Julius Mildenerger, Zhang Jiang, and Philipp Hauke. Gauge-symmetry protection using single-body terms. *PRX Quantum*, 2(4):040311, 2021.
- [90] ERICH POPPITZ and YANWEN SHANG. “light from chaos” in two dimensions. *International Journal of Modern Physics A*, 23(27n28):4545–4556, Nov 2008.
- [91] Alexander Mil, Torsten V. Zache, Apoorva Hegde, Andy Xia, Rohit P. Bhatt, Markus K. Oberthaler, Philipp Hauke, Jürgen Berges, and Fred Jendrzejewski. A scalable realization of local $u(1)$ gauge invariance in cold atomic mixtures. *Science*, 367(6482):1128–1130, 2020.
- [92] Bing Yang, Hui Sun, Robert Ott, Han-Yi Wang, Torsten V. Zache, Jad C. Halimeh, Zhen-Sheng Yuan, Philipp Hauke, and Jian-Wei Pan. Observation of gauge invariance in a 71-site bose–hubbard quantum simulator. *Nature*, 587(7834):392–396, 2020.
- [93] Esteban A. Martinez, Christine A. Muschik, Philipp Schindler, Daniel Nigg, Alexander Erhard, Markus Heyl, Philipp Hauke, Marcello Dalmonte, Thomas Monz, Peter Zoller, and Rainer Blatt. Real-time dynamics of lattice gauge theories with a few-qubit quantum computer. *Nature*, 534(7608):516–519, 2016.
- [94] Christine Muschik, Markus Heyl, Esteban Martinez, Thomas Monz, Philipp Schindler, Berit Vogell, Marcello Dalmonte, Philipp Hauke, Rainer Blatt, and Peter Zoller. $U(1)$ wilson lattice gauge theories in digital quantum simulators. *New Journal of Physics*, 19(10):103020, oct 2017.
- [95] Haifeng Lang, Oriol Vendrell, and Philipp Hauke. Generalized discrete truncated wigner approximation for nonadiabatic quantum-classical dynamics. *The Journal of Chemical Physics*, 155(2):024111, 2021.
- [96] Jian Liu, Xin He, and Baihua Wu. Unified formulation of phase space mapping approaches for nonadiabatic quantum dynamics. *Accounts of chemical research*, 54(23):4215–4228, 2021.

- [97] P Facchi and S Pascazio. Quantum zeno subspaces. *Physical review letters*, 89(8):080401, 2002.
- [98] Paolo Facchi, DA Lidar, and S Pascazio. Unification of dynamical decoupling and the quantum zeno effect. *Physical Review A*, 69(3):032314, 2004.
- [99] Paolo Facchi, Giuseppe Marmo, and Saverio Pascazio. Quantum zeno dynamics and quantum zeno subspaces. volume 196, page 012017. IOP Publishing, 2009.
- [100] Graham A. Worth and Lorenz S. Cederbaum. BEYOND BORN-OPPENHEIMER: Molecular Dynamics Through a Conical Intersection. *Annu. Rev. Phys. Chem.*, 55:127–158, 2004.
- [101] David R Yarkony. Diabolical conical intersections. *Reviews of Modern Physics*, 68(4):985, 1996.
- [102] Jean Dalibard, Fabrice Gerbier, Gediminas Juzeliūnas, and Patrik Öhberg. Colloquium: Artificial gauge potentials for neutral atoms. *Reviews of Modern Physics*, 83(4):1523, 2011.
- [103] C Alden Mead and Donald G Truhlar. Conditions for the definition of a strictly diabatic electronic basis for molecular systems. *The Journal of Chemical Physics*, 77(12):6090–6098, 1982.
- [104] Ewine F van Dishoeck, Marc C van Hemert, AC Allison, and A Dalgarno. Resonances in the photodissociation of oh by absorption into coupled 2π states: Adiabatic and diabatic formulations. *The Journal of chemical physics*, 81(12):5709–5724, 1984.
- [105] Michael Baer. Electronic non-adiabatic transitions derivation of the general adiabatic-diabatic transformation matrix. *Molecular Physics*, 40(4):1011–1013, 1980.
- [106] Michael Baer. Introduction to the theory of electronic non-adiabatic coupling terms in molecular systems. *Physics Reports*, 358(2):75–142, 2002.
- [107] Tibor Pacher, C Alden Mead, Lorenz S Cederbaum, and Horst Köppel. Gauge theory and quasidiabatic states in molecular physics. *The Journal of chemical physics*, 91(11):7057–7062, 1989.
- [108] Michael Baer and Robert Englman. A study of the diabatic electronic representation within the born-oppenheimer approximation. *Molecular Physics*, 75(2):293–303, 1992.
- [109] T Pacher, LS Cederbaum, and H Köppel. Approximately diabatic states from block diagonalization of the electronic hamiltonian. *The Journal of chemical physics*, 89(12):7367–7381, 1988.

- [110] F Spiegelmann and JP Malrieu. The use of effective hamiltonians for the treatment of avoided crossings. i. adiabatic potential curves. *Journal of Physics B: Atomic and Molecular Physics (1968-1987)*, 17(7):1235, 1984.
- [111] F Spiegelmann and JP Malrieu. The use of effective hamiltonians for the treatment of avoided crossings. ii. nearly diabatic potential curves. *Journal of Physics B: Atomic and Molecular Physics (1968-1987)*, 17(7):1259, 1984.
- [112] Milica Pavlović, Jasna Kučar, and Josip Hendeković. Variational construction of diabatic states. *International journal of quantum chemistry*, 32(6):705–710, 1987.
- [113] Josip Hendekovic. Novel variational definition of diabatic states. *Chemical Physics Letters*, 90(3):193–197, 1982.
- [114] Josip Hendeković. Variational approach to diabatic states. *Croatica Chemica Acta*, 56(3):375–382, 1983.
- [115] Robert S Mulliken. Molecular compounds and their spectra. ii. *Journal of the American Chemical Society*, 74(3):811–824, 1952.
- [116] NS Hush. Intervalence-transfer absorption. part 2. theoretical considerations and spectroscopic data. *Progress in Inorganic Chemistry*, 8:391–444, 1967.
- [117] Robert J Cave and Marshall D Newton. Calculation of electronic coupling matrix elements for ground and excited state electron transfer reactions: comparison of the generalized mulliken–hush and block diagonalization methods. *The Journal of chemical physics*, 106(22):9213–9226, 1997.
- [118] Hans-Joachim Werner and Wilfried Meyer. Mcscf study of the avoided curve crossing of the two lowest $1\sigma^+$ states of lif. *The Journal of Chemical Physics*, 74(10):5802–5807, 1981.
- [119] Carlo Petrongolo, Gerhard Hirsch, and Robert J Buenker. Diabatic representation of the $\tilde{a}2a_1$ [btilde] $2b_2$ conical intersection in nh₂. *Molecular Physics*, 70(5):825–834, 1990.
- [120] Gerhard Hirsch, Robert J Buenker, and Carlo Petrongolo. Ab initio study of no₂: Part ii: Non-adiabatic coupling between the two lowest $2a'$ states and the construction of a diabatic representation. *Molecular Physics*, 70(5):835–848, 1990.
- [121] David R Yarkony. On the construction of diabatic bases using molecular properties. rigorous results in the vicinity of a conical intersection. *The Journal of Physical Chemistry A*, 102(42):8073–8077, 1998.

- [122] Clarence Zener. Non-adiabatic crossing of energy levels. *Proceedings of the Royal Society of London. Series A, Containing Papers of a Mathematical and Physical Character*, 137(833):696–702, 1932.
- [123] Lev Davidovich Landau. Zur theorie der energieubertragung ii. *Z. Sowjetunion*, 2:46–51, 1932.
- [124] Ernst Karl Gerlach Stückelberg. *Theorie der unelastischen Stösse zwischen Atomen*. Birkhäuser, 1933.
- [125] Ettore Majorana. Atomi orientati in campo magnetico variabile. *Il Nuovo Cimento (1924-1942)*, 9(2):43–50, 1932.
- [126] Horst Köppel, Joachim Gronki, and Susanta Mahapatra. Construction scheme for regularized diabatic states. *The Journal of Chemical Physics*, 115(6):2377–2388, 2001.
- [127] A Thiel and H Köppel. Proposal and numerical test of a simple diabatization scheme. *The Journal of chemical physics*, 110(19):9371–9383, 1999.
- [128] Clemens Woywod, Wolfgang Domcke, Andrzej L Sobolewski, and Hans-Joachim Werner. Characterization of the s 1–s 2 conical intersection in pyrazine using ab initio multiconfiguration self-consistent-field and multireference configuration-interaction methods. *The Journal of chemical physics*, 100(2):1400–1413, 1994.
- [129] Poul Jørgensen. *Second quantization-based methods in quantum chemistry*. Elsevier, 2012.
- [130] Alexander L Fetter and John Dirk Walecka. *Quantum theory of many-particle systems*. Courier Corporation, 2012.
- [131] Marios-Petros Kitsaras and Stella Stopkowicz. Spin contamination in mp2 and cc2, a surprising issue. *The Journal of Chemical Physics*, 154(13):131101, 2021.
- [132] Douglas R Hartree. The wave mechanics of an atom with a non-coulomb central field. part i. theory and methods. In *Mathematical Proceedings of the Cambridge Philosophical Society*, volume 24, pages 89–110. Cambridge university press, 1928.
- [133] Douglas Rayne Hartree. The wave mechanics of an atom with a non-coulomb central field. part ii. some results and discussion. In *Mathematical Proceedings of the Cambridge Philosophical Society*, volume 24, pages 111–132. Cambridge University Press, 1928.
- [134] DR Hartree. The wave mechanics of an atom with a non-coulomb central field. part iii. term values and intensities in series in optical spectra. In *Mathematical Proceed-*

- ings of the Cambridge Philosophical Society*, volume 24, pages 426–437. Cambridge University Press, 1928.
- [135] DR Hartree. The wave mechanics of an atom with a non-coulomb central field. part iv. further results relating to terms of the optical spectrum. In *Mathematical Proceedings of the Cambridge Philosophical Society*, volume 25, pages 310–314. Cambridge University Press, 1929.
- [136] Vladimir Fock. Näherungsmethode zur lösung des quantenmechanischen mehrkörperproblems. *Zeitschrift für Physik*, 61(1):126–148, 1930.
- [137] V Fock. „selfconsistent field “mit austausch für natrium. *Zeitschrift für Physik*, 62(11):795–805, 1930.
- [138] John C Slater. Note on hartree’s method. *Physical Review*, 35(2):210, 1930.
- [139] John C Slater. A simplification of the hartree-fock method. *Physical review*, 81(3):385, 1951.
- [140] Hans-Joachim Werner and Wilfried Meyer. A quadratically convergent multiconfiguration–self-consistent field method with simultaneous optimization of orbitals and ci coefficients. *The Journal of Chemical Physics*, 73(5):2342–2356, 1980.
- [141] Hans-Joachim Werner and Wilfried Meyer. A quadratically convergent mcsf method for the simultaneous optimization of several states. *The Journal of Chemical Physics*, 74(10):5794–5801, 1981.
- [142] Hans-Joachim Werner and Peter J Knowles. A second order multiconfiguration scf procedure with optimum convergence. *The Journal of chemical physics*, 82(11):5053–5063, 1985.
- [143] Peter J Knowles and Hans-Joachim Werner. An efficient second-order mc scf method for long configuration expansions. *Chemical physics letters*, 115(3):259–267, 1985.
- [144] Giuseppe MJ Barca, Andrew TB Gilbert, and Peter MW Gill. Communication: Hartree-fock description of excited states of h₂. *The Journal of chemical physics*, 141(11):111104, 2014.
- [145] Jochen Schirmer. Beyond the random-phase approximation: A new approximation scheme for the polarization propagator. *Physical Review A*, 26(5):2395, 1982.
- [146] Andreas Dreuw and Michael Wormit. The algebraic diagrammatic construction scheme for the polarization propagator for the calculation of excited states. *Wiley Interdisciplinary Reviews: Computational Molecular Science*, 5(1):82–95, 2015.

- [147] Filipe Menezes, Daniel Kats, and Hans-Joachim Werner. Local complete active space second-order perturbation theory using pair natural orbitals (pno-caspt2). *The Journal of Chemical Physics*, 145(12):124115, 2016.
- [148] Werner Győrffy, Toru Shiozaki, Gerald Knizia, and Hans-Joachim Werner. Analytical energy gradients for second-order multireference perturbation theory using density fitting. *The Journal of Chemical Physics*, 138(10):104104, 2013.
- [149] Paolo Celani and Hans-Joachim Werner. Analytical energy gradients for internally contracted second-order multireference perturbation theory. *The Journal of chemical physics*, 119(10):5044–5057, 2003.
- [150] Toru Shiozaki, Clemens Woywod, and Hans-Joachim Werner. Pyrazine excited states revisited using the extended multi-state complete active space second-order perturbation method. *Physical Chemistry Chemical Physics*, 15(1):262–269, 2013.
- [151] Toru Shiozaki and Hans-Joachim Werner. Communication: Second-order multireference perturbation theory with explicit correlation: Caspt2-f12. *The Journal of chemical physics*, 133(14):141103, 2010.
- [152] Toru Shiozaki, Werner Győrffy, Paolo Celani, and Hans-Joachim Werner. Communication: Extended multi-state complete active space second-order perturbation theory: Energy and nuclear gradients. *The Journal of Chemical Physics*, 135(8):081106, 2011.
- [153] Paolo Celani and Hans-Joachim Werner. Multireference perturbation theory for large restricted and selected active space reference wave functions. *The Journal of Chemical Physics*, 112(13):5546–5557, 2000.
- [154] P Celani, H Stoll, H-J Werner, and PJ Knowles*. The cipt2 method: Coupling of multi-reference configuration interaction and multi-reference perturbation theory. application to the chromium dimer. *Molecular Physics*, 102(21-22):2369–2379, 2004.
- [155] Mihály Kállay and Jürgen Gauss. Calculation of excited-state properties using general coupled-cluster and configuration-interaction models. *The Journal of chemical physics*, 121(19):9257–9269, 2004.
- [156] Hans-Joachim Werner and Peter J Knowles. An efficient internally contracted multiconfiguration–reference configuration interaction method. *The Journal of chemical physics*, 89(9):5803–5814, 1988.
- [157] Peter J Knowles and Hans-Joachim Werner. An efficient method for the evaluation of coupling coefficients in configuration interaction calculations. *Chemical physics letters*, 145(6):514–522, 1988.

- [158] Hans-Joachim Werner and Peter J Knowles. A comparison of variational and non-variational internally contracted multiconfiguration-reference configuration interaction calculations. *Theoretica chimica acta*, 78(3):175–187, 1990.
- [159] Peter J Knowles and Hans-Joachim Werner. Internally contracted multiconfiguration-reference configuration interaction calculations for excited states. *Theoretica chimica acta*, 84(1):95–103, 1992.
- [160] Andreas Berning, Marcus Schweizer, Hans-Joachim Werner, Peter J Knowles, and Paolo Palmieri. Spin-orbit matrix elements for internally contracted multireference configuration interaction wavefunctions. *Molecular Physics*, 98(21):1823–1833, 2000.
- [161] KR Shamasundar, Gerald Knizia, and Hans-Joachim Werner. A new internally contracted multi-reference configuration interaction method. *The Journal of chemical physics*, 135(5):054101, 2011.
- [162] Toru Shiozaki and Hans-Joachim Werner. Explicitly correlated multireference configuration interaction with multiple reference functions: Avoided crossings and conical intersections. *The Journal of chemical physics*, 134(18):184104, 2011.
- [163] Toru Shiozaki, Gerald Knizia, and Hans-Joachim Werner. Explicitly correlated multireference configuration interaction: Mrci-f12. *The Journal of chemical physics*, 134(3):034113, 2011.
- [164] George D Purvis III and Rodney J Bartlett. A full coupled-cluster singles and doubles model: The inclusion of disconnected triples. *The Journal of Chemical Physics*, 76(4):1910–1918, 1982.
- [165] David J Coughtrie, Robin Giereth, Daniel Kats, Hans-Joachim Werner, and Andreas Köhn. Embedded multireference coupled cluster theory. *Journal of Chemical Theory and Computation*, 14(2):693–709, 2018.
- [166] Henrik Koch and Poul Jørgensen. Coupled cluster response functions. *The Journal of chemical physics*, 93(5):3333–3344, 1990.
- [167] John F Stanton and Rodney J Bartlett. The equation of motion coupled-cluster method. a systematic biorthogonal approach to molecular excitation energies, transition probabilities, and excited state properties. *The Journal of chemical physics*, 98(9):7029–7039, 1993.
- [168] Jonathan Romero, Ryan Babbush, Jarrod R McClean, Cornelius Hempel, Peter J Love, and Alán Aspuru-Guzik. Strategies for quantum computing molecular energies using the unitary coupled cluster ansatz. *Quantum Science and Technology*, 4(1):014008, 2018.

- [169] Joonho Lee, William J Huggins, Martin Head-Gordon, and K Birgitta Whaley. Generalized unitary coupled cluster wave functions for quantum computation. *Journal of chemical theory and computation*, 15(1):311–324, 2018.
- [170] Maria Topaler and Nancy Makri. Quantum rates for a double well coupled to a dissipative bath: Accurate path integral results and comparison with approximate theories. *The Journal of chemical physics*, 101(9):7500–7519, 1994.
- [171] Yoshitaka Tanimura. Numerically “exact” approach to open quantum dynamics: The hierarchical equations of motion (heom). *The Journal of chemical physics*, 153(2):020901, 2020.
- [172] Xiao Yuan, Suguru Endo, Qi Zhao, Ying Li, and Simon C Benjamin. Theory of variational quantum simulation. *Quantum*, 3:191, 2019.
- [173] Jutho Haegeman, J Ignacio Cirac, Tobias J Osborne, Iztok Pižorn, Henri Verschelde, and Frank Verstraete. Time-dependent variational principle for quantum lattices. *Physical review letters*, 107(7):070601, 2011.
- [174] Jutho Haegeman, Christian Lubich, Ivan Oseledets, Bart Vandereycken, and Frank Verstraete. Unifying time evolution and optimization with matrix product states. *Physical Review B*, 94(16):165116, 2016.
- [175] Haobin Wang and Hans-Dieter Meyer. On regularizing the ml-mctdh equations of motion. *The Journal of Chemical Physics*, 149(4):044119, 2018.
- [176] Hans-Dieter Meyer and Haobin Wang. On regularizing the mctdh equations of motion. *The Journal of Chemical Physics*, 148(12):124105, 2018.
- [177] Christian Lubich. Time integration in the multiconfiguration time-dependent hartree method of molecular quantum dynamics. *Applied Mathematics Research eXpress*, 2015(2):311–328, 2015.
- [178] Matteo Bonfanti and Irene Burghardt. The projector-splitting integrator for the multi-configurational time-dependent hartree method revisited, 2018.
- [179] Benedikt Kloss, Irene Burghardt, and Christian Lubich. Implementation of a novel projector-splitting integrator for the multi-configurational time-dependent hartree approach. *The Journal of Chemical Physics*, 146(17):174107, 2017.
- [180] David Mendive-Tapia and Hans-Dieter Meyer. Regularizing the mctdh equations of motion through an optimal choice on-the-fly (ie, spawning) of unoccupied single-particle functions. *The Journal of Chemical Physics*, 153(23):234114, 2020.

- [181] Graham A Worth, H-D Meyer, and LS Cederbaum. The effect of a model environment on the s_2 absorption spectrum of pyrazine: A wave packet study treating all 24 vibrational modes. *The Journal of chemical physics*, 105(11):4412–4426, 1996.
- [182] Haobin Wang and Michael Thoss. Numerically exact quantum dynamics for indistinguishable particles: The multilayer multiconfiguration time-dependent hartree theory in second quantization representation. *The Journal of chemical physics*, 131(2):024114, 2009.
- [183] Thomas Weike and Uwe Manthe. The multi-configurational time-dependent hartree approach in optimized second quantization: Imaginary time propagation and particle number conservation. *The Journal of chemical physics*, 152(3):034101, 2020.
- [184] Rui Lin, Paolo Molignini, Luca Papariello, Marios C Tsatsos, Camille Lévêque, Storm E Weiner, Elke Fasshauer, R Chitra, and Axel UJ Lode. Mctdh-x: The multiconfigurational time-dependent hartree method for indistinguishable particles software. *Quantum Science and Technology*, 5(2):024004, 2020.
- [185] Axel UJ Lode, Camille Lévêque, Lars Bojer Madsen, Alexej I Streltsov, and Ofir E Alon. Colloquium: Multiconfigurational time-dependent hartree approaches for indistinguishable particles. *Reviews of Modern Physics*, 92(1):011001, 2020.
- [186] John C Light and Tucker Carrington. Discrete-variable representations and their utilization. *Advances in Chemical Physics*, 114:263–310, 2007.
- [187] Uwe Manthe. A time-dependent discrete variable representation for (multiconfiguration) hartree methods. *The Journal of chemical physics*, 105(16):6989–6994, 1996.
- [188] Daniel Peláez and Hans-Dieter Meyer. The multigrid potfit (mgpf) method: Grid representations of potentials for quantum dynamics of large systems. *The Journal of chemical physics*, 138(1):014108, 2013.
- [189] Oriol Vendrell, Fabien Gatti, David Lauvergnat, and Hans-Dieter Meyer. Full-dimensional (15-dimensional) quantum-dynamical simulation of the protonated water dimer. i. hamiltonian setup and analysis of the ground vibrational state. *The Journal of chemical physics*, 127(18):184302, 2007.
- [190] Oriol Vendrell, Michael Brill, Fabien Gatti, David Lauvergnat, and Hans-Dieter Meyer. Full dimensional (15-dimensional) quantum-dynamical simulation of the protonated water-dimer iii: Mixed jacobi-valence parametrization and benchmark results for the zero point energy, vibrationally excited states, and infrared spectrum. *The Journal of chemical physics*, 130(23):234305, 2009.

- [191] Markus Schröder and Hans-Dieter Meyer. Transforming high-dimensional potential energy surfaces into sum-of-products form using monte carlo methods. *The Journal of Chemical Physics*, 147(6):064105, 2017.
- [192] Anthony J Leggett, SDAFMGA Chakravarty, Alan T Dorsey, Matthew PA Fisher, Anupam Garg, and Wilhelm Zwerger. Dynamics of the dissipative two-state system. *Reviews of Modern Physics*, 59(1):1, 1987.
- [193] Amir O Caldeira and Anthony J Leggett. Quantum tunnelling in a dissipative system. *Annals of physics*, 149(2):374–456, 1983.
- [194] Ian R Craig and David E Manolopoulos. Chemical reaction rates from ring polymer molecular dynamics. *The Journal of chemical physics*, 122(8):084106, 2005.
- [195] Ian R Craig, Michael Thoss, and Haobin Wang. Proton transfer reactions in model condensed-phase environments: Accurate quantum dynamics using the multi-layer multiconfiguration time-dependent hartree approach. *The Journal of chemical physics*, 127(14):144503, 2007.
- [196] Akihito Ishizaki and Graham R Fleming. Unified treatment of quantum coherent and incoherent hopping dynamics in electronic energy transfer: Reduced hierarchy equation approach. *The Journal of chemical physics*, 130(23):234111, 2009.
- [197] Stephen J Cotton and William H Miller. The symmetrical quasi-classical model for electronically non-adiabatic processes applied to energy transfer dynamics in site-exciton models of light-harvesting complexes. *Journal of chemical theory and computation*, 12(3):983–991, 2016.
- [198] Guohua Tao and William H Miller. Semiclassical description of electronic excitation population transfer in a model photosynthetic system. *The Journal of Physical Chemistry Letters*, 1(6):891–894, 2010.
- [199] Seogjoo J Jang and Benedetta Mennucci. Delocalized excitons in natural light-harvesting complexes. *Reviews of Modern Physics*, 90(3):035003, 2018.
- [200] Marcel Schmidt am Busch, Frank Müh, Mohamed El-Amine Madjet, and Thomas Renger. The eighth bacteriochlorophyll completes the excitation energy funnel in the fmo protein. *The journal of physical chemistry letters*, 2(2):93–98, 2011.
- [201] Dale E Tronrud, Jianzhong Wen, Leslie Gay, and Robert E Blankenship. The structural basis for the difference in absorbance spectra for the fmo antenna protein from various green sulfur bacteria. *Photosynthesis research*, 100(2):79–87, 2009.
- [202] RJW Louwe, J Vrieze, TJ Aartsma, and AJ Hoff. Toward an integral interpretation of the optical steady-state spectra of the fmo-complex of *prosthecochloris aestuarii*. 1.

- an investigation with linear-dichroic absorbance-detected magnetic resonance. *The Journal of Physical Chemistry B*, 101(51):11273–11279, 1997.
- [203] RJW Louwe, J Vrieze, AJ Hoff, and TJ Aartsma. Toward an integral interpretation of the optical steady-state spectra of the fmo-complex of *prosthecochloris aestuarii*. 2. exciton simulations. *The Journal of Physical Chemistry B*, 101(51):11280–11287, 1997.
- [204] Simone IE Vulto, Michiel A de Baat, Robert JW Louwe, Hjalmar P Permentier, Tatjana Neef, Mette Miller, Herbert van Amerongen, and Thijs J Aartsma. Exciton simulations of optical spectra of the fmo complex from the green sulfur bacterium *chlorobium tepidum* at 6 k. *The Journal of Physical Chemistry B*, 102(47):9577–9582, 1998.
- [205] Simone IE Vulto, Michiel A de Baat, Sieglinde Neerken, Frank R Nowak, Herbert van Amerongen, Jan Amesz, and Thijs J Aartsma. Excited state dynamics in fmo antenna complexes from photosynthetic green sulfur bacteria: a kinetic model. *The Journal of Physical Chemistry B*, 103(38):8153–8161, 1999.
- [206] Daniel Montemayor, Eva Rivera, and Seogjoo J Jang. Computational modeling of exciton-bath hamiltonians for light harvesting 2 and light harvesting 3 complexes of purple photosynthetic bacteria at room temperature. *The Journal of Physical Chemistry B*, 122(14):3815–3825, 2018.
- [207] Seogjoo Jang, Sara E Dempster, and Robert J Silbey. Characterization of the static disorder in the b850 band of lh2. *The Journal of Physical Chemistry B*, 105(28):6655–6665, 2001.
- [208] Seogjoo Jang, Marshall D Newton, and Robert J Silbey. Multichromophoric förster resonance energy transfer from b800 to b850 in the light harvesting complex 2: evidence for subtle energetic optimization by purple bacteria. *The Journal of Physical Chemistry B*, 111(24):6807–6814, 2007.
- [209] Pengfei Huo and David F Coker. Theoretical study of coherent excitation energy transfer in cryptophyte phycocyanin 645 at physiological temperature. *The Journal of Physical Chemistry Letters*, 2(7):825–833, 2011.
- [210] Elisabetta Collini, Cathy Y Wong, Krystyna E Wilk, Paul MG Curmi, Paul Brumer, and Gregory D Scholes. Coherently wired light-harvesting in photosynthetic marine algae at ambient temperature. *Nature*, 463(7281):644–647, 2010.
- [211] Tihana Mirkovic, Alexander B Doust, Jeongho Kim, Krystyna E Wilk, Carles Curutchet, Benedetta Mennucci, Roberto Cammi, Paul MG Curmi, and Gregory D Sc-

- holes. Ultrafast light harvesting dynamics in the cryptophyte phycocyanin 645. *Photochemical & Photobiological Sciences*, 6(9):964–975, 2007.
- [212] Mi Kyung Lee, Ksenia B Bravaya, and David F Coker. First-principles models for biological light-harvesting: Phycobiliprotein complexes from cryptophyte algae. *Journal of the American Chemical Society*, 139(23):7803–7814, 2017.
- [213] H Köppel. New ultrafast nonradiative decay mechanism in the benzene radical cation. *Chemical Physics Letters*, 205(4-5):361–370, 1993.
- [214] H Köppel, LS Cederbaum, and W Domcke. Interplay of jahn–teller and pseudo-jahn–teller vibronic dynamics in the benzene cation. *The Journal of Chemical Physics*, 89(4):2023–2040, 1988.
- [215] R Schneider and W Domcke. S1-s2 conical intersection and ultrafast s2→s1 internal conversion in pyrazine. *Chemical physics letters*, 150(3-4):235–242, 1988.
- [216] R Schneider and W Domcke. Surface-hopping-induced femtosecond vibrational dephasing in strongly vibronically coupled systems. *Chemical Physics Letters*, 159(1):61–65, 1989.
- [217] Lorenz S Cederbaum, Etienne Gindensperger, and Irene Burghardt. Short-time dynamics through conical intersections in macrosystems. *Physical review letters*, 94(11):113003, 2005.
- [218] Etienne Gindensperger, Irene Burghardt, and Lorenz S Cederbaum. Short-time dynamics through conical intersections in macrosystems. i. theory: Effective-mode formulation. *The Journal of chemical physics*, 124(14):144103, 2006.
- [219] Irene Burghardt, Etienne Gindensperger, and Lorenz S Cederbaum. An effective hamiltonian for the short-time dynamics at a conical intersection. *Molecular Physics*, 104(5-7):1081–1093, 2006.
- [220] Ilya G Ryabinkin, Loïc Joubert-Doriol, and Artur F Izmaylov. When do we need to account for the geometric phase in excited state dynamics? *The Journal of chemical physics*, 140(21):214116, 2014.
- [221] Rami Gherib, Ilya G Ryabinkin, and Artur F Izmaylov. Why do mixed quantum-classical methods describe short-time dynamics through conical intersections so well? analysis of geometric phase effects. *Journal of chemical theory and computation*, 11(4):1375–1382, 2015.
- [222] Jonas Larson, Erik Sjöqvist, and Patrik Öhberg. *Conical Intersections in Physics*. Springer, 2020.

- [223] Xing Gao, Maximilian AC Saller, Yudan Liu, Aaron Kelly, Jeremy O Richardson, and Eitan Geva. Benchmarking quasiclassical mapping hamiltonian methods for simulating electronically nonadiabatic molecular dynamics. *Journal of chemical theory and computation*, 16(5):2883–2895, 2020.
- [224] Xin He, Baihua Wu, Zhihao Gong, and Jian Liu. Commutator matrix in phase space mapping models for nonadiabatic quantum dynamics. *The Journal of Physical Chemistry A*, 125(31):6845–6863, 2021.
- [225] Xin He, Baihua Wu, Youhao Shang, Bingqi Li, Xiangsong Cheng, and Jian Liu. New phase space formulations and quantum dynamics approaches. *Wiley Interdisciplinary Reviews: Computational Molecular Science*, page e1619, 2022.
- [226] William H Miller and Stephen J Cotton. Communication: Wigner functions in action-angle variables, bohr-sommerfeld quantization, the heisenberg correspondence principle, and a symmetrical quasi-classical approach to the full electronic density matrix. *The Journal of chemical physics*, 145(8):081102, 2016.
- [227] Stephen J Cotton and William H Miller. A symmetrical quasi-classical windowing model for the molecular dynamics treatment of non-adiabatic processes involving many electronic states. *The Journal of chemical physics*, 150(10):104101, 2019.
- [228] V. Kasper, F. Hebenstreit, M. K. Oberthaler, and J. Berges. Schwinger pair production with ultracold atoms. *Phys. Lett. B*, 760:742–746, 2016.
- [229] Ali Nassimi, Sara Bonella, and Raymond Kapral. Analysis of the quantum-classical liouville equation in the mapping basis. *The Journal of chemical physics*, 133(13):134115, 2010.
- [230] Andrei A Golosov and David R Reichman. Classical mapping approaches for nonadiabatic dynamics: Short time analysis. *The Journal of Chemical Physics*, 114(3):1065–1074, 2001.
- [231] E Wigner. On the quantum correction for thermodynamic equilibrium. *Phys. Rev.*, 40:749, 1932.
- [232] Nicole Bellonzi, Amber Jain, and Joseph E Subotnik. An assessment of mean-field mixed semiclassical approaches: Equilibrium populations and algorithm stability. *The Journal of Chemical Physics*, 144(15):154110, 2016.
- [233] Jonathan Wurtz and Anatoli Polkovnikov. Quantum diffusion in spin chains with phase space methods. *Physical Review E*, 101(5):052120, 2020.
- [234] RL Stratonovich. On the statistical interpretation of quantum theory. *Soviet Phys. JETP*, 4(891), 1957.

- [235] William K Wootters. A wigner-function formulation of finite-state quantum mechanics. *Annals of Physics*, 176(1):1–21, 1987.
- [236] Jonathan R Mannouch and Jeremy O Richardson. A partially linearized spin-mapping approach for simulating nonlinear optical spectra. *The Journal of Chemical Physics*, 156(2):024108, 2022.
- [237] Xin He, Zhihao Gong, Baihua Wu, and Jian Liu. Negative zero-point-energy parameter in the meyer–miller mapping model for nonadiabatic dynamics. *The Journal of Physical Chemistry Letters*, 12(10):2496–2501, 2021.
- [238] Stephen J Cotton and William H Miller. A new symmetrical quasi-classical model for electronically non-adiabatic processes: Application to the case of weak non-adiabatic coupling. *The Journal of chemical physics*, 145(14):144108, 2016.
- [239] Reinhold A Bertlmann and Philipp Krammer. Bloch vectors for qudits. *Journal of Physics A: Mathematical and Theoretical*, 41(23):235303, 2008.
- [240] Marco Schirò, Florian G Eich, and Federica Agostini. Quantum–classical nonadiabatic dynamics of floquet driven systems. *The Journal of Chemical Physics*, 154(11):114101, 2021.
- [241] Zeyu Zhou, Joseph E Subotnik, and Hsing-Ta Chen. A protocol for spectroscopists to isolate the effect of berry geometric magnetic forces on molecular dynamics. *arXiv preprint arXiv:2008.09752*, 2020.
- [242] Yanze Wu and Joseph E Subotnik. Semiclassical description of nuclear dynamics moving through complex-valued single avoided crossings of two electronic states. *The Journal of Chemical Physics*, 154(23):234101, 2021.
- [243] Gaohan Miao, Nicole Bellonzi, and Joseph Subotnik. An extension of the fewest switches surface hopping algorithm to complex hamiltonians and photophysics in magnetic fields: Berry curvature and “magnetic” forces. *The Journal of chemical physics*, 150(12):124101, 2019.
- [244] Yanze Wu, Xuezhi Bian, Jonathan Rawlinson, Robert G Littlejohn, and Joseph E Subotnik. A phase-space semiclassical approach for modeling nonadiabatic nuclear dynamics with electronic spin. *arXiv preprint arXiv:2202.13973*, 2022.
- [245] Xing Gao, Yifan Lai, and Eitan Geva. Simulating absorption spectra of multiexcitonic systems via quasiclassical mapping hamiltonian methods. *Journal of Chemical Theory and Computation*, 16(10):6465–6480, 2020.
- [246] Tobias Kramer, Matthias Noack, Alexander Reinefeld, Mirta Rodríguez, and Yaroslav Zelinsky. Efficient calculation of open quantum system dynamics and

- time-resolved spectroscopy with distributed memory heom (dm-heom). *Journal of Computational Chemistry*, 39(22):1779–1794, 2018.
- [247] John C Tully. Molecular dynamics with electronic transitions. *The Journal of Chemical Physics*, 93(2):1061–1071, 1990.
- [248] JY Vaishnav and Charles W Clark. Observing zitterbewegung with ultracold atoms. *Physical review letters*, 100(15):153002, 2008.
- [249] Chunlei Qu, Chris Hamner, Ming Gong, Chuanwei Zhang, and Peter Engels. Observation of zitterbewegung in a spin-orbit-coupled bose-einstein condensate. *Physical Review A*, 88(2):021604, 2013.
- [250] Kathleen S Gibbons, Matthew J Hoffman, and William K Wootters. Discrete phase space based on finite fields. *Physical Review A*, 70(6):062101, 2004.
- [251] Uwe Manthe, H-D Meyer, and Lorenz S Cederbaum. Wave-packet dynamics within the multiconfiguration hartree framework: General aspects and application to noel. *The Journal of chemical physics*, 97(5):3199–3213, 1992.
- [252] Daniel F Litim and Cristina Manuel. Semi-classical transport theory for non-abelian plasmas. *Physics reports*, 364(6):451–539, 2002.
- [253] Zhi Wang, Liang Dong, Cong Xiao, and Qian Niu. Berry curvature effects on quasi-particle dynamics in superconductors. *Physical Review Letters*, 126(18):187001, 2021.
- [254] Di Xiao, Ming-Che Chang, and Qian Niu. Berry phase effects on electronic properties. *Reviews of modern physics*, 82(3):1959, 2010.
- [255] Chang-Yu Hsieh, Jeremy Schofield, and Raymond Kapral. Forward–backward solution of quantum-classical liouville equation in the adiabatic mapping basis. *Molecular Physics*, 111(22-23):3546–3554, 2013.
- [256] Stephen J Cotton, Ruibin Liang, and William H Miller. On the adiabatic representation of meyer-miller electronic-nuclear dynamics. *The Journal of chemical physics*, 147(6):064112, 2017.
- [257] In fact, the accuracy for the mapping approaches with the truncation/de-quantization of the quadratic relations [49, 75] of spin variables cannot be guaranteed.
- [258] Giovanni Granucci, Maurizio Persico, and A Toniolo. Direct semiclassical simulation of photochemical processes with semiempirical wave functions. *The Journal of Chemical Physics*, 114(24):10608–10615, 2001.

- [259] Arkajit Mandal, Sharma SRKC Yamijala, and Pengfei Huo. Quasi-diabatic representation for nonadiabatic dynamics propagation. *Journal of chemical theory and computation*, 14(4):1828–1840, 2018.
- [260] Felix Plasser, Giovanni Granucci, Jiri Pittner, Mario Barbatti, Maurizio Persico, and Hans Lischka. Surface hopping dynamics using a locally diabatic formalism: Charge transfer in the ethylene dimer cation and excited state dynamics in the 2-pyridone dimer. *The Journal of chemical physics*, 137(22):22A514, 2012.
- [261] Weiwei Xie, Marin Sapunar, Nađa Došlić, Matthieu Sala, and Wolfgang Domcke. Assessing the performance of trajectory surface hopping methods: Ultrafast internal conversion in pyrazine. *The Journal of chemical physics*, 150(15):154119, 2019.
- [262] Wanghui Zhou, Arkajit Mandal, and Pengfei Huo. Quasi-diabatic scheme for nonadiabatic on-the-fly simulations. *The journal of physical chemistry letters*, 10(22):7062–7070, 2019.
- [263] Gerald V Dunne. Quantum canonical invariance—a moyal approach. *Journal of Physics A: Mathematical and General*, 21(10):2321, 1988.
- [264] H Köppel, Wolfgang Domcke, and Lorenz S Cederbaum. Multimode molecular dynamics beyond the born-oppenheimer approximation. *Advances in chemical physics*, 57:59–246, 1984.
- [265] John Preskill. Quantum computing in the nisq era and beyond. *Quantum*, 2:79, 2018.
- [266] Pei Zeng, Jinzhao Sun, and Xiao Yuan. Universal quantum algorithmic cooling on a quantum computer. *arXiv preprint arXiv:2109.15304*, 2021.
- [267] Ryan J MacDonell, Claire E Dickerson, Clare JT Birch, Alok Kumar, Claire L Edmunds, Michael J Biercuk, Cornelius Hempel, and Ivan Kassal. Analog quantum simulation of chemical dynamics. *Chemical Science*, 12(28):9794–9805, 2021.
- [268] Chee-Kong Lee, Jonathan Wei Zhong Lau, Liang Shi, and Leong Chuan Kwek. Simulating energy transfer in molecular systems with digital quantum computers. *Journal of Chemical Theory and Computation*, 18(3):1347–1358, 2022.
- [269] Sam McArdle, Alexander Mayorov, Xiao Shan, Simon Benjamin, and Xiao Yuan. Digital quantum simulation of molecular vibrations. *Chemical science*, 10(22):5725–5735, 2019.
- [270] Javier Argüello-Luengo, Alejandro González-Tudela, Tao Shi, Peter Zoller, and Ignacio Cirac. Analogue quantum chemistry simulation. *Nature*, 574(7777):215–218, 2019.

- [271] Andrew M Childs. Universal computation by quantum walk. *Physical review letters*, 102(18):180501, 2009.
- [272] Tameem Albash and Daniel A Lidar. Adiabatic quantum computation. *Reviews of Modern Physics*, 90(1):015002, 2018.
- [273] Alastair Kay. Tutorial on the quantikz package. *arXiv preprint arXiv:1809.03842*, 2018.
- [274] David P DiVincenzo. The physical implementation of quantum computation. *Fortschritte der Physik: Progress of Physics*, 48(9-11):771–783, 2000.
- [275] Bjoern Lekitsch, Sebastian Weidt, Austin G Fowler, Klaus Mølmer, Simon J Devitt, Christof Wunderlich, and Winfried K Hensinger. Blueprint for a microwave trapped ion quantum computer. *Science Advances*, 3(2):e1601540, 2017.
- [276] Colin D Bruzewicz, John Chiaverini, Robert McConnell, and Jeremy M Sage. Trapped-ion quantum computing: Progress and challenges. *Applied Physics Reviews*, 6(2):021314, 2019.
- [277] Kenneth R Brown, John Chiaverini, Jeremy M Sage, and Hartmut Häffner. Materials challenges for trapped-ion quantum computers. *Nature Reviews Materials*, 6(10):892–905, 2021.
- [278] Frank Arute, Kunal Arya, Ryan Babbush, Dave Bacon, Joseph C Bardin, Rami Barends, Rupak Biswas, Sergio Boixo, Fernando GSL Brandao, David A Buell, et al. Quantum supremacy using a programmable superconducting processor. *Nature*, 574(7779):505–510, 2019.
- [279] Yulin Wu, Wan-Su Bao, Sirui Cao, Fusheng Chen, Ming-Cheng Chen, Xiawei Chen, Tung-Hsun Chung, Hui Deng, Yajie Du, Daojin Fan, et al. Strong quantum computational advantage using a superconducting quantum processor. *Physical review letters*, 127(18):180501, 2021.
- [280] Warren S Warren. The usefulness of nmr quantum computing. *Science*, 277(5332):1688–1690, 1997.
- [281] Joshua Ramette, Josiah Sinclair, Zachary Vendeiro, Alyssa Rudelis, Marko Cetina, and Vladan Vuletić. Any-to-any connected cavity-mediated architecture for quantum computing with trapped ions or rydberg arrays. *PRX Quantum*, 3(1):010344, 2022.
- [282] Daniel Loss and David P DiVincenzo. Quantum computation with quantum dots. *Physical Review A*, 57(1):120, 1998.

- [283] Han-Sen Zhong, Hui Wang, Yu-Hao Deng, Ming-Cheng Chen, Li-Chao Peng, Yi-Han Luo, Jian Qin, Dian Wu, Xing Ding, Yi Hu, et al. Quantum computational advantage using photons. *Science*, 370(6523):1460–1463, 2020.
- [284] Ehud Altman, Kenneth R Brown, Giuseppe Carleo, Lincoln D Carr, Eugene Demler, Cheng Chin, Brian DeMarco, Sophia E Economou, Mark A Eriksson, Kai-Mei C Fu, et al. Quantum simulators: Architectures and opportunities. *PRX Quantum*, 2(1):017003, 2021.
- [285] Don Coppersmith. An approximate fourier transform useful in quantum factoring. *arXiv preprint quant-ph/0201067*, 2002.
- [286] A Yu Kitaev. Quantum measurements and the abelian stabilizer problem. *arXiv preprint quant-ph/9511026*, 1995.
- [287] Aram W Harrow, Avinatan Hassidim, and Seth Lloyd. Quantum algorithm for linear systems of equations. *Physical review letters*, 103(15):150502, 2009.
- [288] Peter W Shor. Algorithms for quantum computation: discrete logarithms and factoring. In *Proceedings 35th annual symposium on foundations of computer science*, pages 124–134. Ieee, 1994.
- [289] Peter JJ O’Malley, Ryan Babbush, Ian D Kivlichan, Jonathan Romero, Jarrod R McClean, Rami Barends, Julian Kelly, Pedram Roushan, Andrew Tranter, Nan Ding, et al. Scalable quantum simulation of molecular energies. *Physical Review X*, 6(3):031007, 2016.
- [290] Benjamin P Lanyon, James D Whitfield, Geoff G Gillett, Michael E Goggin, Marcelo P Almeida, Ivan Kassal, Jacob D Biamonte, Masoud Mohseni, Ben J Powell, Marco Barbieri, et al. Towards quantum chemistry on a quantum computer. *Nature chemistry*, 2(2):106–111, 2010.
- [291] Lov K Grover. A fast quantum mechanical algorithm for database search. In *Proceedings of the twenty-eighth annual ACM symposium on Theory of computing*, pages 212–219, 1996.
- [292] Seth Lloyd. Universal quantum simulators. *Science*, 273(5278):1073–1078, 1996.
- [293] Markus Heyl, Philipp Hauke, and Peter Zoller. Quantum localization bounds trotter errors in digital quantum simulation. *Science advances*, 5(4):eaau8342, 2019.
- [294] Lukas M Sieberer, Tobias Olsacher, Andreas Elben, Markus Heyl, Philipp Hauke, Fritz Haake, and Peter Zoller. Digital quantum simulation, trotter errors, and quantum chaos of the kicked top. *npj Quantum Information*, 5(1):1–11, 2019.

- [295] Pauline J Ollitrault, Guglielmo Mazzola, and Ivano Tavernelli. Nonadiabatic molecular quantum dynamics with quantum computers. *Physical Review Letters*, 125(26):260511, 2020.
- [296] Simon J Devitt, William J Munro, and Kae Nemoto. Quantum error correction for beginners. *Reports on Progress in Physics*, 76(7):076001, 2013.
- [297] John Preskill. Fault-tolerant quantum computation. In *Introduction to quantum computation and information*, pages 213–269. World Scientific, 1998.
- [298] Peter W Shor. Scheme for reducing decoherence in quantum computer memory. *Physical review A*, 52(4):R2493, 1995.
- [299] Raymond Laflamme, Cesar Miquel, Juan Pablo Paz, and Wojciech Hubert Zurek. Perfect quantum error correcting code. *Physical Review Letters*, 77(1):198, 1996.
- [300] Andrew M Steane. Error correcting codes in quantum theory. *Physical Review Letters*, 77(5):793, 1996.
- [301] John Chiaverini, Dietrich Leibfried, Tobias Schaetz, Murray D Barrett, RB Blakestad, Joseph Britton, Wayne M Itano, John D Jost, Emanuel Knill, Christopher Langer, et al. Realization of quantum error correction. *Nature*, 432(7017):602–605, 2004.
- [302] Christian Kraglund Andersen, Ants Remm, Stefania Lazar, Sebastian Krinner, Nathan Lacroix, Graham J Norris, Mihai Gabureac, Christopher Eichler, and Andreas Wallraff. Repeated quantum error detection in a surface code. *Nature Physics*, 16(8):875–880, 2020.
- [303] Sam McArdle, Suguru Endo, Alán Aspuru-Guzik, Simon C Benjamin, and Xiao Yuan. Quantum computational chemistry. *Reviews of Modern Physics*, 92(1):015003, 2020.
- [304] Marco Cerezo, Andrew Arrasmith, Ryan Babbush, Simon C Benjamin, Suguru Endo, Keisuke Fujii, Jarrod R McClean, Kosuke Mitarai, Xiao Yuan, Lukasz Cincio, et al. Variational quantum algorithms. *Nature Reviews Physics*, 3(9):625–644, 2021.
- [305] Philipp Hauke, Helmut G Katzgraber, Wolfgang Lechner, Hidetoshi Nishimori, and William D Oliver. Perspectives of quantum annealing: Methods and implementations. *Reports on Progress in Physics*, 83(5):054401, 2020.
- [306] Jacob Biamonte, Peter Wittek, Nicola Pancotti, Patrick Rebentrost, Nathan Wiebe, and Seth Lloyd. Quantum machine learning. *Nature*, 549(7671):195–202, 2017.
- [307] Kristan Temme, Sergey Bravyi, and Jay M Gambetta. Error mitigation for short-depth quantum circuits. *Physical review letters*, 119(18):180509, 2017.

- [308] Ying Li and Simon C Benjamin. Efficient variational quantum simulator incorporating active error minimization. *Physical Review X*, 7(2):021050, 2017.
- [309] Nobuyuki Yoshioka, Hideaki Hakoshima, Yuichiro Matsuzaki, Yuuki Tokunaga, Yasunari Suzuki, and Suguru Endo. Generalized quantum subspace expansion. *Physical Review Letters*, 129(2):020502, 2022.
- [310] Sam McArdle, Xiao Yuan, and Simon Benjamin. Error-mitigated digital quantum simulation. *Physical review letters*, 122(18):180501, 2019.
- [311] Pjotr Grišins, Hai Son Nguyen, Jacqueline Bloch, Alberto Amo, and Iacopo Carusotto. Theoretical study of stimulated and spontaneous hawking effects from an acoustic black hole in a hydrodynamically flowing fluid of light. *Physical Review B*, 94(14):144518, 2016.
- [312] Rene Gerritsma, Gerhard Kirchmair, Florian Zähringer, E Solano, R Blatt, and CF Roos. Quantum simulation of the dirac equation. *Nature*, 463(7277):68–71, 2010.
- [313] Filippo M Gambetta, Chi Zhang, Markus Hennrich, Igor Lesanovsky, and Weibin Li. Exploring the many-body dynamics near a conical intersection with trapped rydberg ions. *Physical Review Letters*, 126(23):233404, 2021.
- [314] Frederic Hummel, Matthew T Eiles, and Peter Schmelcher. Synthetic dimension-induced conical intersections in rydberg molecules. *Physical Review Letters*, 127(2):023003, 2021.
- [315] Jinzhao Sun, Xiao Yuan, Takahiro Tsunoda, Vlatko Vedral, Simon C Benjamin, and Suguru Endo. Mitigating realistic noise in practical noisy intermediate-scale quantum devices. *Physical Review Applied*, 15(3):034026, 2021.
- [316] Kohdai Kuroiwa and Yuya O Nakagawa. Penalty methods for a variational quantum eigensolver. *Physical Review Research*, 3(1):013197, 2021.
- [317] Baidyanath Misra and EC George Sudarshan. The zeno’s paradox in quantum theory. *Journal of Mathematical Physics*, 18(4):756–763, 1977.
- [318] Wayne M Itano, Daniel J Heinzen, John J Bollinger, and David J Wineland. Quantum zeno effect. *Physical Review A*, 41(5):2295, 1990.
- [319] Daniel Burgarth, Paolo Facchi, Hiromichi Nakazato, Saverio Pascazio, and Kazuya Yuasa. Generalized adiabatic theorem and strong-coupling limits. *Quantum*, 3:152, 2019.

- [320] Julius Mildenerger, Wojciech Mruczkiewicz, Jad C Halimeh, Zhang Jiang, and Philipp Hauke. Probing confinement in a z_2 lattice gauge theory on a quantum computer. *arXiv preprint arXiv:2203.08905*, 2022.
- [321] Haifeng Lang, Philipp Hauke, Johannes Knolle, Fabian Grusdt, and Jad C Halimeh. Disorder-free localization with stark gauge protection. *arXiv preprint arXiv:2203.01338*, 2022.
- [322] Jad C Halimeh, Hongzheng Zhao, Philipp Hauke, and Johannes Knolle. Stabilizing disorder-free localization. *arXiv preprint arXiv:2111.02427*, 2021.
- [323] Jad C Halimeh, Lukas Homeier, Hongzheng Zhao, Annabelle Bohrdt, Fabian Grusdt, Philipp Hauke, and Johannes Knolle. Enhancing disorder-free localization through dynamically emergent local symmetries. *P R X Quantum*, 3:020345, 2022.
- [324] Mary K Gaillard, Paul D Grannis, and Frank J Sciulli. The standard model of particle physics. *Reviews of Modern Physics*, 71(2):S96, 1999.
- [325] Hagen Kleinert. *Gauge fields in condensed matter*, volume 2. World Scientific, 1989.
- [326] SR Beane, W Detmold, Konstantinos Orginos, and MJ Savage. Nuclear physics from lattice qcd. *Progress in Particle and Nuclear Physics*, 66(1):1–40, 2011.
- [327] John B Kogut. An introduction to lattice gauge theory and spin systems. *Reviews of Modern Physics*, 51(4):659, 1979.
- [328] Wenjian Liu. Ideas of relativistic quantum chemistry. *Molecular Physics*, 108(13):1679–1706, 2010.
- [329] Shailesh Chandrasekharan and U-J Wiese. Quantum link models: A discrete approach to gauge theories. *Nuclear Physics B*, 492(1-2):455–471, 1997.
- [330] J.R. Johansson, P.D. Nation, and Franco Nori. Qutip: An open-source python framework for the dynamics of open quantum systems. *Computer Physics Communications*, 183(8):1760 – 1772, 2012.
- [331] J.R. Johansson, P.D. Nation, and Franco Nori. Qutip 2: A python framework for the dynamics of open quantum systems. *Computer Physics Communications*, 184(4):1234 – 1240, 2013.
- [332] Cirq Developers. Cirq. March 2021. See full list of authors on Github: <https://github.com/quantumlib/Cirq/graphs/contributors>.
- [333] Anmer Daskin and Sabre Kais. Decomposition of unitary matrices for finding quantum circuits: application to molecular hamiltonians. *The Journal of chemical physics*, 134(14):144112, 2011.

-
- [334] James D Whitfield, Jacob Biamonte, and Alán Aspuru-Guzik. Simulation of electronic structure hamiltonians using quantum computers. *Molecular Physics*, 109(5):735–750, 2011.
- [335] Juan Miguel Arrazola, Olivia Di Matteo, Nicolás Quesada, Soran Jahangiri, Alain Delgado, and Nathan Killoran. Universal quantum circuits for quantum chemistry. *Quantum*, 6:742, 2022.
- [336] Maarten Van Damme, Haifeng Lang, Philipp Hauke, and Jad C Halimeh. Reliability of lattice gauge theories in the thermodynamic limit. *arXiv preprint arXiv:2104.07040*, 2021.
- [337] Jad C Halimeh, Haifeng Lang, and Philipp Hauke. Gauge protection in non-abelian lattice gauge theories. *New Journal of Physics*, 24(3):033015, 2022.

Appendices

Appendix A

Explicit time derivatives

In this Appendix, we will list the explicit time derivative expressions of $\langle \hat{O}(t) \rangle_m$ and $\langle \hat{O}(t) \rangle$ the general models, scattering models and spin-boson models.

The first, second, and third time derivatives of $\langle \hat{O}(t) \rangle$ and $\langle \hat{O}(t) \rangle_m$ for the most general observable and Hamiltonian are

$$\frac{d}{dt} \langle \hat{O}(t) \rangle_m = \int dx_0 dp_0 W_{\text{nuc}}(x_0, p_0) - i \langle \langle \text{Tr} \left\{ \hat{J}(\Gamma_0, t) [\hat{O}, \hat{V}(x_t)] \right\} \rangle \rangle, \quad (\text{A.1})$$

$$\frac{d}{dt} \langle \hat{O}(t) \rangle = -i \langle [\hat{O}(t), \hat{V}(t)] \rangle, \quad (\text{A.2})$$

$$\begin{aligned} \frac{d^2}{dt^2} \langle \hat{O}(t) \rangle_m &= \int dx_0 dp_0 W_{\text{nuc}}(x_0, p_0) \{ - \langle \langle \text{Tr} \left\{ \hat{J}(\Gamma_0, t) [[\hat{O}, \hat{V}(x_t)], \hat{V}(x_t)] \right\} \rangle \rangle \\ &\quad - i \langle \langle \text{Tr} \left\{ \hat{J}(\Gamma_0, t) \left[\hat{O}, \frac{\partial \hat{V}(x_t)}{\partial x_t} \frac{p_t}{m} \right] \right\} \rangle \rangle \}, \end{aligned} \quad (\text{A.3})$$

$$\frac{d^2}{dt^2} \langle \hat{O}(t) \rangle = - \langle [[\hat{O}(t), \hat{V}(t)], \hat{V}(t)] \rangle - i \langle [\hat{O}(t), \frac{\partial \hat{V}(t)}{\partial \hat{x}_t} \frac{\hat{p}_t}{2m} + \frac{\hat{p}_t}{2m} \frac{\partial \hat{V}(t)}{\partial \hat{x}_t}] \rangle, \quad (\text{A.4})$$

$$\begin{aligned} \frac{d^3}{dt^3} \langle \hat{O}(t) \rangle_m &= \int dx_0 dp_0 W_{\text{nuc}}(x_0, p_0) \{ i \langle \langle \text{Tr} \left\{ \hat{J}(\Gamma_0, t) [[[\hat{O}, \hat{V}(x_t)], \hat{V}(x_t)], \hat{V}(x_t)] \right\} \rangle \rangle \\ &\quad - 2 \langle \langle \text{Tr} \left\{ \hat{J}(\Gamma_0, t) \left[[\hat{O}, \frac{\partial \hat{V}(x_t)}{\partial x_t} \frac{p_t}{m}], \hat{V}(x_t) \right] \right\} \rangle \rangle - \langle \langle \text{Tr} \left\{ \hat{J}(\Gamma_0, t) \left[[\hat{O}, \hat{V}(x_t)], \frac{\partial \hat{V}(x_t)}{\partial x_t} \frac{p_t}{m} \right] \right\} \rangle \rangle \\ &\quad - i \langle \langle \text{Tr} \left\{ \hat{J}(\Gamma_0, t) \left[\hat{O}, \frac{\partial^2 \hat{V}(x_t)}{\partial x_t^2} \frac{p_t^2}{m^2} + \frac{\partial \hat{V}(x_t)}{\partial x_t} \frac{F(\Gamma_t, x_t) - \partial_{x_t} U(x_t)}{m} \right] \right\} \rangle \rangle \}. \end{aligned} \quad (\text{A.5})$$

$$\begin{aligned}
\frac{d^3}{dt^3} \langle \hat{O}(t) \rangle &= i \langle [[[\hat{O}(t), \hat{V}(t)], \hat{V}(t)], \hat{V}(t)] \rangle - 2 \langle \frac{\hat{p}_t}{2m} [[\hat{O}(t), \frac{\partial \hat{V}(t)}{\partial \hat{x}_t}], \hat{V}(t)] \rangle \\
&- 2 \langle [[\hat{O}(t), \frac{\partial \hat{V}(t)}{\partial \hat{x}_t}], \hat{V}(t)] \frac{\hat{p}_t}{2m} \rangle - \langle \frac{\hat{p}_t}{2m} [[\hat{O}(t), \hat{V}(t)], \frac{\partial \hat{V}(t)}{\partial \hat{x}_t}] \rangle - i \langle \frac{\hat{p}_t^2}{4m^2} [\hat{O}(t), \frac{\partial^2 \hat{V}(t)}{\partial \hat{x}_t^2}] \rangle \\
&+ i \langle [\hat{O}(t), \frac{\partial \hat{V}(t)}{\partial \hat{x}_t}] \frac{\partial U(t)}{\partial \hat{x}_t} \rangle \frac{1}{m} + i \langle [\hat{O}(t), \frac{\partial \hat{V}(t)}{\partial \hat{x}_t}] \frac{\partial \hat{V}(t)}{\partial \hat{x}_t} \rangle \frac{1}{2m} + i \langle \frac{\partial \hat{V}(t)}{\partial \hat{x}_t} [\hat{O}(t), \frac{\partial \hat{V}(t)}{\partial \hat{x}_t}] \rangle \frac{1}{2m} \\
&- i \langle \frac{\hat{p}_t}{2m} [\hat{O}(t), \frac{\partial^2 \hat{V}(t)}{\partial \hat{x}_t^2}] \frac{\hat{p}_t}{m} \rangle - i \langle [\hat{O}(t), \frac{\partial^2 \hat{V}(t)}{\partial \hat{x}_t^2}] \frac{\hat{p}_t^2}{4m^2} \rangle - \langle [[[\hat{O}(t), \hat{V}(t)], \frac{\partial \hat{V}(t)}{\partial \hat{x}_t}] \frac{\hat{p}_t}{2m}] \rangle,
\end{aligned} \tag{A.6}$$

where $U(t) = e^{iHt} U e^{-iHt}$ and $\hat{V}(t) = e^{iHt} \hat{V} e^{-iHt}$.

For \hat{O} spanned by $\hat{\Lambda}_D$ and \hat{H} spanned by $\hat{\Lambda}_D$ and $\hat{\Lambda}_R$, the fourth-order time derivatives of $\langle \hat{O}(t) \rangle$ and $\langle \hat{O}(t) \rangle_m$ at $t = 0$ are

$$\begin{aligned}
\frac{d^4}{dt^4} \langle \hat{O}(t) \rangle|_{t=0} &= \langle [[[[\hat{O}(0), \hat{V}(0)], \hat{V}(0)], \hat{V}(0)], \hat{V}(0)] \rangle + \langle \frac{1}{4m^2} [[\hat{O}(0), \frac{\partial^2 \hat{V}(0)}{\partial \hat{x}_0^2}], \frac{\partial^2 \hat{V}(0)}{\partial \hat{x}_0^2}] \rangle \\
&- \langle \frac{\hat{p}_0^2}{4m^2} \{3 [[\hat{O}(0), \frac{\partial \hat{V}(0)}{\partial \hat{x}_0}], \frac{\partial \hat{V}(0)}{\partial \hat{x}_0}] + 2 [[\hat{O}(0), \frac{\partial^2 \hat{V}(0)}{\partial \hat{x}_0^2}], \hat{V}(0)] + [[\hat{O}(0), \hat{V}(0)], \frac{\partial^2 \hat{V}(0)}{\partial \hat{x}_0^2}] \} \rangle \\
&- \langle \{3 [[\hat{O}(0), \frac{\partial \hat{V}(0)}{\partial \hat{x}_0}], \frac{\partial \hat{V}(0)}{\partial \hat{x}_0}] + 2 [[\hat{O}(0), \frac{\partial^2 \hat{V}(0)}{\partial \hat{x}_0^2}], \hat{V}(0)] + [[\hat{O}(0), \hat{V}(0)], \frac{\partial^2 \hat{V}(0)}{\partial \hat{x}_0^2}] \} \frac{\hat{p}_0^2}{4m^2} \rangle \\
&- \langle \frac{\hat{p}_0}{2m^2} \{3 [[\hat{O}(0), \frac{\partial \hat{V}(0)}{\partial \hat{x}_0}], \frac{\partial \hat{V}(0)}{\partial \hat{x}_0}] + 2 [[\hat{O}(0), \frac{\partial^2 \hat{V}(0)}{\partial \hat{x}_0^2}], \hat{V}(0)] + [[\hat{O}(0), \hat{V}(0)], \frac{\partial^2 \hat{V}(0)}{\partial \hat{x}_0^2}] \hat{p}_0 \} \rangle \\
&+ 2 \langle [[\hat{O}(0), \frac{\partial \hat{V}(0)}{\partial \hat{x}_0}], \hat{V}(0)] \{ \frac{\partial U(0)}{\partial \hat{x}_0} + \frac{\partial \hat{V}(0)}{\partial \hat{x}_0} \} \rangle \frac{1}{2m} \\
&+ \langle [[\hat{O}(0), \hat{V}(0)], \frac{\partial \hat{V}(0)}{\partial \hat{x}_0}] \{ \frac{\partial U(0)}{\partial \hat{x}_0} + \frac{\partial \hat{V}(0)}{\partial \hat{x}_0} \} \rangle \frac{1}{2m} \\
&+ 2 \langle \{ \frac{\partial U(0)}{\partial \hat{x}_0} + \frac{\partial \hat{V}(0)}{\partial \hat{x}_0} \} [[\hat{O}(0), \frac{\partial \hat{V}(0)}{\partial \hat{x}_0}], \hat{V}(0)] \rangle \frac{1}{2m} \\
&+ \langle \{ \frac{\partial U(0)}{\partial \hat{x}_0} + \frac{\partial \hat{V}(0)}{\partial \hat{x}_0} \} [[\hat{O}(0), \hat{V}(0)], \frac{\partial \hat{V}(0)}{\partial \hat{x}_0}] \rangle \frac{1}{2m} \\
&+ \langle \frac{1}{2m} [\hat{O}(0), \frac{\partial \hat{V}(0)}{\partial \hat{x}_0}] [\frac{\partial \hat{V}(0)}{\partial \hat{x}_0}, \hat{V}(0)] \rangle + \langle \frac{1}{2m} [\frac{\partial \hat{V}(0)}{\partial \hat{x}_0}, \hat{V}(0)] [\hat{O}(0), \frac{\partial \hat{V}(0)}{\partial \hat{x}_0}] \rangle.
\end{aligned} \tag{A.7}$$

$$\begin{aligned}
\frac{d^4}{dt^4}\langle\hat{O}(t)\rangle_m|_{t=0} &= \int dx_0 dp_0 W_{\text{nuc}}(x_0, p_0) \left\{ \hat{J}(\Gamma_0, 0) \left\{ \langle\langle \text{Tr} \left\{ -3 \left[[\hat{O}, \frac{\partial\hat{V}(x_0)}{\partial x_0}], \frac{\partial\hat{V}(x_0)}{\partial x_0} \frac{p_0^2}{m^2} \right] \right. \right. \right. \right. \\
&+ \left. \left. \left. \left. \left[[\hat{O}, \hat{V}(x_0)], \hat{V}(x_0) \right], \hat{V}(x_0) \right] - 2 \left[[\hat{O}, \frac{\partial^2\hat{V}(x_0)}{\partial x_0^2}], \hat{V}(x_0) \frac{p_0^2}{m^2} \right] \right. \right. \right. \\
&- \left. \left. \left. \left. \left[[\hat{O}, \hat{V}(x_0)], \frac{\partial^2\hat{V}(x_0)}{\partial x_0^2} \frac{p_0^2}{m^2} \right] - 2 \left[[\hat{O}, \frac{\partial\hat{V}(x_0)}{\partial x_0}], \hat{V}(x_0) \frac{F(\Gamma_0, x_0) - \partial_{x_0}U(x_0)}{m} \right] \right. \right. \right. \\
&- \left. \left. \left. \left. \left[[\hat{O}, \hat{V}(x_0)], \frac{\partial\hat{V}(x_0)}{\partial x_0} \frac{F(\Gamma_0, x_0) - \partial_{x_0}U(x_0)}{m} \right] \right. \right. \right. \\
&+ \left. \left. \left. \left. \frac{1}{m} [\hat{O}, \frac{\partial\hat{V}(x_0)}{\partial x_0}] \text{Tr} \left\{ \hat{F}(\Gamma_0) \left[\frac{\partial\hat{V}(x_0)}{\partial x_0}, \hat{V}(x_0) \right] \right\} \right\} \right\} \right\}, \tag{A.8}
\end{aligned}$$

For \hat{O} spanned by $\hat{\Lambda}_D$ and spin-boson Hamiltonian \hat{H} , the first and second time derivative of the force in the mapping approaches, the fourth, fifth, and sixth order time derivatives of $\langle\hat{O}(t)\rangle$ and $\langle\hat{O}(t)\rangle_m$ are

$$\begin{aligned}
\frac{d}{dt}F(\Gamma_t, x_t) &= i \text{Tr} \left\{ \hat{F}(\Gamma_t) \left[\frac{\partial\hat{V}(x_t)}{\partial x_t}, \hat{V}(x_t) \right] \right\}, \\
\frac{d^2}{dt^2}F(\Gamma_t, x_t) &= \text{Tr} \left\{ \hat{F}(\Gamma_t) \left[\left[\frac{\partial\hat{V}(x_t)}{\partial x_t}, \hat{V}(x_t) \right], \hat{V}(x_t) \right] \right\}, \tag{A.9}
\end{aligned}$$

$$\begin{aligned}
\frac{d^4}{dt^4}\langle\hat{O}(t)\rangle_m &= \int dx_0 dp_0 W_{\text{nuc}}(x_0, p_0) \langle\langle \text{Tr} \left\{ \hat{J}(\Gamma_0, t) \left\{ \left[\left[[\hat{O}, \hat{V}(x_t)], \hat{V}(x_t) \right], \hat{V}(x_t) \right], \hat{V}(x_t) \right] \right. \right. \right. \\
&+ 2i \left[[\hat{O}, \hat{V}(x_t)], \frac{\partial\hat{V}(x_t)}{\partial x_t} \frac{p_t}{m}, \hat{V}(x_t) \right] + i \left[[\hat{O}, \hat{V}(x_t)], \hat{V}(x_t) \right], \frac{\partial\hat{V}(x_t)}{\partial x_t} \frac{p_t}{m} \\
&- \left. \left. \left. \left. \left[[\hat{O}, \hat{V}(x_t)], \frac{\partial\hat{V}(x_t)}{\partial x_t} \frac{F(\Gamma_t, x_t) - \partial_{x_t}U(x_t)}{m} \right] \right\} \right\} \right\rangle, \tag{A.10}
\end{aligned}$$

$$\begin{aligned}
\frac{d^4}{dt^4}\langle\hat{O}(t)\rangle &= \langle \left[\left[[\hat{O}(t), \hat{V}(t)], \hat{V}(t) \right], \hat{V}(t) \right], \hat{V}(t) \rangle + \langle \left[[\hat{O}(t), \hat{V}(t)], \frac{\partial\hat{V}(t)}{\partial \hat{x}_t} \right], \frac{\partial U(t)}{\partial \hat{x}_t} \rangle \frac{1}{m} \\
&+ i \langle \frac{\hat{p}_t}{2m} \{ 2 \left[[\hat{O}(t), \hat{V}(t)], \frac{\partial\hat{V}(t)}{\partial \hat{x}_t} \right], \hat{V}(t) \right] + \left[[\hat{O}(t), \hat{V}(t)], \hat{V}(t) \right], \frac{\partial\hat{V}(t)}{\partial \hat{x}_t} \} \rangle \\
&+ i \langle \{ 2 \left[[\hat{O}(t), \hat{V}(t)], \frac{\partial\hat{V}(t)}{\partial \hat{x}_t} \right], \hat{V}(t) \right] + \left[[\hat{O}(t), \hat{V}(t)], \hat{V}(t) \right], \frac{\partial\hat{V}(t)}{\partial \hat{x}_t} \} \frac{\hat{p}_t}{2m} \rangle \\
&+ \langle \left[[\hat{O}(t), \hat{V}(t)], \frac{\partial\hat{V}(t)}{\partial \hat{x}_t} \right], \frac{\partial\hat{V}(t)}{\partial \hat{x}_t} \rangle \frac{1}{2m} + \langle \frac{\partial\hat{V}(t)}{\partial \hat{x}_t} \left[[\hat{O}(t), \hat{V}(t)], \frac{\partial\hat{V}(t)}{\partial \hat{x}_t} \right] \rangle \frac{1}{2m}, \tag{A.11}
\end{aligned}$$

$$\begin{aligned}
\frac{d^5}{dt^5} \langle \hat{O}(t) \rangle_m &= \int dx_0 dp_0 W_{\text{nuc}}(x_0, p_0) \langle \langle \text{Tr} \left\{ \hat{J}(\Gamma_0, t) \right. \\
&\times \left. \left\{ -i \left[\left[\left[[\hat{O}, \hat{V}(x_t)], \hat{V}(x_t) \right], \hat{V}(x_t) \right], \hat{V}(x_t) \right] \right. \right. \\
&+ 3 \left[\left[[\hat{O}, \hat{V}(x_t)], \frac{\partial \hat{V}(x_t) p_t}{\partial x_t m}, \hat{V}(x_t) \right], \hat{V}(x_t) \right] + 2 \left[\left[[\hat{O}, \hat{V}(x_t)], \hat{V}(x_t) \right], \frac{\partial \hat{V}(x_t) p_t}{\partial x_t m}, \hat{V}(x_t) \right] \\
&+ \left[\left[[\hat{O}, \hat{V}(x_t)], \hat{V}(x_t) \right], \hat{V}(x_t) \right], \frac{\partial \hat{V}(x_t) p_t}{\partial x_t m} \left. \right\} + 3i \left[\left[[\hat{O}, \hat{V}(x_t)], \frac{\partial \hat{V}(x_t) p_t}{\partial x_t m}, \frac{\partial \hat{V}(x_t) p_t}{\partial x_t m} \right] \right. \\
&+ i \frac{F(\Gamma_t, x_t) - \partial_{x_t} U(x_t)}{m} \left. \left\{ 2 \left[\left[[\hat{O}, \hat{V}(x_t)], \frac{\partial \hat{V}(x_t)}{\partial x_t} \right], \hat{V}(x_t) \right] + \left[\left[[\hat{O}, \hat{V}(x_t)], \hat{V}(x_t) \right], \frac{\partial \hat{V}(x_t)}{\partial x_t} \right] \right\} \right. \\
&\left. - \left[[\hat{O}, \hat{V}(x_t)], \frac{\partial \hat{V}(x_t)}{\partial x_t} \left\{ -\frac{\partial_{x_t}^2 U(x_t) p_t}{m^2} + \frac{d}{dt} \frac{F(\Gamma_t, x_t)}{m} \right\} \right] \right\} \rangle, \tag{A.12}
\end{aligned}$$

$$\begin{aligned}
\frac{d^5}{dt^5} \langle \hat{O}(t) \rangle &= -i \langle \left[\left[\left[[\hat{O}(t), \hat{V}(t)], \hat{V}(t) \right], \hat{V}(t) \right], \hat{V}(t) \right] \rangle \\
&+ 2 \left[\left[\left[[\hat{O}(t), \hat{V}(t)], \hat{V}(t) \right], \frac{\partial \hat{V}(t)}{\partial \hat{x}_t} \right], \hat{V}(t) \right] + \left[\left[\left[[\hat{O}(t), \hat{V}(t)], \hat{V}(t) \right], \hat{V}(t) \right], \frac{\partial \hat{V}(t)}{\partial \hat{x}_t} \right] \left. \right\} \\
&+ \langle \left\{ 3 \left[\left[\left[[\hat{O}(t), \hat{V}(t)], \frac{\partial \hat{V}(t)}{\partial \hat{x}_t} \right], \hat{V}(t) \right], \hat{V}(t) \right] + 2 \left[\left[\left[[\hat{O}(t), \hat{V}(t)], \hat{V}(t) \right], \frac{\partial \hat{V}(t)}{\partial \hat{x}_t} \right], \hat{V}(t) \right] \right. \right. \\
&+ \left[\left[\left[[\hat{O}(t), \hat{V}(t)], \hat{V}(t) \right], \hat{V}(t) \right], \frac{\partial \hat{V}(t)}{\partial \hat{x}_t} \right] \left. \right\} \frac{\hat{p}_t}{2m} \rangle + 3i \langle \frac{\hat{p}_t^2}{m^2} \left[\left[[\hat{O}(t), \hat{V}(t)], \frac{\partial \hat{V}(t)}{\partial \hat{x}_t} \right], \frac{\partial \hat{V}(t)}{\partial \hat{x}_t} \right] \rangle \\
&- i \langle \frac{\partial U(t)}{\partial \hat{x}_t} \left\{ 2 \left[\left[[\hat{O}(t), \hat{V}(t)], \frac{\partial \hat{V}(t)}{\partial \hat{x}_t} \right], \hat{V}(t) \right] + \left[\left[[\hat{O}(t), \hat{V}(t)], \hat{V}(t) \right], \frac{\partial \hat{V}(t)}{\partial \hat{x}_t} \right] \right\} \frac{1}{m} \rangle \\
&- i \langle \frac{\partial \hat{V}(t)}{\partial \hat{x}_t} \left\{ 2 \left[\left[[\hat{O}(t), \hat{V}(t)], \frac{\partial \hat{V}(t)}{\partial \hat{x}_t} \right], \hat{V}(t) \right] + \left[\left[[\hat{O}(t), \hat{V}(t)], \hat{V}(t) \right], \frac{\partial \hat{V}(t)}{\partial \hat{x}_t} \right] \right\} \frac{1}{2m} \rangle \\
&- i \langle \left\{ 2 \left[\left[[\hat{O}(t), \hat{V}(t)], \frac{\partial \hat{V}(t)}{\partial \hat{x}_t} \right], \hat{V}(t) \right] + \left[\left[[\hat{O}(t), \hat{V}(t)], \hat{V}(t) \right], \frac{\partial \hat{V}(t)}{\partial \hat{x}_t} \right] \right\} \frac{\partial \hat{V}(t)}{\partial \hat{x}_t} \frac{1}{2m} \rangle \\
&- i \langle \left[\frac{\partial \hat{V}(t)}{\partial \hat{x}_t}, \hat{V}(t) \right] \left[[\hat{O}(t), \hat{V}(t)], \frac{\partial \hat{V}(t)}{\partial \hat{x}_t} \right] \frac{1}{2m} \rangle - i \langle \left[[\hat{O}(t), \hat{V}(t)], \frac{\partial \hat{V}(t)}{\partial \hat{x}_t} \right] \left[\frac{\partial \hat{V}(t)}{\partial \hat{x}_t}, \hat{V}(t) \right] \frac{1}{2m} \rangle \\
&+ \langle \left[[\hat{O}(t), \hat{V}(t)], \frac{\partial \hat{V}(t)}{\partial \hat{x}_t} \right] \frac{\partial^2 U(t)}{\partial \hat{x}_t^2} \frac{\hat{p}_t}{m^2} \rangle + \langle \frac{\hat{p}_t}{2m} \left\{ 3 \left[\left[\left[[\hat{O}(t), \hat{V}(t)], \frac{\partial \hat{V}(t)}{\partial \hat{x}_t} \right], \hat{V}(t) \right], \hat{V}(t) \right] \right\} \rangle, \tag{A.13}
\end{aligned}$$

$$\begin{aligned}
\frac{d^6}{dt^6} \langle \hat{O}(t) \rangle_{\text{m}}|_{t=0} &= \int dx_0 dp_0 W_{\text{nuc}}(x_0, p_0) \langle \langle \text{Tr} \left\{ \hat{J}(\Gamma_0, t) \right. \\
&\times \left\{ - \left[\left[\left[\left[[\hat{O}, \hat{V}(x_0)], \hat{V}(x_0) \right], \hat{V}(x_0) \right], \hat{V}(x_0) \right], \hat{V}(x_0) \right] \right. \\
&+ 8 \frac{p_0^2}{m^2} \left[\left[[\hat{O}, \hat{V}(x_0)], \frac{\partial \hat{V}(x_0)}{\partial x_0} \right], \frac{\partial \hat{V}(x_0)}{\partial x_0} \right], \hat{V}(x_0) \right] + \frac{1}{m} \left\{ - \frac{\partial U(x_0)}{\partial x_0} - \text{Tr} \left\{ \hat{F}(\Gamma_0) \frac{\partial \hat{V}(x_0)}{\partial x_0} \right\} \right\} \\
&\times \left\{ 5 \left[\left[[\hat{O}, \hat{V}(x_0)], \frac{\partial \hat{V}(x_0)}{\partial x_0} \right], \hat{V}(x_0) \right], \hat{V}(x_0) \right] + 3 \left[\left[[\hat{O}, \hat{V}(x_0)], \hat{V}(x_0) \right], \frac{\partial \hat{V}(x_0)}{\partial x_0} \right], \hat{V}(x_0) \right] \left. \right\} \\
&- \frac{1}{m} \text{Tr} \left\{ \hat{F}(\Gamma_0) \left[\frac{\partial \hat{V}(x_0)}{\partial x_0}, \hat{V}(x_0) \right] \right\} 3 \left[[\hat{O}, \hat{V}(x_0)], \frac{\partial \hat{V}(x_0)}{\partial x_0} \right], \hat{V}(x_0) \right] \\
&- \frac{1}{m} \text{Tr} \left\{ \hat{F}(\Gamma_0) \left[\frac{\partial \hat{V}(x_0)}{\partial x_0}, \hat{V}(x_0) \right] \right\} \left[[\hat{O}, \hat{V}(x_0)], \hat{V}(x_0) \right], \frac{\partial \hat{V}(x_0)}{\partial x_0} \right] \\
&- \frac{1}{m} \text{Tr} \left\{ \hat{F}(\Gamma_0) \left[\left[\frac{\partial \hat{V}(x_0)}{\partial x_0}, \hat{V}(x_0) \right], \hat{V}(x_0) \right] \right\} \left[[\hat{O}, \hat{V}(x_0)], \frac{\partial \hat{V}(x_0)}{\partial x_0} \right] \left. \right\} \rangle, \tag{A.14}
\end{aligned}$$

$$\begin{aligned}
\frac{d^6}{dt^6} \langle \hat{O}(t) \rangle|_{t=0} &= \langle - \left[\left[\left[\left[[\hat{O}(0), \hat{V}(0)], \hat{V}(0) \right], \hat{V}(0) \right], \hat{V}(0) \right], \hat{V}(0) \right] \right. \\
&+ 8 \frac{\hat{p}_0^2}{m^2} \left[\left[[\hat{O}(0), \hat{V}(0)], \frac{\partial \hat{V}(0)}{\partial \hat{x}_0} \right], \frac{\partial \hat{V}(0)}{\partial \hat{x}_0} \right], \hat{V}(0) \right] + \frac{1}{m} \left\{ - \frac{\partial U(0)}{\partial \hat{x}_0} - \frac{\partial \hat{V}(0)}{\partial \hat{x}_0} \right\} \\
&\times \left\{ 5 \left[\left[[\hat{O}, \hat{V}(0)], \frac{\partial \hat{V}(0)}{\partial \hat{x}_0} \right], \hat{V}(0) \right], \hat{V}(0) \right] + 3 \left[\left[[\hat{O}(0), \hat{V}(0)], \hat{V}(0) \right], \frac{\partial \hat{V}(0)}{\partial \hat{x}_0} \right], \hat{V}(0) \right] \left. \right\} \\
&- \frac{1}{2m} \left[\frac{\partial \hat{V}(0)}{\partial \hat{x}_0}, \hat{V}(0) \right] \left\{ 3 \left[[\hat{O}(0), \hat{V}(0)], \frac{\partial \hat{V}(0)}{\partial \hat{x}_0} \right], \hat{V}(0) \right] + \left[[\hat{O}(0), \hat{V}(0)], \hat{V}(0) \right], \frac{\partial \hat{V}(0)}{\partial \hat{x}_0} \right\} \\
&- \frac{1}{2m} \left\{ 3 \left[[\hat{O}(0), \hat{V}(0)], \frac{\partial \hat{V}(0)}{\partial \hat{x}_0} \right], \hat{V}(0) \right] + \left[[\hat{O}(0), \hat{V}(0)], \hat{V}(0) \right], \frac{\partial \hat{V}(0)}{\partial \hat{x}_0} \right\} \left[\frac{\partial \hat{V}(0)}{\partial \hat{x}_0}, \hat{V}(0) \right] \\
&- \frac{1}{2m} \left\{ \left[\left[\frac{\partial \hat{V}(0)}{\partial \hat{x}_0}, \hat{V}(0) \right], \hat{V}(0) \right] \left[[\hat{O}(0), \hat{V}(0)], \frac{\partial \hat{V}(0)}{\partial \hat{x}_0} \right] \right. \\
&+ \left. \left[[\hat{O}(0), \hat{V}(0)], \frac{\partial \hat{V}(0)}{\partial \hat{x}_0} \right] \left[\left[\frac{\partial \hat{V}(0)}{\partial \hat{x}_0}, \hat{V}(0) \right], \hat{V}(0) \right] \right\} \rangle, \tag{A.15}
\end{aligned}$$

$$\begin{aligned}
& \frac{d^6}{dt^6} \langle \hat{O}(t) \rangle_m |_{t=0} - \frac{d^6}{dt^6} \langle \hat{O}(t) \rangle |_{t=0} = \langle \frac{1}{2m} \{ [[\frac{\partial \hat{V}(0)}{\partial \hat{x}_0}, \hat{V}(0)], \hat{V}(0)] [[\hat{O}(0), \hat{V}(0)], \frac{\partial \hat{V}(0)}{\partial \hat{x}_0}] \\
& + [[\hat{O}(0), \hat{V}(0)], \frac{\partial \hat{V}(0)}{\partial \hat{x}_0}] [[\frac{\partial \hat{V}(0)}{\partial \hat{x}_0}, \hat{V}(0)], \hat{V}(0)] \} \} \\
& + \frac{1}{2m} \frac{\partial \hat{V}(0)}{\partial \hat{x}_0} \{ 5 [[[[\hat{O}, \hat{V}(0)], \frac{\partial \hat{V}(0)}{\partial \hat{x}_0}], \hat{V}(0)], \hat{V}(0)] \\
& + 3 [[[[\hat{O}(0), \hat{V}(0)], \hat{V}(0)], \frac{\partial \hat{V}(0)}{\partial \hat{x}_0}], \hat{V}(0)] \} \\
& + \frac{1}{2m} [\frac{\partial \hat{V}(0)}{\partial \hat{x}_0}, \hat{V}(0)] \{ 3 [[[\hat{O}(0), \hat{V}(0)], \frac{\partial \hat{V}(0)}{\partial \hat{x}_0}], \hat{V}(0)] + [[[\hat{O}(0), \hat{V}(0)], \hat{V}(0)], \frac{\partial \hat{V}(0)}{\partial \hat{x}_0}] \} \\
& + \frac{1}{2m} \{ 3 [[[\hat{O}(0), \hat{V}(0)], \frac{\partial \hat{V}(0)}{\partial \hat{x}_0}], \hat{V}(0)] + [[[\hat{O}(0), \hat{V}(0)], \hat{V}(0)], \frac{\partial \hat{V}(0)}{\partial \hat{x}_0}] [\frac{\partial \hat{V}(0)}{\partial \hat{x}_0}, \hat{V}(0)] \} \\
& - \frac{1}{m} \int dx_0 dp_0 W_{\text{nuc}}(x_0, p_0) \langle \langle \text{Tr} \left\{ \hat{J}(\Gamma_0, 0) \left\{ \text{Tr} \left\{ \hat{F}(\Gamma_0) [[\frac{\partial \hat{V}(x_0)}{\partial x_0}, \hat{V}(x_0)], \hat{V}(x_0)] \right\} \right\} \right. \\
& \times [[\hat{O}, \hat{V}(x_0)], \frac{\partial \hat{V}(x_0)}{\partial x_0}] + \text{Tr} \left\{ \hat{F}(\Gamma_0) \frac{\partial \hat{V}(x_0)}{\partial x_0} \right\} \left. \{ 5 [[[[\hat{O}, \hat{V}(x_0)], \frac{\partial \hat{V}(x_0)}{\partial x_0}], \hat{V}(x_0)], \hat{V}(x_0)] \right. \\
& + 3 [[[[\hat{O}, \hat{V}(x_0)], \hat{V}(x_0)], \frac{\partial \hat{V}(x_0)}{\partial x_0}], \hat{V}(x_0)] \} + \text{Tr} \left\{ \hat{F}(\Gamma_0) [\frac{\partial \hat{V}(x_0)}{\partial x_0}, \hat{V}(x_0)] \right\} \\
& \times \left. \{ 3 [[[\hat{O}, \hat{V}(x_0)], \frac{\partial \hat{V}(x_0)}{\partial x_0}], \hat{V}(x_0)] + [[[\hat{O}, \hat{V}(x_0)], \hat{V}(x_0)], \frac{\partial \hat{V}(x_0)}{\partial x_0}] \} \right\rangle \rangle, \tag{A.16}
\end{aligned}$$

where we already neglect the trivial canceling terms. Using the properties of Wigner transformation Eq. (3.4,3.3) as well as the properties of the spin–boson model Eq. (3.87), we obtain that the fourth and fifth order derivatives of $\langle \hat{O}(t) \rangle$ and $\langle \hat{O}(t) \rangle_m$ at $t = 0$ coincide, while the sixth order derivatives coincide if the method can sample the intra-electron correlation correctly.

Acknowledgements

Time flies very fast, especially during the Ph.D career with the pandemic. Now it is the end of my Ph.D student time in Heidelberg. Above all, I want to thank my supervisors Philipp Hans Juergen Hauke and Oriol Vendrell Romagosa. Many bachelor students in the world had moved up gradually, I was a bachelor, and then a research assistant in Kirchhoff institute for physics, Heidelberg. In fact, I did not think I would be transferred to the Chemistry department here in Heidelberg. I really appreciate the assistance of Philipp and Oriol. It would never be possible for me to be a Ph.D student in Chemistry department, Heidelberg University without their help.

I would like to use words people used to describe nature to describe the research. It feels like experiencing wind, rain and sometimes cloud or even dark clouds. However sometimes it clears up and makes you excited. Philipp and Oriol guided me a lot to the sunshine. I learned a lot from them, not only the scientific intuition but also excellent writing skills.

A particular thank goes to Jad C Halimeh. He co-supervised me on the quantum simulation projects. We also have plenty of stimulating discussions. More importantly, it is impossible to have the quantum simulations chapters of this thesis without his excellent numerical simulations.

Additionally, I thank all my collaborators during my Ph.D career (in alphabetical order) Maarten Van Damme, Fabian Grusdt, Markus Heyl, Zhang Jiang, Johannes Knolle, Johannes Lang and Julius Mildenerger.

I also thank Hans-Dieter Meyer, Sudip Sasmal and Markus Schröder for their technical support on MCTDH simulations and stimulating discussions. Their support is crucial for the numerical results on the molecular systems in this thesis.

Also, I thank all the other group members in Heidelberg and Trento. The brilliant presentations and helpful discussions on the group seminar boarden my horizons on physics and chemistry.

Special thanks also go to the administration staffs Annette Braun, Monica Cosi, Tatsiana Egorova, Anna Frattin, Dagmar Hufnagel, Christiane Jäger, Beatrice Ricci, Elke Schmetzer and Harald Jacobsen at Heidelberg and Trento. Your assistance provides the possibility to focus on my research.

Last but not least, I would like to thank all the people and organizations who helped me (and will help me) in my entire life. I hope to convey through this thesis my best wishes to all of you.

List of Papers

Results presented in this work:

- **H. Lang**, O. Vendrell, and P. Hauke, “Short-time Accuracy and Intra-electron Correlation for Nonadiabatic Quantum-Classical Mapping Approaches”, in preparation.
- **H. Lang**, O. Vendrell, and P. Hauke, “Generalized Discrete Truncated Wigner Approximation for Nonadiabatic Quantum-Classical Dynamics”, *The Journal of Chemical Physics* 155 (2), 024111.
- **H. Lang**, O. Vendrell, and P. Hauke, “Generalized Discrete Truncated Wigner Approximation for Nonadiabatic Dynamics of Particles in Synthetic Non-Abelian Gauge Fields”, submitted to PRA, in revision.
- JC. Halimeh, **H. Lang**, J. Mildenerger, Z. Jiang, and P. Hauke, “Gauge-symmetry protection using single-body terms”, *PRX Quantum* 2 (4), 040311.

Papers not included in the thesis:

- M. Van Damme, **H. Lang**, P. Hauke, and JC. Halimeh, “Reliability of lattice gauge theories in the thermodynamic limit”, arXiv preprint arXiv:2104.07040. (co-first author)
- **H. Lang**, JC. Halimeh, J. Knolle, F. Grusdt, JC. Halimeh, “Disorder-free localization with stark gauge protection”, arXiv preprint arXiv:2203.01338.
- JC. Halimeh, **H. Lang**, and P. Hauke, “Gauge protection in non-abelian lattice gauge theories”, *New Journal of Physics* 24 (3), 033015.

Eidesstattliche Versicherung

Eidesstattliche Versicherung gemäß §8 der Promotionsordnung der Naturwissenschaftlichen-Mathematischen Gesamtfakultät der Universität Heidelberg

1. Bei der eingereichten Dissertation zu dem Thema “Quantum Dynamics of Chemical Systems with Large Number of Degrees of Freedom: Linearized Phase Space Methods and Quantum Simulations” handelt es sich um meine eigenständig erbrachte Leistung.
2. Ich habe nur die angegebenen Quellen und Hilfsmittel benutzt und mich keiner unzulässigen Hilfe Dritter bedient. Insbesondere habe ich wörtlich oder sinngemäß aus anderen Werken übernommene Inhalte als solche kenntlich gemacht.
3. Die Arbeit oder Teile davon habe ich bislang nicht an einer Hochschule des In- oder Auslands als Bestandteil einer Prüfungs- oder Qualifikationsleistung vorgelegt.
4. Die Richtigkeit der vorstehenden Erklärungen bestätige ich.
5. Die Bedeutung der eidesstattlichen Versicherung und die strafrechtlichen Folgen einer unrichtigen oder unvollständigen eidesstattlichen Versicherung sind mir bekannt.

Ich versichere an Eides statt, dass ich nach bestem Wissen die reine Wahrheit erklärt und nichts verschwiegen habe.

Ort, Datum

Unterschrift